ELECTROMAGNETICALLY TRANSPARENT TRIBAND QUAD-POLARIZATION SHARED APERTURE CROSS DIPOLE ANTENNA DESIGN

A THESIS SUBMITTED TO
THE GRADUATE SCHOOL OF NATURAL AND APPLIED SCIENCES
OF
MIDDLE EAST TECHNICAL UNIVERSITY

BY

ORHUN ÇETİN

IN PARTIAL FULFILLMENT OF THE REQUIREMENTS
FOR
THE DEGREE OF MASTER OF SCIENCE
IN
ELECTRICAL AND ELECTRONICS ENGINEERING

NOVEMBER 2024

Approval of the thesis:

ELECTROMAGNETICALLY TRANSPARENT TRIBAND QUAD-POLARIZATION SHARED APERTURE CROSS DIPOLE ANTENNA DESIGN

submitted by **ORHUN ÇETİN** in partial fulfillment of the requirements for the degree of **Master of Science in Electrical and Electronics Engineering Department, Middle East Technical University** by,

Prof. Dr. Naci Emre ALTUN
Dean, Graduate School of **Natural and Applied Sciences** _____

Prof. Dr. İlkay Ulusoy
Head of Department, **Electrical and Electronics Engineering** _____

Prof. Dr. Gülbin Dural
Supervisor, **Electrical and Electronics Engineering, METU** _____

Examining Committee Members:

Prof. Dr. Sencer Koç
Electrical and Electronics Engineering, METU _____

Prof. Dr. Gülbin Dural
Electrical and Electronics Engineering, METU _____

Prof. Dr. Özlem Aydın Çivi
Electrical and Electronics Engineering, METU _____

Assist. Prof. Dr. Lale Alatan
Electrical and Electronics Engineering, METU _____

Prof. Dr. Birsen Saka
Electrical and Electronics Engineering, Hacettepe University _____

Date:26.11.2024

I hereby declare that all information in this document has been obtained and presented in accordance with academic rules and ethical conduct. I also declare that, as required by these rules and conduct, I have fully cited and referenced all material and results that are not original to this work.

Name, Surname: Orhun Çetin

Signature :

ABSTRACT

ELECTROMAGNETICALLY TRANSPARENT TRIBAND QUAD-POLARIZATION SHARED APERTURE CROSS DIPOLE ANTENNA DESIGN

Çetin, Orhun
M.S., Department of Electrical and Electronics Engineering
Supervisor: Prof. Dr. Gülbin Dural

November 2024, 203 pages

A shared aperture triband antenna is designed and realized to be used in wireless communication applications. Antennas are designed based on frequency-selective surfaces, so that these antennas also have electromagnetically transparent surface characteristics. Hence they can be placed in the vicinity of each other in a shared-aperture form without affecting their radiation characteristics. The triband antenna includes three different antennas as follows: the low-frequency band antenna which is operated between 1 to 1.6 GHz, the middle-frequency band antenna which is operated between 1.8 to 2.9 GHz, which includes 2G/3G/4G communication bands, and the high-frequency band antenna which is operated between 3.3 to 5.5 GHz, which includes 5G communication bands. The low-frequency band antenna is added as a third antenna to observe the extendability of the shared-aperture antenna concept to serve more frequency bands.

Firstly, electromagnetic transparent surfaces are designed and analyzed via ™HFSS program. Then cross-dipole antennas are designed from the transparent surface and simulations are made for single antenna, shared-aperture antenna, and different po-

larizations. Finally, antenna prototypes are fabricated and measurement results are compared with the simulations. Results show that the designed antennas can provide slant +45° and -45° dual polarization as linear polarizations, and both left & right-hand circular polarizations by feeding with a 90° phase shift, for both single and multiband antenna cases.

Keywords: frequency selective surface, cross dipole antenna, shared aperture, electromagnetically transparent, quad-polarization

ÖZ

ELEKTROMANYETİK SAYDAM ÜÇ BANTLI DÖRT POLARİZASYONLU ORTAK AÇIKLIKLI ÇAPRAZ DİPOL ANTEN TASARIMI

Çetin, Orhun
Yüksek Lisans, Elektrik ve Elektronik Mühendisliği Bölümü
Tez Yöneticisi: Prof. Dr. Gülbin Dural

Kasım 2024 , 203 sayfa

Kablosuz iletişim uygulamalarında kullanılmak üzere ortak açıklıklı üç bantlı anten tasarlanmıştır. Antenler aynı zamanda frekans seçici yüzey temelinde tasarlanmış, ve böylece elektromanyetik saydamlık özelliğine sahip olmuştur. Bu sayede antenler, ışınım özellikleri etkilenmeden birbirlerinin yakınına yerleştirilebilecektir. Üç bantlı anten, 1-1.6 GHz aralığında çalışan düşük-frekans anteni, 2G/3G/4G iletişim bantlarını içeren 1.8-2.9 GHz aralığında çalışan orta-frekans anteni ve 5G iletişim bantlarını içeren 3.3-5.5 GHz aralığında çalışan yüksek-frekans anteni olacak şekilde üç farklı anteni içermektedir. Ortak açıklıklı anten konseptinin genişletilerek daha fazla frekans bandına hizmet verebilmesinin gözlemlenmesi için üçüncü anten olan düşük frekans anteni eklenmiştir.

İlk olarak elektromanyetik saydam yüzeyler ™HFSS programı ile tasarlanmış ve analiz edilmiştir. Sonrasında çapraz dipol antenler saydam yüzey üzerinden tasarlanmıştır ve tek anten, ortak açıklıklı anten ve farklı polarizasyonlarda benzetimler yapılmıştır. Son olarak, anten prototipleri üretilmiş ve ölçüm sonuçları benzetimlerle karşılaştırılmıştır. Sonuçlar, tasarlanan antenlerin hem tek anten hem de çok bantlı anten du-

rumlarında doğrusal polarizasyon olarak eğik +45° ve -45° çift polarizasyon ve 90° faz kaymasıyla beslenerek hem sol hem de sağ dairesel polarizasyon sağlayabildiğini göstermiştir.

Anahtar Kelimeler: frekans seçici yüzey, çapraz dipol anten, ortak açıklık, elektromanyetik saydam, dörtlü polarizasyon

To my family's finest, Mualla ÇAM...

ACKNOWLEDGMENTS

Foremost, I would like to thank my supervisor Prof. Dr. Gülbin Dural for her endless and invaluable support, and unending motivation throughout the thesis. Without her guidance and help, this thesis could not be successful and completed.

I offer my sincerest thanks to my thesis defense jury, Prof. Dr. Sencer Koç, Prof. Dr. Özlem Aydın Çivi, Assoc. Prof. Dr. Lale Alatan, and Prof. Dr. Birsen Saka, for attending my defense and sharing their valuable comments and feedback.

Also one of my most sincere thanks must go to Kaan Arda and Mesut Göksu for helping me with measurement laboratories and crucial comments about the thesis in ASELSAN Inc. Their help significantly improved my thesis both theoretically and experimentally.

I appreciate ASELSAN Inc. for the measurement laboratories and resources to fabricate the products.

Lastly, I owe my deepest thanks to my mother Ayşe Gül Çetin, my father Mustafa Çetin, and my brother Onur Arda Çetin for their unrequited and endless love, support, motivation, encouragement, sacrifices, and caring in all cases in my life. They are always by my side emotionally and morally. I would also like to thank Uncle Fatih Çam, and my cousin Orbay Çam for their motivational speeches and encouragement throughout the thesis. I would like to express my utmost gratitude to my grandmother, Mualla Çam, for looking after me, raising me, educating me during my childhood, and becoming the mother of the whole family. You will always be in our hearts, rest in peace.

TABLE OF CONTENTS

LIST OF TABLES

TABLES

LIST OF FIGURES

FIGURES

LIST OF ABBREVIATIONS

ABBREVIATIONS

0G	Zero Generation Technology
1G	First Generation Technology
2D	2 Dimensional
2G	Second Generation Technology
3D	3 Dimensional
3G	Third Generation Technology
4G	Fourth Generation Technology
5G	Fifth Generation Technology
AMC	Artificial Magnetic Conductor
BW	Bandwidth
CP	Circular Polarization
EC	Equivalent Circuit
EM	Electromagnetic
EDGE	Enhanced Data Rates for GSM Evolution
FDTD	Finite Difference Time Domain
FEM	Finite Element Method
FSS	Frequency Selective Surface
Gbps	Gigabits per second
GHz	Gigahertz
GND	Ground
GPRS	General Packet Radio Service
GPS	Global Positioning System

GSM	Global System for Mobile Communications
HB	High Band
HIS	High Impedance Surface
HPBW	Half Power Beamdwidth
Kbps	Kilobits per second
kHz	kilohertz
LB	Low Band
LHCP	Left-Hand Circular Polarization
MB	Middle Band
Mbps	Megabits per second
MHz	Megahertz
MoM	Method of Moments
PCB	Printed Circuit Board
PTFE	Polytetrafluoroethylene
PTS	Partially Transmitting Surface
RCS	Radar Cross Section
RFID	Radio Frequency Identification
RHCP	Right-Hand Circular Polarization
SAR	Synthetic Aperture Radar
SMA	Sub-Miniature Version A
SNR	Signal-to-noise-ratio
TZ	Transmission Zero
WLAN	Wireless Local Area Network

CHAPTER 1

INTRODUCTION

1.1 Background

Undoubtedly, antennas have been one of the crucial devices in data transmission since the beginning of 20^{th} century. They have been used in various fields, such as communications, airborne, weather forecasting, satellites, intelligence, and military. Considering the technological advancements throughout history, various antennas have been designed, developed, and used according to their application purposes. The fundamental features of the designed antennas -like bandwidth, operating frequency, gain, polarization type, beamwidth, etc.- have changed and improved in the course of time.

One of the most common application areas of antennas is wireless communication systems. Mobile communication has become more effective with the wide usage of antenna systems. Thanks to mobile communication systems, people can reach one another at further distances within seconds. At first, communication capabilities were limited in terms of distance, data rate, signal quality, and bandwidth. Initially, communication links were designed with wires instead of antennas. Unfortunately, wired systems had drawbacks in efficiency, reliability, cost, flexibility, and weather durability. Wireless systems were designed to overcome these disadvantages, especially after World War 2. [8]

The first wireless implementations are called "Zero Generation Technology" (0G). Sent and received signals were analog, and calls were arranged by a mobile operator. It should be noted that analog signals have disadvantages in terms of signal quality, information security, and handset device size. An improved version of 0G, called 0.5G, could provide data rate in the order of kilobits per second (Kbps). In the 1980s,

the First Generation Technology (1G) was introduced. 1G was based on analog frequency modulation and frequency division multiplexing techniques, so sent signals could be transferred between antenna towers. But still, analog signals were used. Outstanding improvements were seen with Second Generation Technology (2G) in the early 1990s. Digital signals and digital signal processing techniques were used with the Global System for Mobile Communications (GSM) standard. 2G offered a more efficient spectrum and internet browsing capability. Messaging became possible. The data rate increased dramatically with the updated version of 2G. General Packet Radio Service (GPRS) technology was applied for 2.5G, and Enhanced Data Rates for GSM Evolution (EDGE) was applied for 2.75G in the early 2000s. With the Third Generation Technology (3G), data rate could reach megabits per second (Mbps), and internet browsing become faster. The provided channel bandwidth was increased to several MHz from kHz levels. Videotelephony could be made, so image data transfer became possible. With the emergence of Fourth Generation Technology (4G), the data rate has increased at least ten times that of 3G, with better efficiency and security. Finally, Fifth Generation Technology (5G) was introduced recently. 5G provides more reliability, less outage, and data rate in the order of gigabits per second (Gbps). [8]

Considering this perspective, it can be said that wireless communication capabilities are expanding exponentially with the tremendous increase in users and requirements. In order to meet the requirements, different types of antennas have been designed and used. As communications technology and its use increases, more and more challenges arise in the required antenna design. These challenges are basically:

- Miniaturization
- High and Stable Gain
- Compact Size
- Wide Bandwidths
- Multiple Bands
- Low Cost

- Ease of Fabrication and Integration
- Stable Radiation Pattern
- High Isolation
- Low Cross Polarization

Base station antennas are crucial for mobile communication [9]. They include numerous antennas for different bands and frequencies. Regarding bandwidth and frequencies, the 2G operation band is 1710-1920 MHz [10, 11]. 3G operates at 1880–2170 MHz. 4G frequency ranges are 2300-2400 MHz and 2570-2690 MHz [12]. For 5G bands, The Ministry of Industry and Information Technology of China determined the frequency range as 3300–3600 MHz and 4800–5000 MHz for sub-6GHz, and millimeter-wave frequency bands [10]. Additionally, 5G bands are 3400-3800 MHz in Europe, 3100-3550 MHz, and 3700-4200 MHz in the USA [12]. In the foreseen future, 5G will be the dominant communication technology; however, 2G/3G/4G technologies will still be operational for many countries for years [13].

5G technology has a transmission range deficiency, so there should be more base stations or antenna emplacements around residential areas [12]. Hence, 2G/3G/4G/5G antennas should be implemented at the base station. However, there will be placement issues for different antennas of different bands. At this point, miniaturized compact-size antennas become significant. Having small antennas may not be enough to solve the problem of the available area. Designing multi-band antennas can be a solution. Multi-band antennas have gain, efficiency, and bandwidth disadvantages. For example, in [14], the designed multiband antenna can operate over the frequency bands of 1.71-2.69 GHz, 3.3-3.5 GHz, and 5.15-5.825 GHz with the antenna gain value between 0.5-3dBi, which is quite low for base station antennas. In [15], a four-band antenna consisting of 4.6, 5.05, 5.8, and 6.3 GHz bands is designed for wireless communications. Gain values for the operation bands are above 5dBi, and gain varies between around 5-10 dBi; on the other hand, operation bandwidths are at most 2%, which is too narrow. Similar drawbacks are also mentioned for the multiband antenna in [16]. Antenna gain at different frequencies varies between 1.62 dBi to 5.95 dBi, and antenna efficiency is between 42% and 82%.

Instead of multiband antennas, single-band antennas -which cover the necessary bands- can be used together, and a multiband antenna system can be obtained. These antennas are placed near each other so that antennas can share the same radiation area. This placement formation of antennas can be called as "shared aperture antennas". Shared aperture placement greatly reduces the installation space so that more antennas can be installed and more efficient base stations can be obtained, or shared aperture multiband systems can be installed in array formations to increase the signal quality. Shared aperture antennas are quite popular nowadays due to their promising features of compact size, space reuse efficiency, low cost, freedom of controlling the antenna gains, and radiation properties [13, 17–19].

These aperture antennas were patch antennas in earlier designs. Even though they have low cost and small & compact size properties, their bandwidth is narrow and insufficient for the required bands [20, 21]. For instance, a shared aperture triband patch antenna system is proposed in [22], where patch antennas' bandwidths are 3.6% for X-band, 6.7% for Ku-band, and 5.3% Ka-bands, respectively. Patch antennas' bandwidth can be improved with shape adjustments; for example, bandwidth can be increased to 10% with the corner truncation. Apart from that, a stacked-patch antenna with a bandwidth of 19% is designed in [23]. Using a slot antenna is another option. But slot antennas also have the disadvantage of narrow bandwidth [17, 24]. The designed K-band slot antenna in [25] has a bandwidth of 4.8%, and the designed polarization reconfigurable slot antenna in [26] has a bandwidth of 4% for circular polarization and 19% for linear polarization, respectively. Even though linear polarization bandwidth is improved, peak gain is only 3 dBi at most. To obtain wide bandwidth, a crossed-bowtie antenna is designed in [27] with a fractional bandwidth of 56% for use in 2G, 3G, and 4G applications.

A different type of antenna is the 'crossed-dipole' antenna. Two dipole antennas are placed perpendicularly to each other to form a crossed-dipole shape. They can be used in a large-scale frequency range, from radio frequency (RF) ranges to millimeter-wave frequency ranges. They can operate in larger bandwidths than normal dipole antennas due to the existence of extra resonance frequency with the mutual coupling. They can be used in various applications, such as communications, wireless local area networks (WLAN), navigation systems, broadcasting, and many more. Initially, they were

designed as wire dipole antennas, and then differently shaped cross-antennas were designed with many modifications to obtain wider bandwidth and miniaturization in order to fulfill the requirements of today's communication networks. Also, reflectors are added to cross-dipole antennas to obtain uni-directional radiations with higher gains to improve efficiency in the radiation [28]. Owing to their suitable structure, they have been widely used recently in dual-polarization and circular polarization applications.

Furthermore, dual-polarization antennas are recently preferred in base station antennas since they reduce the number of antennas and provide less space occupation. Two identical antennas are placed orthogonally and close to each other, so two orthogonal linear polarizations, or namely dual-polarization, are obtained. Dual-polarized antennas also have reduced multipath fading and interference problems [9, 17]. Dual-polarization provides higher channel and data capacity [29] and can improve the signal-to-noise ratio (SNR) [30]. If there is a situation in which the polarization direction is uncertain, dual-polarized antennas are more advantageous for polarization mismatches and losses than single-polarized antennas [31]. Additionally, dual-polarization antennas can be used in synthetic aperture radars (SAR) to improve the information content with the orthogonal scattering data from the cross-polarization [32, 33].

Crossed-dipole antennas can operate either in a single band form or in a multiband shared aperture form. A dual-polarized cross-dipole antenna is designed in [31] with a bandwidth of 83.5%. A base station cross-dipole antenna with a bandwidth of 1.7 GHz to 2.69 GHz is designed in [20]. In [34], low band crossed-dipole antenna operated between 1.71 GHz to 2.69 GHz, and the second antenna is operated at 3.4 GHz to 3.8 GHz in a shared aperture antenna form. Very similar bands of 1.8-2.7 GHz and 3.3-3.8 GHz band shared apertures antennas are designed in [35]. In another shared aperture example, the low-frequency antenna bandwidth is 820-960 MHz, and the high-frequency antenna bandwidth is 3.4-3.6 GHz in [36].

Likewise, circularly polarized (CP) antennas have the similar advantages with the dual-polarization. They have wide application areas such as broadband wireless communication, satellite communication, radar, Global Positioning System (GPS),

Radio Frequency Identification (RFID), etc [37]. By changing the feeding system or feeding phase, cross-dipole antennas can be used as CP antennas. Usually, a vacant-quarter feeding method is used to obtain 90° phase difference between the two dipoles. In [37], an ultra-wideband circularly polarized antenna is designed with a bandwidth of 121%. In [38], a multiband circularly polarized cross-dipole antenna is designed for navigation applications.

Although the shared aperture idea seems quite reasonable, it comes with serious challenges. One of the challenges is the undesired effect of coupling of the antennas. Since they are placed very close to each other, unwanted current is induced from the out-of-band antenna, causing destructive interference of radiated waves, which is expected and inevitable. The coupling can occur for both different band and same band antennas, which results in deterioration of radiation and reduction of antenna efficiency [39]. Isolation methods are widely applied in shared aperture systems to prevail over coupling. One of the isolation techniques is introducing chokes [40]. For different band antennas, chokes suppress the induced current at lower band antennas, which is induced by higher band antennas. Without the induced currents, high band antenna performance is not affected by low band antenna [41]. So, cross-band isolation is ensured. However, chokes narrow the bandwidth and decrease the gain of low band antenna [41, 42]. Another method is applying slots with different shapes to low band antenna so that induced current distribution and direction are changed in such a way that eliminates the cross-band scattering while maintaining the impedance match of the antenna [34, 43]. An alternative method is using filtering antennas. Filtering structures are used together with the antennas so that cross bands are isolated from each other. Coupling rings, shorting vias, shorting pins, slots, and resonator structures [44] can be applied to designs for isolation. In [35], a coupling ring is applied to the high band antenna; the ring decreases the cross-band coupling and also prevents the gain reduction of the low band antenna. Moreover, in [35], a high pass filtering shape is implemented to feed the network of the multiband antenna to eliminate the low band antenna-induced current. However, it is worth mentioning that filtering structures may increase antennas' dimensions, making it difficult for base station installation [13]. An alternative widely used method is implementing frequency selective surfaces (FSS) to multiband antenna systems [25, 36, 45].

Frequency-selective surfaces (FSS) are periodic electromagnetic structures that can work as spatial filters. They filter the electromagnetic waves by reflecting, scattering, or transmitting through them. Hence, they can be thought of as well-known filters like bandpass or bandstop filters in the RF domain; however, FSSs are also dependent on the incidence angle of the incoming wave. FSSs popularity has increased rapidly recently because they are used in a number of applications such as radomes [46], radar cross section (RCS) reduction [47], indoor wireless signal filtering [48], broadband communication, etc. FSSs are also cheap to build, have small dimensions, and are easy to design and implement, which makes them popular for many applications.

FSS-based surfaces have been used lately in multiband shared aperture antennas to improve isolation between the separate antenna bands to improve their gains, efficiency, and also the bandwidth. A cross-dipole antenna is designed based on a bandpass unit cell and becomes electromagnetically transparent to another frequency band in [35], hence they form a dual-band shared aperture antenna. Another example of a dual-band cross-dipole antenna is given in [13]. There are two different cross-dipole antennas operating at different bands of 690-960 MHz and 3.5-4.9 GHz. An FSS in the middle provides the isolation by acting as a bandstop filter to the high-frequency antenna and a bandpass filter to the low-frequency antenna. In [17], FSS is used for the triple-band antenna; it reflects the frequency range between 35-40 GHz in the Ka-band, and it transmits the waves in the frequency range between 24-28 GHz in the K-band.

1.2 Thesis Motivation

In this thesis, a triple-band shared aperture antenna system is designed and implemented. Two of the designed antennas' bandwidths are selected as the base station antenna bandwidths, the third antenna is added later with an arbitrary frequency range to observe whether the double-band can be expanded to triple-band or not. They are designed as cross-dipole antennae to provide both dual-polarization and circular polarization for bandwidths that are wide enough. These antennas also have EM transparent characteristics to ensure stable radiation patterns for all of the antennas. In order to further improve the signal quality, a two-element middle-frequency band

antenna array, and a four-element high-frequency band antenna array are formed. Finally, all the antennas are supported by a copper ground plane to provide unidirectional radiation. The designed antenna system's radiation characteristic is given in Figure 1.1. Low band (LB) antenna operates in the lower frequency band. It is transparent to the middle band (MB) antenna and high band (HB) antenna, which is shown in blue. MB antenna is transparent to HB antenna shown in red. HB antenna shows EM transparency to both LB and MB antennas shown in green.

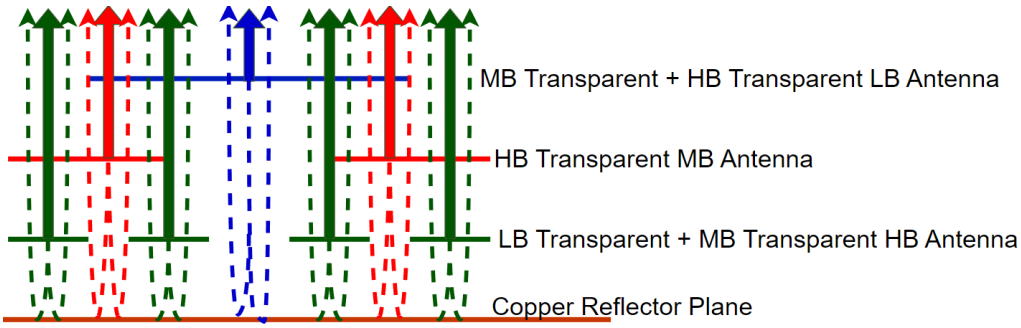

Figure 1.1: Block scheme of the multiband antenna radiation

Multiband shared aperture antenna design challenges are aforementioned in the previous section. To satisfy all or most of the design challenges, a multiband shared aperture cross-dipole antenna design is selected. Because:

- Miniaturization: Due to the shared aperture antenna concept, antennas are stacked together to a smaller area rather than separated antenna apertures.
- High and Stable Gain: Shared aperture antennas require stable and high gain characteristics to ensure signal quality. Cross-dipole antenna configuration ensures high gain within a wide bandwidth. Additionally, antenna arrays can also be used in the shared aperture system, significantly improving antenna gain and stability. In this thesis, antenna arrays are applied, and high gains are obtained.
- Compact Size: Similar to miniaturization, shared aperture antenna configuration uses the area more efficiently with denser designs. In this study, the total number of seven antennas are placed close to each other to ensure compactness.
- Wide Bandwidths: With the use of cross-dipole antennas, fractional bandwidth between 45-50% can be obtained, which is quite sufficient for the communica-

tion bands. In this thesis, designed antennas' bandwidths are within 1-1.6 GHz, 1.8-2.95 GHz, and 3.35-5.4 GHz, with the fractional bandwidths of 46.15%, 47.92%, 46.6%, respectively.

- Multiple Bands: Shared aperture antennas are usually designed in different bands to serve different communication technologies and protocols. High band antenna is designed to serve within 5G bands, and middle band antenna is designed to serve within 2G/3G/4G bands. At first, only middle band and high antennas were used. Then, a third antenna is added with an arbitrary band to test the expandability of the double-band shared aperture antenna to the triple-band shared aperture antenna.

- Low Cost: Antenna elements are designed on the printed circuit board (PCB) by using only two layers. Antennas are supported by plastic screws and nuts. A copper reflector plane is used, and sub-miniature A (SMA) connectors are used with RF coaxial cables. There are no other components. These materials can be easily obtained in the market without a significant cost.

- Ease of Fabrication and Integration: As mentioned in the previous item, PCBs can be easily integrated with screws and nuts to the copper reflector plane. For coaxial cables, the SMA connector and PCB antenna are soldered on either side of the coaxial cable, and the integration is completed. PCBs can also be quickly fabricated since they are small and not complex.

- Stable Radiation Pattern: Shared aperture antennas should have a stable radiation pattern to have reliable communication within the bandwidth. This design ensures radiation patterns with the passband transmitting surfaces and antenna arrays.

- High Isolation: Most of the shared aperture antennas are operated as dual-polarized. These two polarizations can be operated independently with the cross-dipole antenna. In this thesis, the isolation between the two polarizations is also explained in detail.

- Low Cross Polarization: Shared aperture antennas should not be affected by the other antennas' radiation. In this study, antennas are also designed as passband

transmitting surfaces, so the radiation of different antennas is not affected by each other.

1.3 Novelty and Contributions

In this thesis, designed multiband shared aperture antennas are hybrid structures that can operate as both electromagnetic transparent surface and antenna. All antennas have wider bandwidths than previously designed shared aperture crossed dipole antennas in terms of both transparent surface and antenna. For all antennas, polarization diversities are explained in detail. Besides, antenna designs are simple, low-cost, and easy to manufacture. There are only antenna elements and supporting spacers with a copper reflector plane, which makes it easier to design and install the antenna system. In previous works, the third antenna is designed with the concept of eliminating induced currents from the other antenna by slots and branches. In this thesis, the third antenna is also made with the concept of passband FSS and cross-dipole antenna with larger fractional bandwidth from other designs. Hence, it is also shown that hybrid FSS and cross-dipole antenna concepts can be expanded to multiband shared aperture antenna systems.

1.4 Thesis Organization

In brief, this thesis can be organized as follows:

In Chapter 2, EM transparent surface design is explained in detail. Since the transparent surface is obtained from the FSS, the FSS unit cell design is explained in detail first. Theoretical design formulas and simulations are given. Design parameter iterations and their effects on FSS performance are shown. Then, designed transparent surfaces are tested with hypothetical Hertzian-dipole electric fields to see the transparency characteristics.

In Chapter 3, cross dipole antenna design is explained in detail. Initially, theoretical background is given. Secondly, cross-dipole antenna design is explained in steps. Then, designed antenna characteristics are examined in both simulation and prototype

measurements. These procedures are followed for three separate antennas, two of which are operated as both cross-dipole antenna and electromagnetically transparent surface that are designed in Chapter 2.

In Chapter 4, a multiband shared aperture antenna design is presented. Designed antennas in Chapter 3 are merged in shared aperture configuration, and their results are shown for both simulation and real-life environments. By this configuration and tests, both EM transparent surface and cross dipole antenna designs have been tested.

In Chapter 5, the conclusion of the thesis and possible future works are discussed.

CHAPTER 2

ELECTROMAGNETIC TRANSPARENT SURFACE DESIGN

2.1 Introduction

As the name implies, in a given frequency range, electromagnetic waves can pass through the electromagnetic transparent surface with minimal loss and deterioration. The electromagnetic (EM) waves without this frequency range are reflected back. This behavior is similar to the passband filter, and the EM wave spatial filter can be designed with the idea of frequency selective surfaces (FSS).

Frequency-selective surfaces are structures that can work as filters for electromagnetic waves that are incident to them. They are composed of metallic parts and dielectric with various shapes for different filtering characteristics. These filters are well-known filters, such as low-pass, high-pass, bandpass, or bandstop filters, but FSSs are designed as filters for the EM plane waves incident to the FSS in the 3D environment. For bandpass FSS, incident waves are transmitted through, and incident waves are reflected for band-reject FSS according to incident wave frequency. Incoming waves in the free space are transmitted or reflected by the FSS, so they can also be called "spatial filters" [49].

FSS designs are based on unit cells, and the structure of FSS is periodically formed by several unit cells. The unit cell designs mainly determine the FSS filtering characteristics and performance. From the initial research of FSS, many FSSs are designed with numerous different unit cells. These unit cells are generally examined in four groups according to their shapes, shown in Figure 2.1 [1]. The first group of FSS unit cell shapes are connected with a mutual joint at the center. They are usually used in wideband FSS applications since inter-element spacing can be lowered enough,

which helps to obtain wideband filtering. The second group is loop unit cells. Loops' circumference should be nearly around λ of the incident wave for the resonance frequency of the FSS. The third group, plate type or patch type FSS, is disadvantageous for bandwidth since their resonance frequency is obtained when the patch dimension is about $\lambda/2$, which increases the inter-element spacing. Thus, in Group 4 unit cells, the combination is preferred. These types of FSS are combinations of the three types of unit cells to improve FSS performance. Other than that, dielectric plating, multi-layer, and meandered FSS are also designed and used in many applications [49, 50].

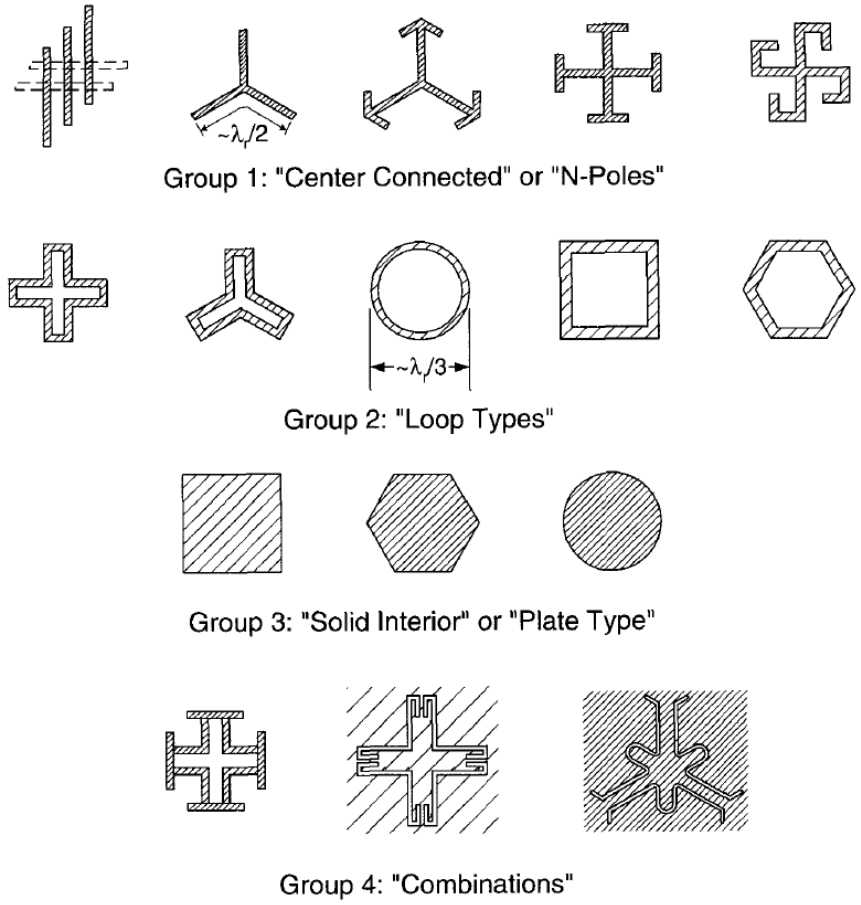

Figure 2.1: FSS Unit Cell Types [1]

FSS unit cell design can be done in many ways, as mentioned, and there are essential requirements of FSS that an FSS designer should take into account to design a stable and reliable FSS. In this thesis, two EM transparent surfaces are designed with the idea of bandpass FSS. The significant parameters of the FSS design will be discussed in the next part.

2.2 FSS Design Requirements

When designing an FSS, its critical properties should be taken into account. These parameters should be ensured according to application requirements. FSS shape, dimensions, and filter type can be adjusted. The essential parameters of FSS are:

- Angular Stability
- Low Profile
- Polarization Independence
- Required Bandwidth
- Resonant Frequency

Electromagnetic waves can reach FSS with normal or oblique incidence with an incidence angle. As shown in Figure 2.2, the FSS bandwidth and resonant frequency change with the angle of incidence. The higher the angle of arrival, the more significant the difference from the normal incidence case. If the designed FSS properties do not change significantly with the increasing angle of arrival, then the FSS is said to be "angularly stable". Oblique incidence is inevitable in most cases, so the designed FSS must be angularly stable for the required bandwidth. Munk states that unit cells and spacing between unit cells must be as small as possible to have better angular stability [1]. Multilayer FSS designs considerably improve angular stability [49, 51].

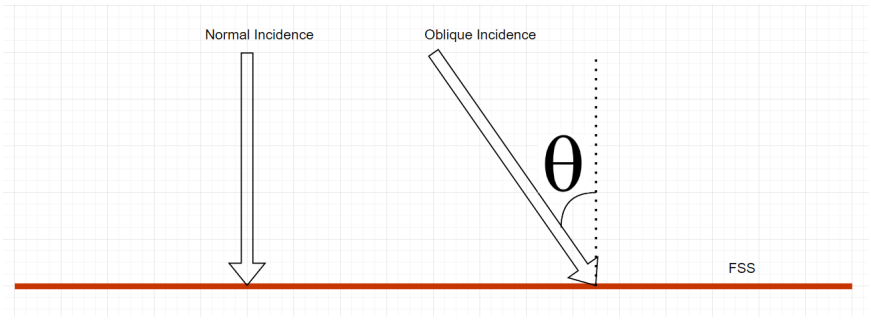

Figure 2.2: Normal and oblique incidence cases for FSS

A low-profile structure is usually a desirable property for almost any design. FSS with low thickness with respect to wavelength does not increase the overall dimensions

significantly, especially the single-layer and double-layer FSS structures. Multilayer FSS structures are also very thin with respect to wavelength, but if different FSSs are separated with a specific distance, then the system may not be low profile anymore. Also, having smaller dimensions in FSS can be achieved with different geometries like meandered lines, slots, vias, etc., for achieving the same resonance frequency [52]. Small-sized unit cells and low inter-element spacing FSS are advantageous for angular stability and bandwidth [1].

Polarization-independent FSS shows the same or almost identical radiation properties for TE and TM polarizations. The designed FSS unit cell should be symmetric to both the x and y axes to have polarization independence according to cartesian coordinate system.

FSS bandwidth can be arranged using different designs. The number of layers in FSS, substrate thickness, substrate dielectric constant, and unit cell shape affect the bandwidth. Small unit size and inter-element spacing provide the higher bandwidth since unwanted peaks do not occur, and they start at higher frequency [1].

The resonant frequency of FSS is the frequency at which maximum transmission occurs for bandpass FSS, and maximum reflection occurs for bandstop FSS. Similar to bandwidth, resonant frequency is affected by the substrate, incidence angle, and unit cell design.

It can be concluded that the designed FSS must have good angular stability for larger incidence angles; it also must be polarization-independent to both TE and TM polarizations and have a low profile with smaller unit cells with minimum inter-element spacing. While arranging the resonant frequency and bandwidth of FSS, the frequency range of antennas or incident waves must be considered.

2.3 FSS Design Methods and Procedures

To design and analyze an FSS, first the FSS properties must be determined. There are two common methods to design an FSS: equivalent circuit (EC) method and full-wave electromagnetic (EM) solver. In the EC method, FSS unit cell components

correspond to lumped or distributed circuit components with several formulations. These formulations can be solved by computational programs like MATLAB. The latter method is drawing the 3D shape of the FSS and using the 3D full-wave EM solvers. ™HFSS and ™CST are the most used programs [53] [54].

2.3.1 Equivalent Circuit Method

For equivalent circuit representation of FSS, unit cell design is crucial. In the simplest case, metal patch and metal grid-shaped FSS can be seen in Figure 2.3. The yellow parts are the dielectric substrate and the orange color is represented as the copper part. When a high-frequency plane wave moves towards a metal patch FSS, it is mostly reflected. And low-frequency plane wave is mostly transmitted within the FSS, which means metal patch FSS acts as a low pass filter characteristic, and it is indicated as a capacitance [55]. Metal grid is the complementary version of metal patch shape, and metal grid FSS acts as a high pass filter. Thus its characteristic is inductive. The dimension D is the periodicity of the unit cell, s and w are the gap distance between patches for metal patch FSS, and slots for metal grid FSS, respectively.

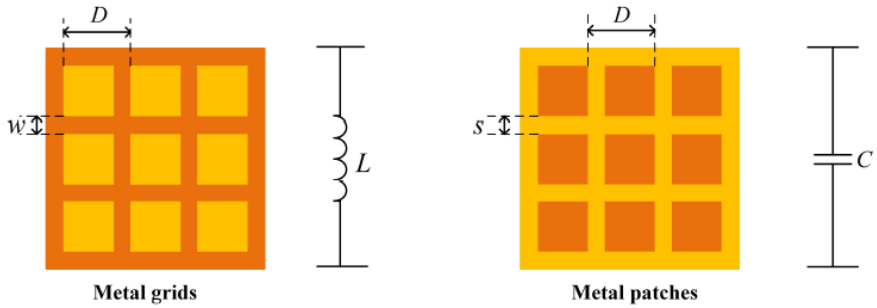

Figure 2.3: Metal grid FSS and metal patch FSS [2]

To obtain bandpass or bandstop filter FSS characteristics, a metal grid and patch shapes can be mixed and modified. The well-known mixture FSS forms are square loop and square slot FSS, which can be seen in Figure 2.4. Like the metal patch and metal grid FSS, square loop and square slot FSS are complementary to each other. For the square loop, loop edges act differently with respect to the polarization direction. The edges that are aligned to the plane wave electric field act as the inductive

part, and the perpendicular edges act as the capacitive part [51]. For example, if the electric field is polarized in the vertical direction, then vertical edges are inductive, and horizontal edges are capacitive. Square loop FSS is a bandstop filter, and its equivalent circuit is a series LC resonator. Reversely, square slot FSS acts as a bandpass filter. Slot inductance is the inductance of inner squares, and slot capacitance is the combination of the capacitance between inner square and metal with g width and the capacitance between g width metals. L_1 inductance is the inductance of w width metal lines and L_{slot} is affected by L_1.

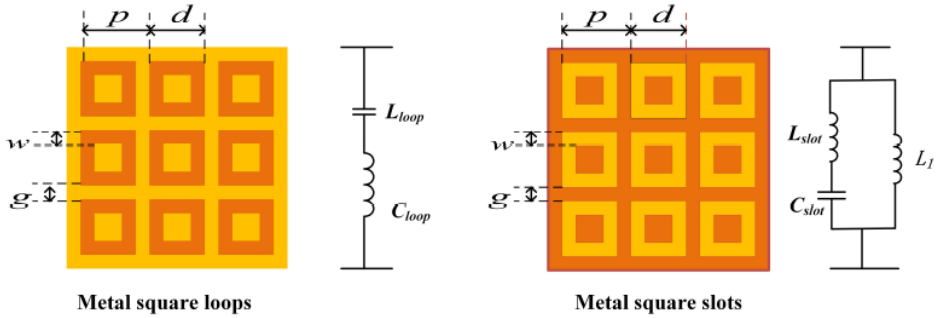

Figure 2.4: Square loop FSS and square slot FSS [2]

For the single layer square loop and square slot FSS, inductance, and capacitance values are dependent on parameters of periodicity p, edge length d, edge width w, inter loop distance g, the incidence angle θ of spherical coordinates, relative dielectric constant ϵ_r, and dielectric thickness h. The given parameters are used for the calculation of square loop and square slot EC capacitance and inductance values with Marcuvitz equations [56]. A square slot single-layer FSS design is used. Formulations, results, and EC representation will be explained in detail in the upcoming part of the chapter.

Apart from that, the EC method can also be applied to different FSSs, such as multilayer FSS, multiple loop/slot FSS, and FSS with different unit cells. In [3], a multilayer FSS with an equivalent circuit is presented. Multilayer FSS is designed with hexagonal slot unit cells with a double layer at first. The unit cell is modeled as a parallel LC resonator, and the dielectric between them is modeled as a transmission line with a length equal to dielectric thickness. Figure 2.5 displays the double-layer FSS and its equivalent circuit. Extra metal patch layers as capacitance layers are added to both the top and bottom of the hexagonal FSS to improve angular stability. So, the

new FSS EC model is symmetrically expanded with transmission line-capacitance networks. The new multilayer FSS is shown in Figure 2.6.

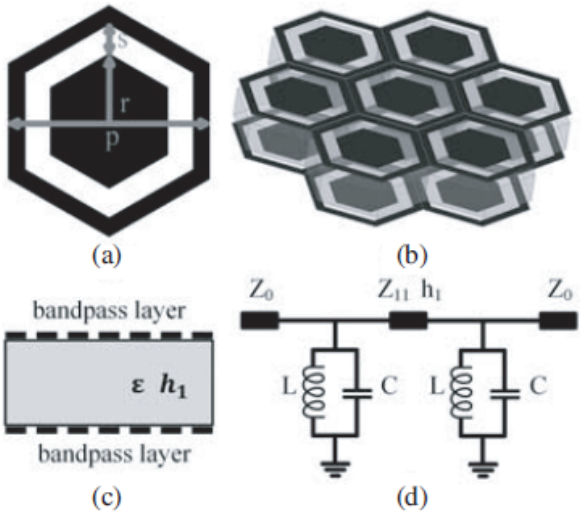

Figure 2.5: Double layer hexagonal FSS. (a) Unit cell of FSS. (b) Double layer FSS 3D view (c) Double layer FSS layers. (d) Double layer FSS equivalent circuit. [3]

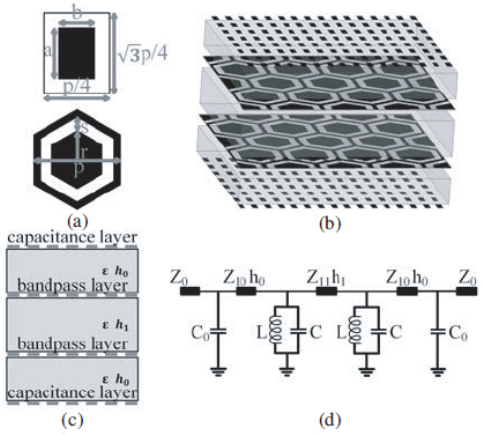

Figure 2.6: Multilayer FSS. (a) Unit cells of FSS. (b) Multilayer FSS 3D view (c) Multilayer FSS layers. (d) Multilayer FSS equivalent circuit. [3]

The work presented in [4] is an example of a double circular slot FSS. Initially, only one circular slot unit cell is shown with its equivalent circuit in Figure 2.7. The EC model is the same as the square slot EC model. Formulations are very similar, with some changes and additions due to shape differences. Then, another circular slot is defined in the unit cell in Figure 2.8 (a). A smaller circular patch and a circular ring

are formed rather than a large circular patch. EC model is given in Figure 2.8 (b). L_3-C_2 components are determined by the circular patch and the ring relationship. L_2-C_1 are the interaction of the metal ring in between and the outer metal with the width g. L_1 is due to the outer metal.

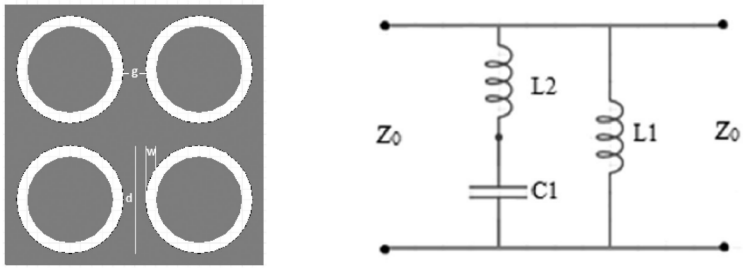

(a) (b)

Figure 2.7: (a) Unit cell view and (b) EC model of the circular slot FSS [4]

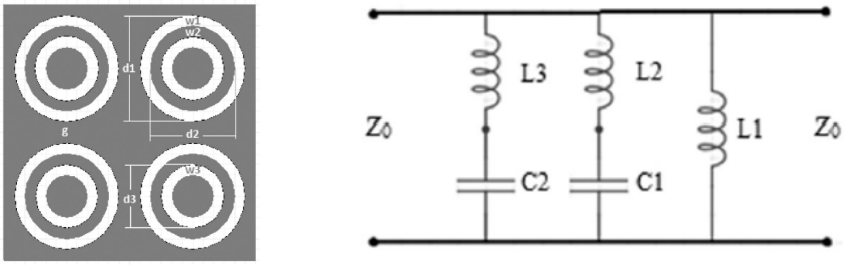

(a) (b)

Figure 2.8: (a) Unit cell view and (b) EC model of the double circular slot FSS [4]

In addition to loop and patch type FSS, unique unit cell designs are quite intriguing. In [5], double layer FSS with meander lines is used to design double bandstop FSS. Meander lines are used for miniaturization of FSS such that the unit cell is only $\sim 0.04\lambda$ of the first resonant frequency. The meander line design is given in Figure 2.9 (a). By adding four meander lines and merging them, an FSS unit cell is obtained. In Figure 2.9 (b), the orange color unit cell is located at the top layer, and the green color is located at the bottom. Also, the inductance and capacitance of the cell are shown in the figure. The 3D view of the FSS and its EC model are given in Figure 2.10. Each layer is shown as a series LC resonator showing bandstop characteristics, Z_h is the transmission line model of the substrate, and L_3 is the vias' inductance. EC components' values change according to meander line length, width, the gap between

meander lines, substrate thickness, and diameter.

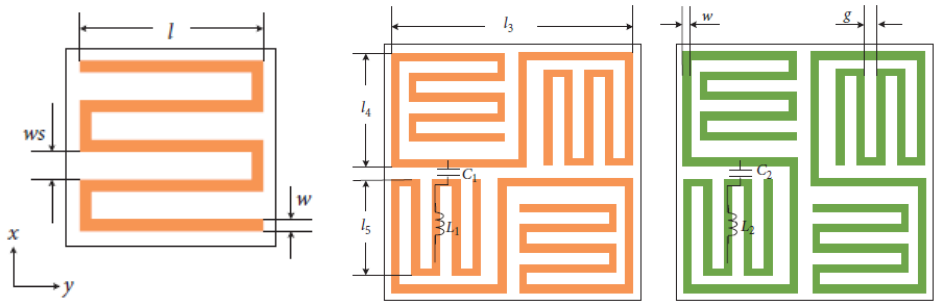

(a) (b)

Figure 2.9: (a) Meander line shape, orange top layer, and (b) green bottom layer meander line unit cell. [5]

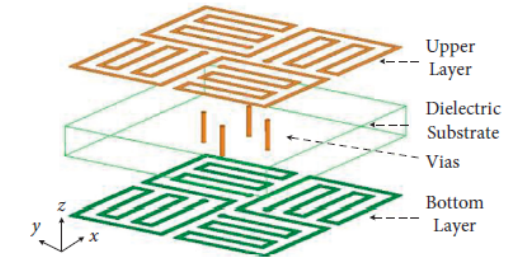

(a)

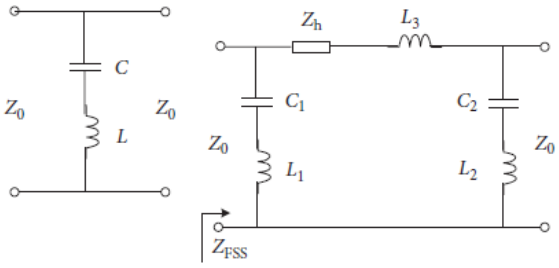

(b)

Figure 2.10: (a) 3D View of FSS and (b) single layer EC model and double layer EC model [5]

2.3.2 Full-wave 3D EM Solver Method

As can be seen from examples, EC modeling helps the FSS design. However, as the incident angle increases, or as the complexity of FSS design increases - number

of layers, conformal designs, etc. - the EC method calculations become inaccurate. At this point, numeric EM solution methods can be used. These methods are the Method of Moments (MoM), Finite Element Method (FEM), and Finite Difference Time Domain (FDTD) methods. [50]

MoM provides the solution for induced currents and fields caused by incoming plane waves to the FSS surface. By solving the currents and fields, FSS characteristics can be determined. But if FSS has multilayers, the MoM solution workload becomes higher and longer. FEM can be used for bounded 3D structure solutions. There should be necessary boundary condition definitions for FSS to observe the FSS characteristics. But, FEM needs a significant amount of computation capacity. FDTD method can be used for broadband solutions, and it has less effort to solve rather than FEM and MoM. However, FDTD has data storage drawbacks due to data load [50].

Most FSS design simulations are based on the unit cell solution approach. Only the FSS unit cell is drawn, and necessary boundary conditions are defined for the unit cell shape. Since FSS is a periodic structure, boundary conditions must satisfy the periodicity condition. These boundary conditions are infinite array boundary conditions, in other words, the FSS unit cell extends to infinity in two axes like an infinite plane. Only one unit cell is drawn, and boundary conditions are applied in the 3D EM solver programs like ™CST and ™HFSS. In Figure 2.11, an example of a square slot bandpass FSS unit cell is given.

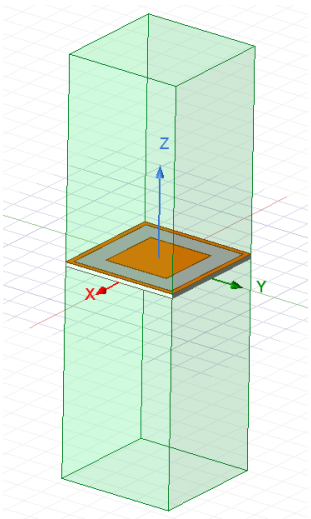

Figure 2.11: Unit cell of square slot FSS

In Figure 2.11, the green box defines the solution box for the unit cell. The infinite array boundary conditions are defined for the four side cells of the solution box. In ™HFSS, "master" (or "primary") and "slave" (or "secondary") boundaries are defined for the periodic structures. Boundary assignment is made for two opposite faces for one dimension; one of the faces is the primary, and the latter one is the secondary boundary. So, a four-face boundary assignment is made for two-dimensional periodicity. The boundary definitions are shown in Figure 2.12. Primary boundaries are shown in lime and dark green. The upward arrow in the middle of the unit cell indicates the incidence angle. In Figure 2.12, it is directly towards the z-axis, which means normal incidence. Oblique incidence angles are obtained with periodic boundaries phase difference [50]. θ and ϕ values can be changed for the incidence angle.

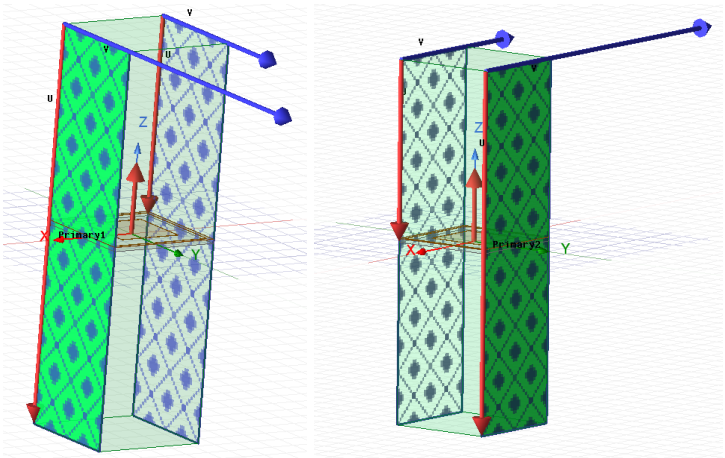

(a) (b)

Figure 2.12: (a) Primary-secondary boundaries for x-axis and (b) primary-secondary boundaries for y-axis

For the top and the bottom faces of the box, "Floquet" ports are defined for the plane wave excitation with the TE and TM polarizations. Floquet ports can be seen in Figure 2.13, and the polarizations can be seen in Figure 2.14. In Figure 2.14, it can be observed that TE polarization is towards the y-axis and TM polarization is towards the x-axis. The TE and TM polarizations can be defined with different modes. But for analysis of FSS, the fundamental modes are necessary. Higher-order TE and TM modes must diminish.™HFSS has the "mode calculator" property. Their attenuation is defined in terms of dB per unit length. The Floquet port mode calculator screen can

be seen in Figure 2.15. The fundamental modes have zero attenuation with distance, and the higher-order modes have nonzero attenuation. To guarantee good enough attenuation of unwanted modes, the distance between Floquet ports and the unit cell is increased. Since the phase of the wave changes with the changing distance between ports and the FSS surface, this distance should be de-embedded for the phase information of reflection and transmission properties of the FSS. By using the de-embed option of the Floquet port, which can be demonstrated in Figure 2.16, FSS phase characteristics can be seen.

In the following two sections, two FSS designs are made using both EC and full-wave EM solver methods. FSS designs are designed according to the designed antenna frequency range and bandwidth.

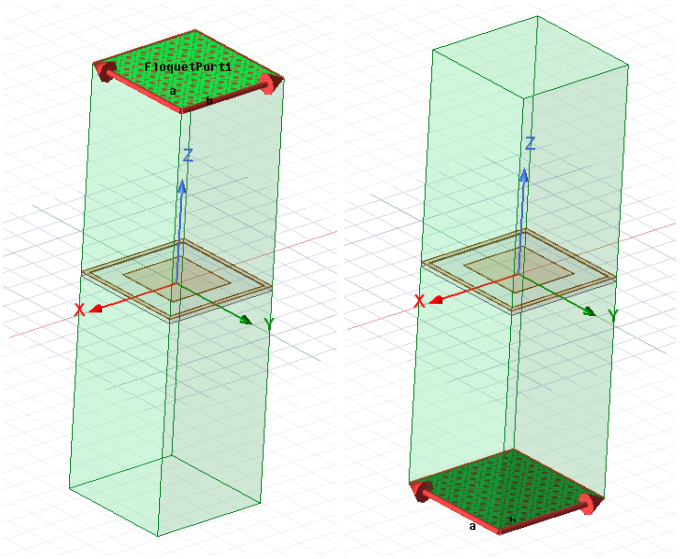

(a) (b)

Figure 2.13: (a) Upper Floquet port and (b) lower Floquet port

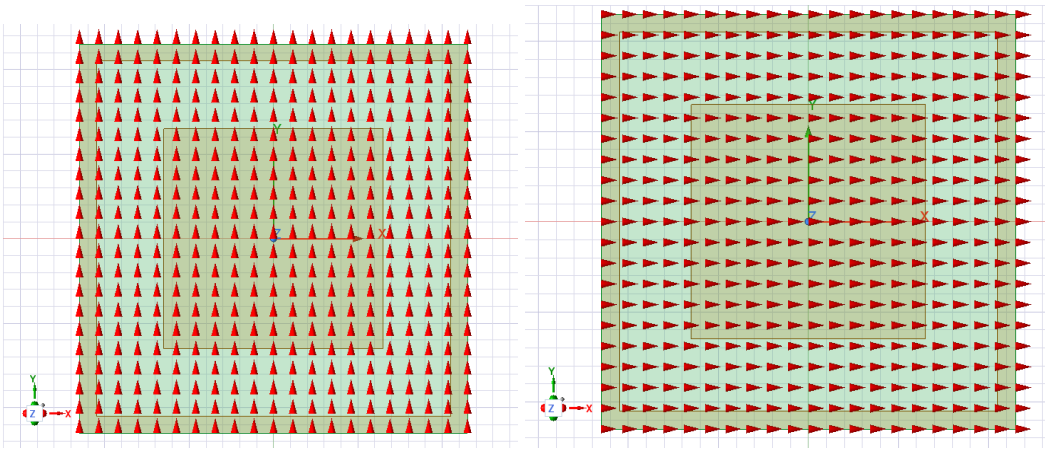

(a) (b)

Figure 2.14: (a)TE polarization and (b) TM polarization

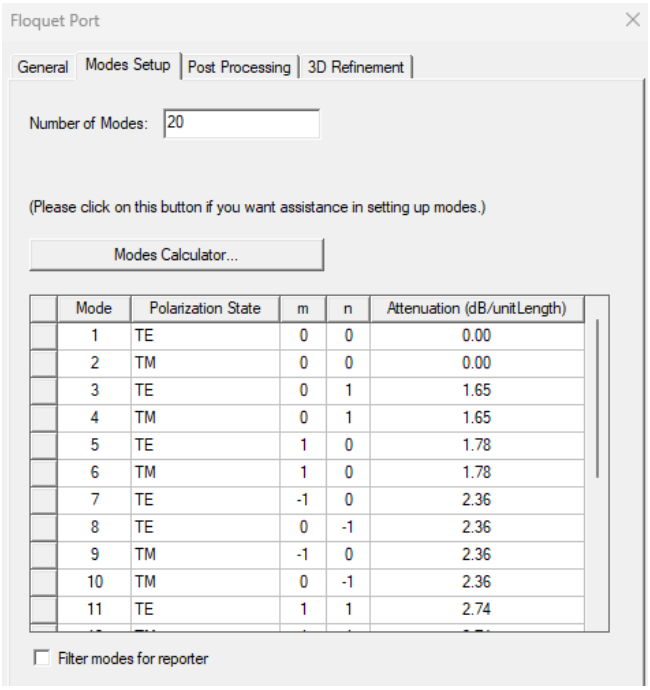

Mode	Polarization State	m	n	Attenuation (dB/unitLength)
1	TE	0	0	0.00
2	TM	0	0	0.00
3	TE	0	1	1.65
4	TM	0	1	1.65
5	TE	1	0	1.78
6	TM	1	0	1.78
7	TE	-1	0	2.36
8	TE	0	-1	2.36
9	TM	-1	0	2.36
10	TM	0	-1	2.36
11	TE	1	1	2.74

Figure 2.15: Mode calculator screen of the Floquet port

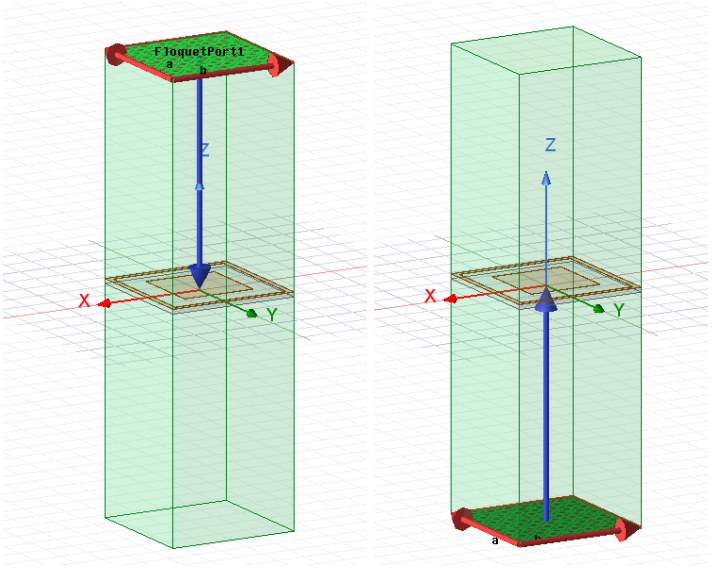

(a) (b)

Figure 2.16: (a) De-embed from upper Floquet port and and (b) De-embed from lower Floquet port

2.4 FSS Design for High Band Antenna

The required unit cell must act as a passband in high-band antenna bandwidth, especially in 5G bands. So in the frequency range between 3.3GHz and 5.5GHz, FSS must be transparent for the 5G antenna. Besides, a middle band antenna will also be included in this FSS design, meaning that the design is both a middle band antenna operating between 1.85-2.95 GHz and high band FSS at the same time.

The parameters of FSS must be determined. The parameters can be seen in Figure 2.17. The dimension d is the edge length of the square slot, s is the thickness of the square slot, $g/2$ is the copper thickness of the outer edge copper, and h is substrate thickness.

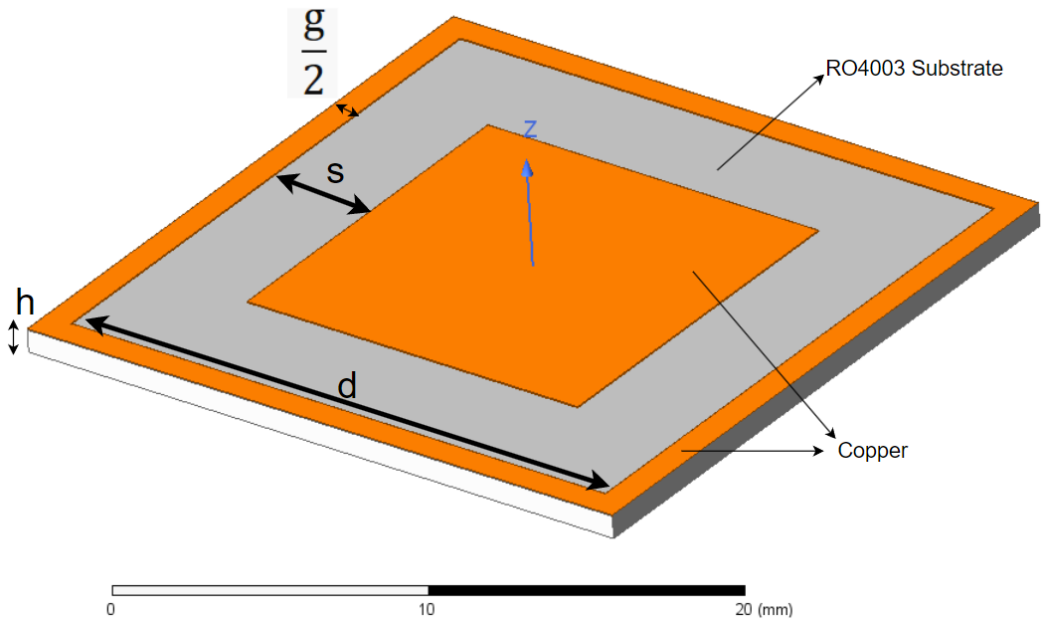

Figure 2.17: High band FSS unit cell

It should be noted that FSS unit cells also operate as a dipole antenna. So the dimension d is determined according to the antenna design parameter, which is explained in detail in Chapter 3. The d formula is given in Equation 2.1.

$$d = \frac{\lambda_m}{4\sqrt{2}} \tag{2.1}$$

λ_m is the wavelength of the middle band antenna center frequency. The middle band antenna frequency is 2.4GHz, so d is calculated as 22.1 mm. So, d can initially be selected as 22mm. The dielectric substrate is RO4003 with ϵ_r = 3.55 with a thickness of h = 0.813 mm. The copper thickness is 43 μm including 0.5 oz (18 μm) and 25μm copper plating. Marcuvitz equations can be used for determining the s and g [56]. The required design formulas are listed as follows:

$$p = d + g \tag{2.2}$$

$$\beta = sin\left(\frac{\pi w}{2p}\right) \tag{2.3}$$

$$A_{\pm} = \frac{1}{\sqrt{1 \pm \frac{2psin\theta}{\lambda} - \left(\frac{pcos\theta}{\lambda}\right)^2}} - 1 \tag{2.4}$$

$$G(p, w, \lambda, \theta) = \frac{1}{2} * \frac{(1-\beta^2)^2 \left[\left(1 - \frac{\beta^2}{4}\right)(A_+ + A_-) + 4A_+A_-\beta^2\right]}{\left(1 - \frac{\beta^2}{4}\right) + \beta^2\left(1 + \frac{\beta^2}{2} - \frac{\beta^4}{8}\right)(A_+ + A_-) + 2A_+A_-\beta^6} \tag{2.5}$$

$$F(p, w, \lambda, \theta) = \frac{p}{\lambda}\left[ln\left(csc\frac{\pi w}{2p}\right) + G(p, w, \lambda, \theta)\right] \tag{2.6}$$

$$\frac{X_{L1}}{Z_0} = \omega L_1 = cos\theta F(p, g, \lambda, \theta) \tag{2.7}$$

$$\frac{X_{L2int}}{Z_0} = \frac{p - 2s}{p} cos\theta F(p, d - 2s, \lambda, \theta) \tag{2.8}$$

$$\frac{X_{L2}}{Z_0} = \omega L_2 = \frac{X_{L2int}}{Z_0} + \frac{s}{d + g - 2s}\frac{X_{L1}}{Z_0} \tag{2.9}$$

$$\frac{B_{C1}}{Y_0} = 4sec\theta F(p, d, \lambda, \theta) \tag{2.10}$$

$$\frac{B_{C2}}{Y_0} = 4sec\theta F(d - s, s, \lambda, \theta) \tag{2.11}$$

$$\frac{B_C}{Y_0} = \omega C = \left(1.75\frac{B_{C1}}{Y_0} + 0.6\frac{B_{C2}}{Y_0}\right)\epsilon_{eff} \tag{2.12}$$

p is the periodicity of FSS unit cell, θ is the incidence angle, λ is the wavelength of the desired passband FSS center frequency, X_{L1} is the inductance of g width unit cell edge copper lines, X_{L2} is the inductance of metal patch in the middle and it is affected by X_{L1} which is indicated with Equation 2.9. The capacitance is calculated in two

steps. In the first step, capacitance between g width parallel copper lines is evaluated in Equation 2.10. Then, the capacitance between g width lines and the square patch is evaluated in Equation 2.11, then both capacitances are combined in Equation 2.12 to obtain total capacitance.

$$\epsilon_{eff} = \frac{\epsilon_r + 1}{2} \tag{2.13}$$

$$\epsilon_{Corr} = \epsilon_{eff} = \frac{\epsilon_r + 1}{2} + \frac{\epsilon_r - 1}{2} e^{-955h} - \frac{155s^2}{d} \tag{2.14}$$

$$f_{res} = \frac{1}{2\pi\sqrt{(L_1 + L_2)C}} \tag{2.15}$$

Initially, the effective dielectric constant is calculated as given in Equation 2.13 [1]. But in [57], it is stated that bandpass characteristics change significantly with the increase of substrate thickness. So, an empirical equation is used for the correction of the dielectric constant, named ϵ_{Corr} in Equation 2.14. Finally, the passband center frequency of the equivalent circuit is calculated in Equation 2.15. Equation 2.15 is derived in the Appendix A part. The equivalent circuit of the bandpass FSS is given in Figure 2.18.

The parameters shown in Figure 2.17 are swept to obtain the desired FSS traits. Firstly, d is swept between 16-24 mm with 2 mm steps. The plot of $|S_{21}|$ is shown in Figure 2.19. the x-axis indicates the frequency in the GHz scale, and the y-axis is the $|S_{21}|$ value in the dB scale. Since the $|S_{21}|$ indicates the insertion loss, high $|S_{21}|$ and low $|S_{11}|$ values are desired for the bandpass filter. Bandwidth of the bandpass filter FSS can be defined in different ways, such as 0.5dB bandwidth, 1dB bandwidth, and 3dB bandwidth. While the d value decreases, resonance frequency and the bandwidth increases.

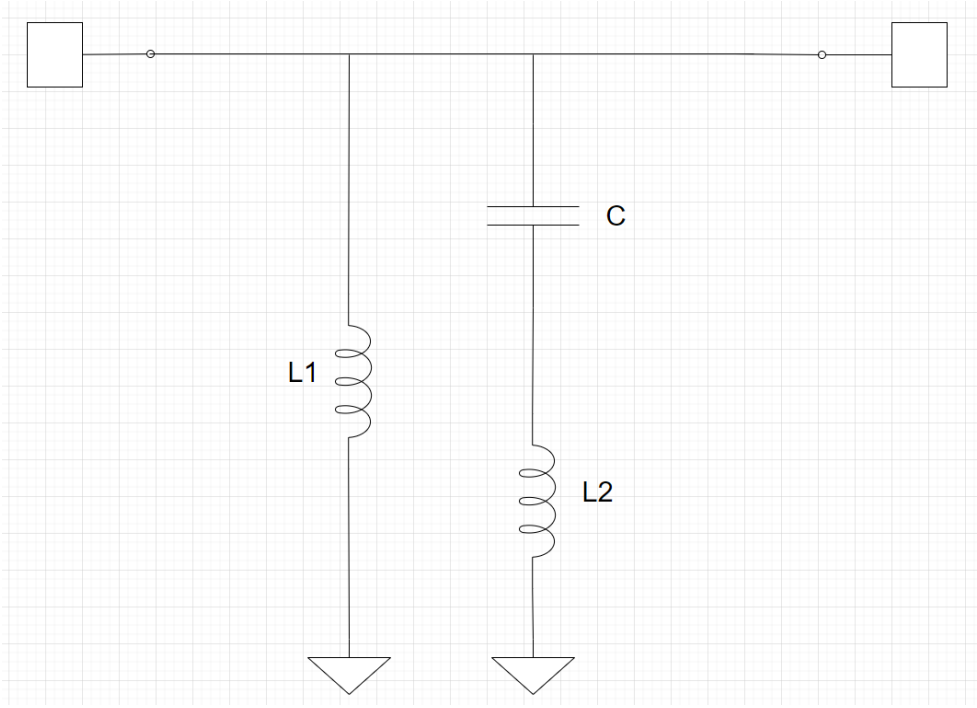

Figure 2.18: EC model of FSS unit cell

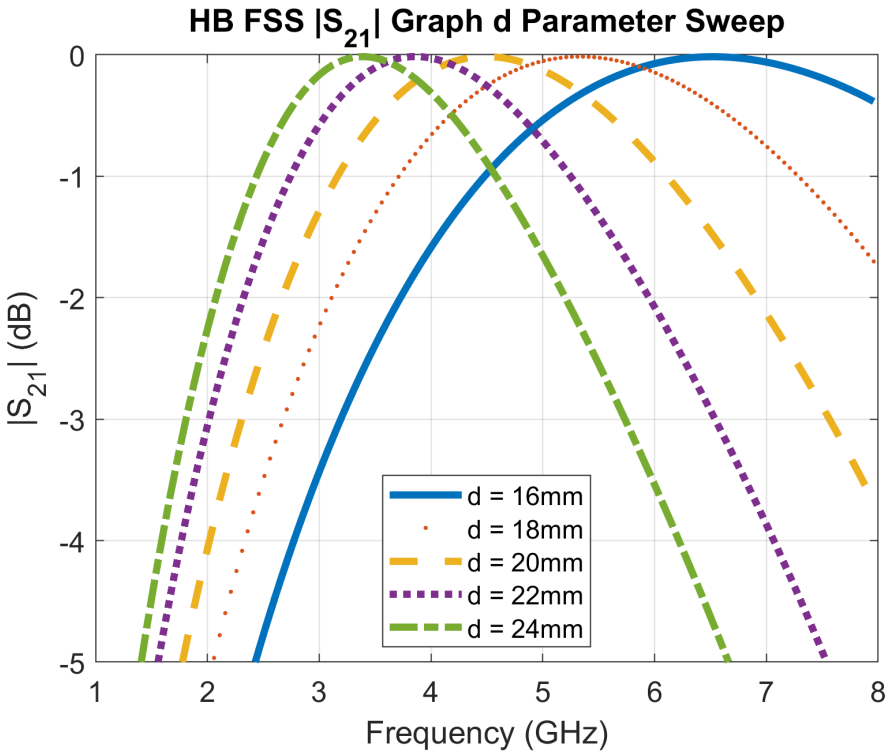

Figure 2.19: FSS d sweep results

The second parameter is the thickness of the square slot, s. From Figure 2.20, it can be seen that increasing the s value means an increase in both bandwidth and resonant frequency. The third parameter g variaion is displayed in Figure 2.21. Increasing g increases the resonant frequency slightly. Low cutoff frequency becomes higher. For 0.5dB and 1dB bandwidth, the upper cutoff frequency becomes higher, but cutoffs become nearly equal at 3dB bandwidth. So, overall bandwidth decreases slightly with increasing the g. The final parameter is h; when substrate thickness increases, bandwidth becomes narrower with a slightly lower resonance frequency. The substrate thickness change effect can be seen in Figure 2.22.

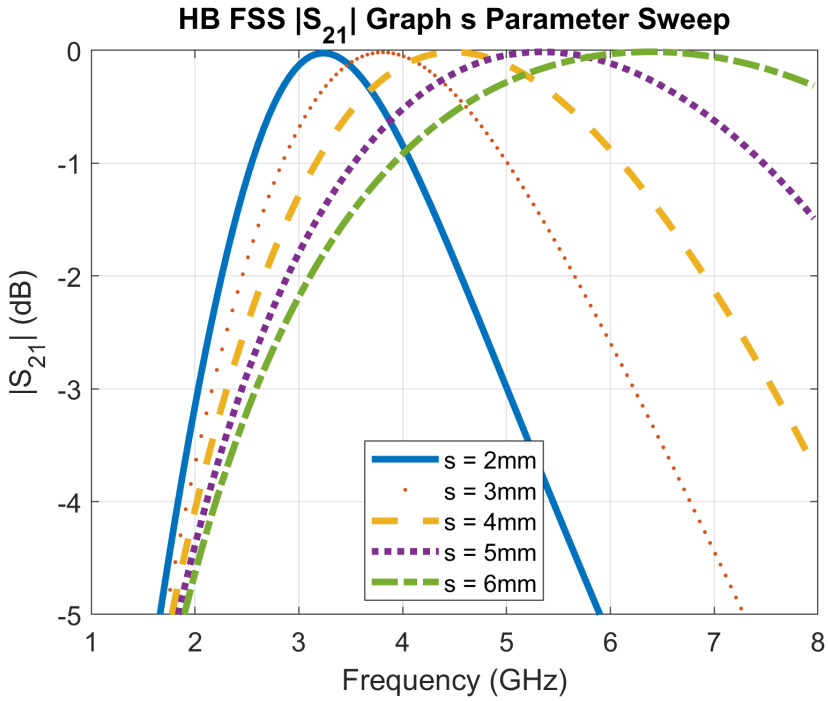

Figure 2.20: FSS s sweep results

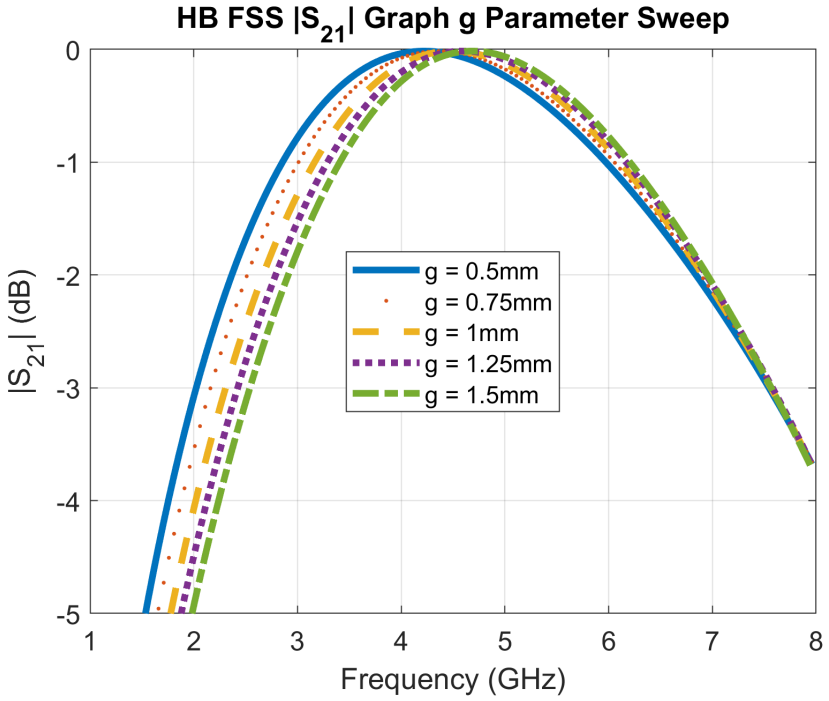

Figure 2.21: FSS g sweep results

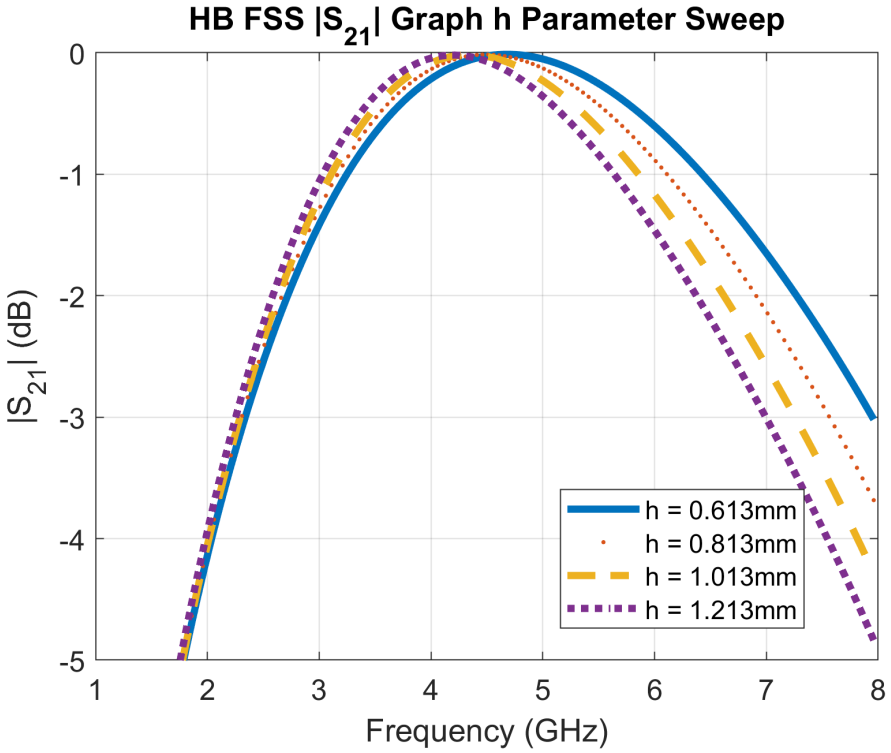

Figure 2.22: FSS h sweep results

The aim of the designed FSS is to be transparent for the high-band antenna operating at 3.3-5.5 GHz. The average value of 4.4 GHz can be selected as the desired resonance frequency of the FSS. Using the aforementioned equations and ™HFSS simulator, the optimal FSS is designed. Its parameters are listed in Table 2.1. Also, the obtained resonance frequency and desired resonance frequency are compared in Table 2.2. resultant resonance frequencies obtained from the EC model and ™HFSS are very close to the desired frequency. The obtained EC inductance and capacitance values are applied in the LTSpice program [58]. The equivalent circuit is given in Figure 2.23. The calculated inductance and capacitance values are $L_1 = 25.06pH$, $L_2 = 8.78pH$ and $C = 36.7pF$, respectively. The circuit's maximum power is transferred to output at 4.5GHz, which is close to 4.4GHz. Besides, ™HFSS plots of both TE and TM modes are shown in Figure 2.26. TE-TM modes' S_{11} and S_{21} are almost identical to each other, meaning polarization independence. This is expected because the unit cell is symmetric with respect to both the x and y axes.

The resonance frequency can also be seen in the reflection magnitude and phase angle variation. The minimum point of the reflection curve is the resonance frequency, and the point where the phase variation of reflection crosses 0° is the resonance frequency. In Figure 2.24, the resonance frequency can be seen as 4.46 GHz. The zero crossing phase is also valid for transmission phase variation. Furthermore, the interval between the angles -90° and 90° is the 'in-phase band' of the FSS [59]. In Figure 2.25, TE and TM mode transmission phase angles are shown. At resonance frequency, the phase angle is 0°, and the phase angle is 28° and -21° at 3.3 and 5.5 GHz, respectively. Hence, it can be said that FSS is in phase in passband.

Table 2.1: Optimum Design Parameter Values

Design Parameter	Value (mm)
d	21
s	4
g	2
h	0.813

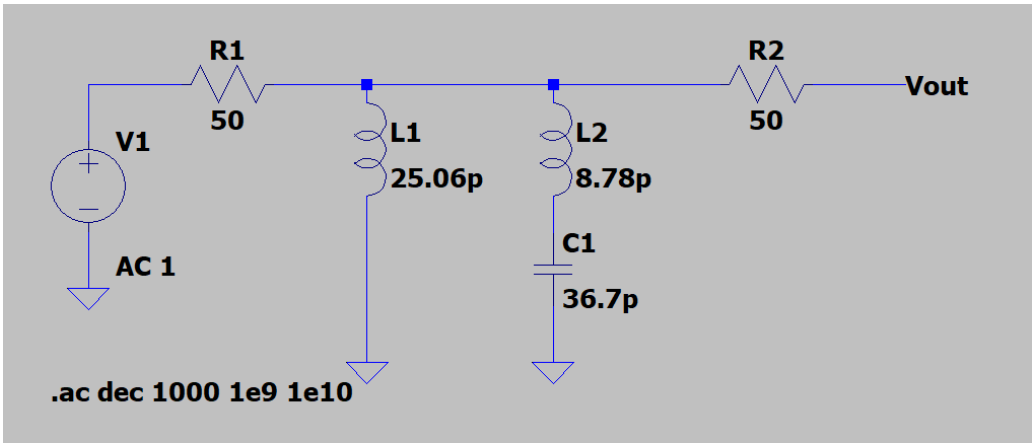

Figure 2.23: FSS EC Model in LTSpice

Table 2.2: Resonance Frequency Comparison

Used Program	Obtained Frequency (GHz)	Frequency Difference (%)
MATLAB	4.516	2.64
™HFSS	4.46	1.36
LTSpice	4.5	2.27

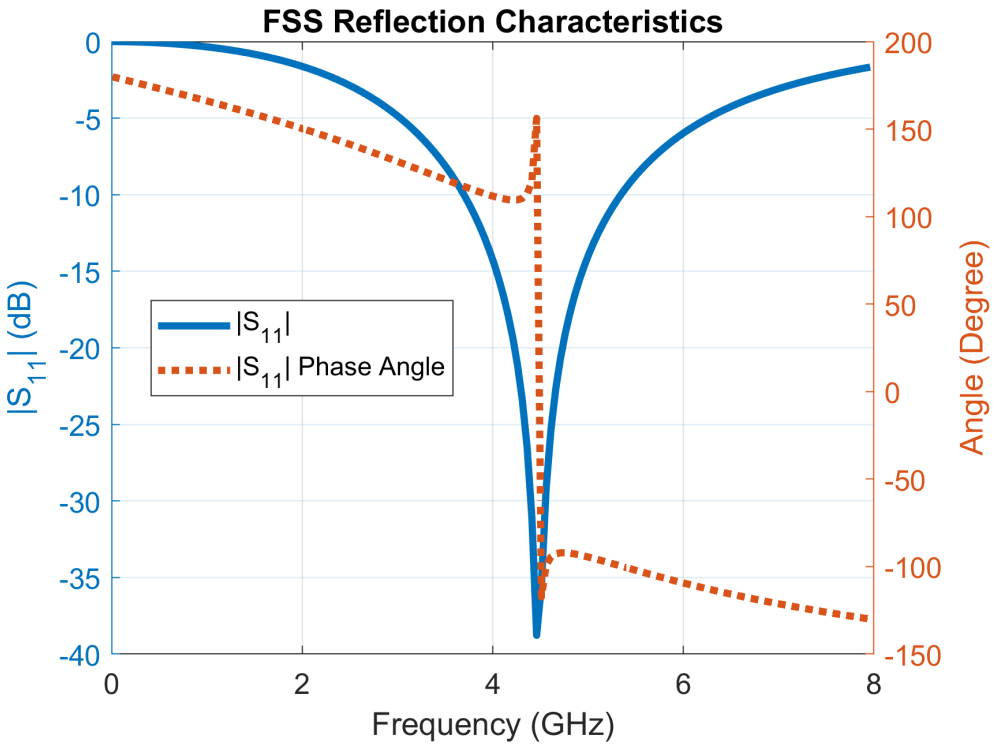

Figure 2.24: FSS reflection characteristics with respect to phase angle

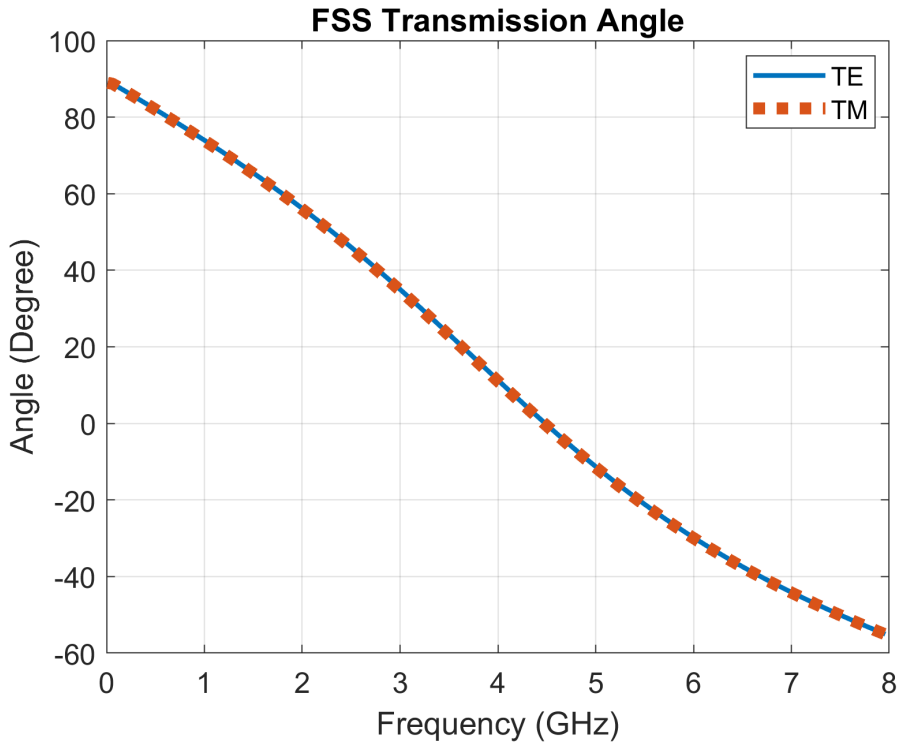

Figure 2.25: FSS transmission characteristics with respect to phase angle

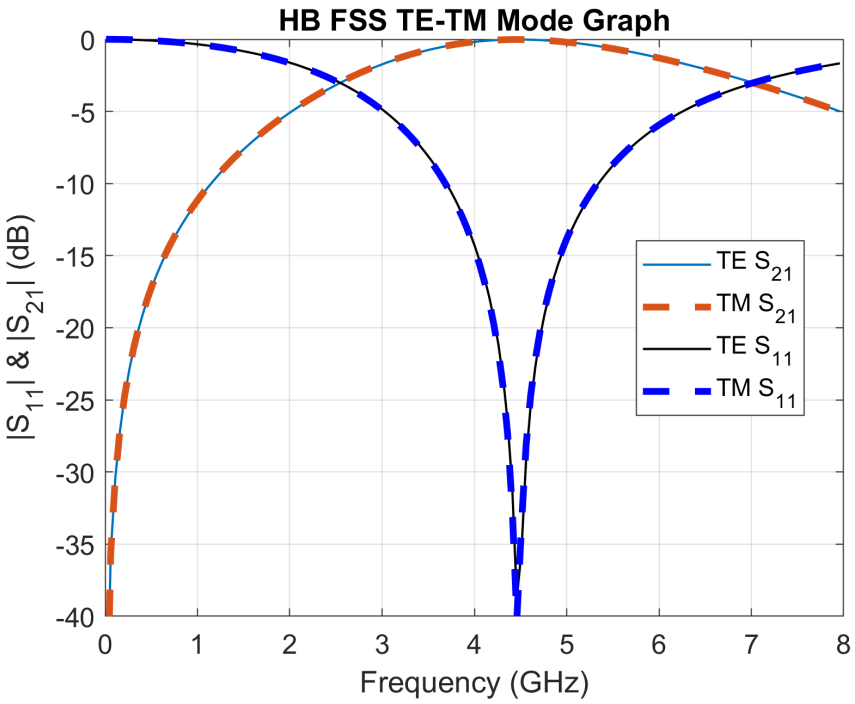

Figure 2.26: TE-TM Polarizations S-parameters of FSS

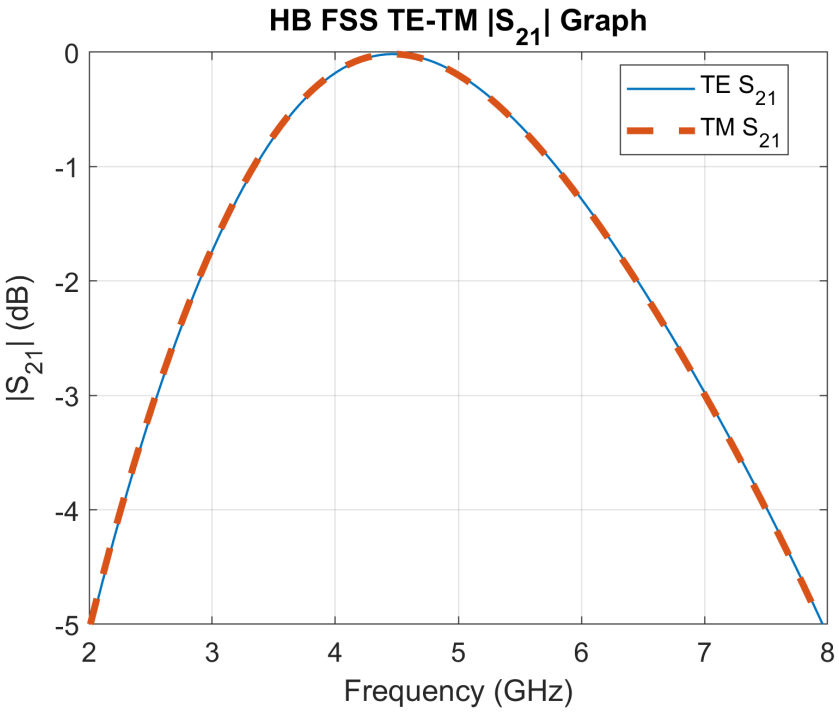

Figure 2.27: TE-TM Polarizations S_{21} of FSS

Examining Figure 2.27, the 0.5dB bandwidth of both polarizations is 3.66-5.37 GHz,

1dB bandwidth is 3.30-5.80 GHz, and 3dB bandwidth is 2.54-7.00 GHz. Hence, the plane waves radiating in the 3.34-5.8 GHz frequency band can freely transmit with at most 1dB insertion loss. So the high band (HB) antenna, operating in the 3.3-5.4 GHz band, right under this FSS, will have at most 1 dB transmission loss.

On the other hand, there will be spacers right under the FSS to support and stabilize the FSS. So, the HB antenna cannot be replaced directly under the FSS. In addition to vertical distance, there will also be horizontal distance, which results in a nonzero incidence angle. Nonzero incidence angle cases must be observed to see the angular stability of the designed FSS. The TE mode with different incidence angles can be seen in Figure 2.28. The resonance frequency is decreased minimally, but the bandwidth decrease is significant with the increasing incidence angle for the TE polarization. TE wave impedance varies with $Z_o/cos(\theta)$ [7], where Z_o is the characteristic impedance of the electromagnetic wave, which affects the quality factor of the FSS filter resonator [60]. As the angle increases, TE wave impedance increases, the quality factor increases, and the bandwidth decreases. In Figure 2.28, insertion loss is at most 2dB within the HB antenna bandwidth at 45°. For 60° case, 3dB bandwidth is between 3.39-5.37 GHz and covers most of the HB bandwidth, indicating that FSS is stable up to 60° for TE polarization in terms of 3dB bandwidth. But it should be noted that there is an unexpected bump at 7.5 GHz for 60° incidence, which means there is an unwanted peak of the FSS. Equation 2.16 explains the relationship between the unwanted peaks and design parameters. According to this relation, the first observation is decreasing the FSS dimensions (or periodicity) would decrease the number of unwanted peaks or shift them to higher frequencies. The second observation is increasing incidence angle creates more unwanted peaks in the vicinity of the passband or even in the passband if the angle increases more. The third observation is that more unwanted peaks will occur in the higher frequencies because λ is decreasing. So, while designing FSS, periodicity must kept smaller to have high angular stability and zero or less unwanted peaks [61].

$$p(1 + sin(\theta)) = (d + g)(1 + sin(\theta)) < \lambda \tag{2.16}$$

For the TM polarization, wave impedance varies with $Z_o cos(\theta)$. Wave impedance is

decreasing with the increasing incidence angle θ. Oppositely, to the TE polarization, the quality factor is decreasing, but bandwidth becomes narrower again except θ = 60° at 1dB bandwidth. The reason is that there is a transmission zero (TZ) at the higher frequencies of the EC circuit in Figure 2.18 with the formula given in Equation 2.17. When θ increases, C increases, and L_2 decreases, L_2C multiplication increases, and consequently, TZ frequency decreases. For TE, the low cutoff becomes higher, and the high cutoff becomes lower, meaning a notable decrease in bandwidth. For TM, both low and high cutoffs become lower, and unwanted peaks occur for lower frequencies than TE polarization. 1dB and 3dB bandwidths are decreasing in general. TM mode results can be seen in Figure 2.29. There is at most 2dB attenuation in TM polarization for 60°, and resonance frequency is almost the same with 0°. Considering the 60° angular stability in TM mode, designed FSS is stable up to 60° in both TE and TM polarizations. It should also be noted that FSS is reciprocal, meaning that the transmission and reflection properties for both polarizations are the same for both Floquet ports.

$$f_{TZ} = \frac{1}{2\pi\sqrt{L_2C}} \tag{2.17}$$

The TE phase angle variation with the incidence angle change is given in Figure 2.30 (a). As the θ increases, phase variation increases. At 3.3 GHz, phase angle increases to 47.35° from 28°; and phase decreases to -48.4° from -21° at 5.5 GHz. Results show that FSS is still in the in-phase band, but phase angles are getting closer to ±90° borders. And zero crossings are nearly the same for all incidence angle cases. Apart from that, there are instant phase changes after 7 GHz. The instant jump occurs at the TZ of the FSS, and then the zero crossing after the jump is the unwanted peak maximum transmission. TM phase variation graph is in Figure 2.30 (b). Increasing θ decreases the low cutoff phase angle (from 28° to 16.6°) and the high cutoff phase angle as well (from -21° to -42.7°). Another point is that increasing θ crosses 0° at lower frequencies, which can also be called zero crossings, but resonance frequency does not change that significantly, as can be seen in Figure 2.29. Hence, looking at TM S_{21} magnitude graph and reflection phases' zero crossings gives a better idea about resonance frequency, which is given in Figure 2.31. Zero crossing at θ = 60° is 4.33 GHz for reflection phase, and transmission phase zero crossing is 4.18 GHz.

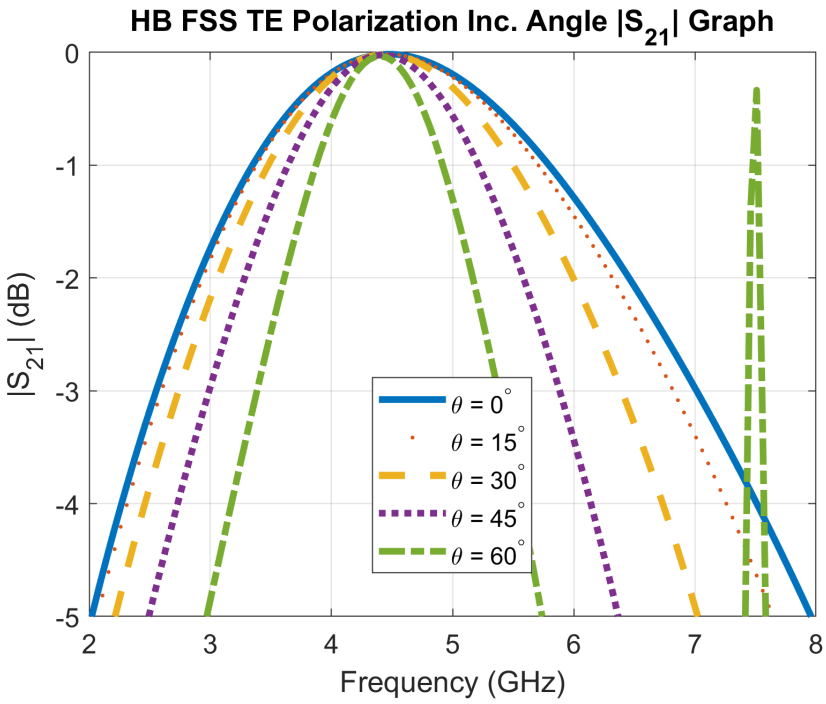

Figure 2.28: TE polarization S_{21} with different incidence angles

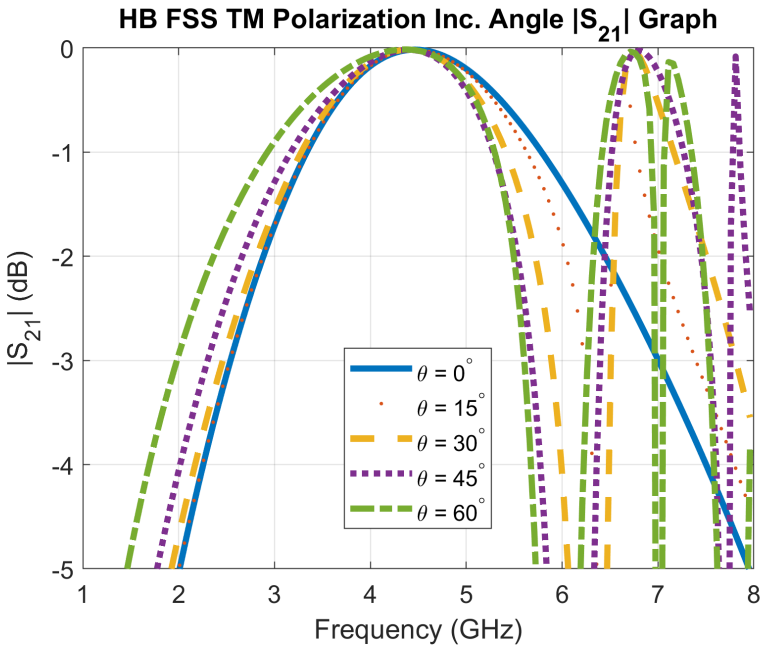

Figure 2.29: TM polarization S_{21} with different incidence angles

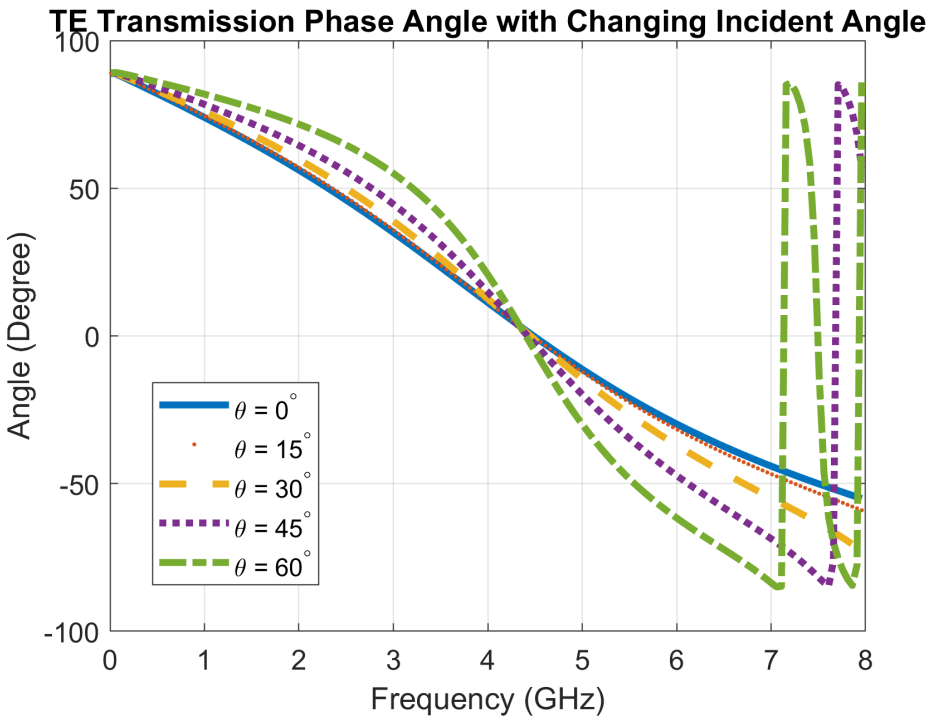

(a)

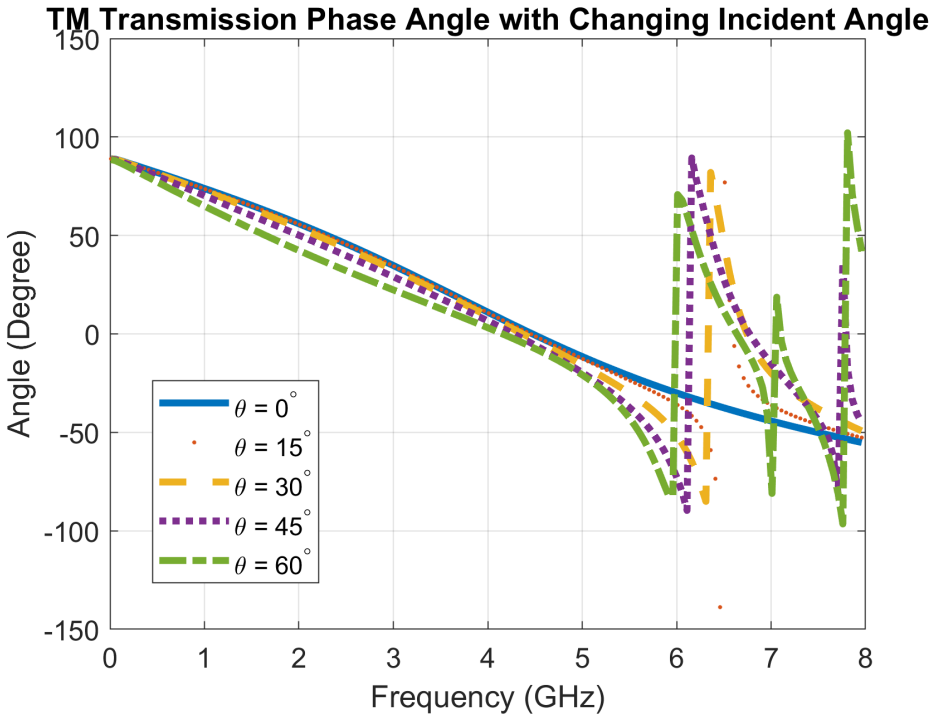

(b)

Figure 2.30: TE (a) and TM (b) transmission phase angle plots

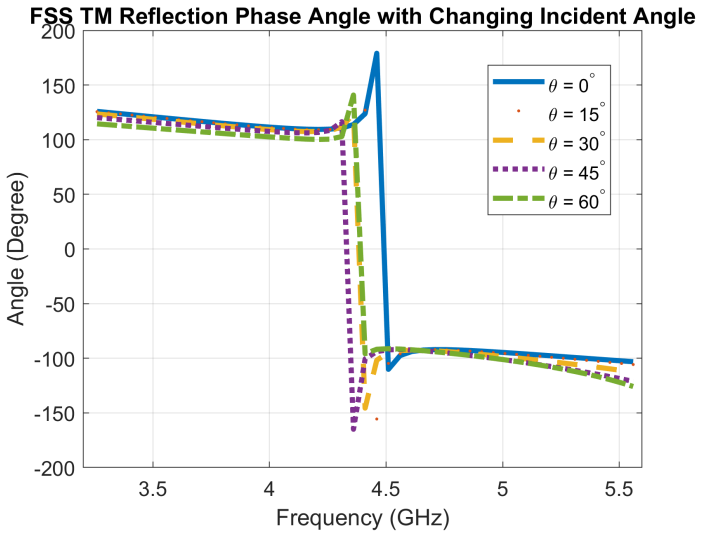

Figure 2.31: TM polarization reflection phase angle with different incidence angles

If both antenna inputs are fed with 90° phase difference, then the designed antennas can also be operated in both right-hand circular polarization (RHCP) and left-hand circular polarization (LHCP). Hence, the FSS bandpass characteristic must be observed in circular polarization modes as well as TE-TM modes. Circular polarization characteristics can be derived from TE and TM modes.

Firstly, the incidence wave vectors towards the FSS unit cell are $\mathbf{a}$ and $\mathbf{b}$, and scattered (or transmitted) wave vectors from the FSS unit cell are $\mathbf{c}$ and $\mathbf{d}$. Scattered wave vectors $\mathbf{c}$ and $\mathbf{d}$ can be extracted in terms of incident wave vectors $\mathbf{a}$ and $\mathbf{b}$ as:

$$\begin{bmatrix} \mathbf{c}^{TE} \\ \mathbf{c}^{TM} \\ \mathbf{d}^{TE} \\ \mathbf{d}^{TM} \end{bmatrix} = \begin{bmatrix} s_{11}^{TE,TE} & s_{11}^{TE,TM} & s_{12}^{TE,TE} & s_{12}^{TE,TM} \\ s_{11}^{TM,TE} & s_{11}^{TM,TM} & s_{12}^{TM,TE} & s_{12}^{TM,TM} \\ s_{21}^{TE,TE} & s_{21}^{TE,TM} & s_{22}^{TE,TE} & s_{22}^{TE,TM} \\ s_{21}^{TM,TE} & s_{21}^{TM,TM} & s_{22}^{TM,TE} & s_{22}^{TM,TM} \end{bmatrix} \begin{bmatrix} \mathbf{a}^{TE} \\ \mathbf{a}^{TM} \\ \mathbf{b}^{TE} \\ \mathbf{b}^{TM} \end{bmatrix} \tag{2.18}$$

In Equation 2.18, the TE and TM on the top right of the incident and scattering wave vector indicate the polarization. For S-parameters, i indicates the Floquet port to which the scattered wave goes, and j indicates the Floquet port which the incident wave comes from. For the exponent part of the S-parameters, the left polarization indicates the scattered wave's polarization and the right polarization indicates the incident wave's polarization. The S-parameter matrix $\mathbf{S}$ can also be written in terms

of reflection and transmission parameters in Equation 2.19 [62].

$$\Big[\mathbf{S}\Big] = \begin{bmatrix} R_1^{y,y} & R_1^{y,x} & T_2^{y,y} & T_2^{y,x} \\ R_1^{x,y} & R_1^{x,x} & T_2^{x,y} & T_2^{x,x} \\ T_1^{y,y} & T_1^{y,x} & R_2^{y,y} & R_2^{y,x} \\ T_1^{x,y} & T_1^{x,x} & R_2^{x,y} & R_2^{x,x} \end{bmatrix} \tag{2.19}$$

In Equation 2.19, R means reflection, and T means transmission coefficient. Since TE is y polarized and TM is x polarized, TE and TM polarizations are written in x and y. The number at the right bottom is the incident Floquet port number. For two Floquet ports, transmission or reflection characteristics can be observed, thus $\mathbf{S}$ matrix can be examined in four submatrices of R_1, R_2, T_1, T_2. Since bandpass FSS is examined, analyses are mostly focused on transmission characteristics. And it is known that FSS is reciprocal, i.e. $T_1^{p1,p2}$ = $T_2^{p2,p1}$, where the $p1$ and $p2$ indicate the polarizations, therefore only T_1 matrix can be calculated to see the transmission performance for circular polarization (CP). If both $p1$ and $p2$ are the same, then transmission occurs in co-polarization, if $p1$ and $p2$ are different, cross-polarization transmission occurs. Since TE and TM polarizations are orthogonal to each other, cross-polarization effects are expected to be minimal. The T_1 matrix can be written in Equation 2.20 as $\mathbf{T}$.

$$\Big[\mathbf{T}\Big] = \begin{bmatrix} T_1^{y,y} & T_1^{y,x} \\ T_1^{x,y} & T_1^{x,x} \end{bmatrix} = \begin{bmatrix} T^{y,y} & T^{y,x} \\ T^{x,y} & T^{x,x} \end{bmatrix} \tag{2.20}$$

From $\mathbf{T}$, $\mathbf{T_{CP}}$ circular polarization transmission matrix can be obtained. The TE and TM polarization matrix is on a linear basis, and mapping is required on a circular basis for the CP realization. Mapping is shown in Equation 2.21 and 2.22. $T^{inc,rec}$ term in the matrix indicates the CP transmission direction as incidence and as received, respectively. R means RHCP, and L means LHCP. As expected, the same incidence and received polarization mean co-polarization and different polarization means cross-polarization. Thus, CP transparency of the FSS can be seen with the linear polarization results.

$$\left[\mathbf{T_{CP}}\right] = \begin{bmatrix} T^{R,R} & T^{R,L} \\ T^{L,R} & T^{L,L} \end{bmatrix} \tag{2.21}$$

$$\left[\mathbf{T_{CP}}\right] = \frac{1}{2}\begin{bmatrix} T^{y,y} + T^{x,x} + i\left(T^{x,y} - T^{y,x}\right) & T^{x,x} - T^{y,y} - i\left(T^{x,y} + T^{y,x}\right) \\ T^{x,x} - T^{y,y} + i\left(T^{x,y} + T^{y,x}\right) & T^{y,y} + T^{x,x} - i\left(T^{x,y} - T^{y,x}\right) \end{bmatrix} \tag{2.22}$$

The RHCP transmission graph is shown in Figure 2.32, and the LHCP graph is shown in Figure 2.33 with varying incidence angles by using the Equation 2.22. CP plots look almost the same because co-polarization terms $T^{x,x} + T^{y,y}$ are common, and cross-polarization terms $T^{x,y}$, $T^{y,x}$ magnitudes are very low with respect to co-polarization terms. That being said, cross-polarization terms do not significantly affect the transmission characteristics of co-polarization. With the TE and TM coefficients' sum, low cutoffs remain relatively similar except 60°. High cutoffs decrease with increasing angle as expected. 1dB bandwidth angular stability is obtained at 30° and 3dB bandwidth angular stability is obtained at 60°.

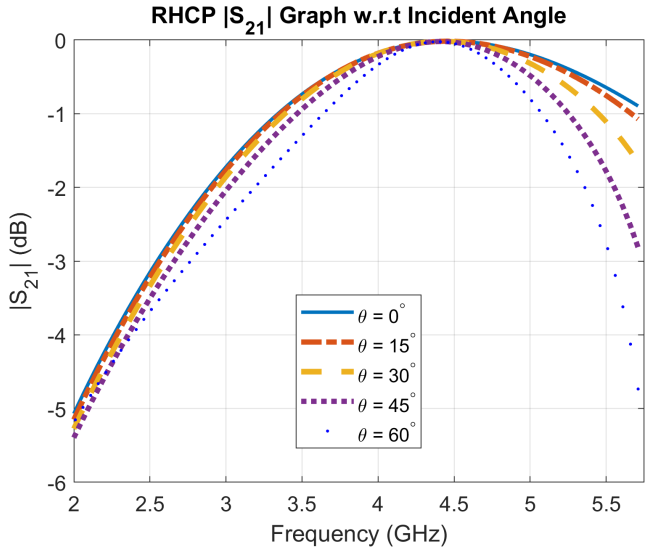

Figure 2.32: RHCP FSS transmission for different incidence angles

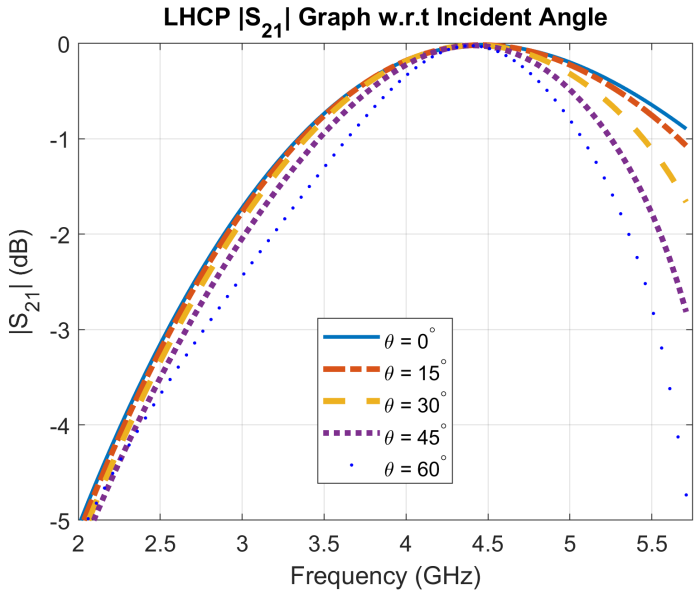

Figure 2.33: LHCP FSS transmission for different incidence angles

Up to now, FSS simulations have been made with the assumption that the FSS unit cell is periodic and extends to infinity. However, the designed FSS will be used as an antenna, and it will contain only four unit cells with a 2×2 form. Hence, infinite array Floquet ports simulations help the design of the unit cell, but the designed finite FSS structure should also be examined. So, the FSS structure's periodicity property decreases to only 2×2. From this point, the designed structure can be called an 'EM transparent' surface. For this examination, a hypothetical Hertzian dipole antenna is defined under the EM transparent surface to represent high-band antenna radiation. A non-model sheet is defined in the direction of the Hertzian dipole and to the z-axis to see the electric field propagation. The Hertzian dipole is placed under the transparent surface with a distance of 14 mm, which is the height distance between the middle-band and high-band antenna. The dipole and non-model sheet are shown in Figure 2.34.

It is known that the Hertzian dipole's electric field in Figure 2.34 is towards $\pm$z direction. Figure 2.35 gives the Hertzian dipole electric field without any surface.

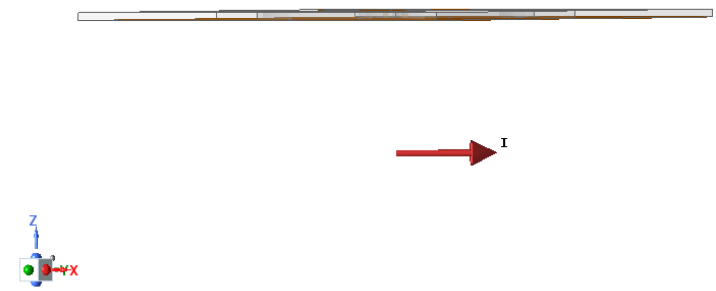

(a)

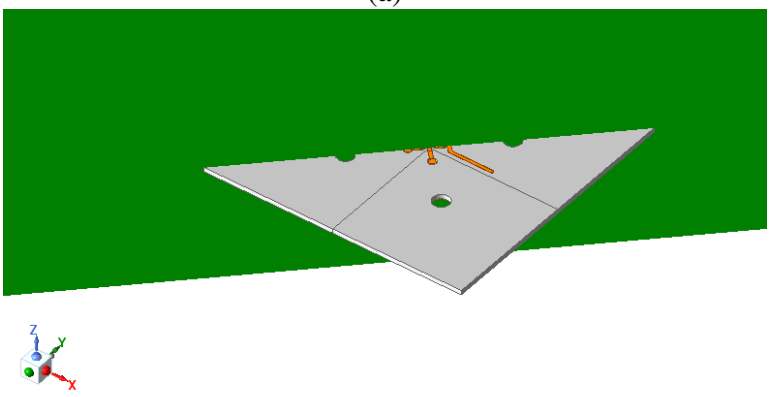

(b)

Figure 2.34: (a) Hertzian dipole and (b) non-model sheet

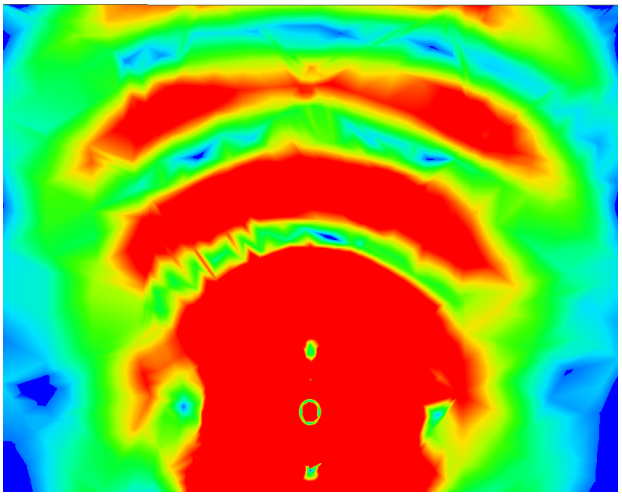

Figure 2.35: Hertzian dipole electric field distribution alone with no surface

Apart from that, a different significant observation can be made with no patch in the middle of the unit cell. In that case, the FSS unit cell becomes a square loop FSS, which shows bandstop filter characteristics. The transparency characteristic of the unit cell is given in Figure 2.36. The bandstop frequency is at 2 GHz, and partially transmitting characteristics can be seen between the frequency band of the HB with fluctuations on the S_{21} curve. However, it is lower than the original square slot unit cell design.

The electric field patterns of five different frequencies of the HB antenna are given in Figure 2.37. As the plots show, electric field patterns are the same and do not distort the original Hertzian dipole fields in the broadside direction. It should be noted that the EM transparent surface is shown with a horizontal linear at the center bottom of the plots. Thus, the designed surface shows an EM transparent surface even though it is not an infinite array of FSS unit cells. By comparing the fields with and without a surface, it can be seen that field distributions are close to each other. Additionally, the Hertzian electric field transparency behavior of the no-patch surface is given in Figure 2.38, which still protects the radiation towards the broadside direction.

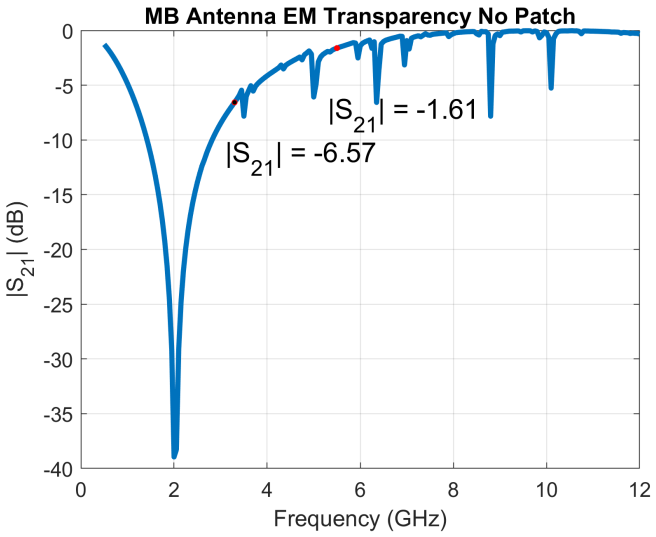

Figure 2.36: Transparency characteristic of the HB FSS without the patch

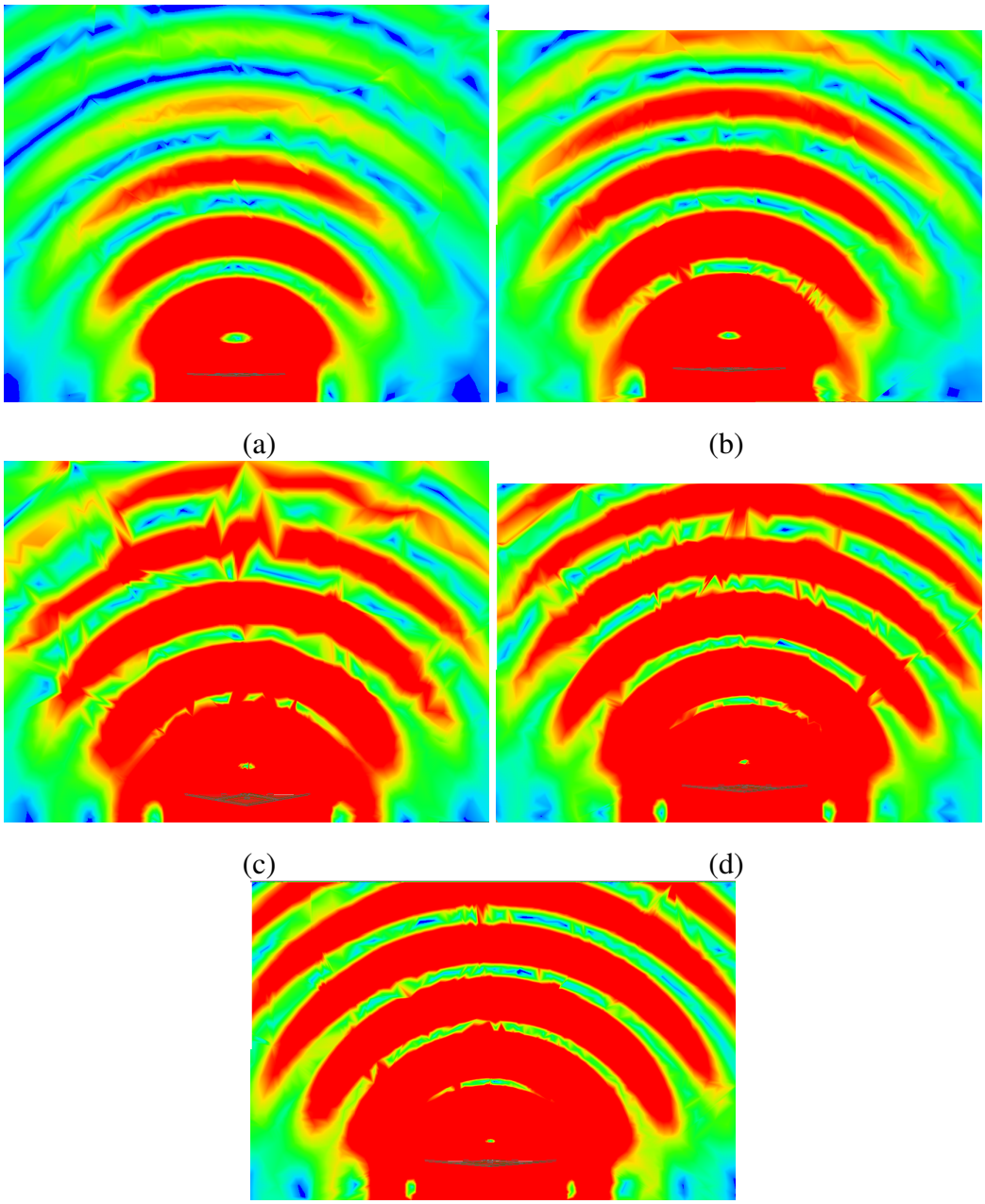

Figure 2.37: Hertzian dipole electric field distribution in the frequencies of (a) f = 3.4 GHz, (b) f = 3.9 GHz, (c) f = 4.4 GHz, (d) f = 4.9 GHz and (e) f = 5.4 GHz

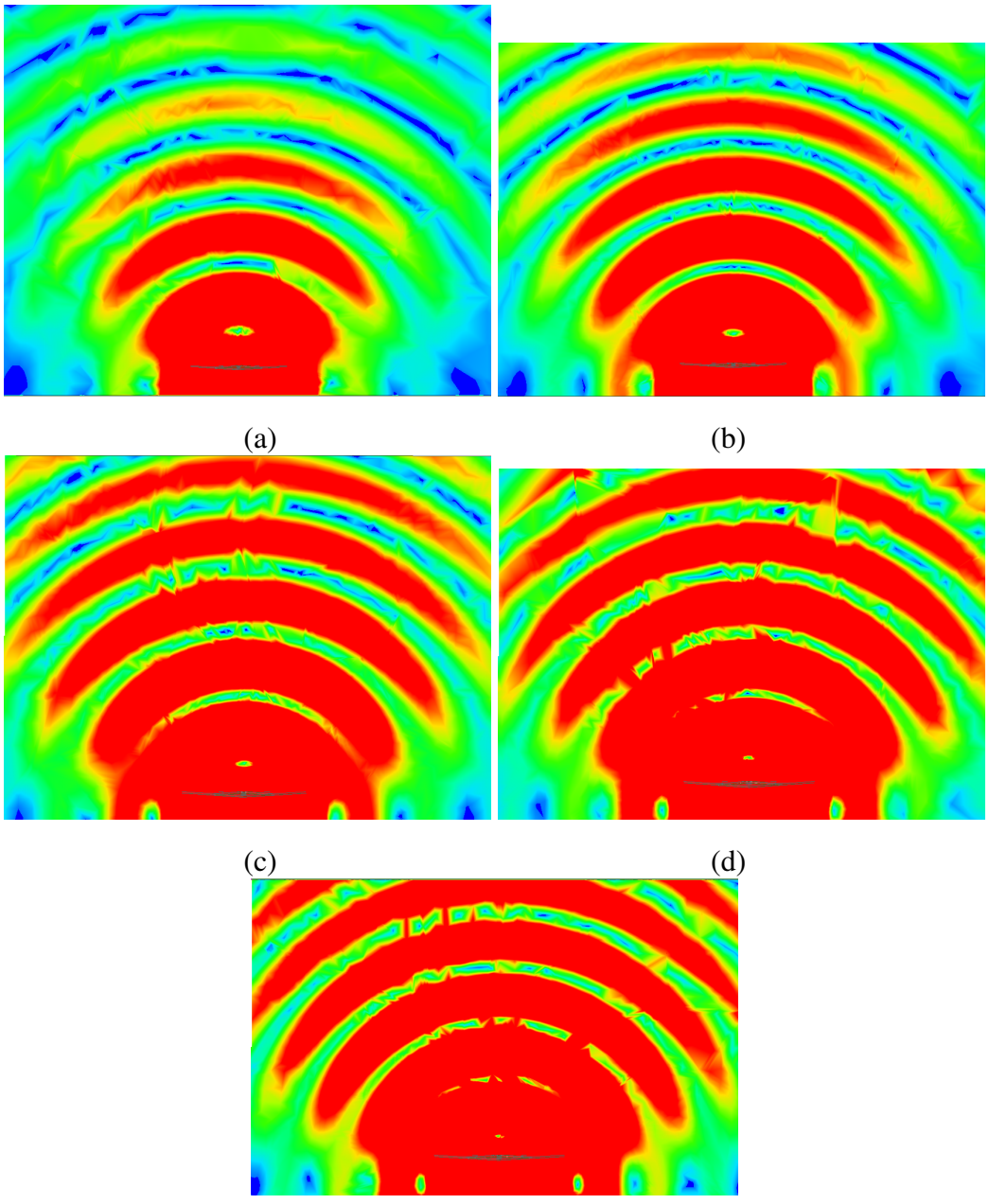

(a) (b)

(c) (d)

(e)

Figure 2.38: Hertzian dipole electric field distribution for the MB surface without a patch in the frequencies of (a) f = 3.4 GHz, (b) f = 3.9 GHz, (c) f = 4.4 GHz, (d) f = 4.9 GHz and (e) f = 5.4 GHz

2.5 FSS Design for Middle Band & High Band Antenna

The second FSS unit cell is designed as a wideband bandpass FSS and a low band cross dipole antenna operating between 1-1.6 GHz. Considering the middle band antenna (1.85-2.95 GHz) and high band antenna (3.3-5.5 GHz) bandwidths, a bandpass FSS between 1.85-5.5 GHz bandwidth is required. The second FSS is designed with a similar structure to the first designed FSS. Designing an almost 3:1 ratio BW bandpass FSS with the square slot single-layer unit cell is challenging. Hence the second design FSS acts as a partial passband, meaning that transmission losses are expected to be a little higher for the designed antennas.

The design process of the new FSS unit cell is the same as the previous one. Figure 2.39 shows the designed FSS with the same parameter definitions.

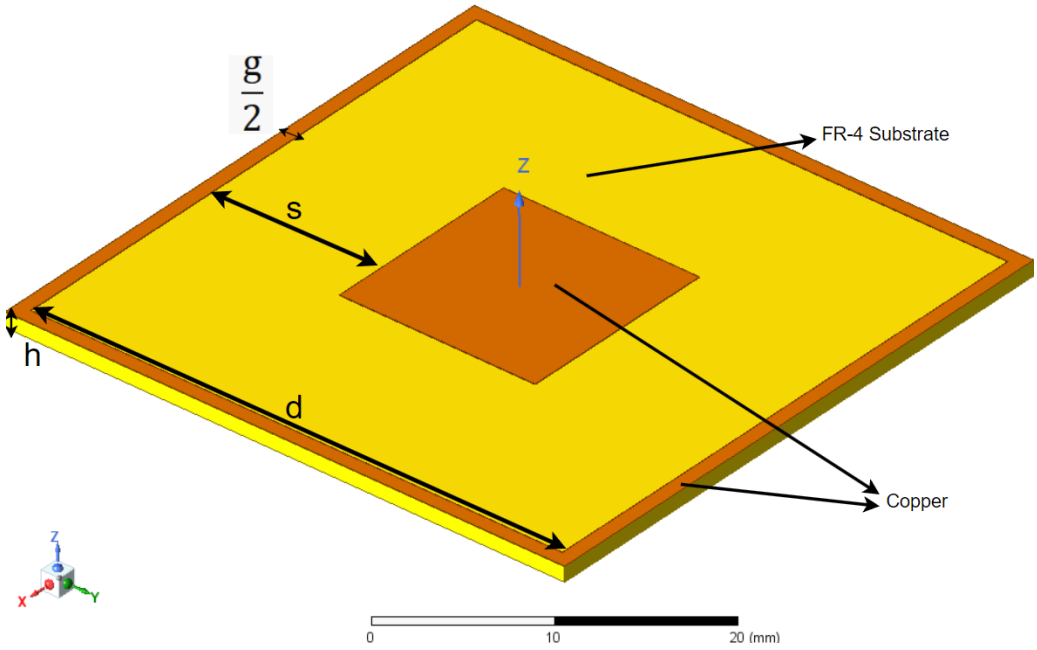

Figure 2.39: Middle Band & High band FSS unit cell

Previously, Equation 2.1 is used to determine unit cell d dimension with the idea of middle band antenna center frequency wavelength. In this design, d is determined from the low band antenna center frequency of 1.3 GHz. With Equation 2.1, d is calculated as 40.7 mm. The substrate used is FR-4 with ϵ_r = 4.4 with a thickness of h = 1 mm. The next step is using the Marcuvitz equations between Equation 2.3

and Equation 2.12 with Equations 2.14 and 2.15. The center frequency of the FSS is 3.675GHz. After solving Marcuvitz equations and applying ™HFSS simulations, the design parameters are determined as in Table 2.3.

Table 2.3: Optimum Design Parameter Values

Design Parameter	Value (mm)
d	38
s	12
g	2
h	1

Increasing s will increase the bandwidth, which is mentioned earlier; that is why s is larger than the previous FSS. Besides, having larger ϵ_r decreases the resonance frequency. Thus, the dielectric substrate is selected as FR-4 due to low cost and larger ϵ_r value than the RO4003. From the EC method, lumped elements are calculated as L_1 = 57.1 pH, L_2 = 49 pH and C = 21.32 pF shown in Figure 2.40. The MATLAB and equivalent circuit results deviate more than the 3D EM solver since the s value is increased significantly. The applied EC method evaluates the resonant frequency of the FSS but does not give any idea about the FSS bandwidth. Hence in order to increase the bandwidth, ™HFSS is mainly used. To satisfy the required bandwidth, the resonance frequency of the FSS is shifted to 3.48 GHz, which is only a 5.3% shift. The obtained resonance frequencies are given in Table 2.4. Comparison is made with the desired resonant frequency of 3.675 GHz.

In the next step, TE and TM modes are plotted in Figure 2.41. For θ = 0°, TE and TM polarizations are equal, satisfying the polarization independence. For the middle band (MB) antenna, losses at cutoffs are 1.62 dB and 0.18 dB for low and high cutoffs, respectively. Losses are 0.07 dB and 2.9 dB for the HB antenna cutoffs. So, designed MB & HB FSS can be operated as a partially transmitting surface (PTS) for the required antennas. Even in the θ = 0° case, unwanted peaks can be seen in Figure 2.41 because of the fact that periodicity length p is increased significantly with the increase of d while λ of the resonance frequency is increased slightly. According to

Equation 2.16, unwanted peaks are inevitable, which is a drawback for the angular stability performance.

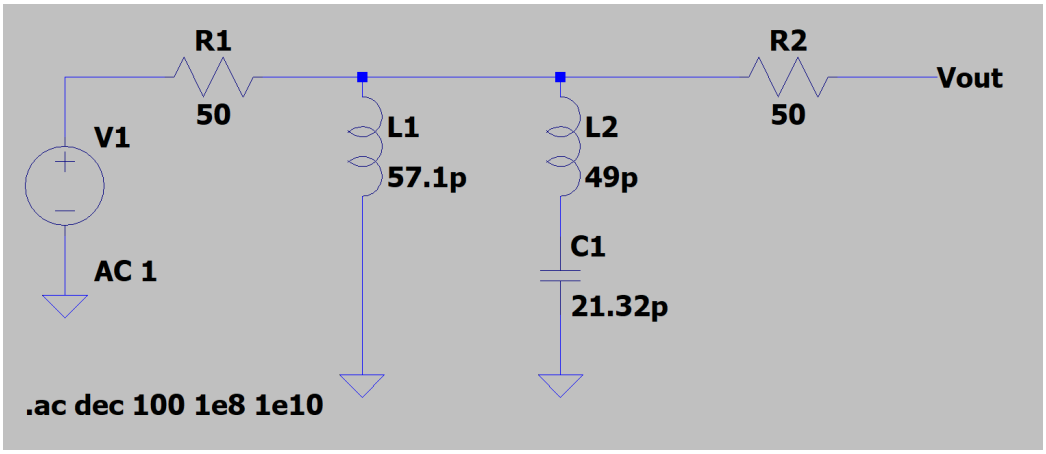

Figure 2.40: FSS EC Model in LTSpice

Table 2.4: Resonance Frequency Comparison

Used Program	Obtained Frequency (GHz)	Frequency Difference (%)
MATLAB	3.346	-8.95
™HFSS	3.48	-5.3
LTSpice	3.31	-9.93

The S_{11} magnitude and phase graph are given in Figure 2.42. The resonance frequency is 3.48 GHz for the MB & HB FSS. In Figure 2.43, both TE and TM mode phase variations are displayed. The zero crossing is at 3.5 GHz, close to 3.48 GHz. The phase angle for the low cutoff of 1.85 GHz is 33.7° and -40° for the high cutoff of 5.4 GHz. In both Figures 2.42 and 2.43, there are instant phase variations owing to the unwanted peaks and transmission zeroes, which are relatable to magnitude graphs of the FSS S_{11} and S_{21}.

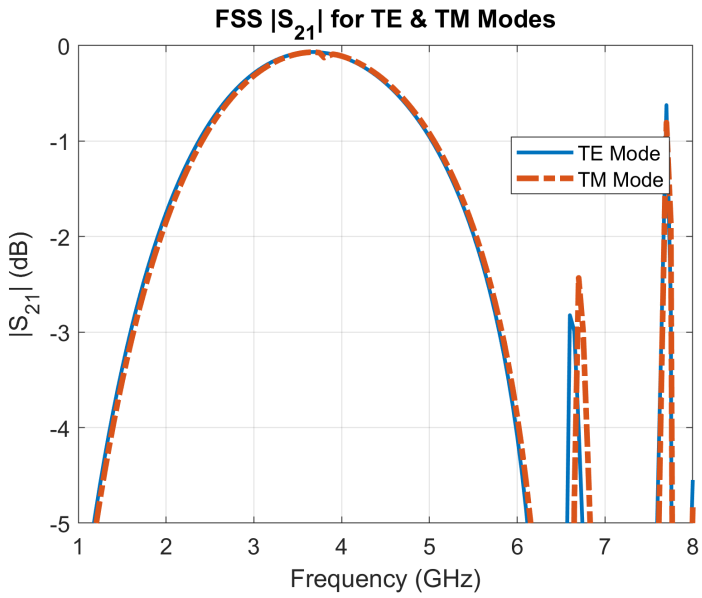

Figure 2.41: TE-TM Polarizations' S_{21} of MB & HB FSS

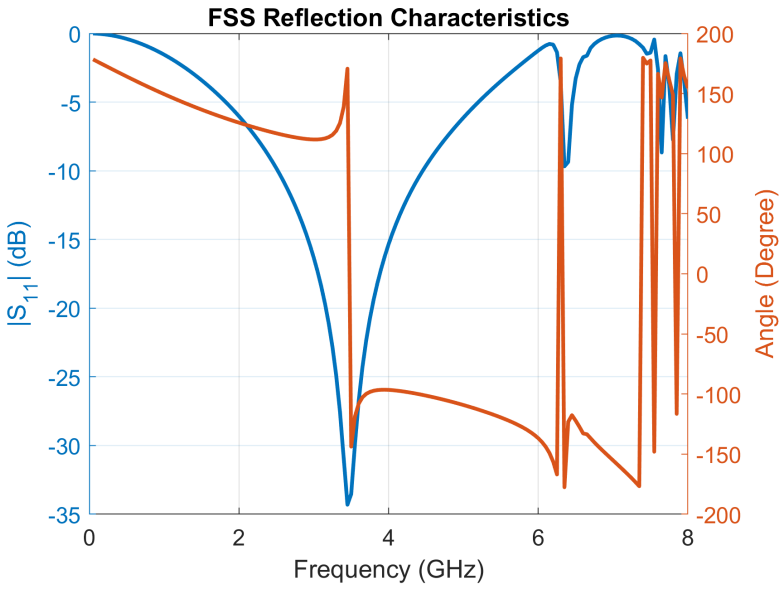

Figure 2.42: S_{11} Magnitude and Phase Plot of MB & HB FSS

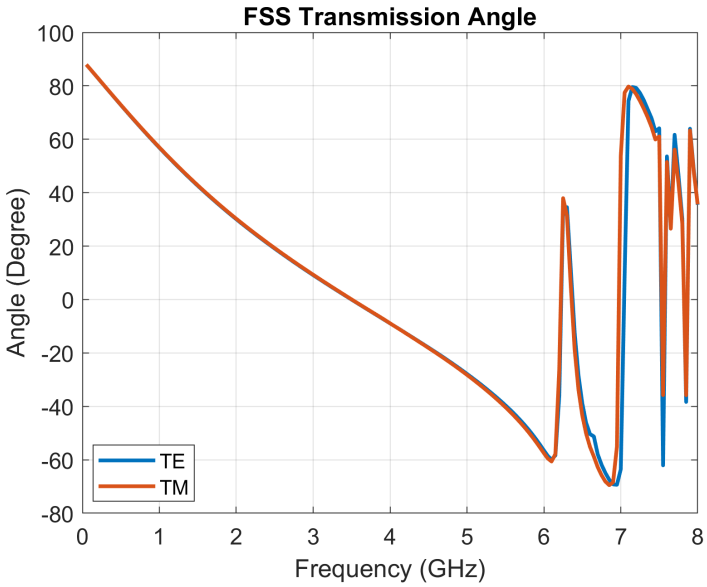

Figure 2.43: S_{21} Angle Variation of MB & HB FSS

The next step is to observe the FSS angular stability. Even for the $\theta = 0°$ there are unwanted peaks. With the θ increase, many more unwanted peaks are expected. Thus, the MB & HB FSS angular stability is expected to be much less with respect to HB FSS designed in Chapter 2.4. The transmission coefficients for different incidence angles are shown in Figures 2.44 and 2.45. The bolder lines are the higher θ to show the number of unwanted peaks and the bandwidth degradation. Unwanted peaks start to occur inside of the required band such that the partially transmitting surface (PTS) property is lost for the HB band. The FSS works as PTS up to only $\theta = 15°$.

Considering the low angular stability of the MB & HB FSS, the designed antennas' placement should be considered. Placing antennas right under the FSS cannot be done due to the spacer and supply cables. So, antennas are placed as close as to FSS in the x and y axes to weaken the high incidence angle effect. The antenna and FSS placements are explained in Chapter 4 in more detail.

The next step includes the CP transmission. The same method of the HB FSS is applied to MB & HB FSS. The results in Figures 2.46 and 2.47 show that the PTS property is also valid for the CP cases.

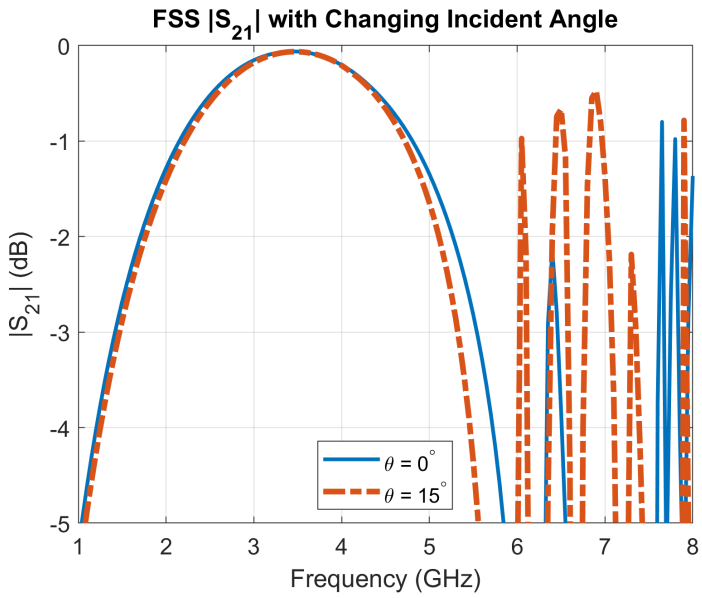

Figure 2.44: S_{21} Magnitude Variation of MB & HB FSS at $\theta = 0°$ and $\theta = 15°$

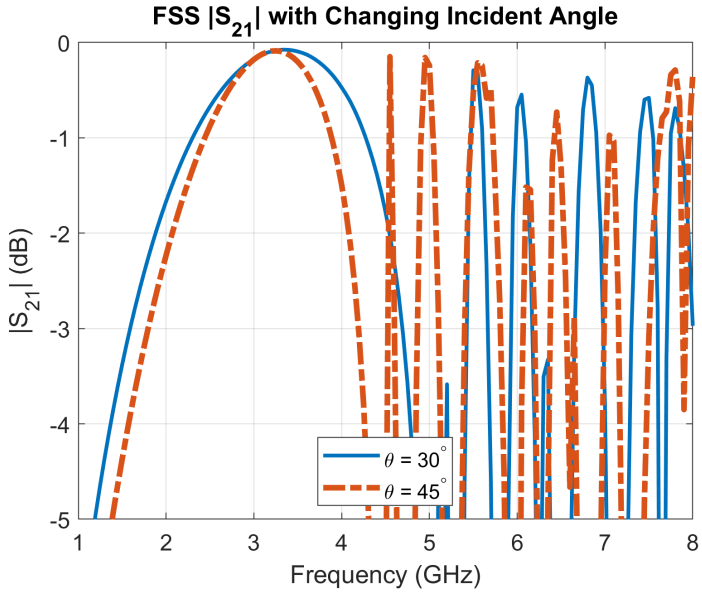

Figure 2.45: S_{21} Magnitude Variation of MB & HB FSS at $\theta = 30°$ and $\theta = 45°$

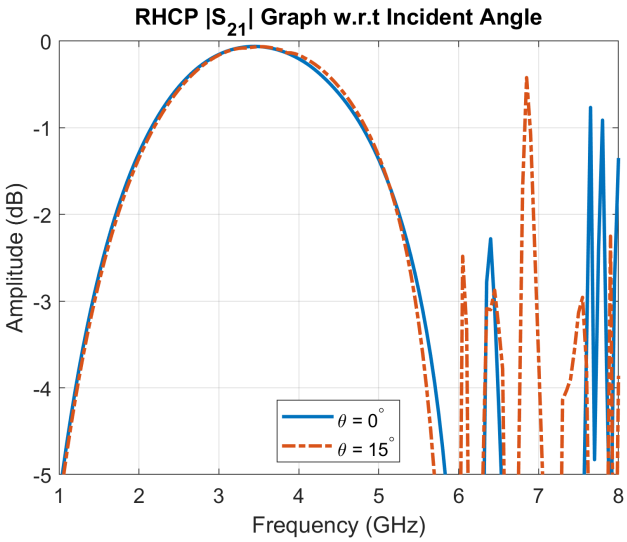

Figure 2.46: RHCP S_{21} plot of the MB & HB FSS

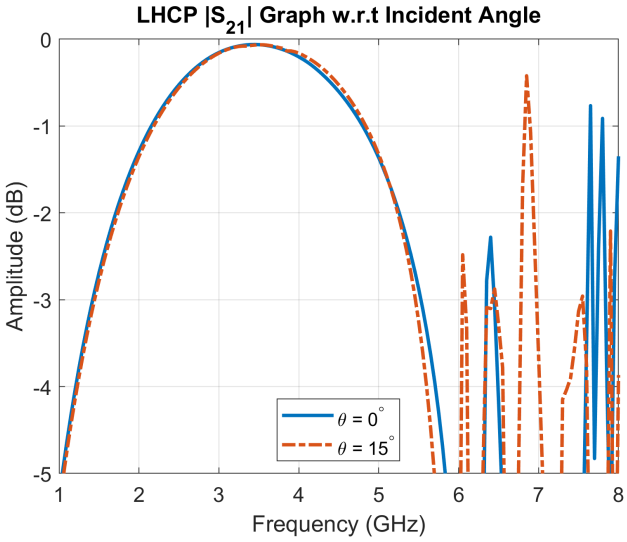

Figure 2.47: LHCP S_{21} plot of the MB & HB FSS

FSS unit cell with no patch approach is also applied for the MB & HB FSS surface to see the difference. The transparency plot is given in Figure 2.48. It has a higher loss at the beginning of the MB antenna frequencies, then losses become less compared to the square slot unit cell design. But still, there are some fluctuations in the bandwidth. The bandstop filter notch is around 1 GHz.

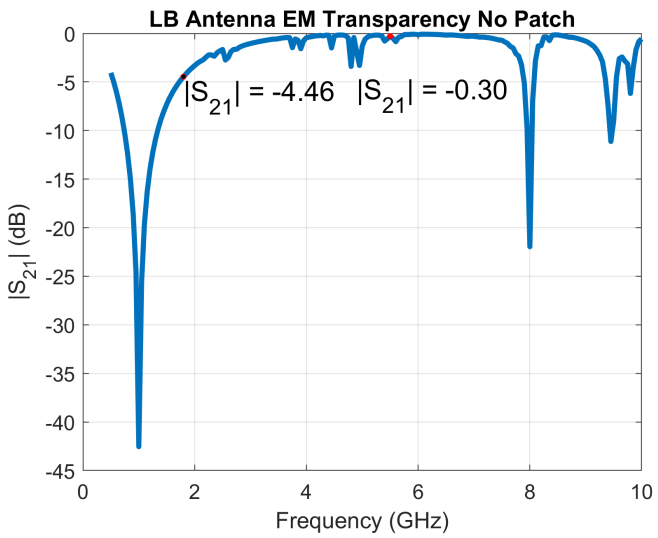

Figure 2.48: Transparency of the MB & HB FSS with no patch

Similar to the MB surface, finite array simulations are also applied to the MB & HB transparent surface to observe the EM transparent surface performance. For the MB antenna, the Hertzian dipole is defined as 25 mm under the surface, and 40 mm for the HB antenna. Hertzian dipole electric fields for the MB antenna are shown in Figure 2.49, and electric fields for the HB antenna are given in Figure 2.50. For both antennas, the main beam direction is towards the broadside direction. Besides, MB & HB transparent surface's no-patch simulations are also made. Electric field densities are similar for the MB antenna frequencies in Figure 2.51. However, field densities become lower for the HB antenna frequencies in Figure 2.52.

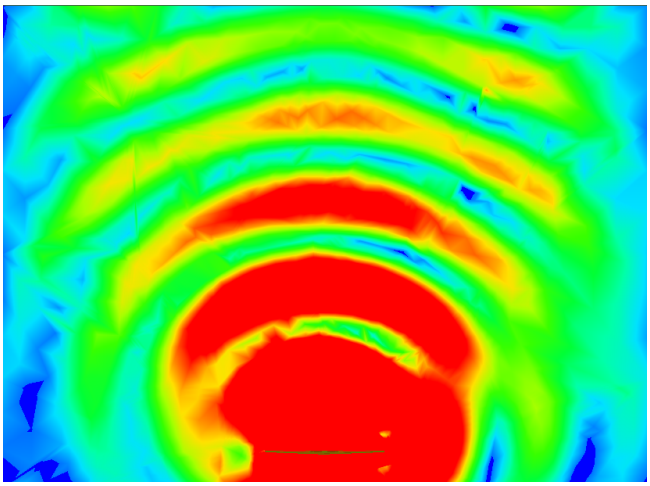

(a)

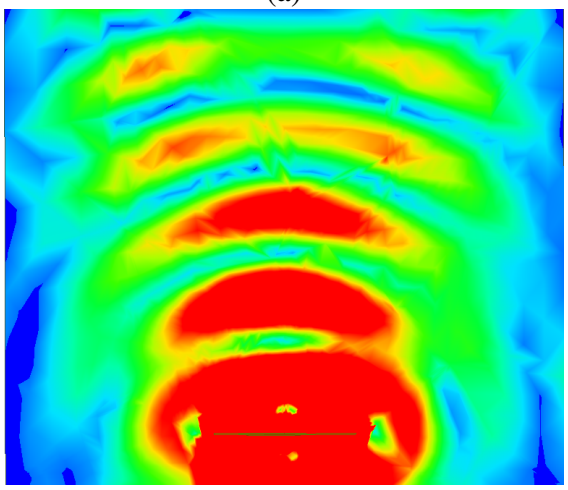

(b)

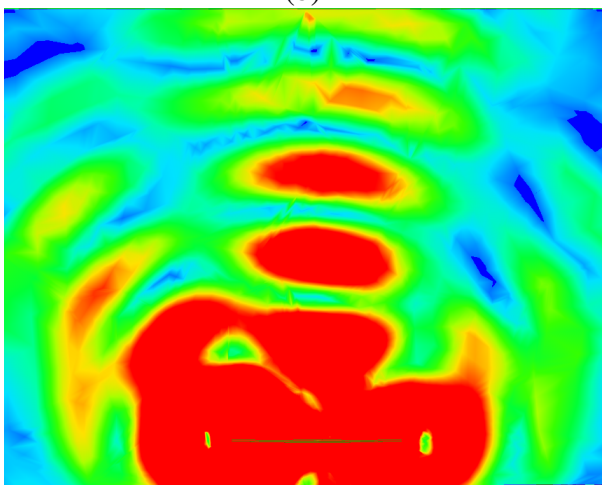

(c)

Figure 2.49: Hertzian dipole electric fields for the MB antenna frequencies of (a) f = 1.9 GHz, (b) f = 2.4 GHz, and (c) f = 2.9 GHz

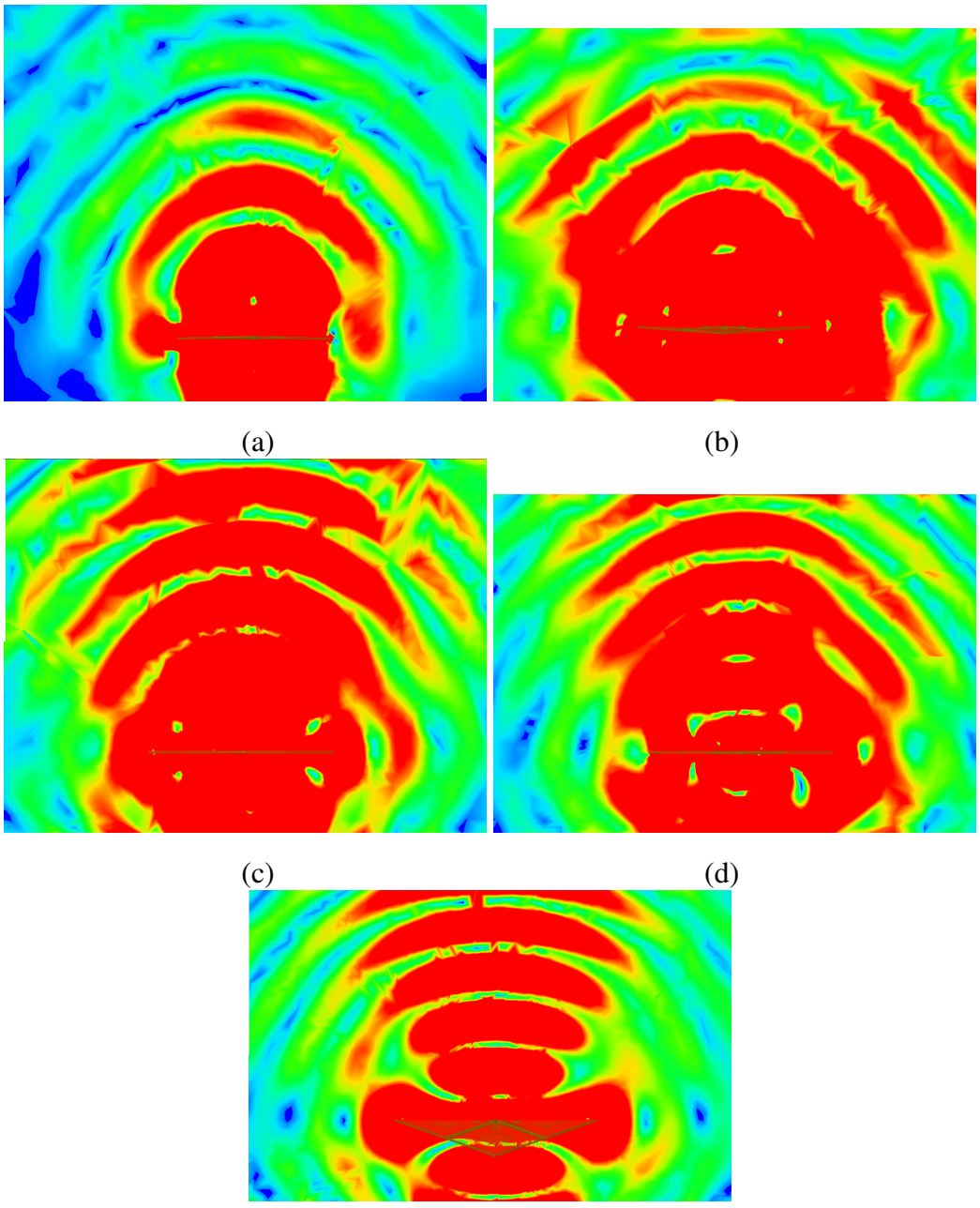

(a) (b)

(c) (d)

(e)

Figure 2.50: Hertzian dipole electric fields for the HB antenna frequencies of (a) f = 3.4 GHz, (b) f = 3.9 GHz, (c) f = 4.4 GHz, (d) f = 4.9 GHz, and (e) f = 5.4 GHz

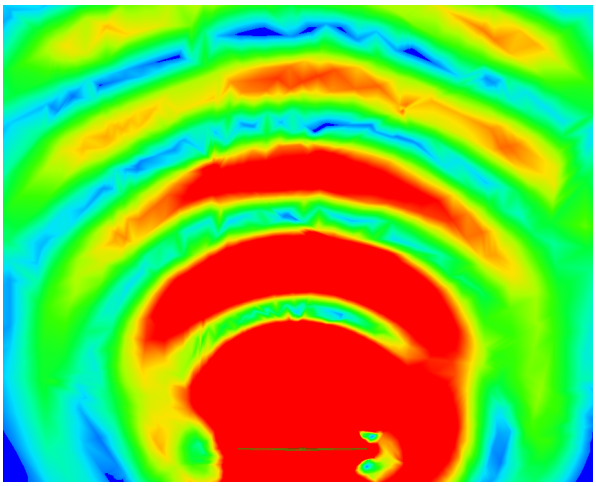

(a)

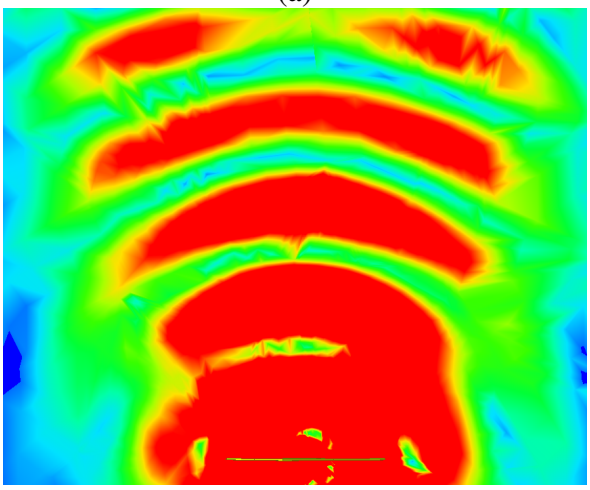

(b)

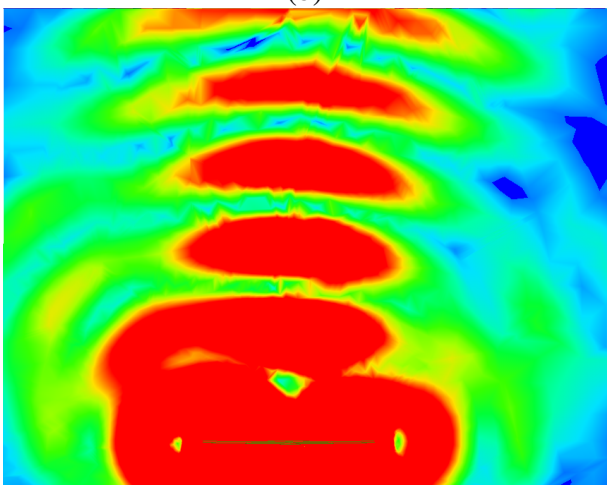

(c)

Figure 2.51: Hertzian dipole electric fields for the MB antenna with no patched surface in the frequencies of (a) f = 1.9 GHz, (b) f = 2.4 GHz, and (c) f = 2.9 GHz

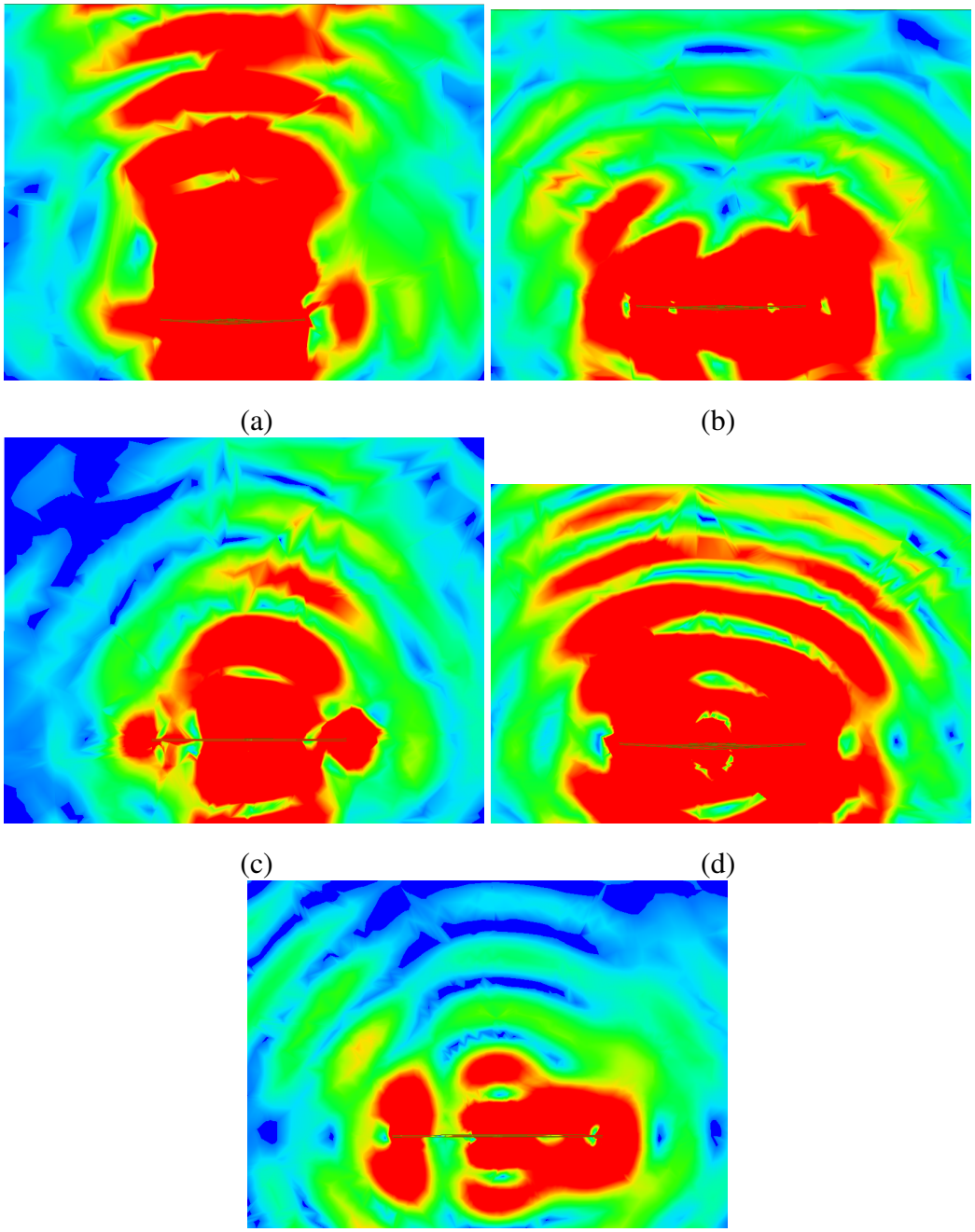

(a) (b)

(c) (d)

(e)

Figure 2.52: Hertzian dipole electric fields for the HB antenna with no patched surface in the frequencies of (a) f = 3.4 GHz, (b) f = 3.9 GHz, (c) f = 4.4 GHz, (d) f = 4.9 GHz, and (e) f = 5.4 GHz

2.6 EM Transparency Properties of High Band Antenna

High band antenna design is detailed in Chapter 3. At first, the HB antenna was designed without any transparent properties. However, low band (LB) and medium band (MB) antennas are designed as both EM transparent surfaces and antennas. Because of the fact that all three antennas are in the vicinity of each other with the shared aperture formation, the transparency property of the HB antenna should also be examined. In this design, HB FSS must have passband characteristics for the LB and HB antennas since all three antennas also radiate to the -z direction. Then they will reflect from the reflector and radiate to the +z direction. For this reason, LB and MB waves pass through the HB antenna two times. Figure 2.53 shows the shared aperture antenna system. At the bottom, the copper reflector plane is displayed with an orange color. Then, the four HB antennas are placed and displayed as green. MB antennas are shown in gray color. At the top, the LB antenna is displayed in yellow. Shared aperture antenna structure is explained in Chapter 4. Figure 2.53 is added here to emphasize the necessity of analyzing the LB & MB passband FSS property of the HB antenna.

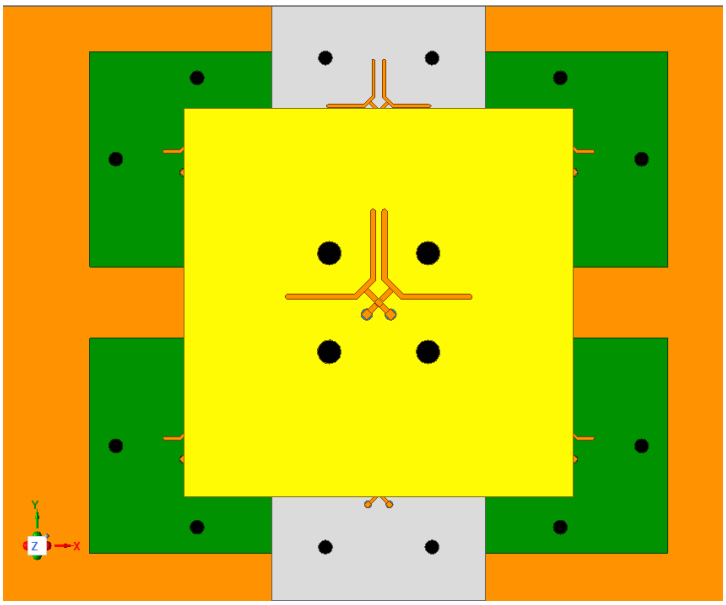

Figure 2.53: Shared aperture antenna & FSS system top view

HB antenna unit elements look similar to loop-type FSS unit cells. The distance between the HB antenna's loops and the substrate edges is high. There are four holes

for antenna spacers. The HB antenna can be seen in Figures 2.54 and 2.55. Considering the HB antenna shape, it is easier to use the 3D EM solver method rather than the square unit cell FSS equivalent circuit method to evaluate the transparency properties.

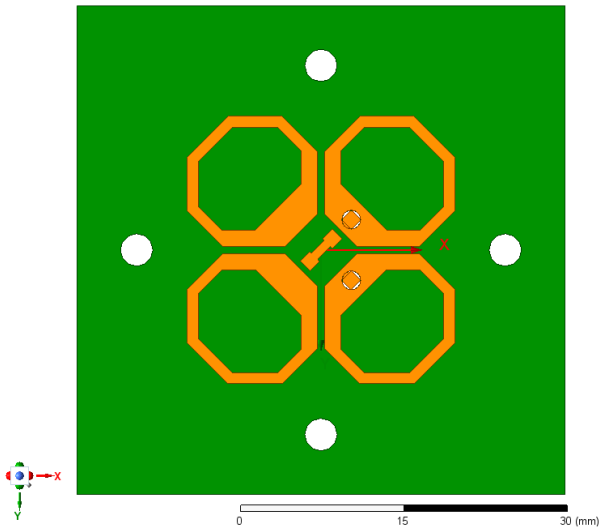

Figure 2.54: LB & MB passband FSS unit cell bottom view

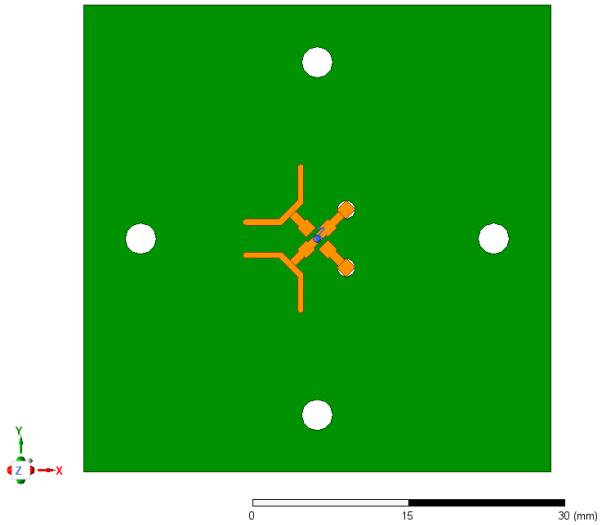

Figure 2.55: LB & MB passband FSS unit cell top view

TE and TM polarization S_{21} plots are given in Figures 2.56 and 2.57 as TE and TM polarizations, respectively. For both polarizations and all incidence angles, transmission losses are minimal, which shows that the HB antenna is EM transparent FSS for LB and MB antennas. For TE polarization, the maximum loss is 1.6dB at MB antenna

cutoff (at 2.95 GHz) with θ = 60°, and 0.47dB with θ = 60° at the same frequency for the TM polarization. The difference in TE and TM polarization loss is due to the wave impedance change and asymmetry of the HB antenna owing to the top layer. There are two Y structures and two vias between the bottom of Y shapes and two loops. Since Y shapes cause asymmetry, polarization characteristics are different for the HB antenna transparency properties.

Circular polarization passband curves are given in Figures 2.58 and 2.59. HB antenna can transmit both the RHCP and RHCP with at most 0.82 dB transmission loss for the 60° incidence angle.

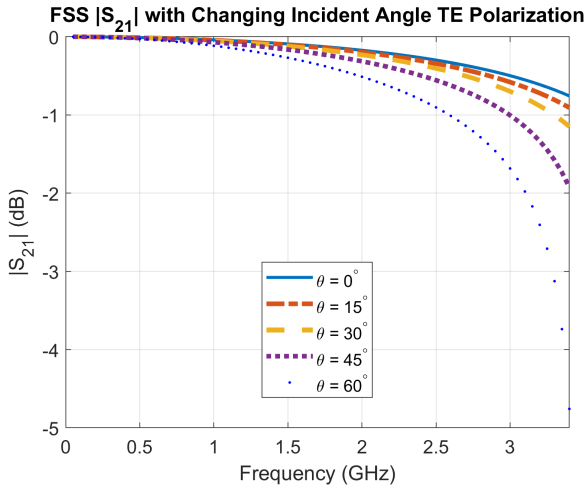

Figure 2.56: LB & MB Passband FSS TE S_{21} Graph

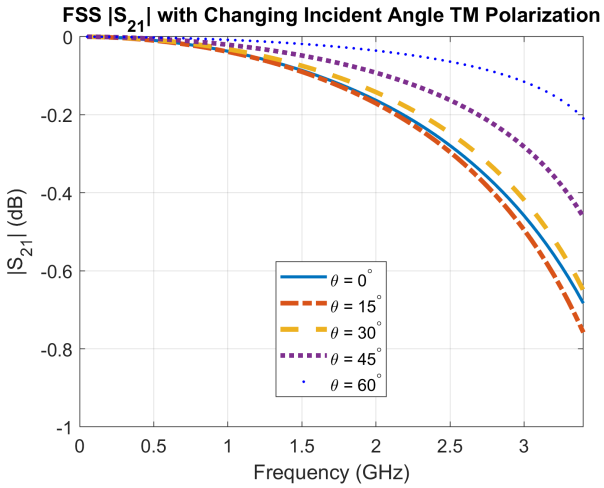

Figure 2.57: LB & MB Passband FSS TM S_{21} Graph

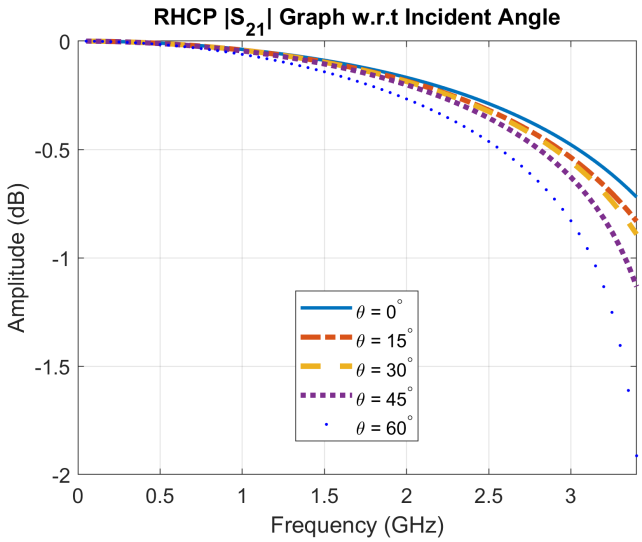

Figure 2.58: RHCP S_{21} plot of the LB & MB FSS

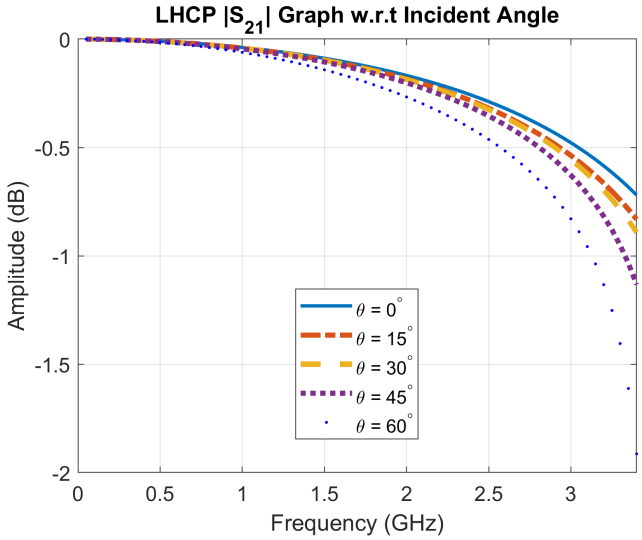

Figure 2.59: LHCP S_{21} plot of the LB & MB FSS

2.7 Chapter Conclusion

In this chapter, FSS design properties are discussed using two methods: the equivalent circuit method and the 3D EM solver methods, respectively. Two EM transparent surfaces are designed as HB transparent and MB & HB transparent surfaces with the idea of bandpass FSS. HB transparent surface characteristics such as bandwidth, angular

stability, transmission amplitude and phase variation, and circular polarization wave transmission are quite good for the HB antenna band, such that 60° angular stability is obtained. Yet, MB & HB transparent surface is designed as a partially transmitting surface, so transmitting loss is higher than the HB one for all polarizations. Also, phase angle variation and angular stability are much worse since dimensions are quite large for this surface, and it is designed as a wideband transparent surface, so its role is determined as a partially transmitting surface. Since they are also cross-dipole antennas, a 2×2 finite array form of the FSS units' EM transparency performance is tested by a hypothetical Hertzian dipole antenna. Electric field distribution results of the Hertzian dipole antenna show that both surfaces can also be used as EM transparent surfaces for the required frequency bandwidths. Also, the no-patch versions of the transparent surfaces are made for comparison. HB FSS shows better performance for the insertion loss of the HB antenna wave, and Hertzian dipole field characteristics are similar. Even though MB & HB FSS transparency is better for no-patch, Hertzian fields at HB frequencies are much worse. Thus, using a square slot unit cell is the better option. Finally, it is shown that the designed HB antenna shows EM transparent characteristics for both LB and MB antenna bandwidths. Hence, all three antennas can operate together with the provided EM transparency traits of the antenna surfaces.

CHAPTER 3

CROSS DIPOLE ANTENNA DESIGN

3.1 Introduction

As aforementioned, today's wireless communication antennas require compact size, low cost, easy integration, good signal quality, stable radiation pattern, and wider bandwidth properties, which is a challenge to satisfy all of them at once. At this point, dipole antennas can be a candidate for the solution of this problem. The dipole antenna is one of the most basic and well-known antenna types. Its design methods and field characteristics are well known. Its structure is simple and can easily be integrated into antenna systems at a low cost. Dipole antenna's drawbacks are low gain values and narrow bandwidth. Hence, the dipole antenna design is changed so that a second dipole antenna is placed orthogonal to the first dipole antenna to improve the antenna performance. This shape is called as 'cross-dipole' antenna. With the crossed-dipole designs, bandwidth is improved thanks to the extra resonance frequency owing to the strong mutual coupling. Also dual-polarized and circular-polarized radiation options are obtained. Complexity and cost are increased a little, but antenna performances and requirements are fulfilled. As a result, they are one of the most common wireless communication antennas nowadays.

There are a number of cross-dipole antenna designs published in the literature. In [38], a multiband crossed dipole antenna is designed. Dipole arms are multi-branched in such a way that the antenna can be operated at different frequencies of the GPS. Cross-dipole antenna design is presented in Figure 3.1. The yellow arms are on the top of the substrate, and the dark blue arms are on the bottom side of the substrate. So, the crossed dipoles' one half is on the top, and the latter half is on the bottom side.

There is an inverted pyramidal cavity to provide a unidirectional radiation pattern for the antenna. There is only one feeding, and circular polarization is obtained with the 90° phase delay line by the vacant-quarter ring on the top. Dipole arms have an arrow-type shape with meandered lines in the middle. These changes provide miniaturization for the dipole antenna. By these changes, half-wave dipole antennas can be designed with a length of around 0.3 λ. With gain values around 7.5 dBi to 8 dBi, this type of crossed-dipole antenna can be used in narrow multi-band circular polarization antenna applications.

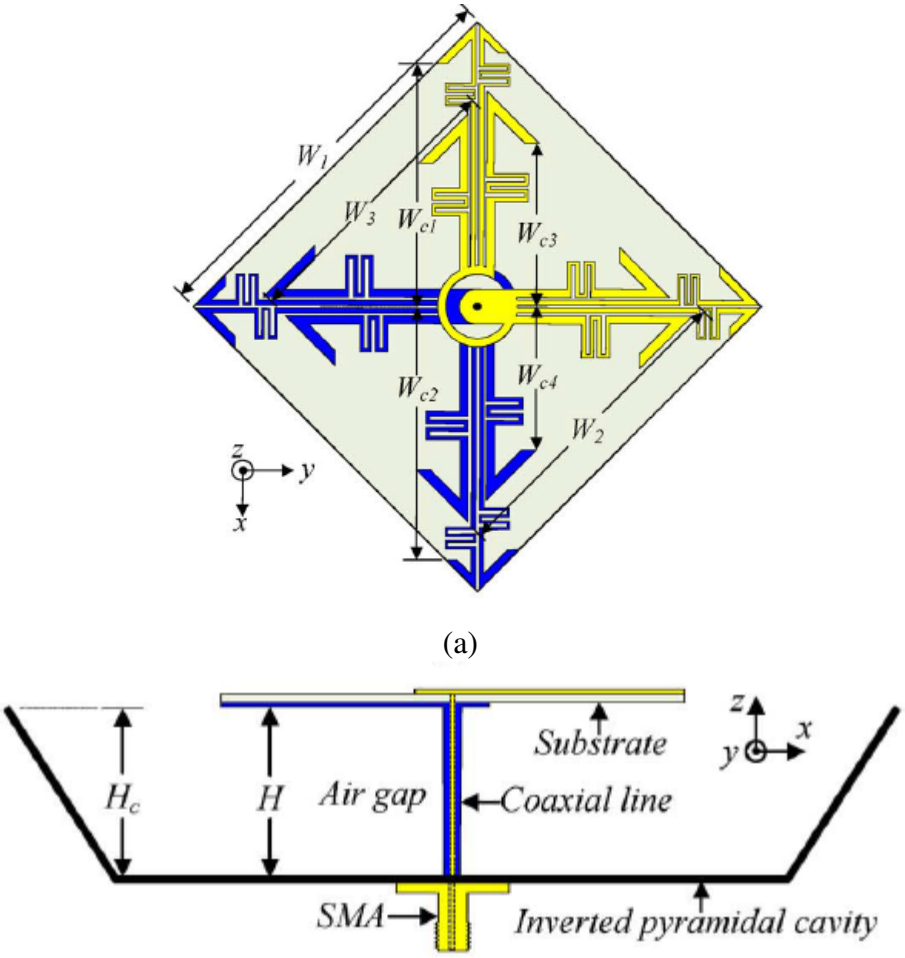

Figure 3.1: (a) GPS multiband antenna substrate and (b) the antenna system

Unlike the previous example, single wideband crossed-dipole antennas are also designed, like the one presented in [63]. An impedance bandwidth of 3.14-6.34 GHz and a 3 dB axial ratio bandwidth of 3.83-6.62 GHz were aimed, so that it can be used

in broadband circular polarization applications. This design is very similar to the previous design. Yellow arms are on the top side, and blue lines are on the bottom side. It is supported by a cavity reflector with a single feeding. There is a cross loop with a gap introduced outer of the cross-dipole antenna, which significantly improves both impedance and 3 dB axial ratio bandwidth. This antenna has an average gain of 8.2 dBi.

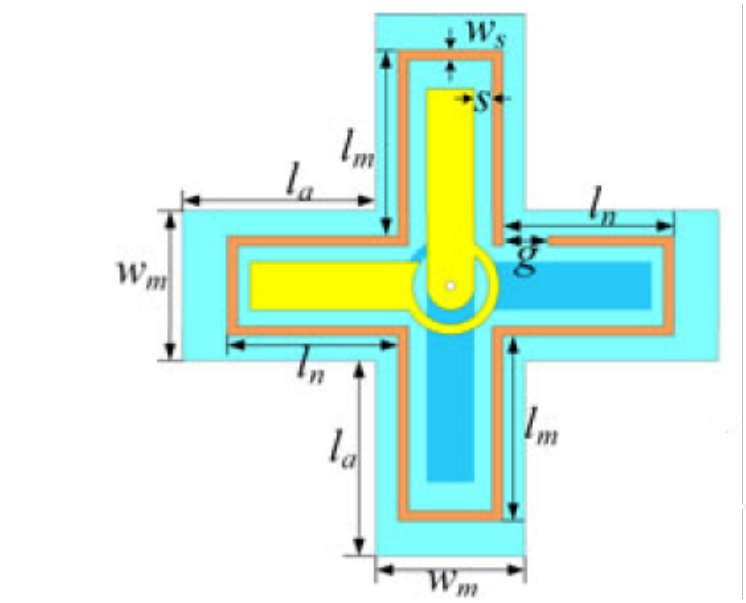

(a)

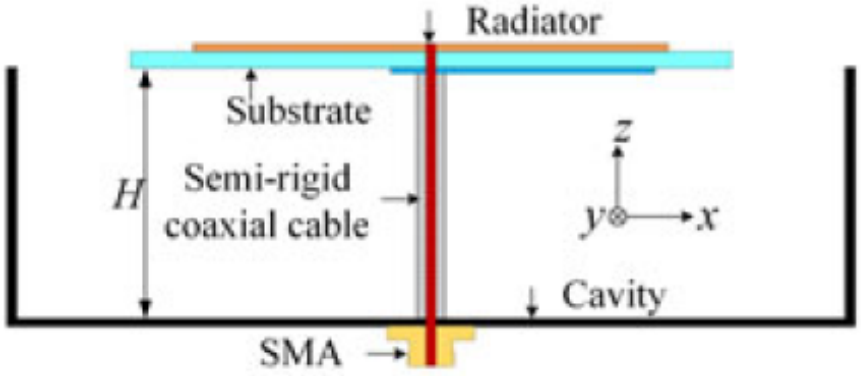

(b)

Figure 3.2: (a) Wideband cross-dipole antenna and (b) the antenna system

Apart from that, [29] is an example of a dual-polarized cross-dipole antenna. Its bandwidth is 1.69-3.6 GHz, which can cover 2G/3G/4G and some 5G bands. It has a Y-shaped feeding on the top, and the loop dipoles are placed on the bottom side. There are extra triangles around the center, which creates an extra resonance on the

higher frequencies and improves the bandwidth. This antenna has an average gain of 8 dBi. The designed antenna shape is given in Figure 3.3. Since there are two ports in the system for the two dipoles, coupling between the dipoles is also important for cross-polarization. Isolation is better than 25 dB between the two dipoles.

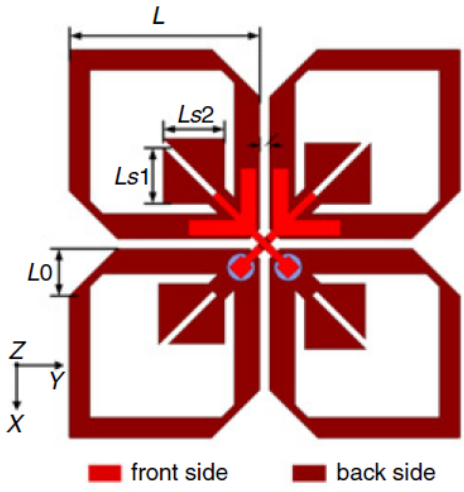

(a)

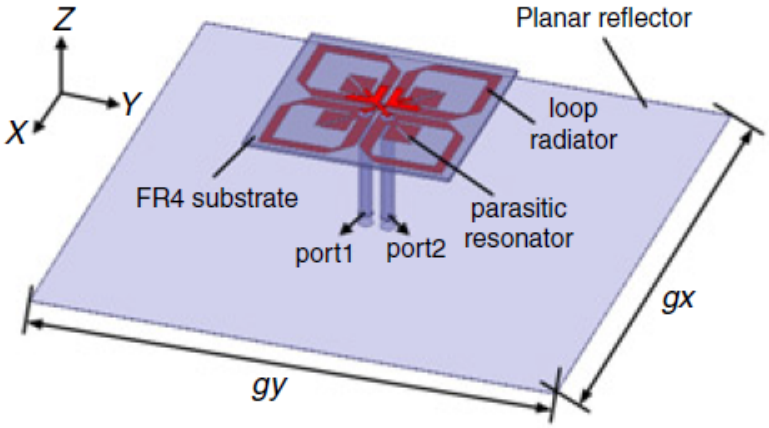

(b)

Figure 3.3: (a) 5G dual-polarized cross-dipole antenna and (b) the antenna system

Another dual-polarized cross-dipole antenna is given in [21]. It operates in 3.2-5.22 GHz with an average gain of 9 dBi. Its design purpose is to cover most of the 5G band frequencies in the sub-6 GHz range. This design also has a loop-shaped dipole arm, but the arm shape and operating frequency are different from the previous one. Isolation between the ports is better than 35 dB for this design. The antenna is given in the Figure 3.4.

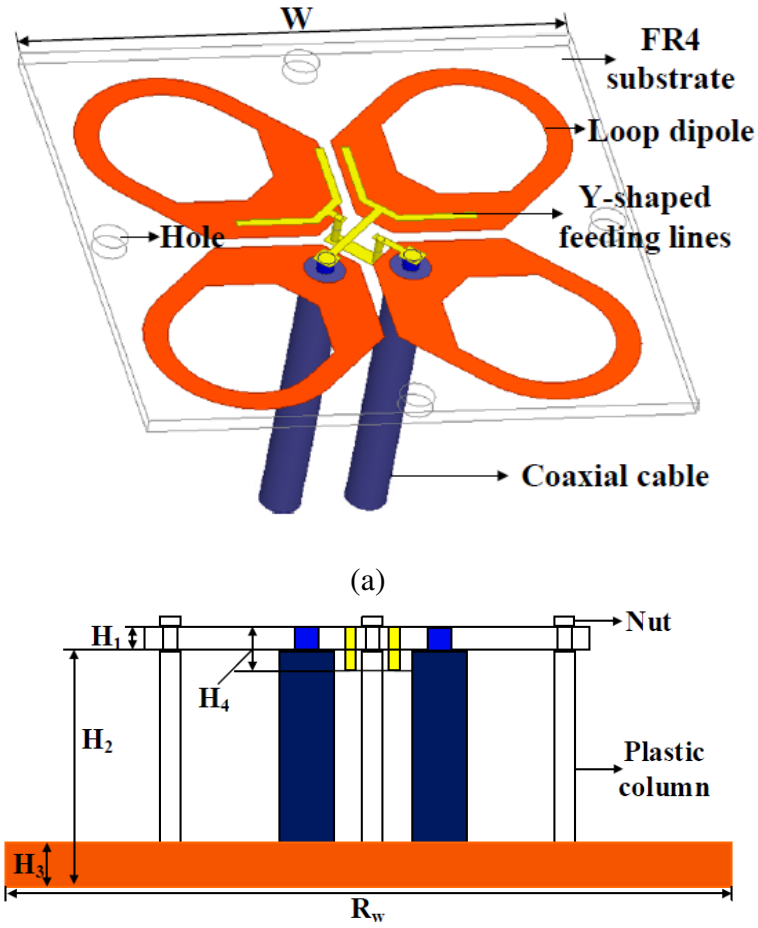

Figure 3.4: (a) Dual-polarized cross-dipole antenna substrate and (b) the antenna system

As can be seen, cross-dipole antennas are widely used and designed. They can be designed for mobile communication bands of 2G/3G/4G/5G and for global positioning, and they can be used in different areas. In this chapter, three different cross-dipole antennas for three different bands will be designed and examined. The first antenna is designed for the 5G bands, the second antenna is designed for the 2G/3G/4G bands. The third antenna band is designed to observe the shared aperture antenna extendability. It can cover most of the global positioning bands. Their design, antenna properties, simulation, and measurement results will be explained in detail.

3.2 Necessary Considerations for the Antenna Design

Like most previously designed cross-dipole antennas, all three band antennas are designed on a ground plane to have broadside radiation to $\theta = 0°$. In theory, half-wave dipoles' gain is around 2.15 dBi (1.64 in linear), and its radiation pattern is towards both sides perpendicular to its dipole arms. If there is a ground plane with a dipole antenna, antenna radiation and gain characteristics would change according to the image theory. The designed antennas form the shape of a horizontal electric dipole antenna on a ground plane. Their theoretical calculations and patterns are given in the Appendix B part.

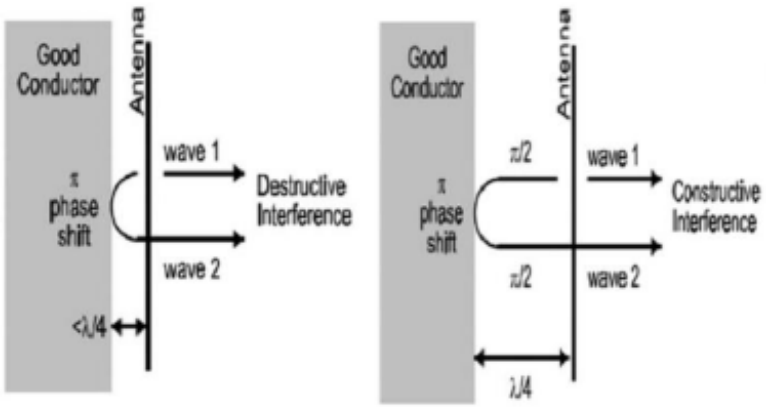

Figure 3.5: Ground plane interference effect [6]

The ground plane creates interference between reflected and broadside radiated EM waves. Figure 3.5 shows the interference conditions of the reflector plane. If the distance between the antenna and the reflector is $< \lambda/4$ or $> \lambda/4$, then reflected waves from the image currents on the reflector are not in phase with the broadside waves, so radiation performance degrades with the destructive interference. However, having $\lambda/4$ ensures the in-phase superposition. The wave travels $\lambda/4$ towards the reflector, which corresponds to $\pi/2$ phase shift, then the wave is reflected with π phase shift, and again wave travels the $\lambda/4$ distance with the $\pi/2$ phase shift. Finally, 2π phase shift means a complete period latency is obtained and superposed with a second period broadside wave.

3.3 High Band Antenna Design

The main motivation for designing the high band (HB) antenna is to cover most of the predetermined sub-6G 5G bands. These frequency bands are 3300–3600 MHz and 4800–5000 MHz in China, 3400-3800 MHz in Europe, 3100-3550 MHz, and 3700-4200 MHz in the USA [10, 12]. Regarding the bandwidths, the start frequency can be selected between 3 and 3.4 GHz, and the stop frequency can be 5 GHz for wider bandwidth antenna designs. Since dual polarization with a proper gain is preferred in base station antennas, cross-dipole antennas with wide bandwidths are mostly designed and used. Hence, a 5G cross dipole antenna is designed as an HB antenna.

3.3.1 High Band Antenna Design Steps

Initially, as in step 1, a dipole antenna is designed on a printed circuit board (PCB). The dipole antenna is placed in $\pm 45^{\circ}$ slant configuration onto the bottom of the PCB. Y feeding is placed on the top layer of the PCB to provide capacitive coupling feed. There is a via to allow the pass of the inner conductor of coax and solder to Y feeding. The outer conductor is soldered to one arm of the dipole. Used coax cable is the "SUCOFORM-86" cable with the dimensions of d_{inner} = 0.51mm, $d_{dielectric}$ = 1.65mm and d_{outer} = 2.1mm. The dielectric between the conductors is 'polytetrafluoroethylene' (PTFE), also known as Teflon with ϵ_r = 2.5. The used PCB is RO4003 with a dielectric constant of ϵ_r = 3.38 thickness of h = 0.813mm and copper thickness of t = 43μm. The designed antenna is given in Figure 3.6 with providing both layers. Both faces are shown together in Figure 3.7. Four spacers support the antenna shown in black color, the PCB color is gray and the copper is shown with orange color. The red color is the defined wave port for the coax cable. The ground (GND) plane is hidden in this figure. The dipole antenna with the GND plane is shown in Figure 3.8. The GND plane is made of copper, and its distance is determined with respect to the center frequency of the required bandwidth. According to the 5G bands, the HB antenna bandwidth goal can be selected between 3.3 and 5 GHz. The center frequency is 4.15GHz, and $\lambda/4$ of this frequency is 18.07mm, so the GND plane distance is selected as 18mm. Dipole arms are as wide as the dipole arm length since increasing arm width increases the bandwidth, and S_{11} performance is better for both radiation

and out-of-band. Considering the dipole arm length, increasing arm length decreases resonating frequency due to the inverse relationship between frequency and wavelength. Dipole arm width and length sweeps are given in Figure 3.9 and Figure 3.10. The bold curve parameters are selected as design values. The resonance frequency of the antenna is 3.4GHz, which is lower than calculated with Equation 2.1 because of ϵ_{eff} of the dielectric substrate and air. The -10 dB bandwidth of the antenna is between 3.15-3.79 GHz, and the -15 dB bandwidth is 3.26-3.61 GHz. Additionally, the antenna radiation pattern at its resonance frequency of 3.4GHz is shown in Figure 3.11. Radiation is towards broadside direction with the gain of 8.3 dBi at θ = -8° and 8.13 dBi at 0°. Since the antenna direction is towards ϕ = 45°, the radiation pattern at ϕ = 45° is examined.

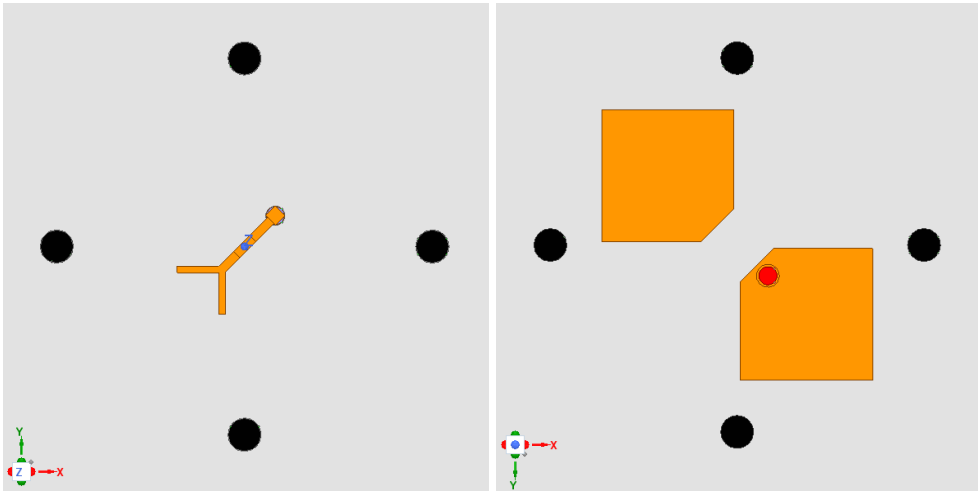

(a) (b)

Figure 3.6: (a) HB Antenna Step-1 Top Layer and (b) Bottom Layer

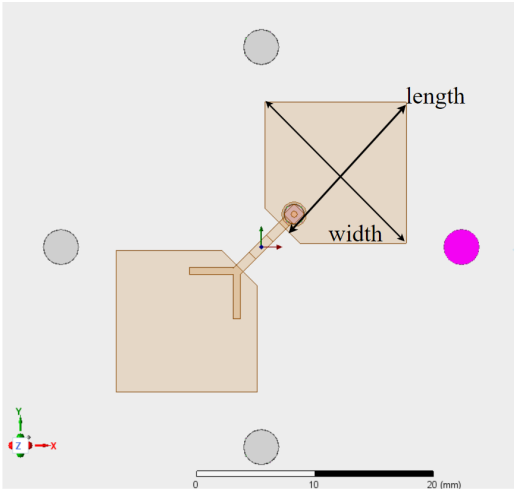

Figure 3.7: HB antenna design in step-1

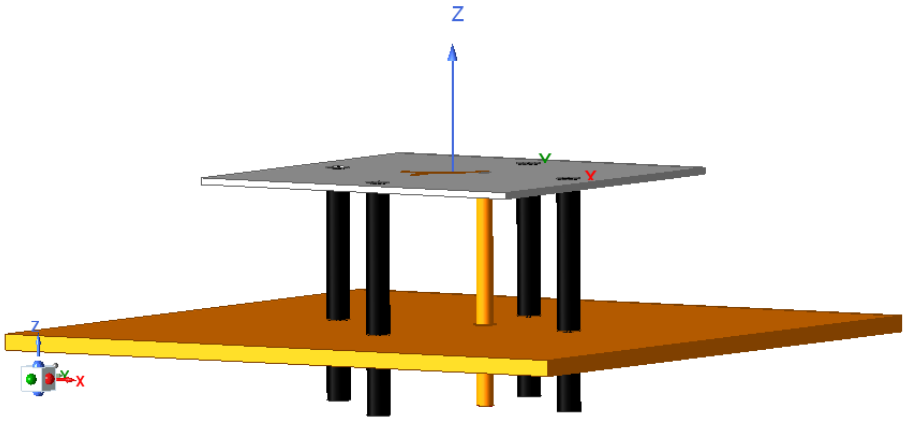

Figure 3.8: HB antenna design with the GND plane in step-1

The HPBW angle is shown with the command 'xdb10Beamwidth(3)' in the radiation pattern menu of the ™HFSS, shown in Figure 3.12. So, radiation patterns' -3dB HPBW angle range can be automatically calculated with respect to the maximum gain angle. The HPBW of the pattern given in Figure 3.11 is calculated around 60.3° in Figure 3.12.

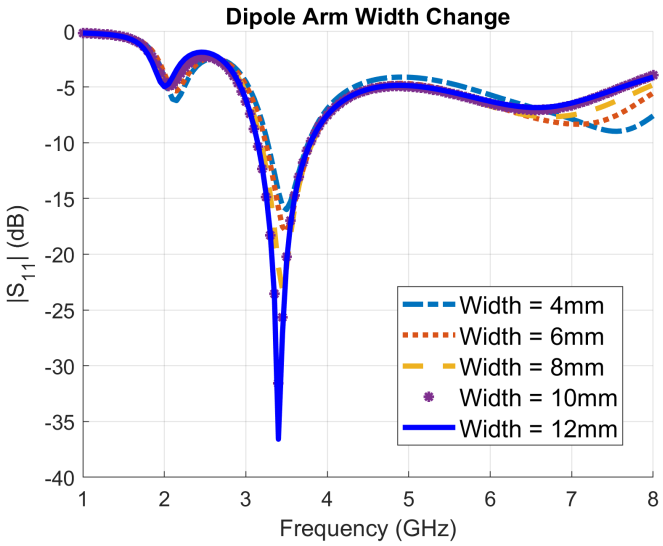

Figure 3.9: Step 1 dipole arm width change

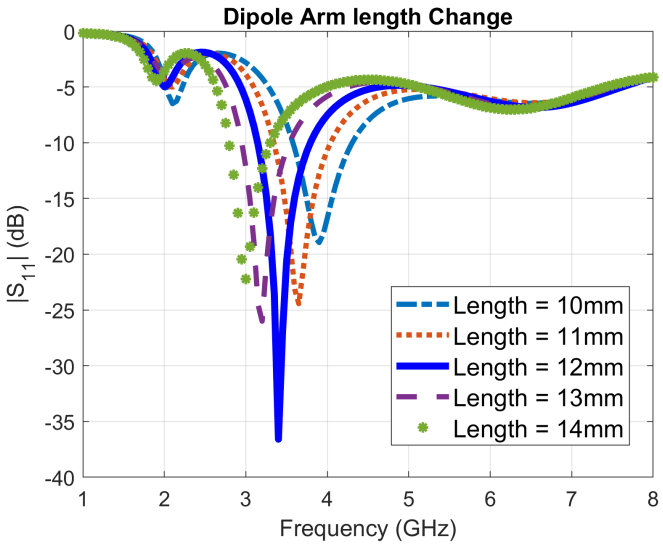

Figure 3.10: Step 1 dipole arm length change

In step 2, dipole arms' corners are chamfered, as shown in Figure 3.13. So, the dipole arm length becomes shorter with the furthest corner chamfer, meaning a resonance frequency increase. Other corners are chamfered for the next step's preparation. The step 2 antenna's S_{11} graph is given in Figure 3.14. The bandwidth broadens slightly, and the resonance band shifts towards a higher frequency. The -10 dB bandwidth of the antenna is between 3.31-3.99 GHz, and the -15 dB bandwidth is 3.44-3.78 GHz.

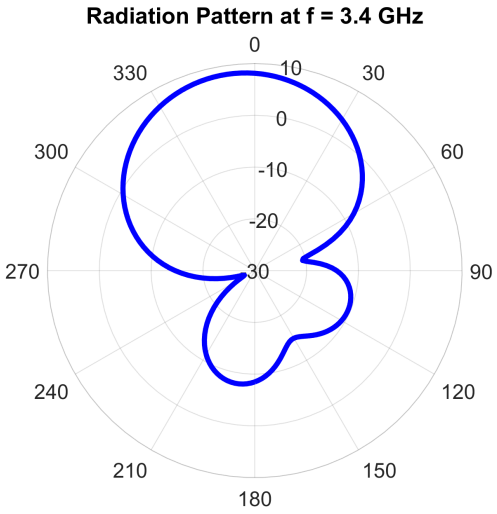

Figure 3.11: Step 1 dipole arm radiation pattern

	xdb10Beamwidth(3)
dB(RealizedGainTotal) Setup1 : LastAdaptive Freq='3.4GHz' Phi='45deg'	60.3134

Figure 3.12: Step 1 dipole HPBW angle

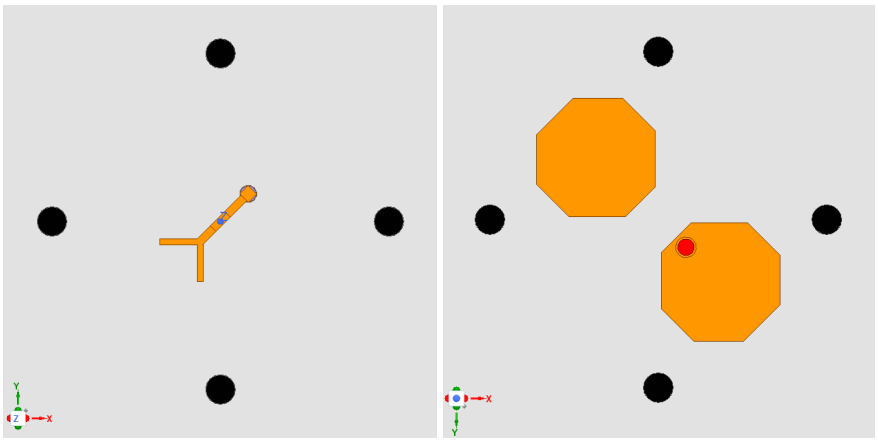

(a) (b)

Figure 3.13: (a) HB Antenna Step-2 Top Layer and (b) Bottom Layer

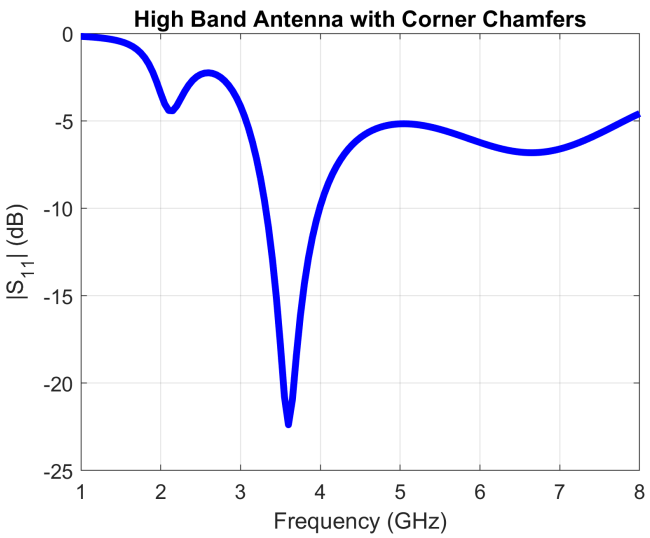

Figure 3.14: Step 2 dipole antenna S_{11} graph with chamfered corners

In step 3, the second dipole antenna is placed orthogonal to the first antenna. The new form of the antenna is shown in Figure 3.15. Figure 3.16 and Figure 3.17 also show the antenna with both layers and the GND plane. There are two Y-feedings on the top layer in Figure 3.15. To prevent a short circuit between two Y-feedings, one of the Y-feeds moves to the bottom layer with via and then moves back to the top layer with another via. There is a large gap distance between the two dipole arms to provide enough length for Y-feeding at the bottom layer. The bandwidth of the antenna is dramatically increased with the addition of a second dipole since the second dipole acts as a parasitic element to the first dipole, creating a coupling between two dipoles, and a second resonance frequency is obtained at higher frequencies with respect to the first resonance which is related to the dipole arm length. By changing the edge lengths close to other dipole arms or the gap distance between dipole arms, the second resonance point can be controlled [64]. Changing edge length is possible by adding chamfers, so the coupling length between dipole arms is changed, so the second resonance frequency can be changed accordingly [65]. This design also shows why the dipole arm width must be similar or equal to the dipole arm length to provide mutual coupling between two dipoles. S_{11} and S_{22} plots are given in Figure 3.18. Reflection loss parameters are almost the same for both antennas. Two resonance points cannot be seen clearly, but -10 dB and -15 dB bandwidth is extended to 3.65-5.15 GHz and 3.95-4.90 GHz, respectively. The high cutoff frequency of the bandwidth is satisfied

for the 5G bands, but more adjustments are required for the low cutoff frequency to cover wider bandwidths of 5G bands.

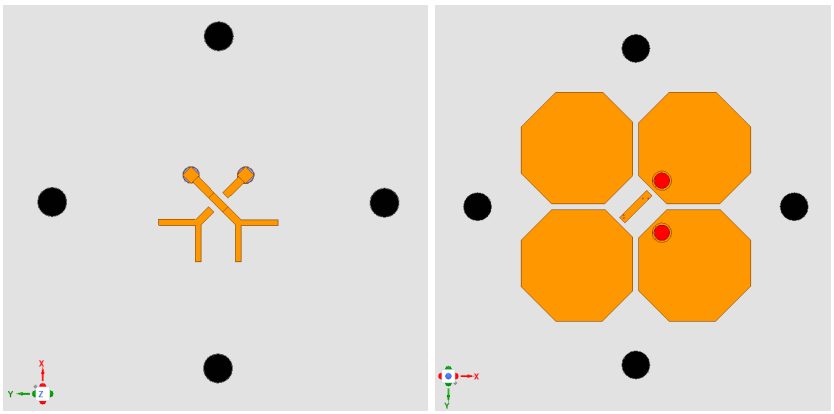

(a) (b)

Figure 3.15: (a) HB Antenna Step-3 Top Layer and (b) Bottom Layer

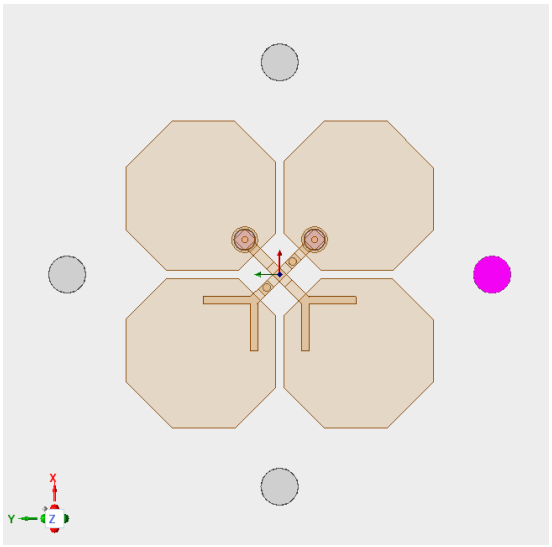

Figure 3.16: Both layers of HB antenna in step-3

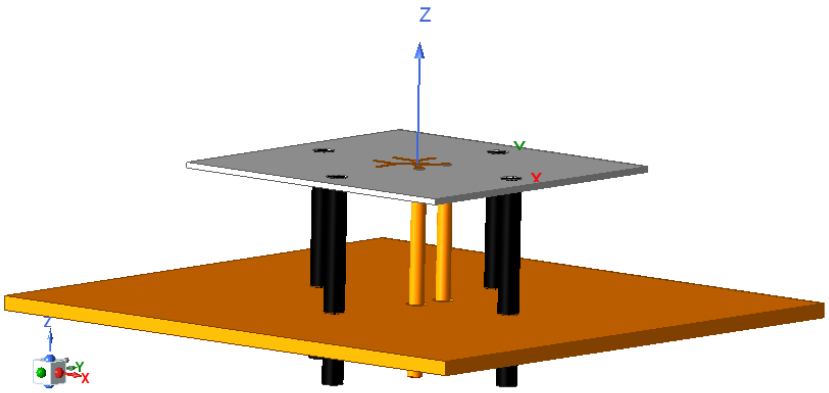

Figure 3.17: HB antenna with GND plane

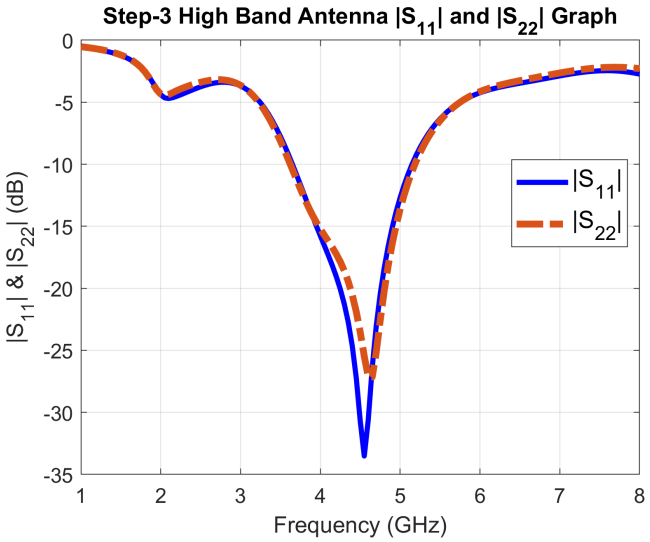

Figure 3.18: HB step-3 S_{11} and S_{22} graph

Mutual coupling in step 3 is beneficial for the bandwidth increase. Still, the isolation of the two ports might be affected negatively because the two dipoles are very close to each other. Since base station antennas work as dual-polarized, isolation between two antennas must be analyzed. The flowing current density vectors J are shown in both dipole antennas in Figure 3.19. Let α be assumed as the phase; the current vectors are shown in six phases. Input is applied only to port-1, and port-2 is terminated with 50 Ω or matched load. For the three cases of $\alpha = 45°$, $\alpha = 90°$, and $\alpha = 135°$, the excited current of dipole 1 is directed towards the upper right corner. Whereas induced current -thanks to the strong mutual coupling between dipoles- on dipole 2 rotates around the

dipole arm symmetrically with respect to the center of the antenna. This case indicates no potential difference between the dipole arms of dipole 2. The current directions are reversed for the other three cases of α = 225°, α = 270°, and α = 315°. Since this antenna is a symmetric structure, even if dipole 2 is fed and dipole 1 is terminated with a matched load, the same result would be obtained. Thus, high isolation between different ports is obtained. In addition to this case, Figure 3.20 shows the S_{21} of the antenna. S_{21} indicates the isolation between the dipole antenna ports. So this value must be as low as possible. Isolation is more than 25 dB within the antenna bandwidth, which is quite good for suppressing the cross-polarization. Despite the fact that mutual couplings are not desired and avoided in most of the conventional cross-dipole antenna designs, the cross-dipole antenna design mentioned in step 3 uses mutual coupling to enhance the antenna performance [66].

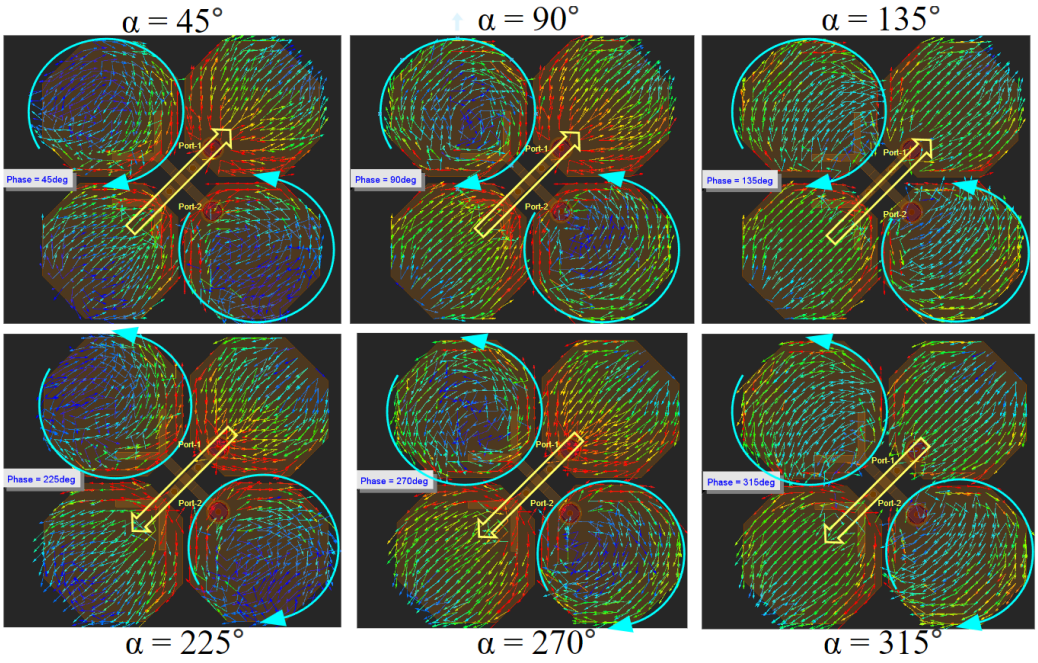

Figure 3.19: HB step-3 current graph with respect to phases

In this design step, port 1 is defined in 135°-315° direction, and port 2 is defined in 45°-225° direction. The radiation pattern for port 1 is plotted in ϕ = 135° and ϕ = 45° for port 2. Radiation patterns of the step 3 HB antenna for 4.2GHz are given in Figure 3.21. HPBW angle of port 1 is 59.6°, and port 2 is 59° with a gain of 8.62 dBi to the broadside direction. When both ports are feeding with the same phase, the radiation patterns in Figure 3.22 are obtained. Different port feedings are

symmetrical to $\theta = 0°$, hence their patterns are also symmetrical to $\theta = 0°$. Since ports are isolated from each other with more than 25 dB of isolation, the radiation patterns of the ports do not change significantly. Hence, dual-polarization is obtained in the slant configuration. Gain and HPBW are increased with the double feeding to 8.8 dBi and 67°, respectively.

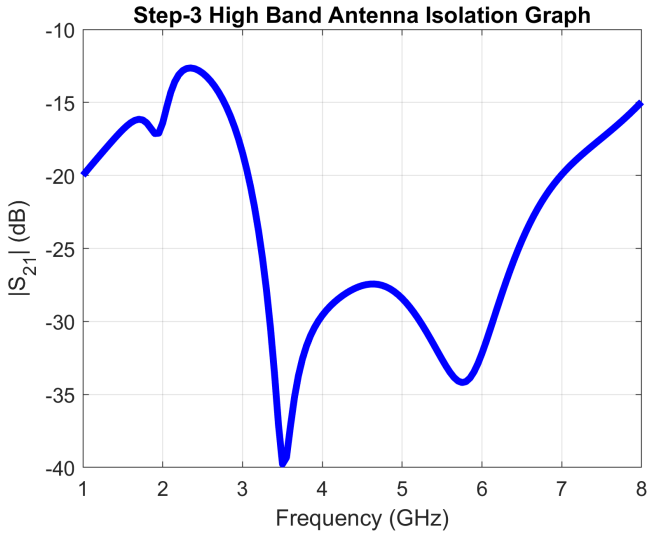

Figure 3.20: Step-3 HB antenna isolation graph

If these ports are fed by 90°phase with equal power, then circular polarization is obtained. Figure 3.23 and Figure 3.24 explain the current flow direction for the circular polarization. Port 2 is lagging 90° from port 1 in the scenario. It is well known that the current density vector is in the same direction as the electric field as described in Equation 3.1. So, the net electric field directions of the antenna with respect to phases are shown in Table 3.1. Considering the net electric field rotation is counter-clockwise direction, it can be clearly seen that radiation is right-hand circular polarization (RHCP). If the port 2 phase is leading 90°, then left-hand circular polarization (LHCP) would be obtained. Consequently, operating two ports together with the same phase results in dual polarization in the $\pm 45°$ as linear polarization; if these ports are fed with 90° phase difference, then both RHCP and LHCP polarizations can be obtained according to which port is leading or lagging. Since four polarizations can be obtained for the designed antenna, it can be said that this antenna operates as a 'quad-polarization' antenna.

$$\mathbf{J} = \sigma \mathbf{E} \tag{3.1}$$

Table 3.1: Net Electric Field Direction of Circularly Polarized Antenna

$\alpha = 0°$	$\alpha = 45°$	$\alpha = 90°$	$\alpha = 135°$
$\swarrow$	$\downarrow$	$\searrow$	$\rightarrow$
$\alpha = 180°$	$\alpha = 225°$	$\alpha = 270°$	$\alpha = 315°$
$\nearrow$	$\uparrow$	$\nwarrow$	$\leftarrow$

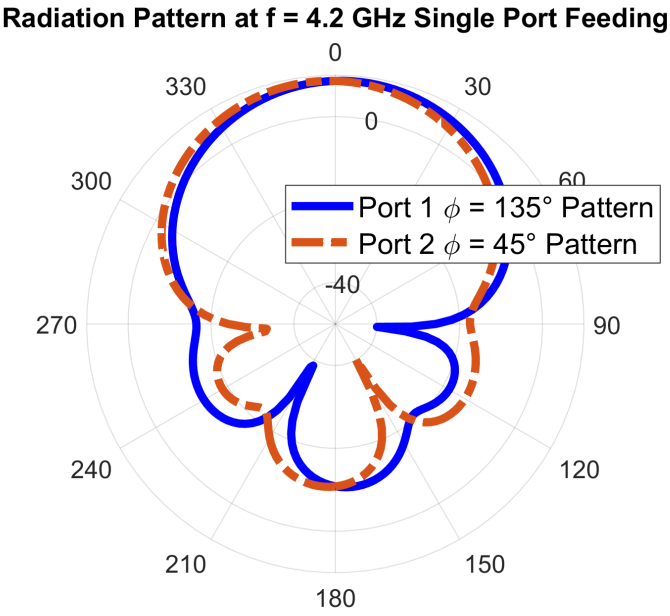

Figure 3.21: Step 3 dipole arm radiation patterns with single port feedings

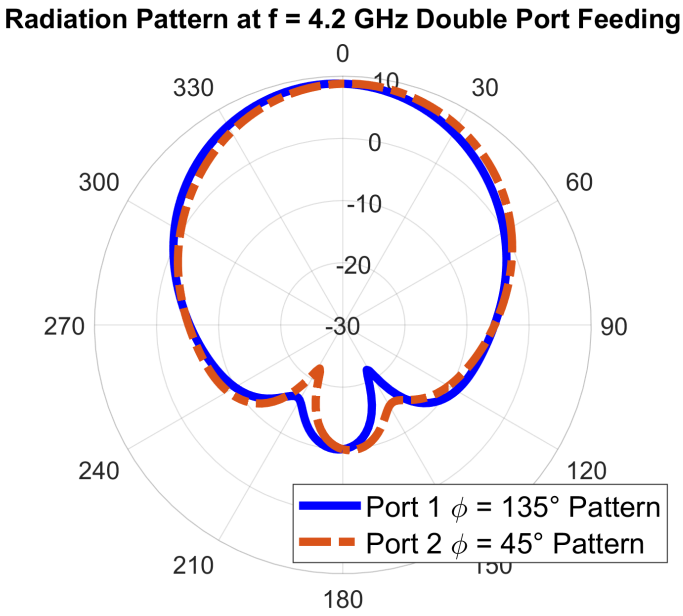

Figure 3.22: Step 3 dipole arm radiation patterns with both port feedings

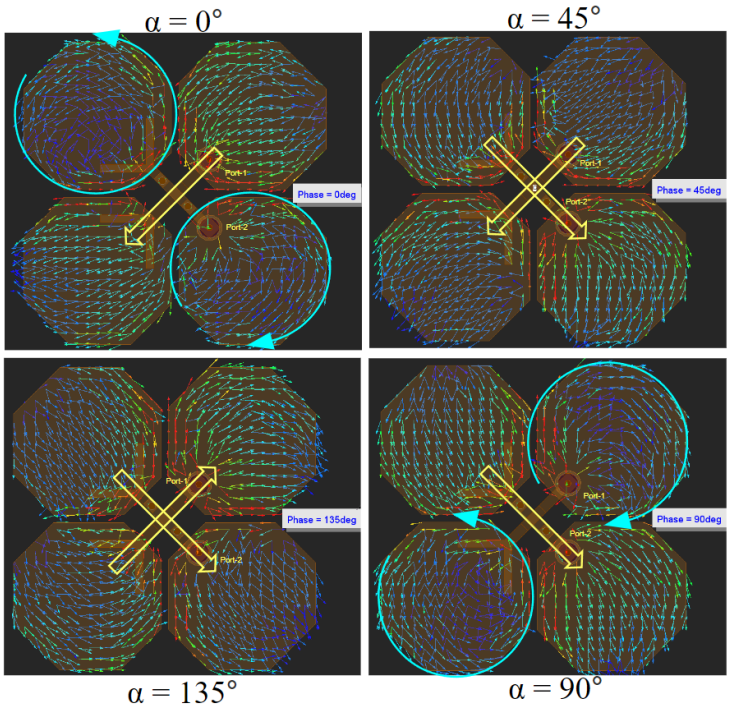

Figure 3.23: First half period of the current flow of circular polarization

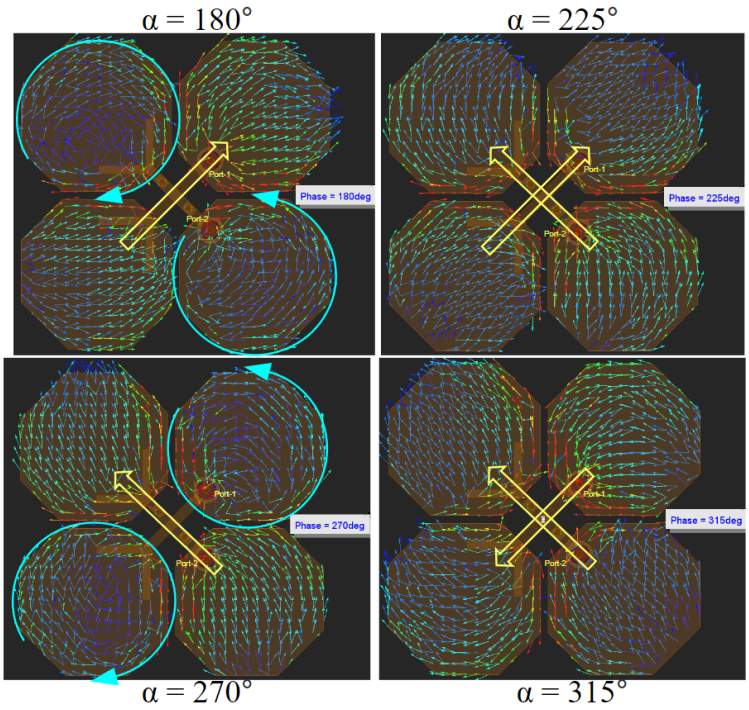

Figure 3.24: Second half period of the current flow of circular polarization

In step 4, slots are defined to dipole arms. These slots extend the current path lengths, increasing bandwidth in the low frequencies. Step-4 design is shown in Figure 3.25. Dipole arm lengths' copper widths are wider in the center to provide enough space for the coax cable outer conductor soldering and better impedance match of the antennas. Figure 3.26 shows S_{11} and S_{22} of the step-4 antenna. The current change improves the input impedance since both -10 dB and -15 dB bandwidths are extended to 3.52-5.22 GHz and 3.83-4.99 GHz, respectively. Isolation does not change significantly. It is still higher than 25 dB, as seen in Figure 3.27. Within the bandwidth, antenna impedance is close to the chart center, which means impedance is matched.

It should be noted that the first resonance is also shifted to higher frequencies with the second dipole addition, so the new structure's center frequency becomes nearly $4\sqrt{2}$ times the truncated square edge length. The resonant frequency also changes with the distance between the adjacent dipole arms, which will be shown in Section 3.3.2.1.

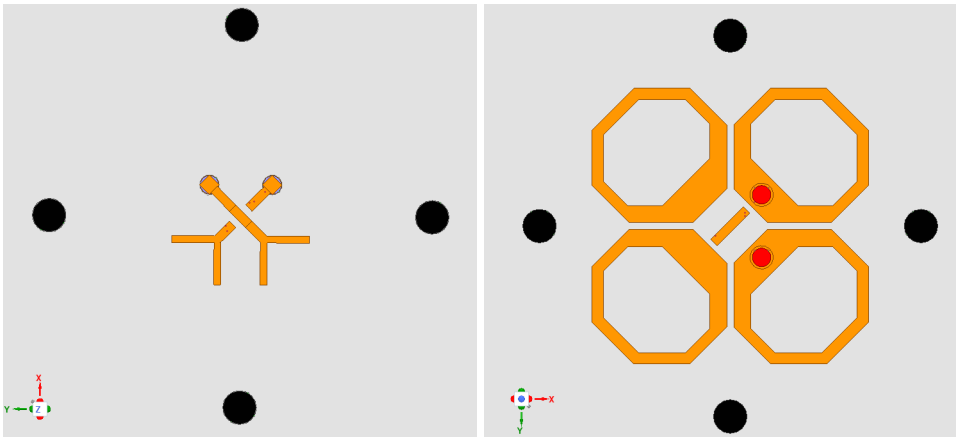

(a) (b)

Figure 3.25: (a) HB Antenna Step-4 Top Layer and (b) Bottom Layer

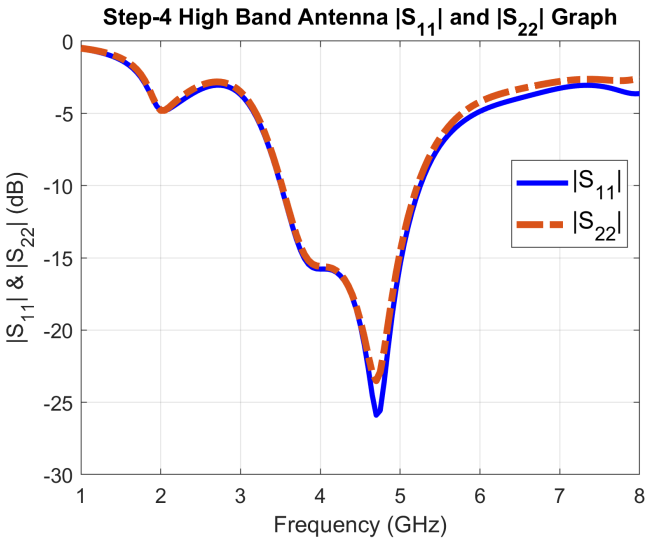

Figure 3.26: HB step-4 S_{11} and S_{22} graph

In step 5, Y-feedings are rearranged so that feeding arms extend in the form of dipole arms rather than 90° in the previous steps. Figure 3.28 and Figure 3.29 displays the antenna design. Changing the Y feeding arms changes the cutoff frequencies without changing the bandwidth, as shown in Figure 3.30. The first resonance becomes more clear, and the second resonance becomes starts to be less visible. The -10 dB bandwidth is 3.34-5 GHz, and -15dB bandwidth is 3.51-4.69 GHz. Besides, although the curves look very similar, isolation improves with a few dB, as shown in Figure 3.31.

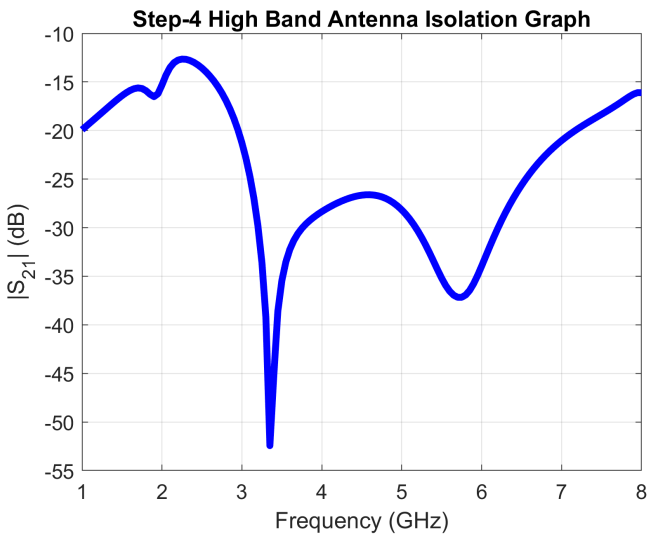

Figure 3.27: Step-4 HB antenna isolation graph

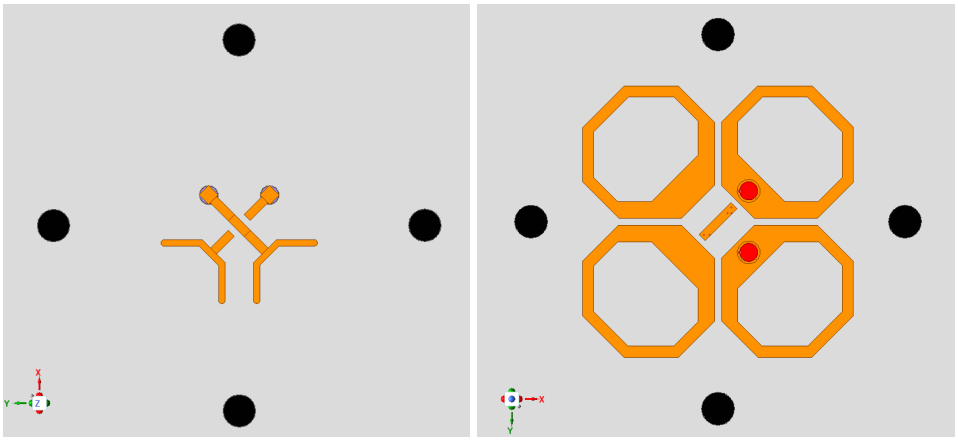

(a) (b)

Figure 3.28: (a) HB Antenna Step-5 Top Layer and (b) Bottom Layer

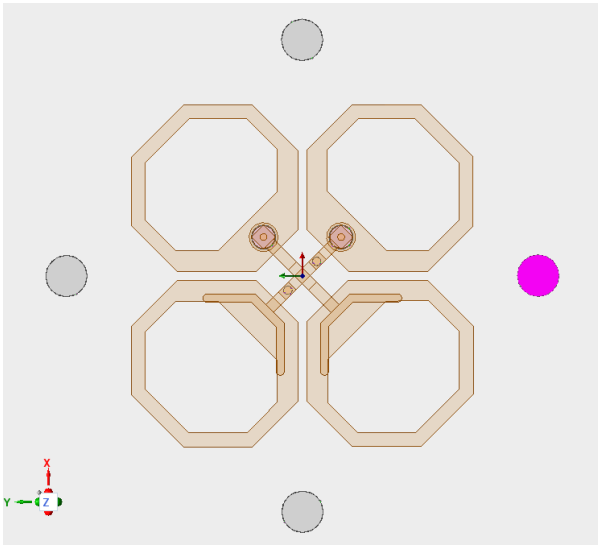

Figure 3.29: HB antenna design in step-5

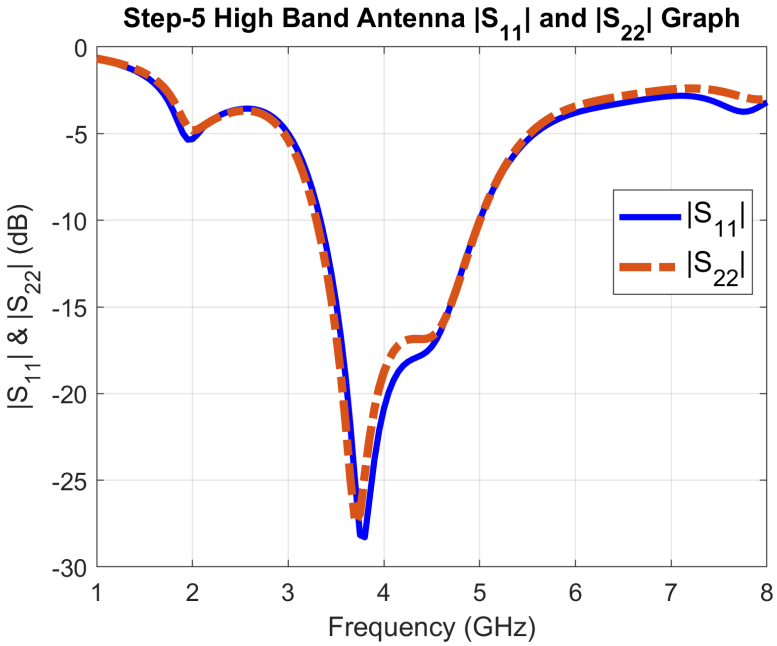

Figure 3.30: HB step-5 S_{11} and S_{22} graph

In the last step, four square patches are defined on two sides of two vias, and another two square patches are defined onto the Y-feeding for symmetry. The last design is shown in Figure 3.32 and Figure 3.33. These additions increase the bandwidth between 3.3-5.11 GHz, especially from the low-frequency side. S-parameter graphs are shown in Figure 3.34 and 3.35. As a result, a cross-dipole antenna that covers most of the well-known 5G bands can be covered in the sub-6GHz range. Also, the Smith chart of the step 6 antenna is given in Figure 3.36.

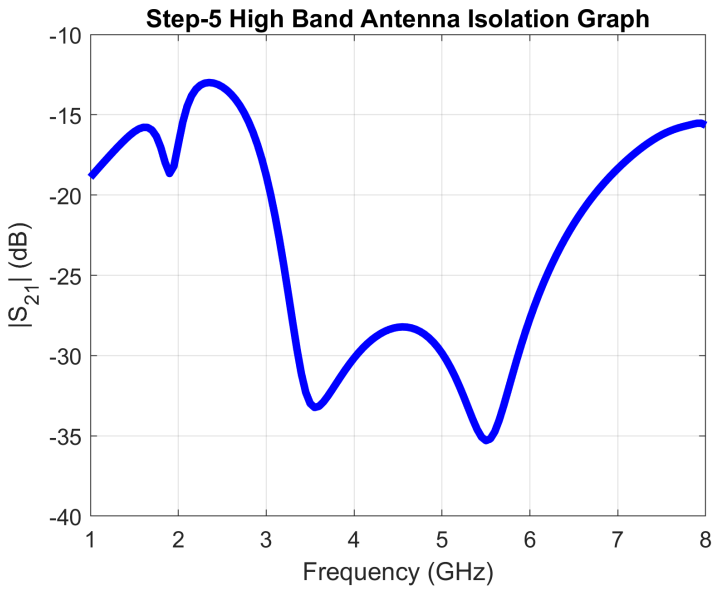

Figure 3.31: Step-5 HB antenna isolation graph

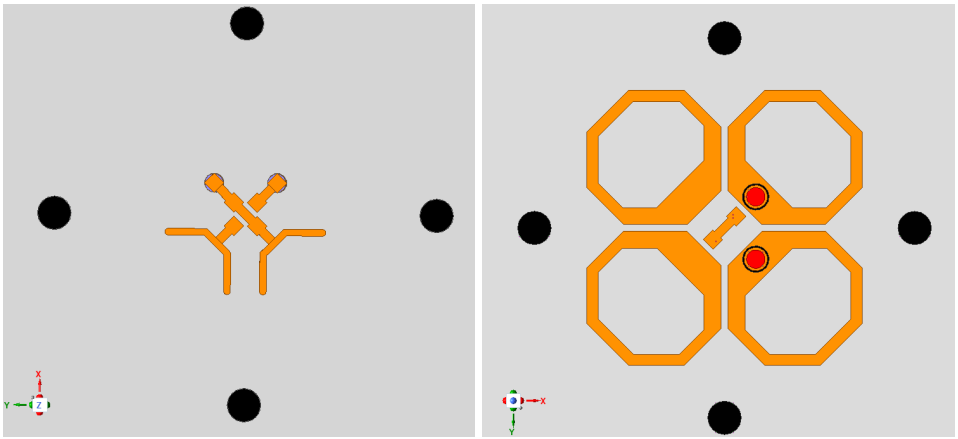

(a) (b)

Figure 3.32: (a) HB Antenna Step-6 Top Layer and (b) Bottom Layer

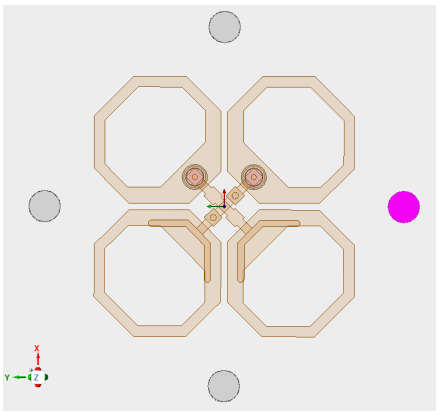

(a)

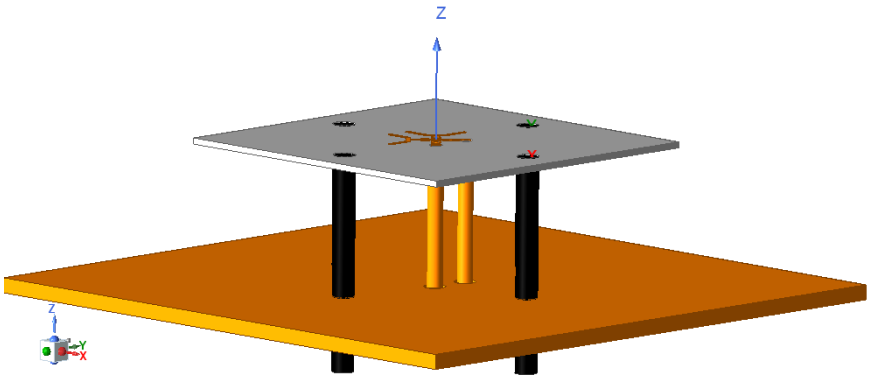

(b)

Figure 3.33: (a) Both layers of HB antenna in step-6 and (b) HB antenna with GND plane

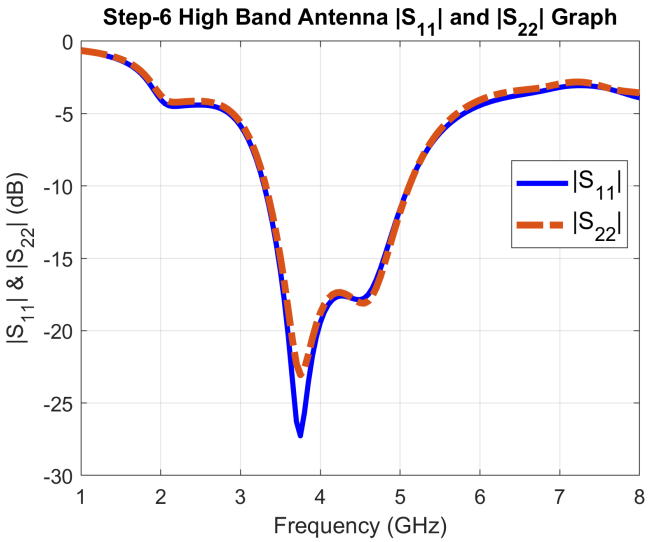

Figure 3.34: HB step-6 S_{11} and S_{22} graph

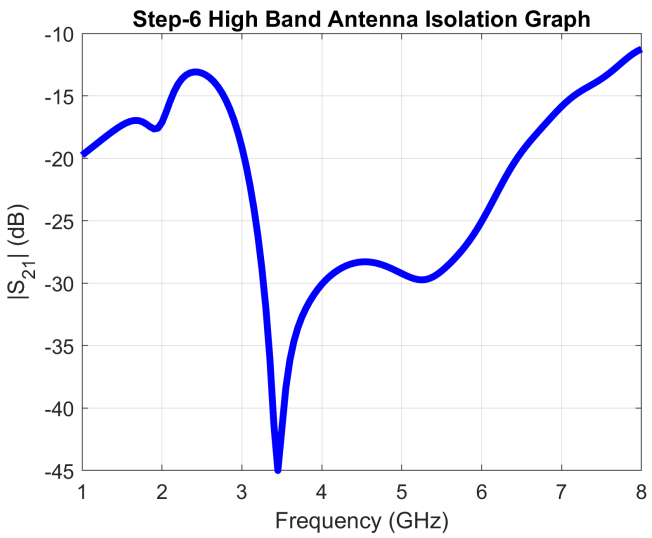

Figure 3.35: Step-6 HB antenna isolation graph

Figure 3.37 displays the radiation pattern of the last step. The gain is 8.86 dBi, and the HPBW angle is approximately 59.3 ° for both ports. Different port feedings do not change the radiation pattern significantly due to the symmetry of the dipoles. When port 1 is fed with 90° leading, the RHCP pattern is realized in Figure 3.38 (a) with its cross-polarization, LHCP. Reversely, the LHCP pattern is shown in Figure 3.38 (b) when port 2 is leading by 90°. HPBW angles for RHCP and LHCP are 66.2° and 65.3°, respectively.

Figure 3.40 demonstrates the normalized radiation patterns of theoretical horizontal dipole antenna given in the Appendix B and the simulation of the designed antenna for ϕ = 135°. Radiation pattern shapes are similar for both of them with different half-power beamwidth angles. Figure 3.39 shows the bandwidths of the design steps of the HB antenna. The last step is shown with a bolder curve. There is a term called 'front-to-back-ratio'; it is the power ratio of the maximum gain of the main radiation to the power of the opposite radiation. θ = 0° gain is 8.8 dBi and θ = 180° is -9.5 dBi that can be seen from Figure 3.37, which gives a ratio of 18.3dB, which is quite good for the designed antenna.

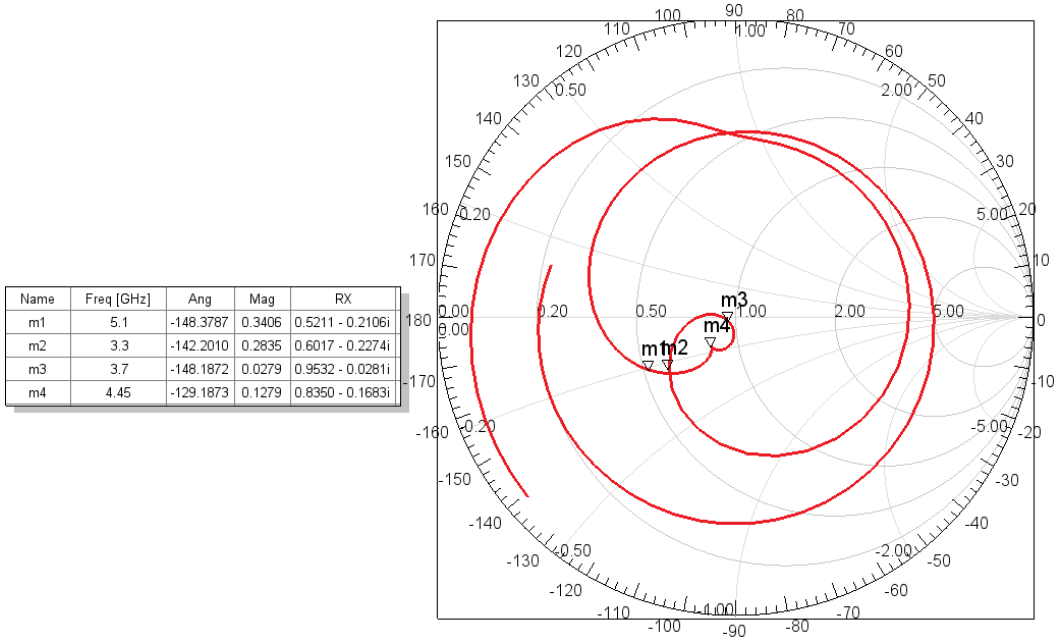

Figure 3.36: Step-6 HB antenna Smith chart of step 6 HB dipole antenna

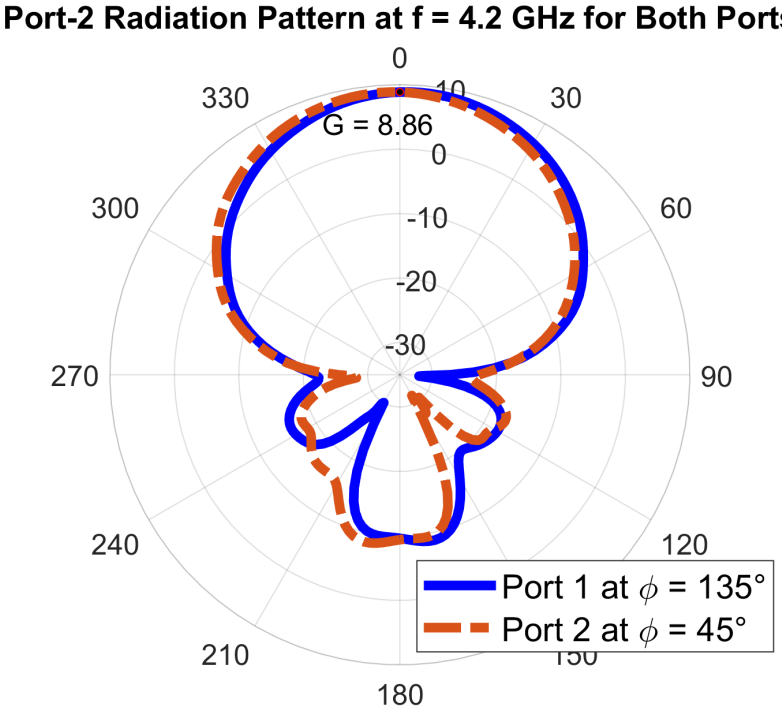

Figure 3.37: Step 6 dipole arm radiation pattern of both ports

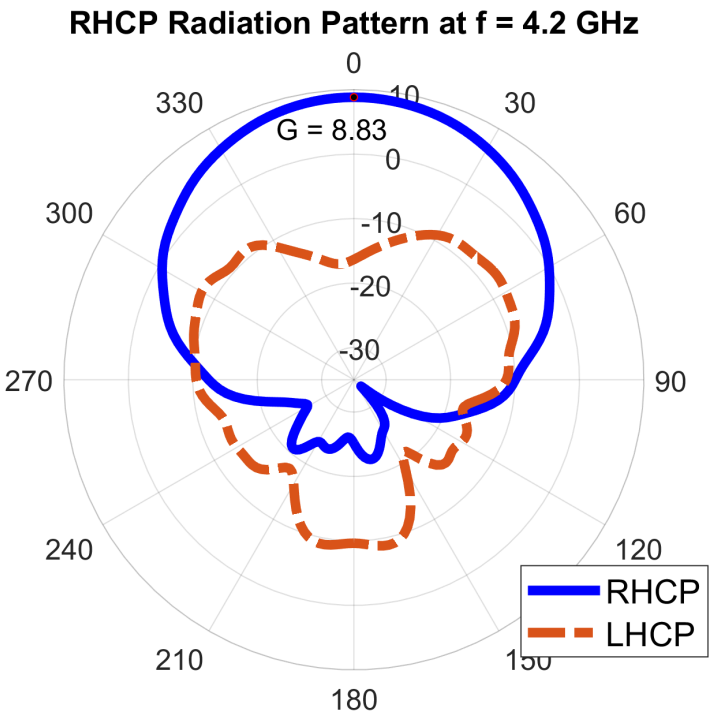

(a)

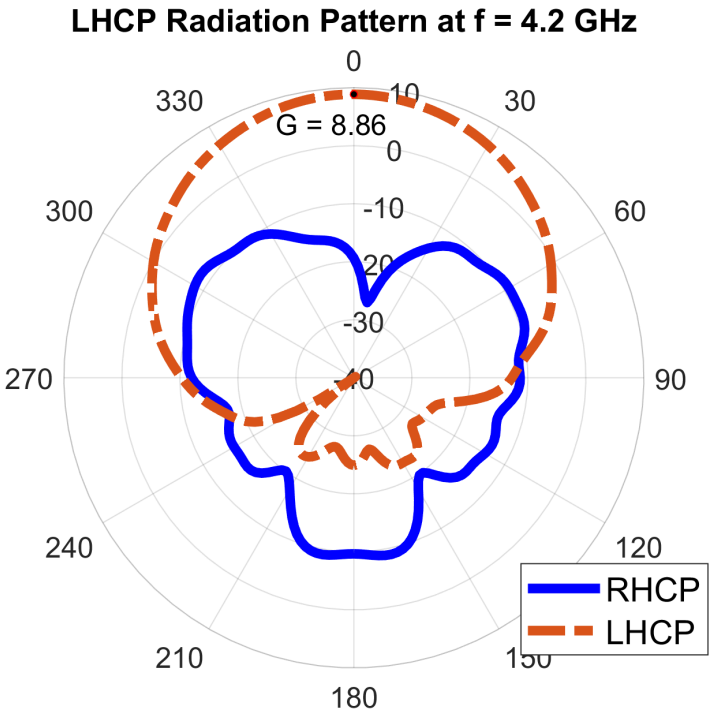

(b)

Figure 3.38: (a) Step 6 antenna RHCP pattern and (b) LHCP pattern

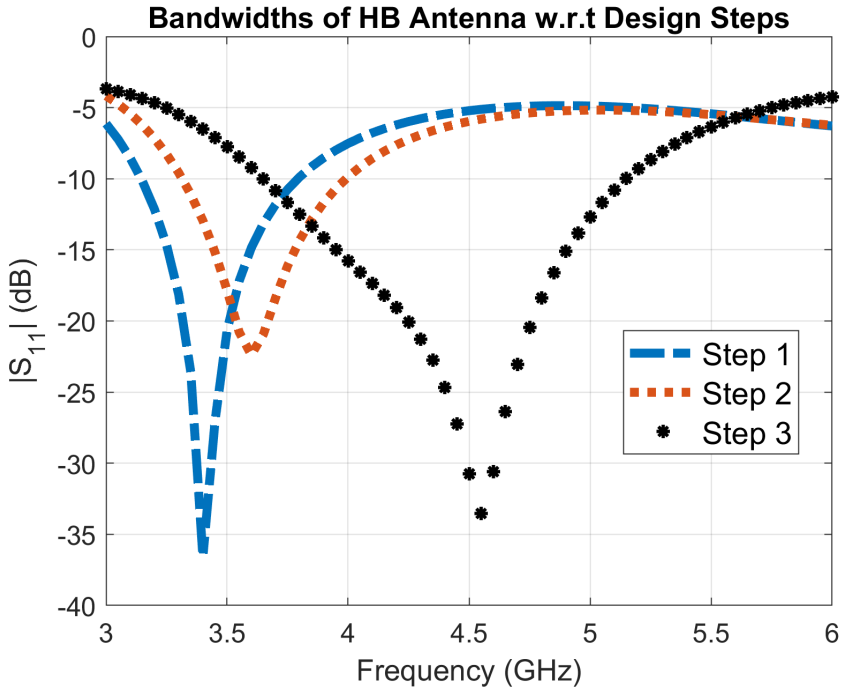

(a)

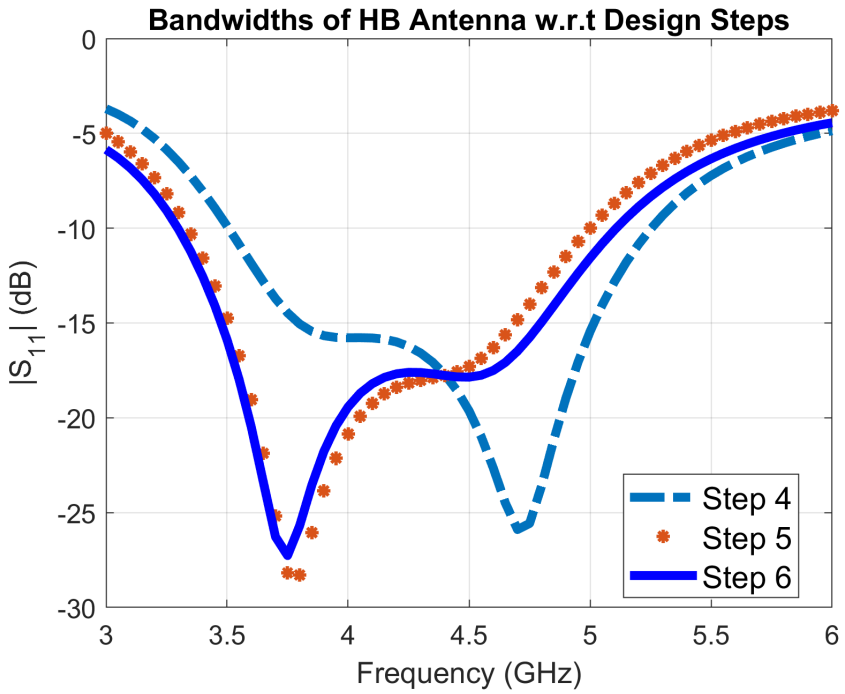

(b)

Figure 3.39: (a) Comparison of HB design with first three steps and (b) last three steps

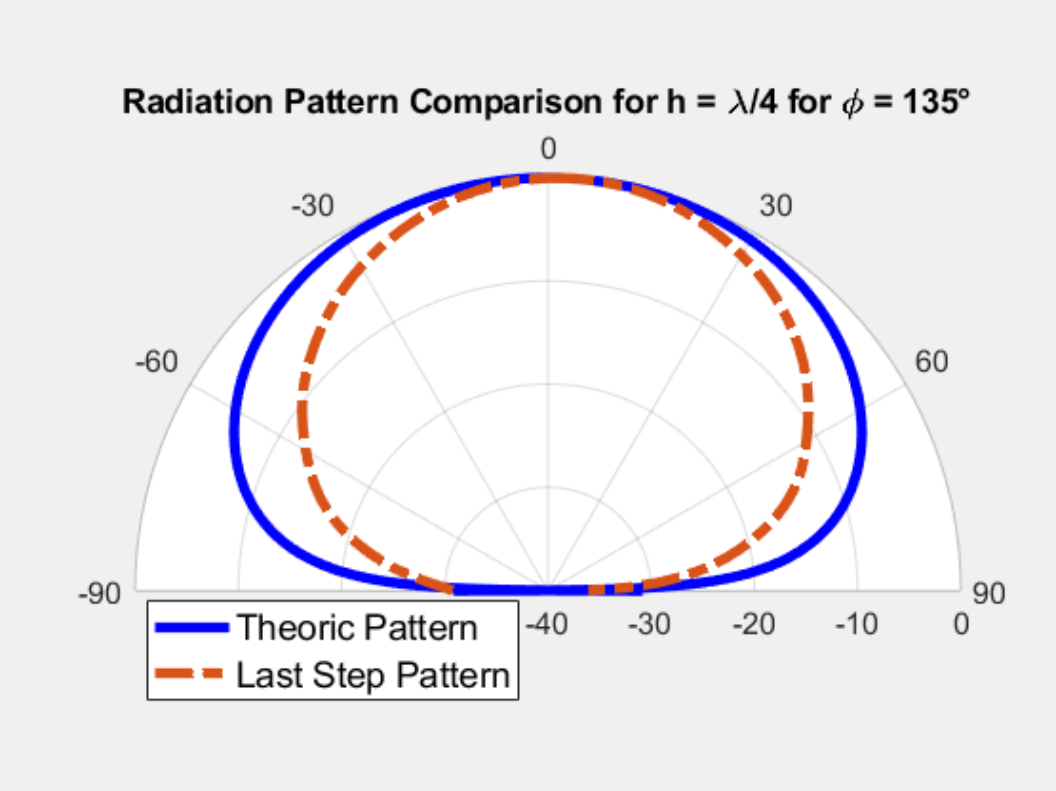

Figure 3.40: Theoric and simulation radiation pattern comparison at $\phi = 135°$

3.3.2 High Band Antenna Simulations

3.3.2.1 High Band Design Parameter Sweep

Important design parameters of the HB antenna are examined with parameter sweep simulations. All dimensions of the HB antenna are given in Figure 3.41 and Figure 3.42, and their lengths in Table 3.2. Dimension names are based on abbreviations. Since Y-feeds affect the antenna performance significantly, they are important design parameters to sweep. Their actual names are given within the simulations. Only the terms "YFCL" and "YFTL" is not swept, and their names are "Y-feed center length" and "Y-feed tail length", respectively. The variable t is the copper thickness on the PCB.

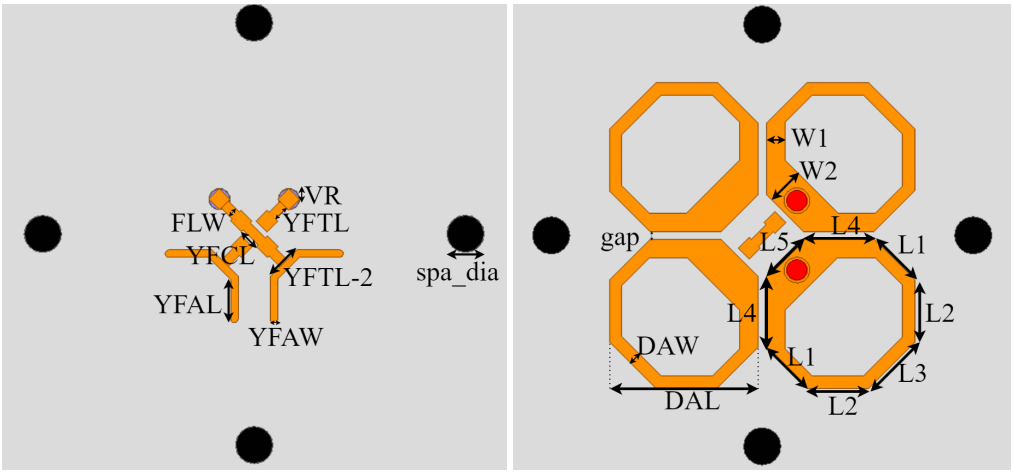

(a) (b)

Figure 3.41: (a) HB antenna parameters on top layer and (b) bottom layer

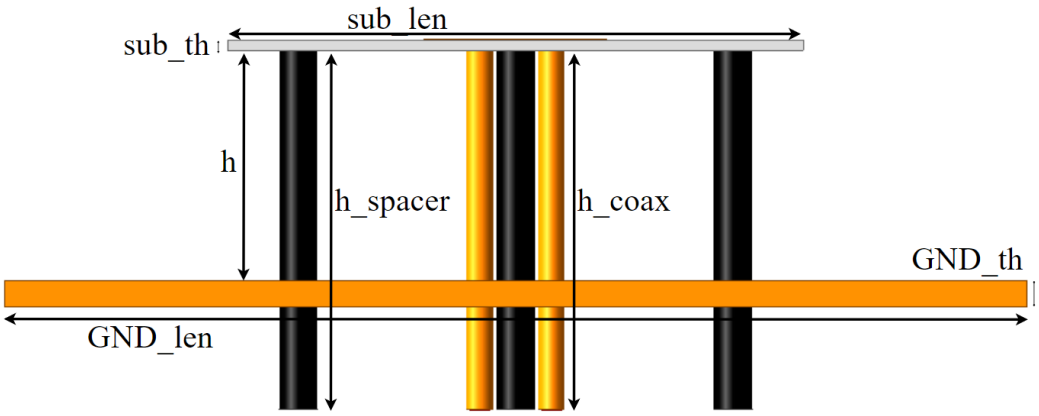

Figure 3.42: HB antenna parameters from side view

The first swept parameter is Y-feedline width. Sweep results are shown in Figures 3.43 and 3.44. Increasing the width increases the bandwidth with the second resonance frequency shift. The first resonance frequency also increases but much less compared to the second resonance. The first resonance starts to disappear, and the second resonance starts to be clearly visible. However, increasing feedwidth negatively affects the isolation. For the required bandwidth, 0.8mm is selected as the optimum value.

Table 3.2: HB Antenna Dimensions

HB Dimensions	Value (mm)	HB Dimensions	Value (mm)
sub_len	45	gap	0.63
YFAL	3.75	DAW	1
FLW	0.8	DAL	12
YFCL	1.7	L1	4.65
VR	0.875	L2	4.96
YFAW	0.6	L3	5.3
YFTL-1	1.24	L4	5.71
YFTL-2	3	L5	4.25
spa_dia	3	W1	1.5
W2	3	sub_th	0.813
h	18	GND_len	100
h_spacer	28	h_coax	28
GND_th	2	t	0.043

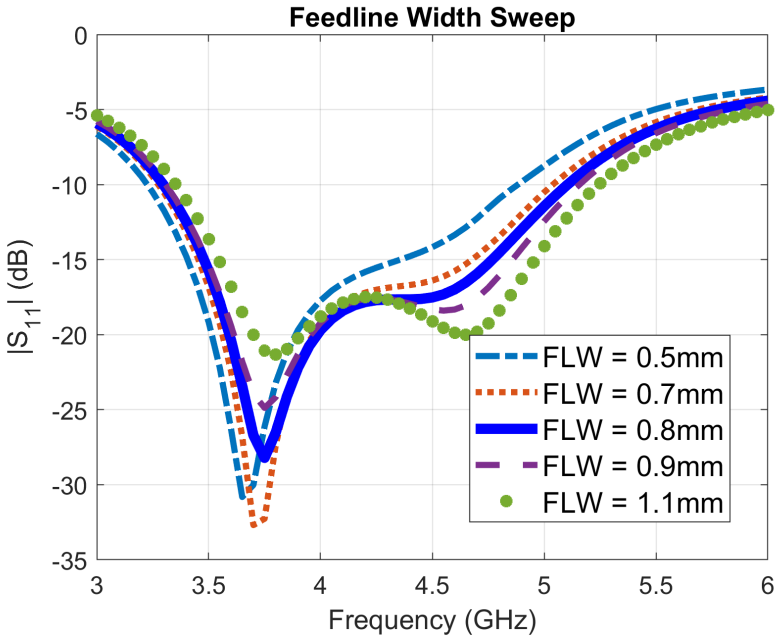

Figure 3.43: Feedline width sweep S_{11}

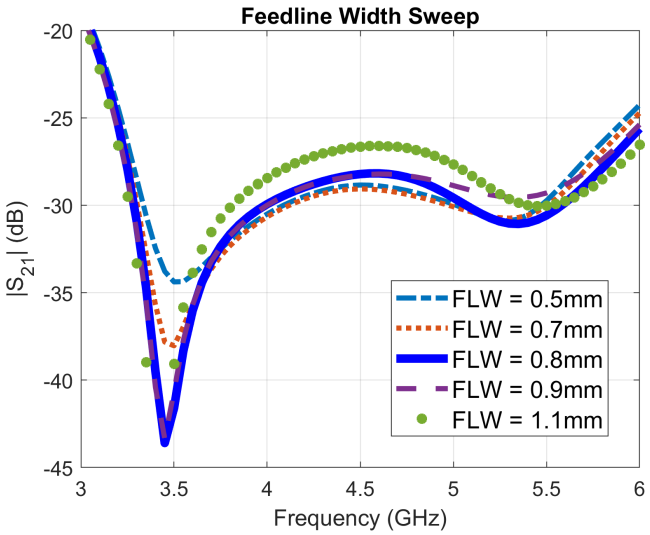

Figure 3.44: Feedline width sweep S_{21}

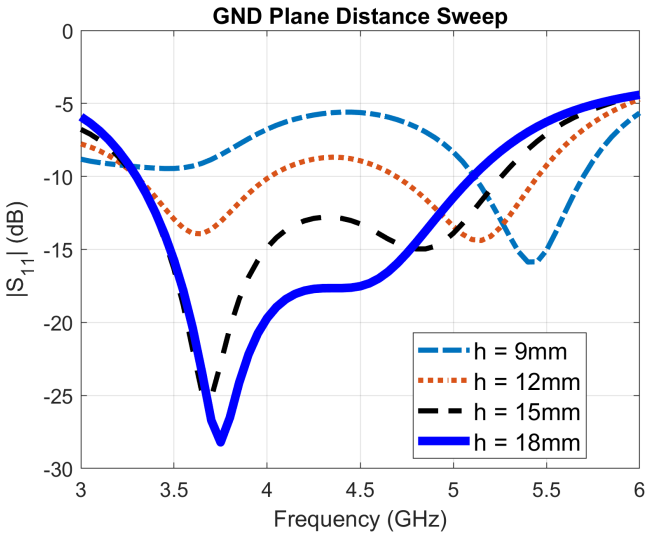

Figure 3.45: GND plane distance sweep S_{11}

The second swept parameter is GND plane distance, and its results are shown in Figure 3.45 and Figure 3.46. As mentioned before, GND plane distance greatly affects the bandwidth. The distance does not significantly change the first resonance but changes its impedance. Arranging the distance as $\lambda/4$ of the center frequency of the bandwidth is necessary for the designed antenna. For the designed antenna, 18mm is the optimal solution for the design.

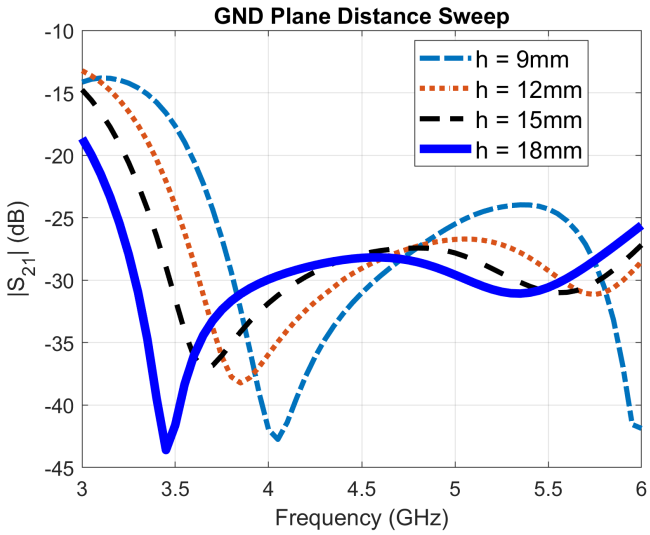

Figure 3.46: GND plane distance sweep S_{21}

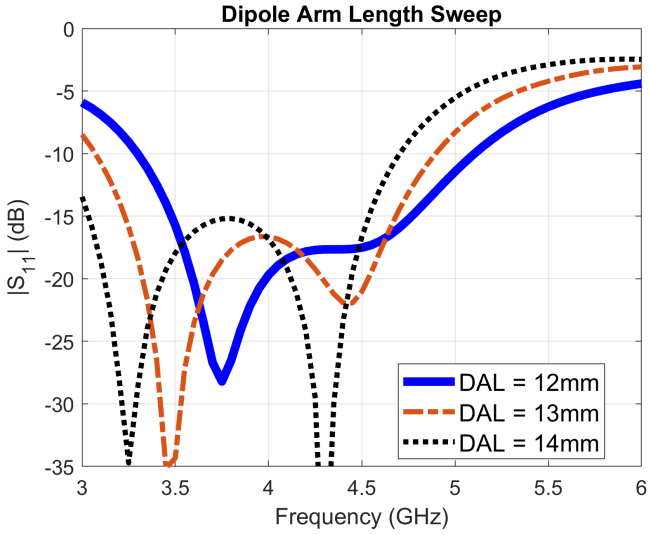

Figure 3.47: Dipole arm length sweep S_{11}

Dipole arm length variation is presented in Figure 3.47 and Figure 3.48. Since resonance frequency is inversely proportional to the wavelength, increasing arm length decreases the resonance frequency. Besides, the second resonance frequency is also decreased due to the decrease of the length L_1. Isolation is also better with lower arm lengths. It should be noted that dipole arm length is actually $\sqrt{2}$ times the variable "DAL", or namely dipole arm length. 12mm is selected for the required bandwidth.

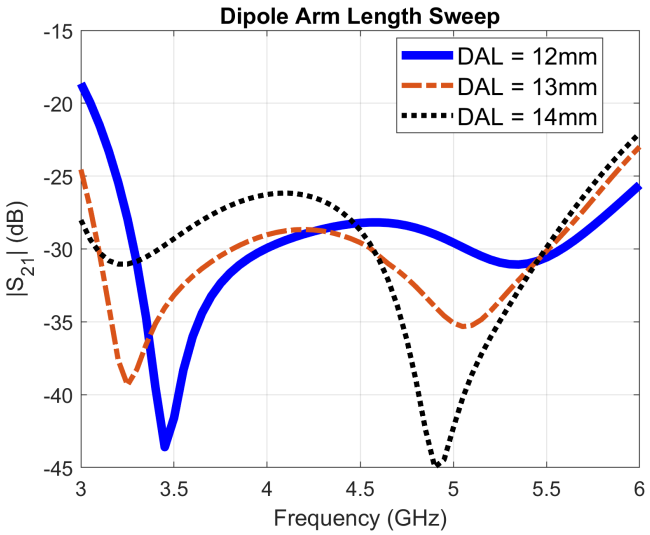

Figure 3.48: Dipole arm length sweep S_{21}

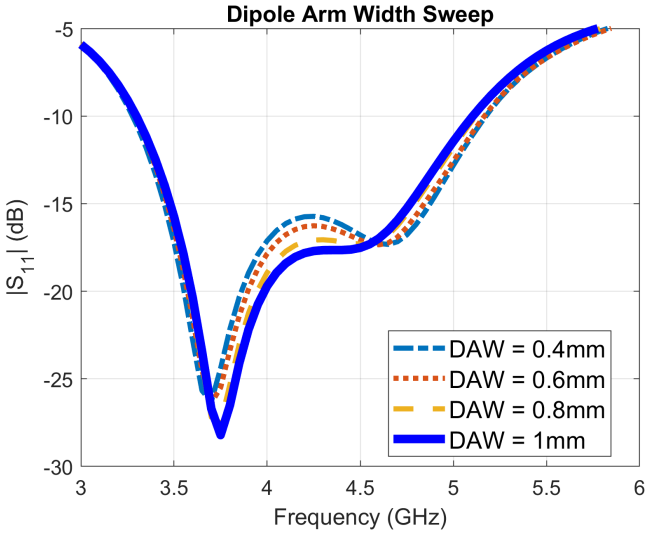

Figure 3.49: Dipole arm width sweep S_{11}

Dipole arm width does not affect isolation significantly but improves impedance matching of the antenna around the center frequency, as shown in Figure 3.49 and Figure 3.50. The bandwidth of the antenna does not change significantly at a low cutoff frequency, but a wider arm width narrows the bandwidth at a high cutoff frequency. 1 mm of arm width is chosen as the optimal solution owing to the better impedance characteristics of the antenna.

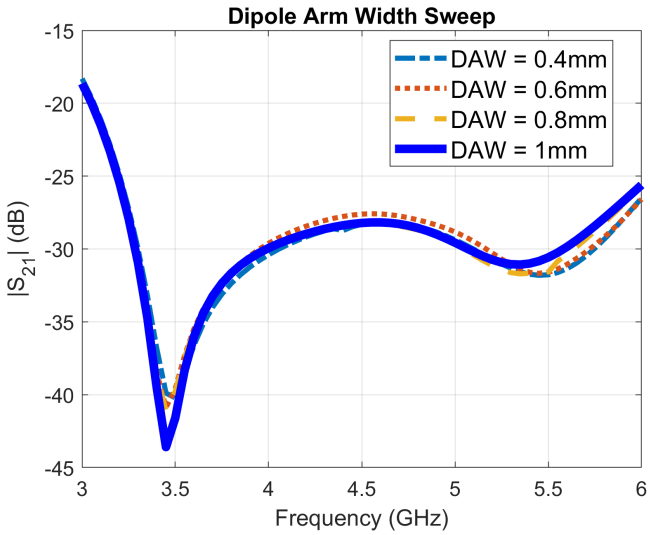

Figure 3.50: Dipole arm width sweep S_{21}

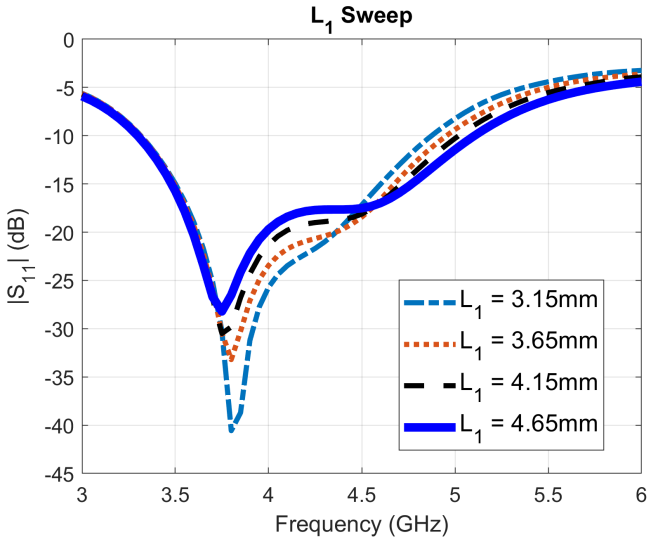

Figure 3.51: L1 sweep S_{11}

$L1$ is crucial for the second resonance of the cross dipole. From the $L1$ length, dipoles have mutual coupling and broaden the bandwidth. Having a shorter $L1$ extends the $L4$, and this increases the coupling between dipole arms. The second resonance frequency shifts to lower frequencies with increasing mutual coupling capacitance. The first and second resonances start to become closer to each other and merge with the larger $L1$ values shown in Figure 3.51. S_{21} value is shown in Figure 3.52.

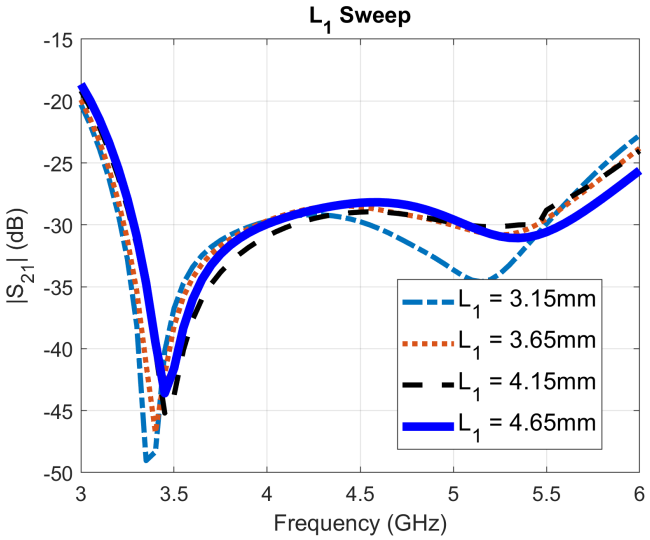

Figure 3.52: L1 sweep S_{21}

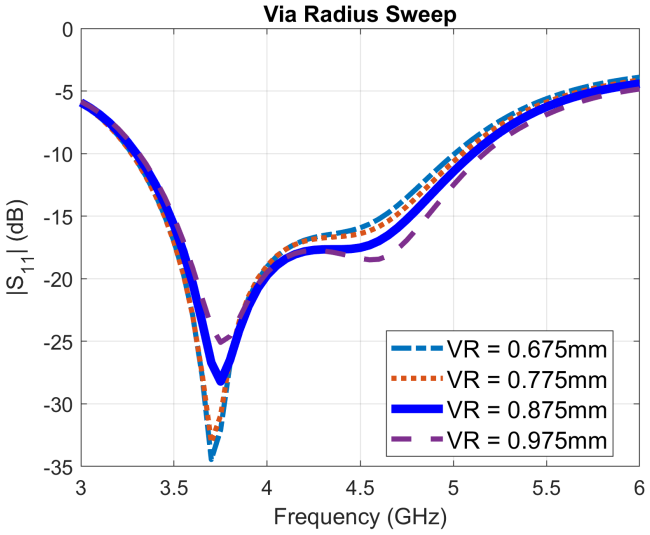

Figure 3.53: Via radius sweep S_{11}

The via mentioned here is for the transfer of the inner conductor of the coax cable to Y feeding, and its radius affects the antenna performance. The results are shown in Figure 3.53 and Figure 3.54. Having a larger radius increases the bandwidth but decreases the isolation. Hence, 0.875 mm is selected for the desired bandwidth and isolation.

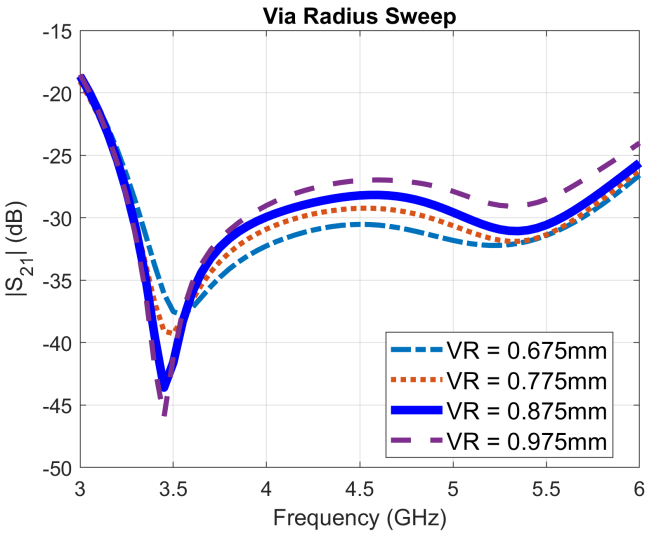

Figure 3.54: Via radius sweep S_{21}

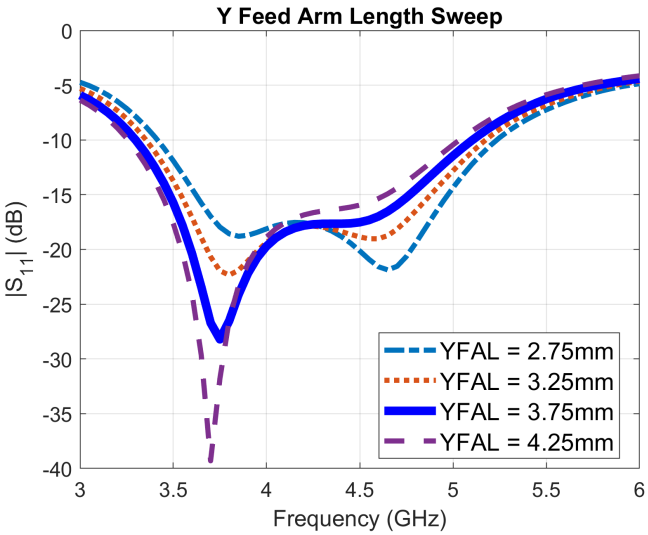

Figure 3.55: Y feed arm length sweep S_{11}

Regarding the antenna feeding done by Y feeding, its design parameters are vital for the antenna. Figure 3.55 and Figure 3.56 display the arm length variations, and Figure 3.57 and Figure 3.58 display the arm width variations. Since Y-feeding is capacitive coupled feeding, increasing arm length or width increases the capacitive coupling area, so the capacitance. Hence, resonance frequencies are shifted to lower frequencies. Also, having shorter arm length results in worse isolation capabilities. 3.75mm of arm length and 0.6mm of arm width are selected for better isolation and

required bandwidth for the HB antenna.

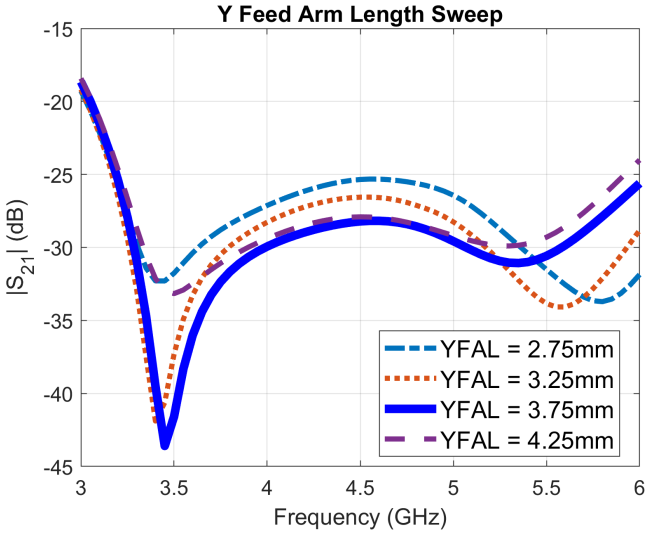

Figure 3.56: Y feed arm length sweep S_{21}

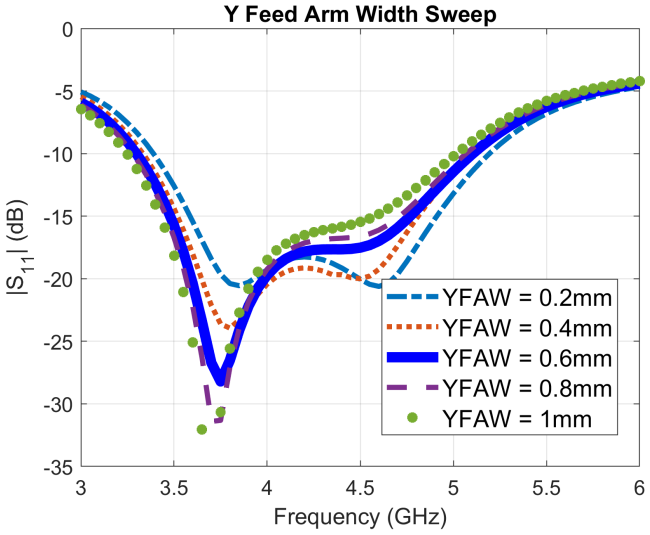

Figure 3.57: Y feed arm width sweep S_{11}

Similar effects can be seen with the second part of the Y-feeding tail length. Increasing the dimensions increases the capacitive coupling feeding with dipole arms, decreasing the resonance frequency. The second Y feed tail length of 3 mm is selected for the desired bandwidth.

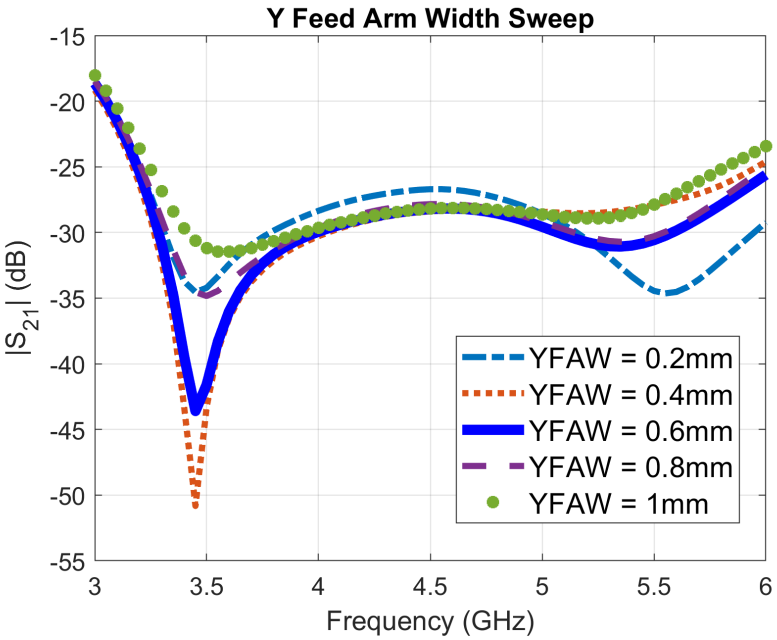

Figure 3.58: Y feed arm width sweep S_{21}

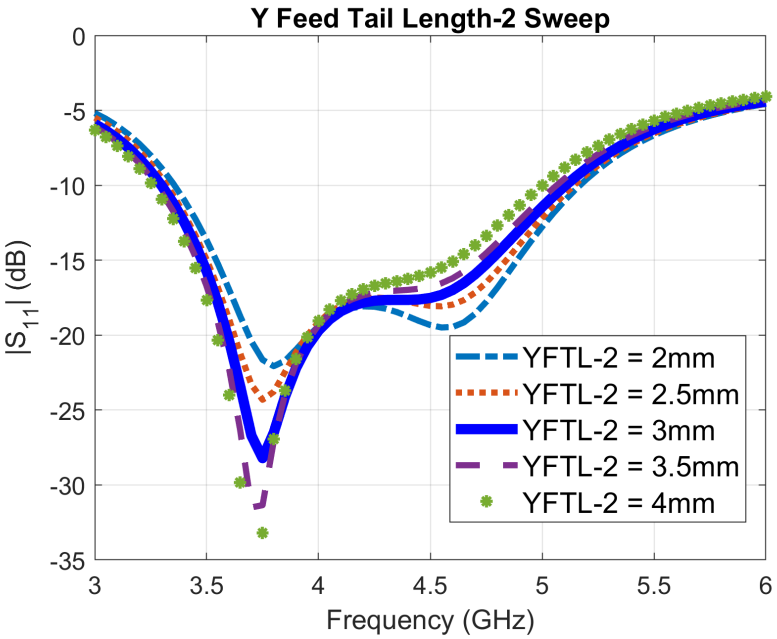

Figure 3.59: Y feed tail length-2 sweep S_{11}

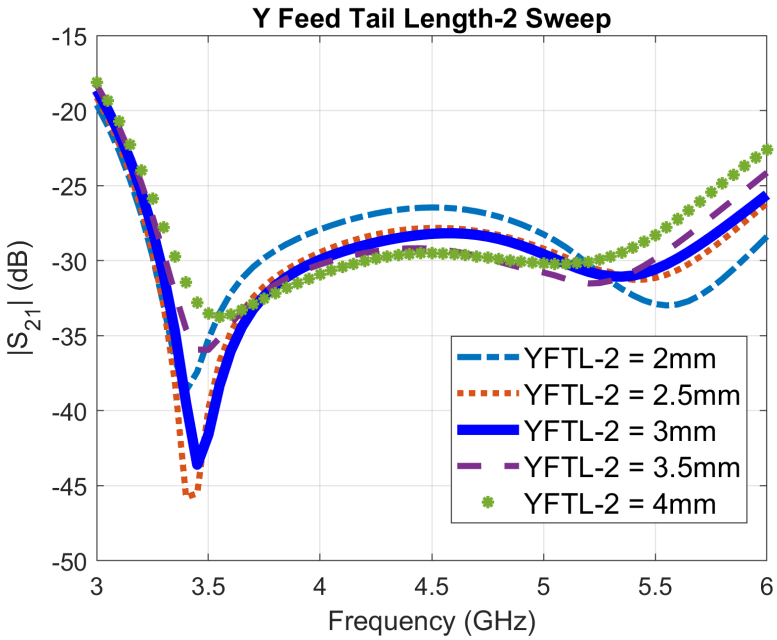

Figure 3.60: Y feed tail length-2 sweep S_{21}

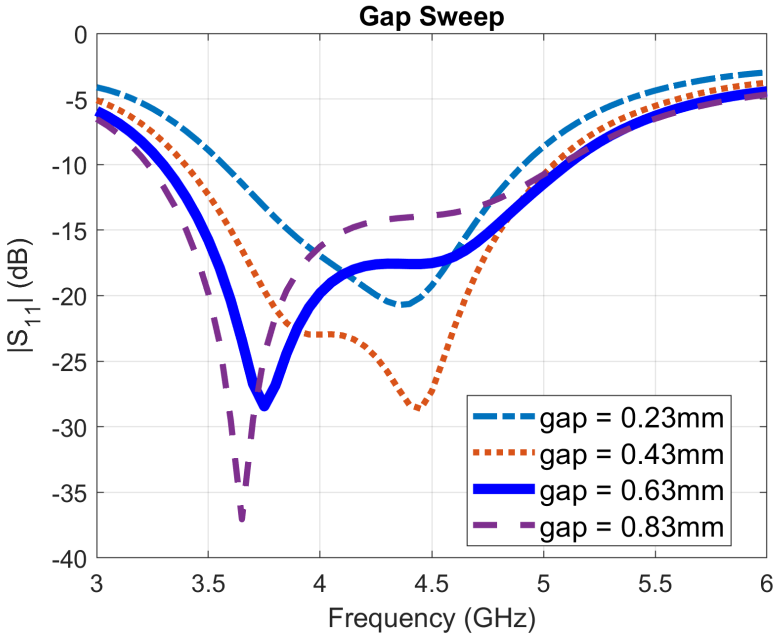

Figure 3.61: Gap sweep S_{11}

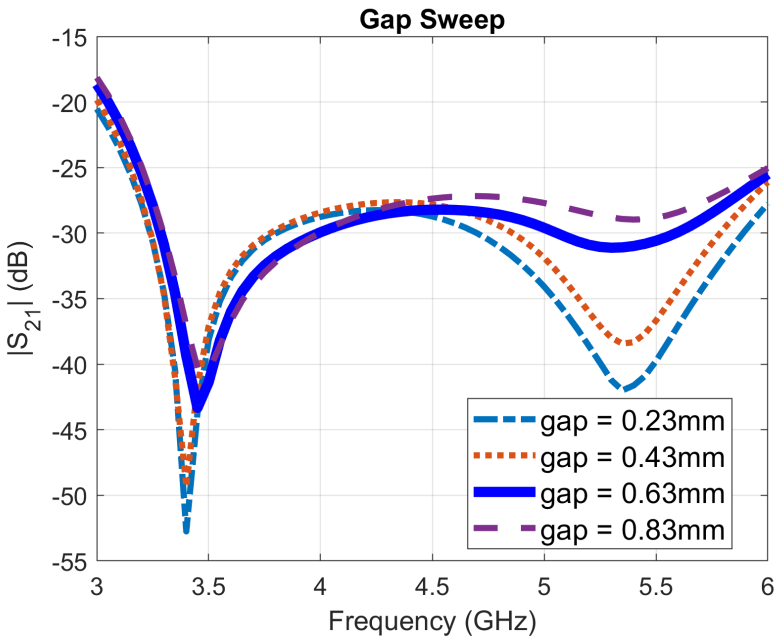

Figure 3.62: Gap sweep S_{21}

The parameter "gap" variation with respect to frequency is given in Figure 3.61 and Figure 3.62. If the distance between the neighbor dipole arms increases, mutual coupling decreases between the cross dipoles. Hence, the first resonance shifts to lower frequencies and becomes more visible. The second resonance point starts to disappear with the gap increase. But gap decrease also narrows the bandwidth with a worse impedance match. So gap value is arranged as 0.63 mm for better impedance match and bandwidth.

3.3.2.2 High Band Final Form Simulations

After the parametric sweeps and optimum values are selected, antenna performance is analyzed. In the final form of the HB antenna, radiation patterns in specific frequencies, and the axial ratio of the HB antenna are shown for circular polarization. In Figure 3.63, S-parameters of S_{11}, S_{22} and S_{21} is shown together. Due to the symmetric structure of the dipole antennas, except for the Y feeding transition, S_{11} and S_{22} are almost the same. The bandwidth for the HB antenna is nearly 3.27-5.11 GHz, and its isolation between two different ports is at least 28 dB at the highest point, which can be seen from S_{21} curve. Radiation patterns are given in five specific frequencies,

3.4 GHz, 3.9 GHz, 4.4 GHz, 4.9 GHz, and 5.4 GHz, in Figure 3.64 and Figure 3.65. Port 1 patterns are obtained when the port 2 is matched, and vice versa. Circular polarization (CP) patterns are obtained with 90° phase difference. The realized gain value is expressed at $\theta = 0°$ is also given in the plots. Gain values are changing between 7 and 8.5 dBi. Since dipole antennas are symmetric with respect to $\theta = 0°$, their radiation patterns are also symmetrical with respect to $\theta = 0°$. Even though 5.4 GHz is out of the bandwidth, its radiation characteristics and gain are still promising. It should be noted that throughout the thesis, all circular polarization patterns are shown as RHCP for simplicity. If port phase variation is interchanged, then LHCP is already achieved.

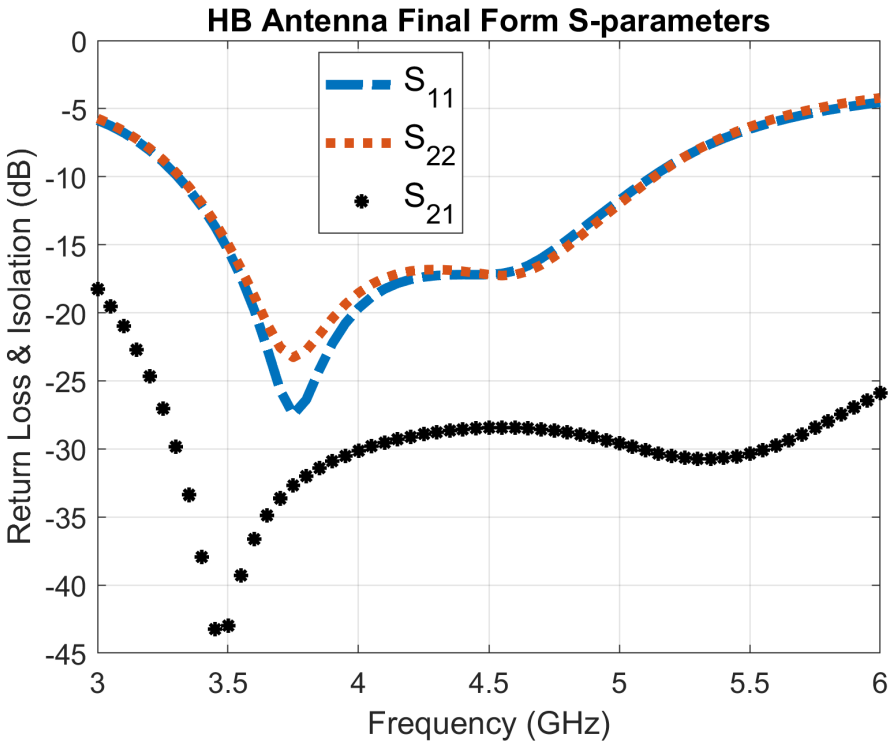

Figure 3.63: HB final form S-parameters

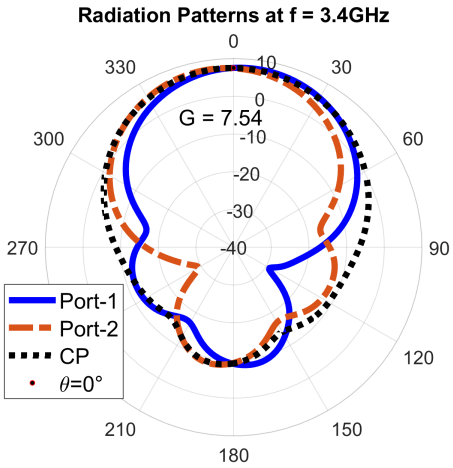

(a)

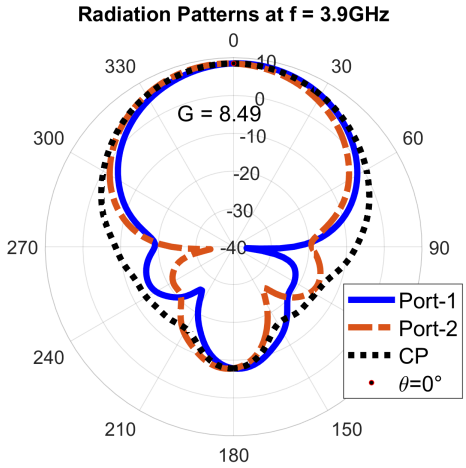

(b)

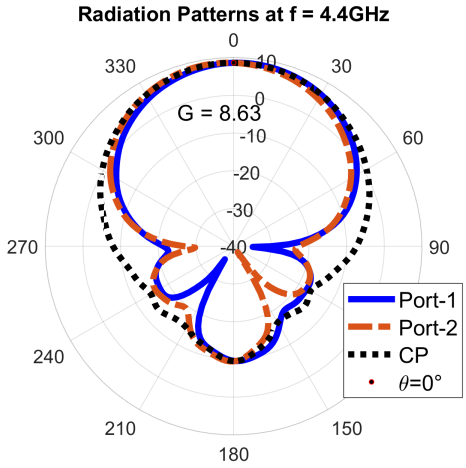

(c)

Figure 3.64: HB patterns at (a) f = 3.4 GHz, (b) f = 3.9 GHz and (c) f = 4.4 GHz

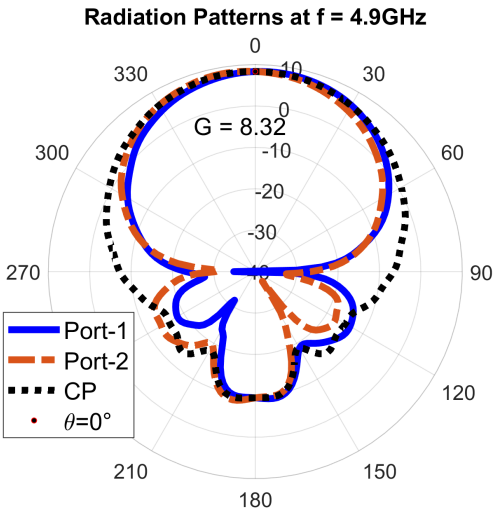

(a)

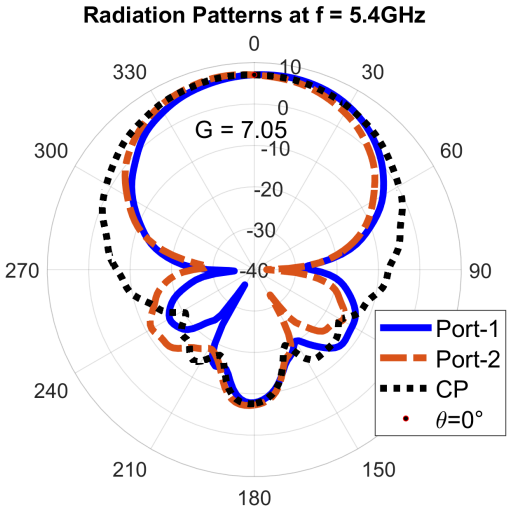

(b)

Figure 3.65: HB radiation patterns at (a) f = 4.9 GHz, (b) f = 5.4 GHz

3.3.3 High Band Antenna Measurements

After the simulations are done, the HB antenna prototype is fabricated, and the S-parameter and radiation properties are measured in ™Rohde-Schwarz ZVA 40 vector network analyzer and ™Satimo antenna measurement system [67], respectively. In order to measure the antenna properties easily, a 7 cm coax cable is soldered to the antenna, and a Sub-Miniature Version A (SMA) connector is used. Hence, ™HFSS simulations are made with a 7 cm coax cable. The fabricated antenna prototype and its connection in the anechoic chamber are given in Figure 3.66 and 3.67. Only one port can be fed in the anechoic chamber. There are four screws as spacers to support the antenna, and they are connected with three nuts to fix the ground plane-antenna distance. If desired, ground distance can be changed and rearranged by loosening the nuts, moving the screws, and tightening the nut again. Both screws and nuts are made of plastic as insulator material in order not to affect antenna radiation performance.

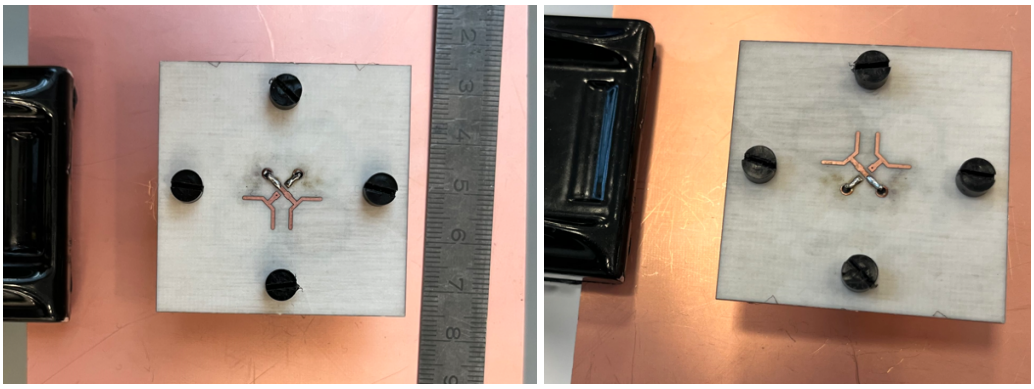

Figure 3.66: HB antenna prototype

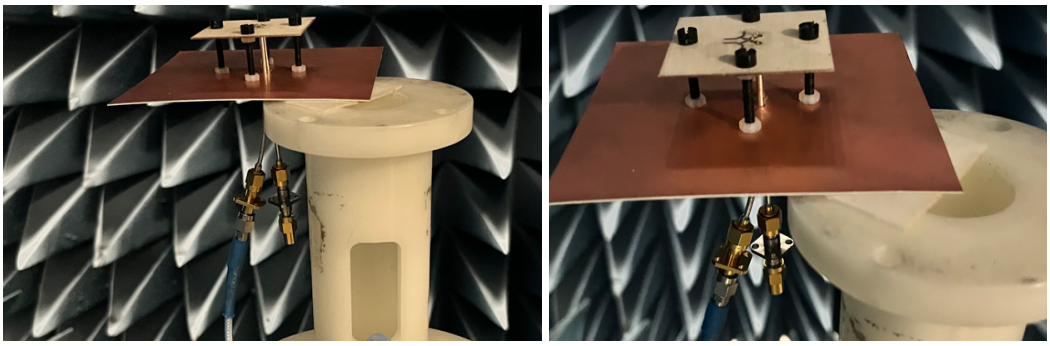

Figure 3.67: HB antenna inside of an anechoic chamber

The S-parameter simulation results of the HB antenna with longer coax cables and measurement are given in Figure 3.68. Two resonance points are visible in both simulation and measurement results. The prototype antenna has a shifted bandwidth with respect to the simulated antenna with a worse impedance match. This may be due to imperfect production of exact dimensions, SMA connectors, SMA connector adapters, network analyzer's cable losses, and measurement errors. The simulated antenna bandwidth is 3.27-5.21 GHz, and the measured antenna bandwidth is 3.5-5.4 GHz. Cutoff frequency shifts are 7% and 3.65% for low cutoff and high cutoff, respectively. Isolation is higher than 23 dB in the bandwidth except in the 3.5 GHz region. Isolation at 3.5GHz decreases to 16 dB. Lower isolation deteriorates the dual-band polarization and circular polarization performance due to unwanted cross-coupling of the ports.

Radiation pattern measurements of the HB antenna are given in Figure 3.69 and 3.70. As can be seen from the figures, simulation and measurement patterns are aligned in the range of $\theta = \pm 90^{\circ}$. Measured broadside gain is smaller than simulation gain in general; this is expected due to the effects of insertion adapter, cable losses, and imperfect measurements. Port-2 measurements are symmetrical with respect to the $\theta = 0^{\circ}$ axis of the port-1 measurements with minor differences. So for simplicity, port-2 results are not shown.

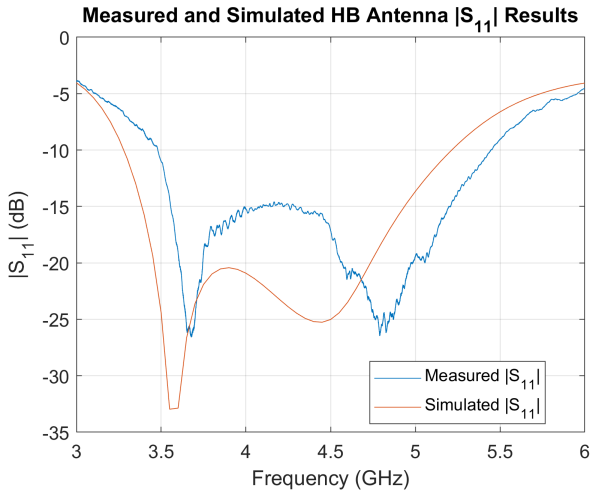

(a)

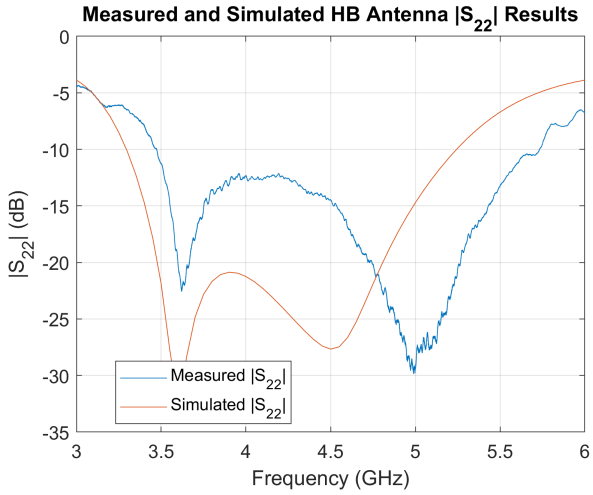

(b)

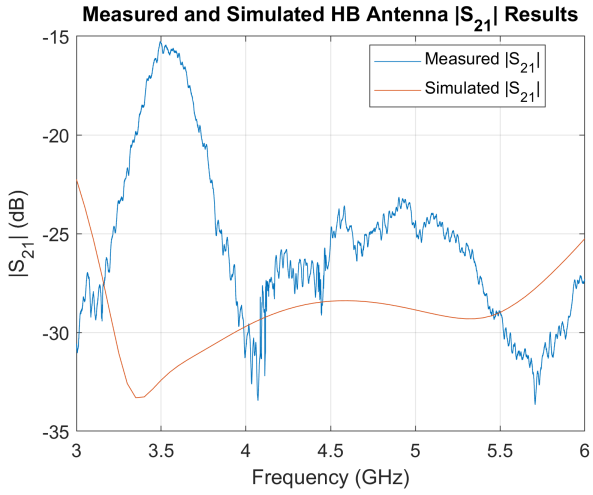

(c)

Figure 3.68: HB antenna prototype S-parameters vs. simulation

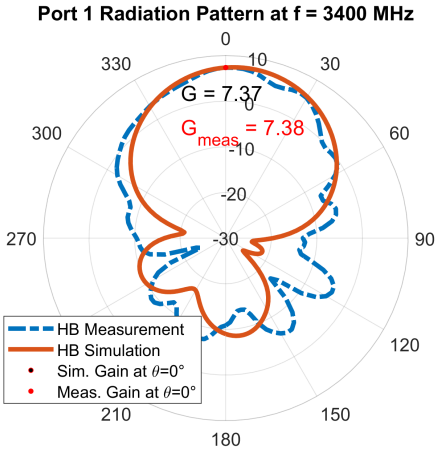

(a)

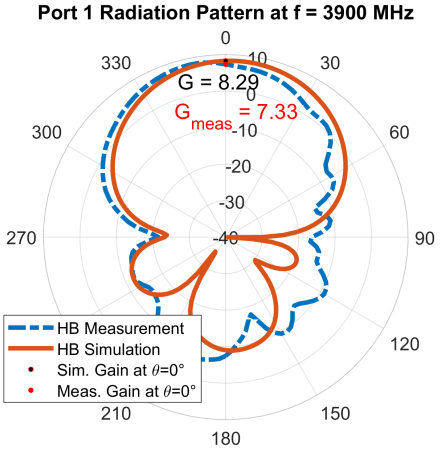

(b)

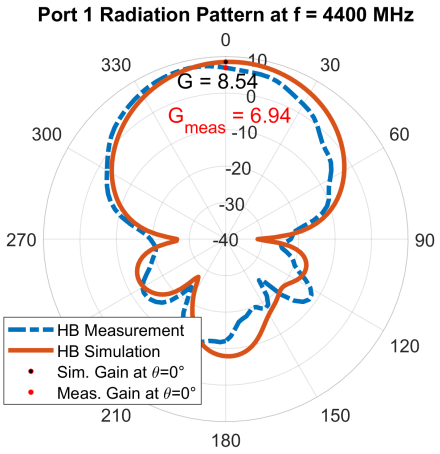

(c)

Figure 3.69: HB antenna port 1 radiation patterns at specific frequencies of (a) f = 3.4 GHz, (b) f = 3.9 GHz, (c) f = 4.4 GHz

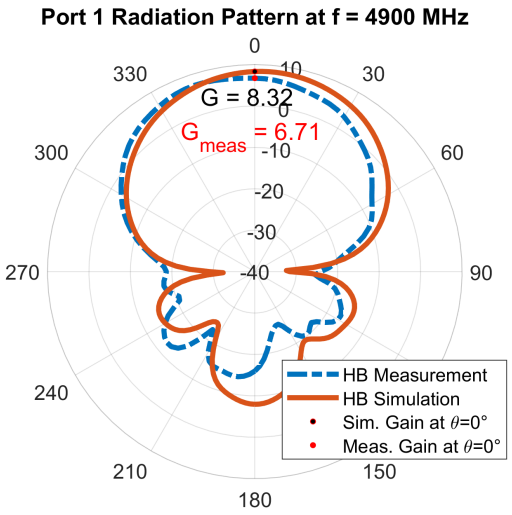

(a)

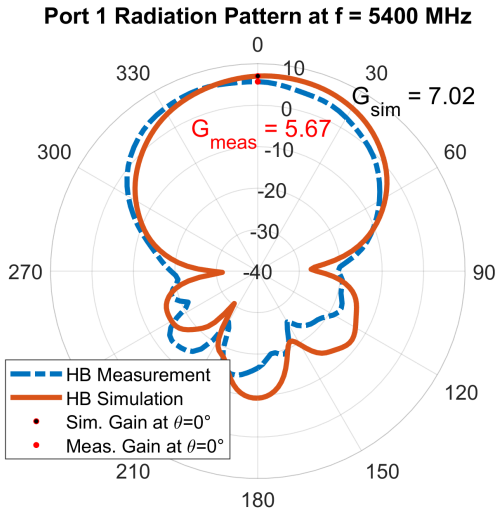

(b)

Figure 3.70: HB antenna port 1 radiation patterns at specific frequencies of (a) f = 4.9 GHz, (b) f = 5.4 GHz

3.3.4 Dual and Circular Polarization Realization of Cross-Dipole Antenna

It is previously mentioned that, designed cross-dipole antennas can also be operated as dual and circularly polarized. For dual and circular polarization, both ports of the cross-dipole antenna should be fed with the same magnitude of power. Both port feedings are in-phase for the dual polarization, and 90° phase shifted feeding of one

port is applied for circular polarization.

In ™HFSS, ports' power and phase can be easily arranged for in-phase and circular polarization from the "Edit Sources" option. Then, the measurement results are taken port by port. For the measurement case, electric field components in specific frequencies are extracted to observe the pattern and gain characteristics. Calculations from the electric field components to the radiation pattern and gain values are given in Appendix C.

Measured dual polarization patterns can be seen in Figure 3.71 and 3.72 for both dipole antennas. Stable and similar radiation patterns can be obtained for both ports. Hence, it can be said that the designed HB antenna can operate as a dual-polarized antenna. Apart from that, the CP pattern is given in Figure 3.73 and 3.74. The bold blue lines indicate the measured pattern, and the red line shows the simulated pattern. Also, the yellow line shows the cross-polarization pattern. Simulated and measured patterns are in fit in most of the θ angles. Cross-polarization gain values are at least around 10 dB lower in the broadside direction.

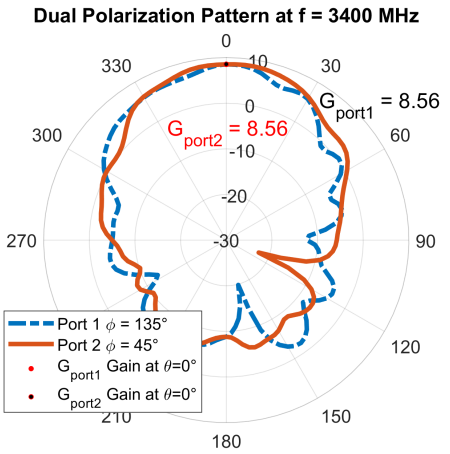

(a)

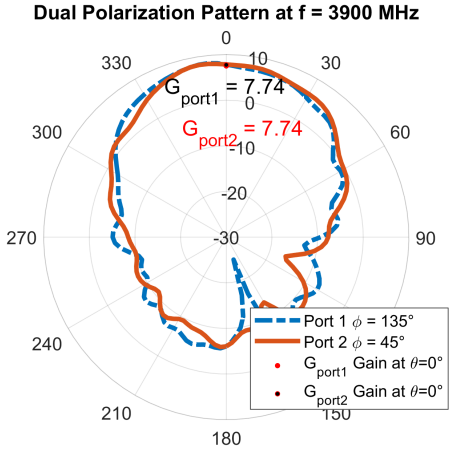

(b)

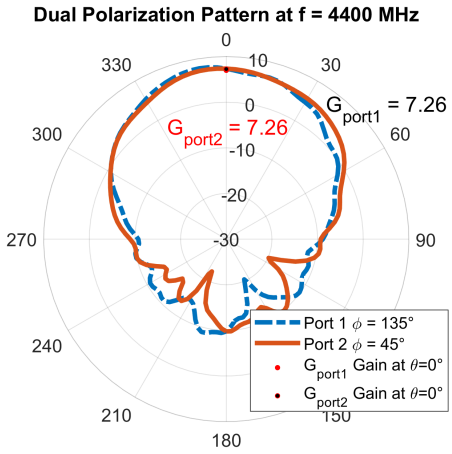

(c)

Figure 3.71: HB antenna dual polarization patterns at specific frequencies of (a) f = 3.4 GHz, (b) f = 3.9 GHz, (c) f = 4.4 GHz

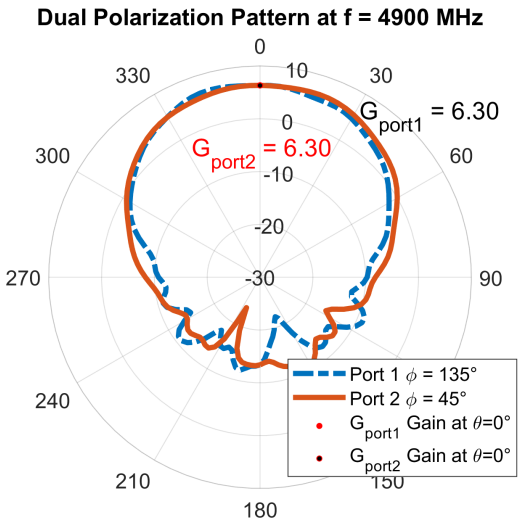

(a)

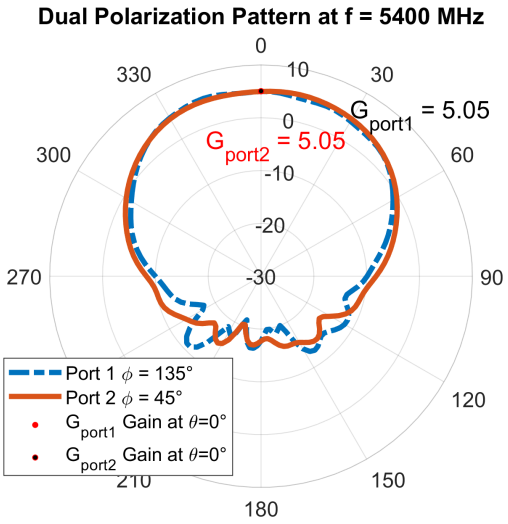

(b)

Figure 3.72: HB antenna dual polarization patterns at specific frequencies of (a) f = 4.9 GHz, (b) f = 5.4 GHz

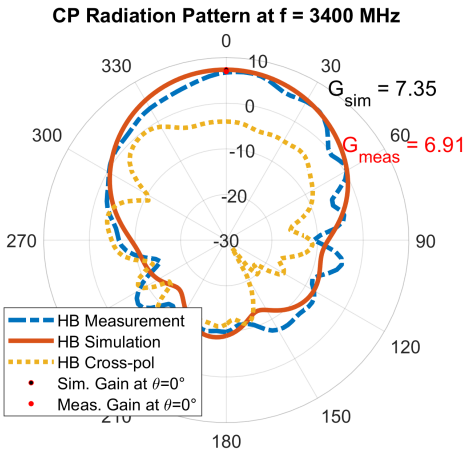

(a)

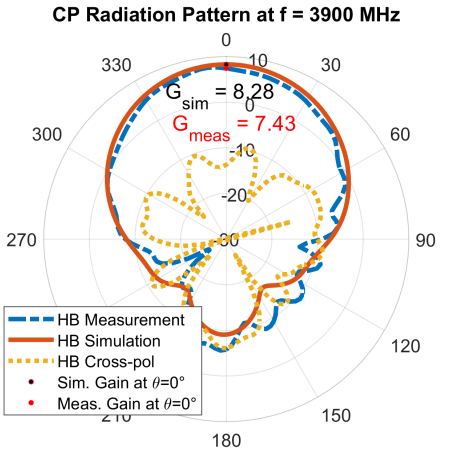

(b)

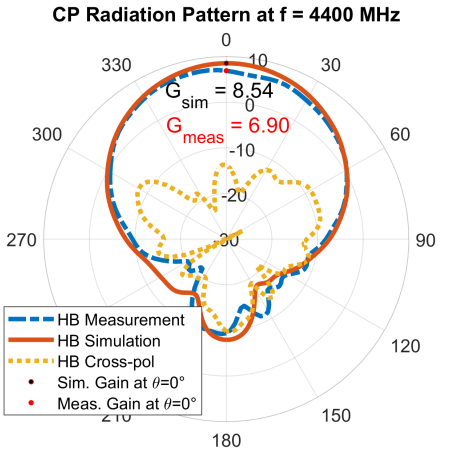

(c)

Figure 3.73: HB antenna RHCP patterns at specific frequencies of (a) f = 3.4 GHz, (b) f = 3.9 GHz, (c) f = 4.4 GHz

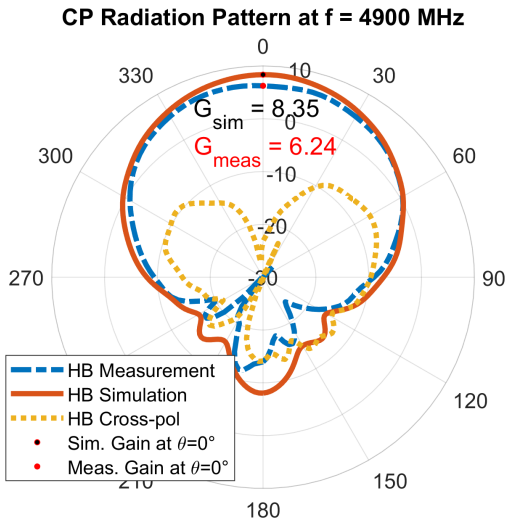

(a)

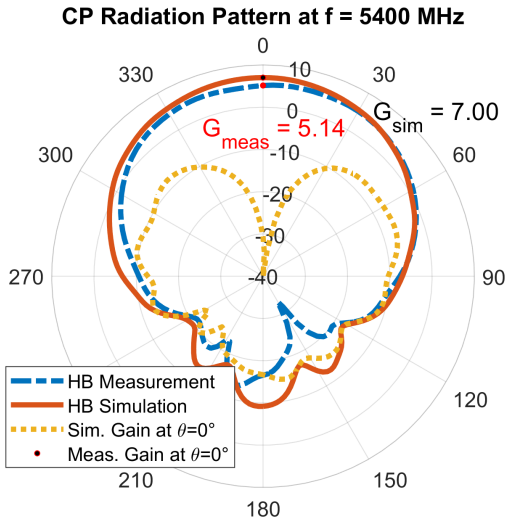

(b)

Figure 3.74: HB antenna RHCP patterns at specific frequencies of (a) f = 4.9 GHz, (b) f = 5.4 GHz

3.4 Middle Band Antenna Design

The purpose of the middle band antenna design is to cover the 2G, 3G, and 4G frequency bands. 2G band is between 1710-1920 MHz, 3G band is between 1880–2170 MHz, 4G bands are 2300-2400 MHz and 2570-2690 MHz. So, the target antenna

bandwidth can be selected as between 1.7-2.8 GHz. However, this designed antenna also has EM transparent characteristics for the HB antenna, so antenna dimensions are dependent on both antenna frequency and EM transparent unit cell dimensions. Hence, the MB antenna is designed from the unit cell to the cross-dipole antenna.

3.4.1 Middle Band Antenna Design Steps

MB antenna design steps can be seen in Figures 3.75, 3.76 and 3.77. In step 1, the designed EM transparent unit cell is shown. In step 2, a gap is introduced to provide a separate distance from dipole arms. In step 3, one corner of the dipole arm copper is extended and chamfered to provide enough space to solder the coax cable. In step 4, the other two corners, which are neighbors to the dipole arms, are chamfered, and the EM transparent unit cell is extended to 2×2 for having a cross-dipole antenna shape, and the top layer has two orthogonal Y-feeding lines. Four 3mm circle vias are defined for the spacers. In step 5, four spacers are placed in Figure 3.77 as shown in black color.

These design steps affect the EM transparency characteristic, and their transparency plots are shown in Figure 3.78. These S_{21} values are taken for $\theta = 0^{\circ}$ incidence. It can be seen that transparency decreases from 1 dB to 3 dB for the low frequencies of the HB antenna. However, transparency losses are minimal for the higher frequencies. Thus, from FSS unit cell to cross-dipole antenna transformation degrades the transparency performance only for lower frequencies.

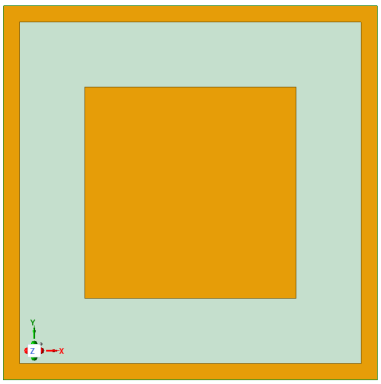

Figure 3.75: MB antenna design step 1

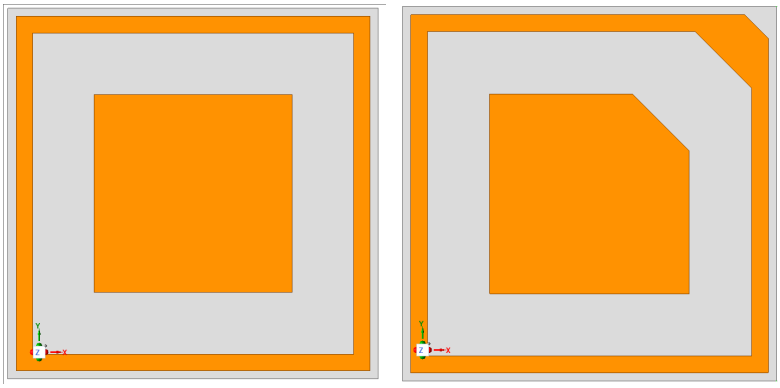

(a) (b)

Figure 3.76: MB antenna (a) design step 2 and (b) design step 3

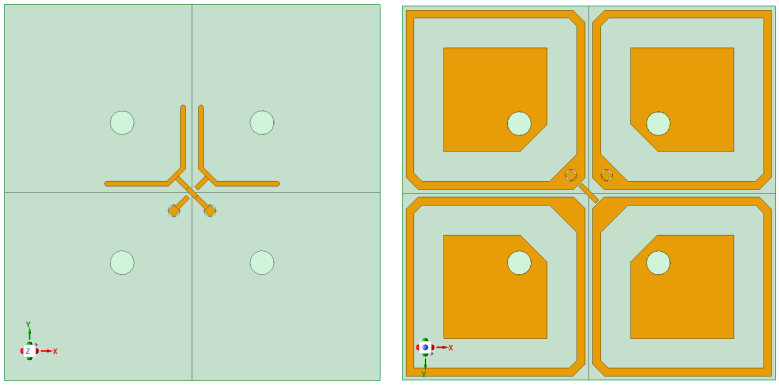

(a)

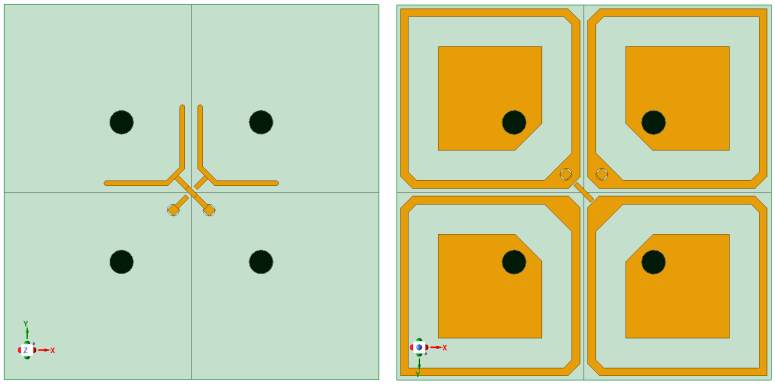

(b)

Figure 3.77: MB antenna (a) design step 4, and (b) design step 5

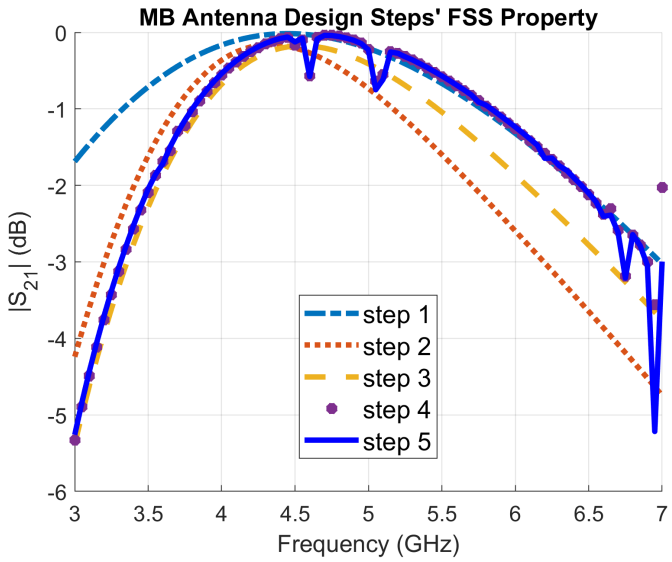

Figure 3.78: MB antenna design steps' transparency graph

3.4.2 Middle Band Antenna Design Parameters

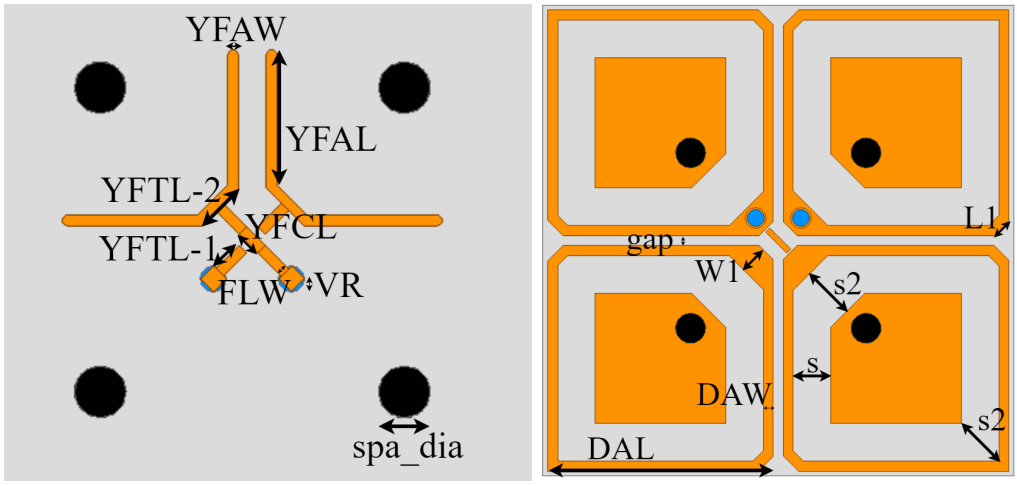

(a) (b)

Figure 3.79: MB antenna parameters on (a) top layer and (b) bottom layer

Similar to the HB antenna, the design parameters of the MB antenna are shown in Figures 3.79 and 3.80. The optimum design dimensions are given in Table 3.3. From the Chapter 2.4, the FSS unit cell d formula is calculated with Equation 2.1, which corresponds to the length DAL in Figure 3.79. The dipole antenna arm is square loop-

shaped, and antenna arm length is the diagonal length of the square loop. Since this antenna is a half-wavelength dipole, the length DAL can be calculated by Equation 2.1.

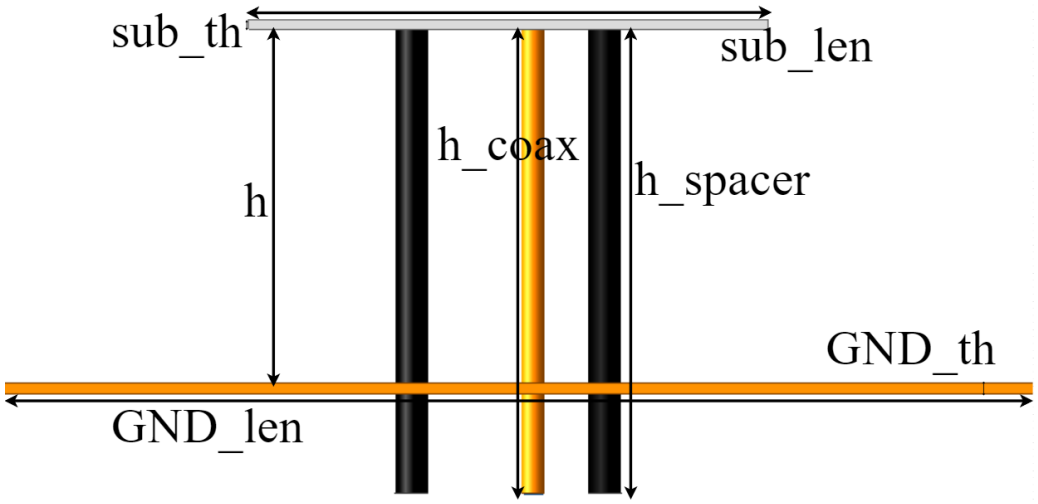

Figure 3.80: MB antenna parameters from side view

Table 3.3: MB Antenna Dimensions

MB Dimensions	Value (mm)	MB Dimensions	Value (mm)
sub_len	47	gap	1
YFAL	7.75	DAW	1
FLW	0.6	DAL	22.5
YFCL	1.5	L1	2.12
VR	0.75	s	3.75
YFAW	0.6	s2	5.3
YFTL-1	1.9	W1	2.83
YFTL-2	3	spa_dia	3
h	32	GND_len	150
h_spacer	42	h_coax	42
GND_th	2	t	0.043
sub_th	0.813		

3.4.3 Middle Band Antenna Simulations

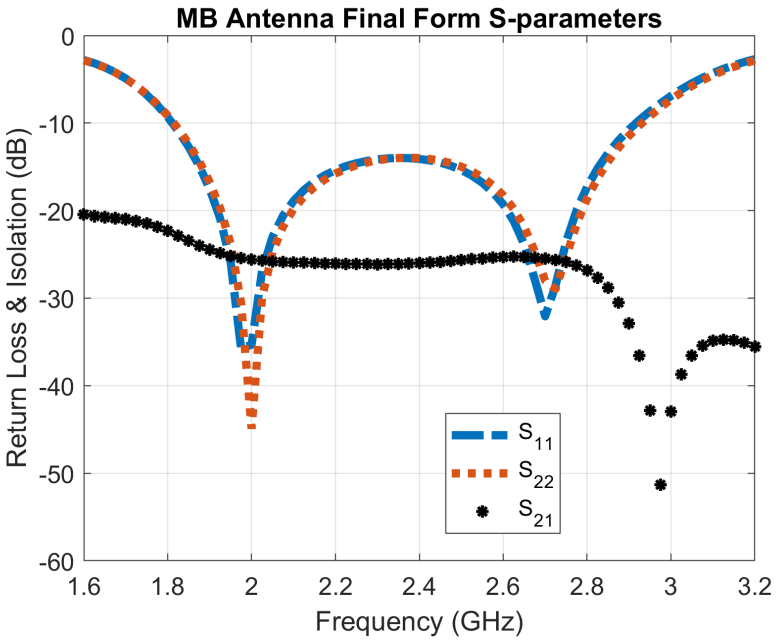

Figure 3.81: MB final form S-parameters

MB antenna simulation S-parameters are shown in Figure 3.81. S_{11} and S_{22} bandwidths are around 1.8-2.9 GHz with two clearly visible resonance points. S_{21} value is lower than 20 dB in the bandwidth, so isolation between ports is ensured.

MB antenna simulation radiation pattern simulations at f = 1.9 GHz, f = 2.4 GHz, and f = 2.9 GHz are displayed in Figure 3.82. Separate ports are almost the same, with promising gain value and pattern shape. The CP radiation pattern is also given in the same plots with promising results.

In the previous chapter, the transparency characteristic of the HB FSS, or the MB antenna surface, is mentioned. The no-patch MB antenna is shown in Figure 3.83. The MB antenna characteristics with patch and without patch are given in Figure 3.84. Reflection loss and isolation characteristics are almost the same with minor differences. Also, the dual polarization pattern comparison at 2.4 GHz is given in Figure 3.85. Patterns are almost identical with a minimal gain loss.

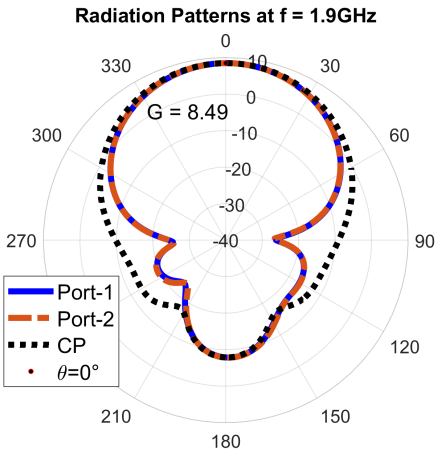

(a)

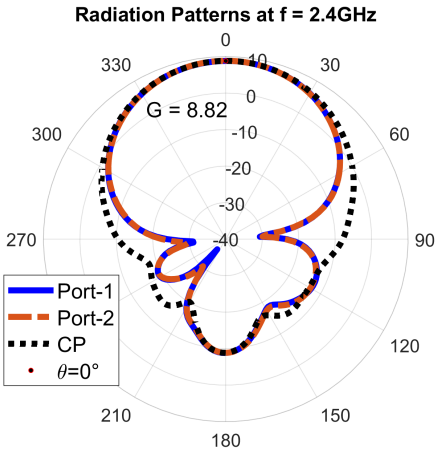

(b)

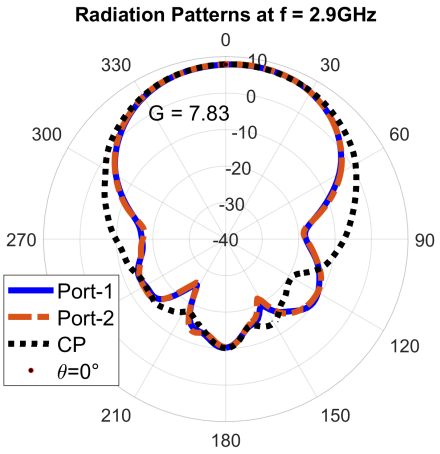

(c)

Figure 3.82: MB antenna radiation patterns at specific frequencies of (a) f = 1.9 GHz, (b) f = 2.4 GHz, (c) f = 2.9 GHz

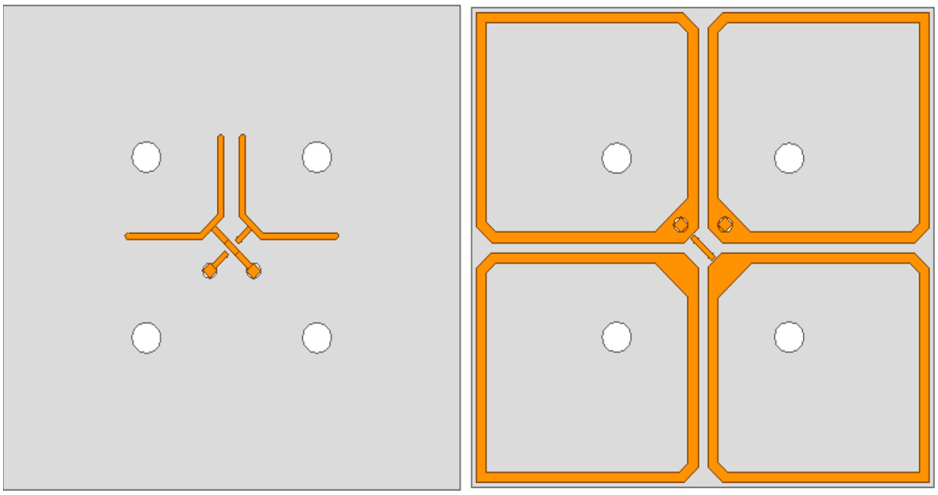

(a) (b)

Figure 3.83: MB antenna with no patch (a) top layer and (b) bottom layer

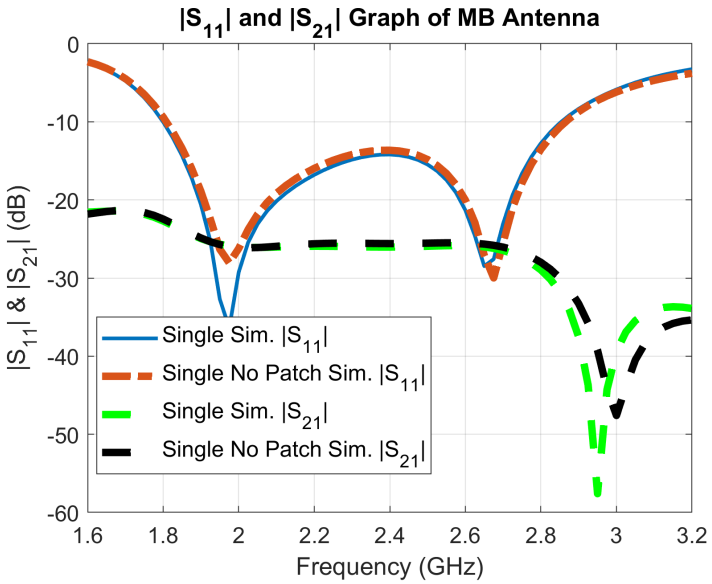

Figure 3.84: MB S-parameters with and without patch

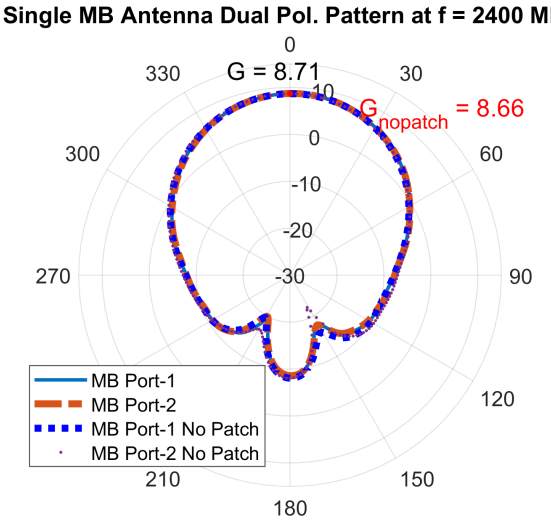

Figure 3.85: MB radiation pattern with and without patch

3.4.4 Middle Band Antenna Measurements

After the simulations, the fabricated MB antenna is shown in Figure 3.86 and 3.87. The coax cable length of the MB antenna is longer than the HB antenna, which is 85mm since the MB antenna level is higher than the HB antenna. Also, the spacer locations of the MB antenna are closer to the center of the PCB to provide more space for the HB antenna to be placed. Thus, overall design space can be reduced. It is important to note that locating the spacers closer to the center almost does not affect the EM transparency and MB antenna performance.

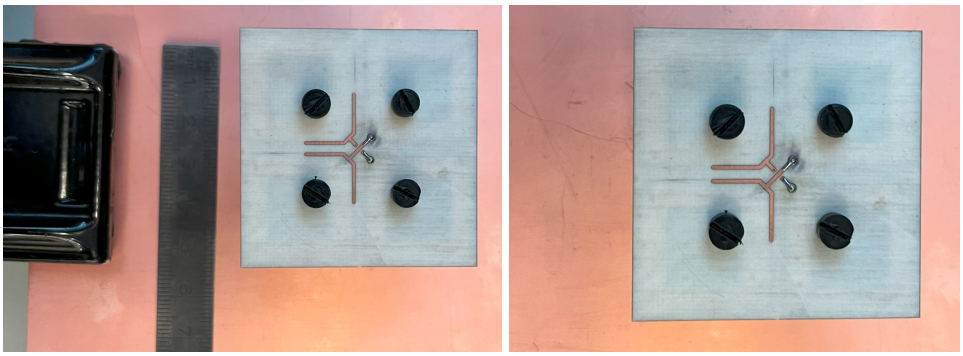

Figure 3.86: MB antenna prototype

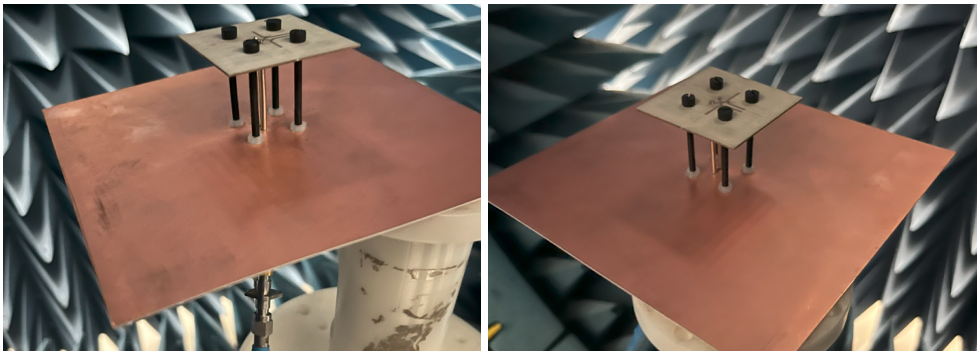

Figure 3.87: MB antenna inside of the anechoic chamber

Simulated and measured S-parameters are shown in Figure 3.88. Measured S_{11} is very close to the simulated plot with minor differences in bandwidth. Measured S_{22}'s first resonance return loss is lower, but the resonance point is the same as the simulation. On the other hand, the second resonance of measured S_{22} is deeper than the simulation. Bandwidth is larger in the measured plot. Isolation is better than 25 dB for both measured and simulated S_{21}.

Port-1 radiation pattern comparison is given in Figure 3.89. Gain values at the broadside direction are very close, but after $\theta = \pm 30^{\circ}$ measured, the radiation pattern has a higher gain compared to the simulation results. The difference becomes obvious, especially after $\theta = \pm 60^{\circ}$. So, single-port operations would have a little higher θ angle coverage than simulation results. Dual polarization patterns are given in Figure 3.90. It can be said that both ports' characteristics are almost the same. CP patterns are given in Figure 3.91. Simulation and measurement results are almost identical. Cross-polarization levels are at least 20 dB lower for the broadside direction. From the measurements, it can be seen that measured and simulated gain values are close to each other.

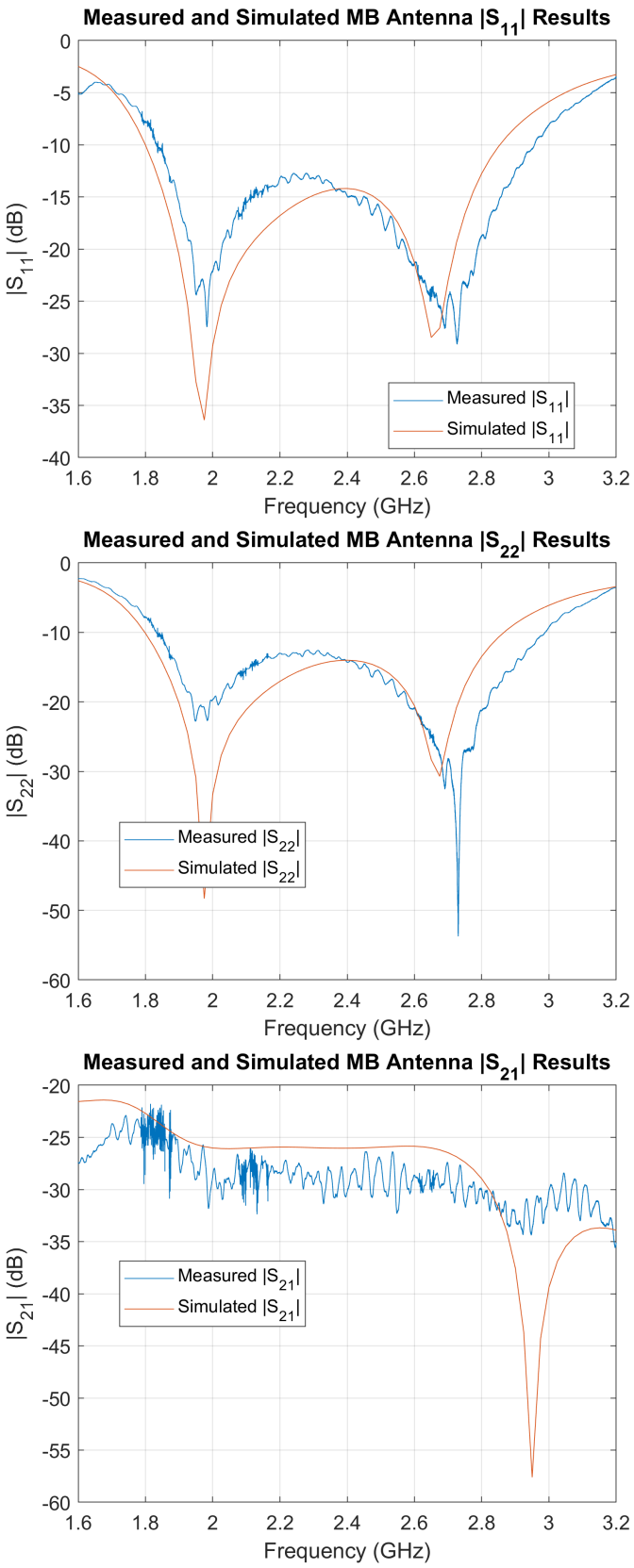

Figure 3.88: MB antenna prototype S-parameters vs. simulation

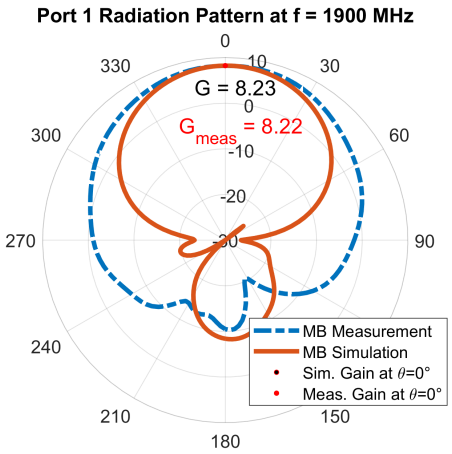

(a)

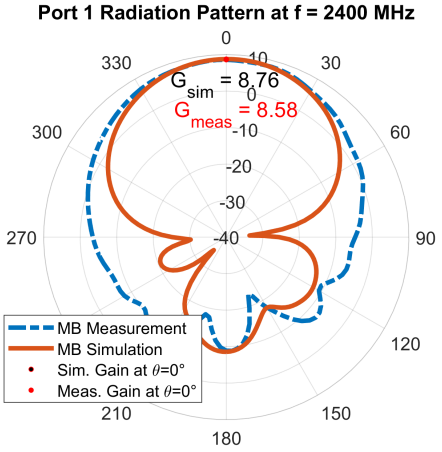

(b)

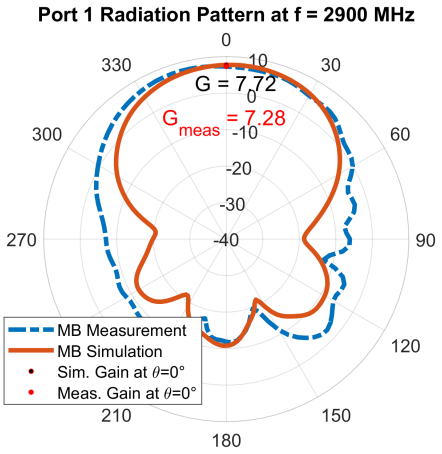

(c)

Figure 3.89: MB antenna port 1 radiation patterns at specific frequencies of (a) f = 1.9 GHz, (b) f = 2.4 GHz, (c) f = 2.9 GHz

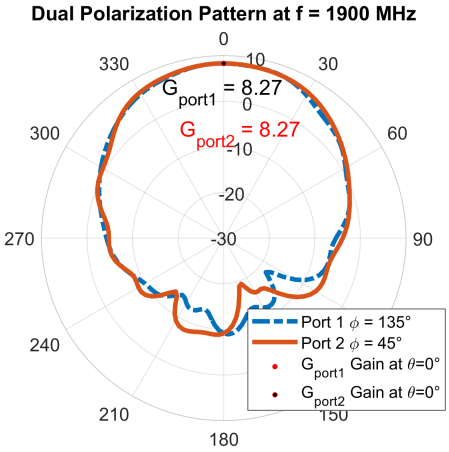

(a)

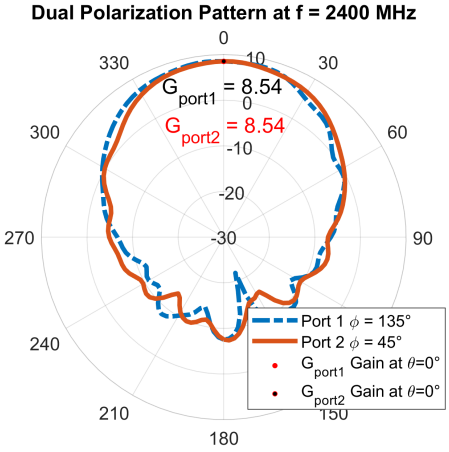

(b)

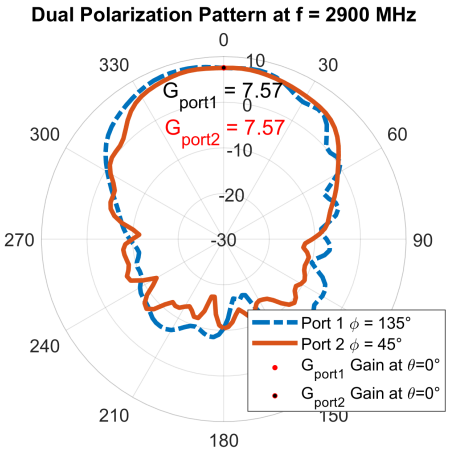

(c)

Figure 3.90: MB antenna dual polarization patterns at specific frequencies of (a) f = 1.9 GHz, (b) f = 2.4 GHz, (c) f = 2.9 GHz

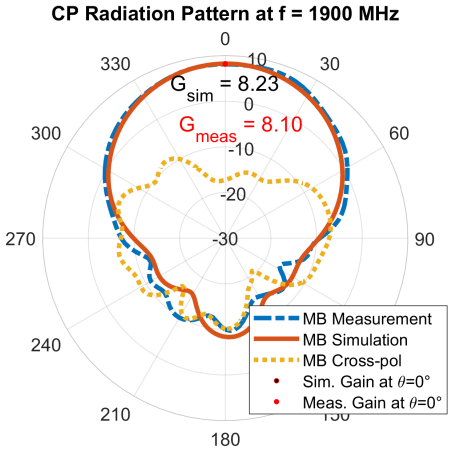

(a)

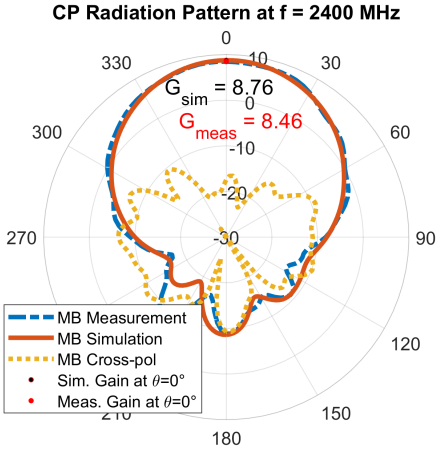

(b)

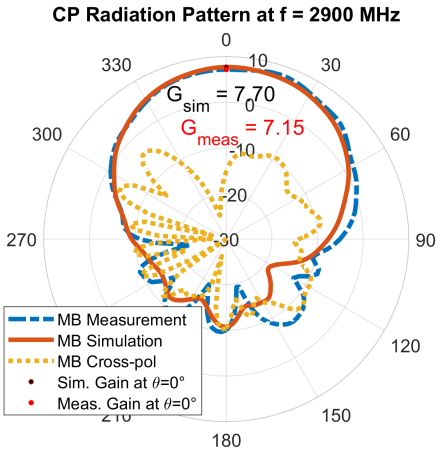

(c)

Figure 3.91: MB antenna RHCP patterns at specific frequencies of (a) f = 1.9 GHz, (b) f = 2.4 GHz, (c) f = 2.9 GHz

3.5 Low Band Antenna Design

The low-band antenna is designed after the design of both middle-band and high-band antennas. It is added to the dual-band shared aperture antenna configuration to observe the extendability of the shared aperture antenna concept to triband or more bands. LB antenna's bandwidth is selected between 1000-1600 MHz. This frequency bandwidth is chosen arbitrarily, but in this range, almost all of the global positioning system frequencies can be covered. It must also be EM transparent for both MB and HB antennas apart from being a cross-dipole antenna. Hence, at first, the LB antenna is formed from the EM transparent unit cell, which is designed in Chapter 2.5 similar to the middle band antenna design case.

3.5.1 Low Band Antenna Design Steps

Considering that the LB antenna and MB antenna shapes are almost identical without the dimensions, the LB antenna design steps are shown in Figures 3.92, 3.93 and 3.94 in five steps like MB antenna steps. Also, all design steps are the same as the MB design steps and have the same purpose.

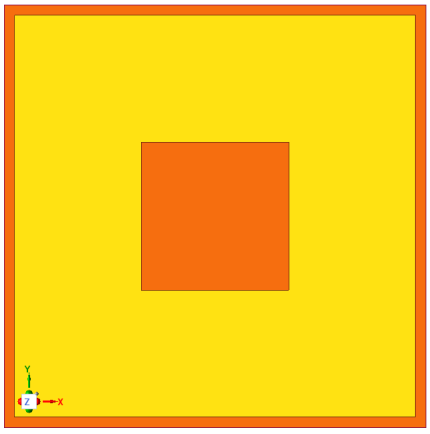

Figure 3.92: LB antenna design step 1

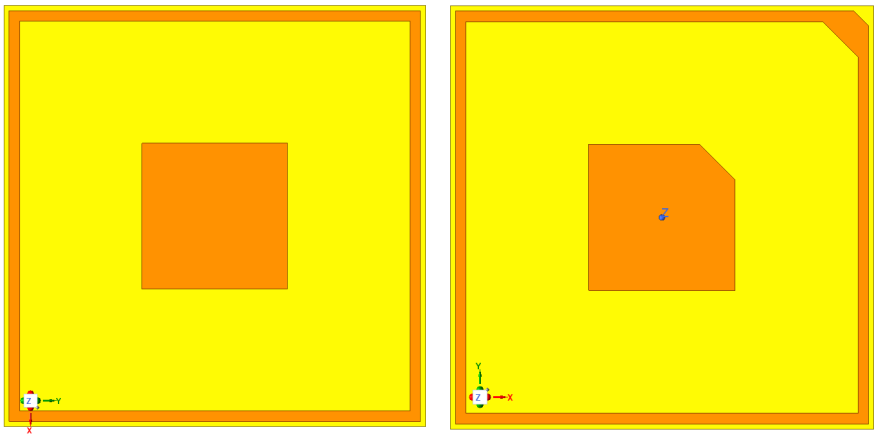

(a) (b)

Figure 3.93: LB antenna (a) design step 2, and (b) design step 3

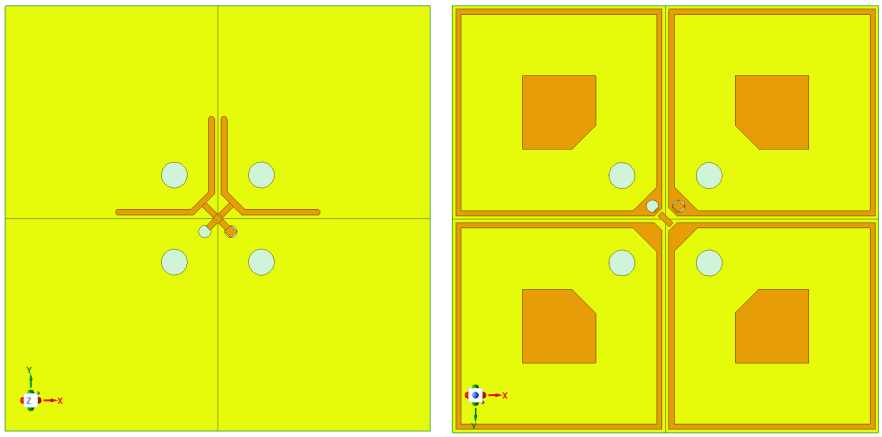

(a)

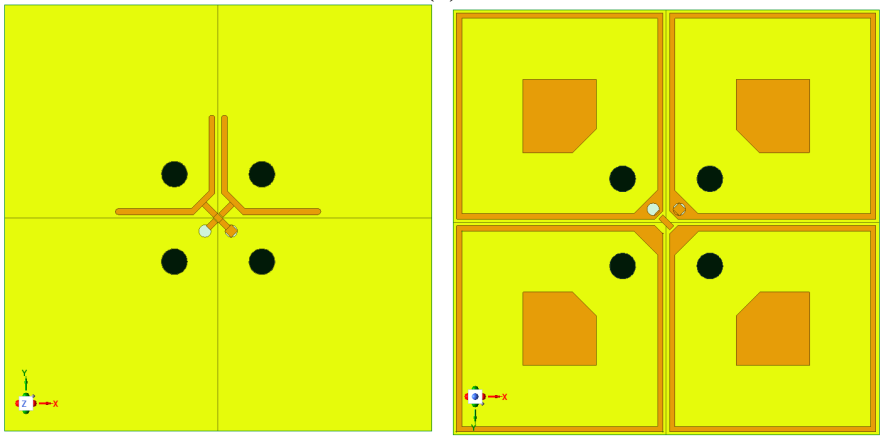

(b)

Figure 3.94: LB antenna (a) design step 4, and (b) design step 5

These design steps' EM transparency performance is given in Figure 3.95. Similar to the MB design case, transparency loss increases for the lower frequencies. But, different from the MB case, transparency loss decreases for the higher frequencies. It should also be noted that some transparency fluctuations start to occur within the transparency bandwidth after the design steps are applied.

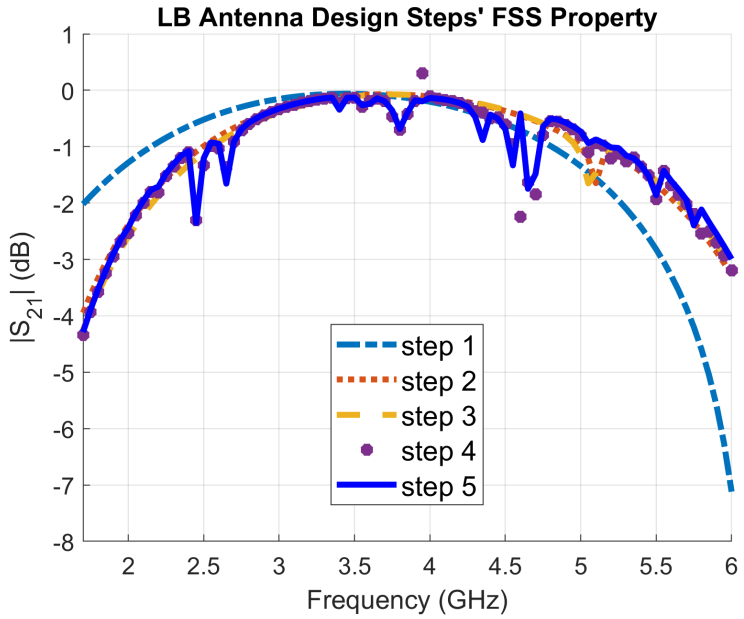

Figure 3.95: LB antenna design steps' FSS passband S_{21} graph

3.5.2 Low Band Antenna Design Parameters

Low band antenna design dimensions are given in Figures 3.96 and 3.97. Since the height h and spacer height h_spacer increases, the spacer diameter spa_dia is selected to be 5 mm rather than 3 mm to ensure the durability of the screw spacer. The optimum design parameters are given in Table 3.4. Similar to the MB antenna, the length DAL is calculated for the low band antenna dipole arm length by Equation 2.1, and then the transparent surface design is applied in Chapter 2.5.

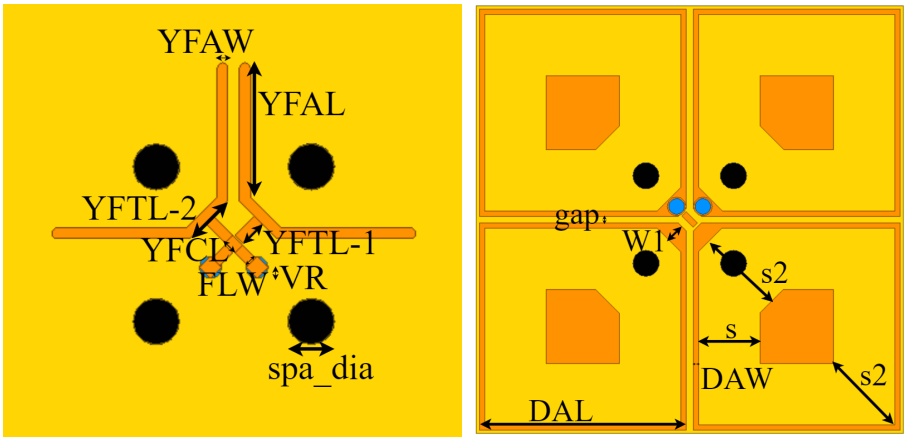

(a) (b)

Figure 3.96: LB antenna parameters on (a) top layer and (b) bottom layer

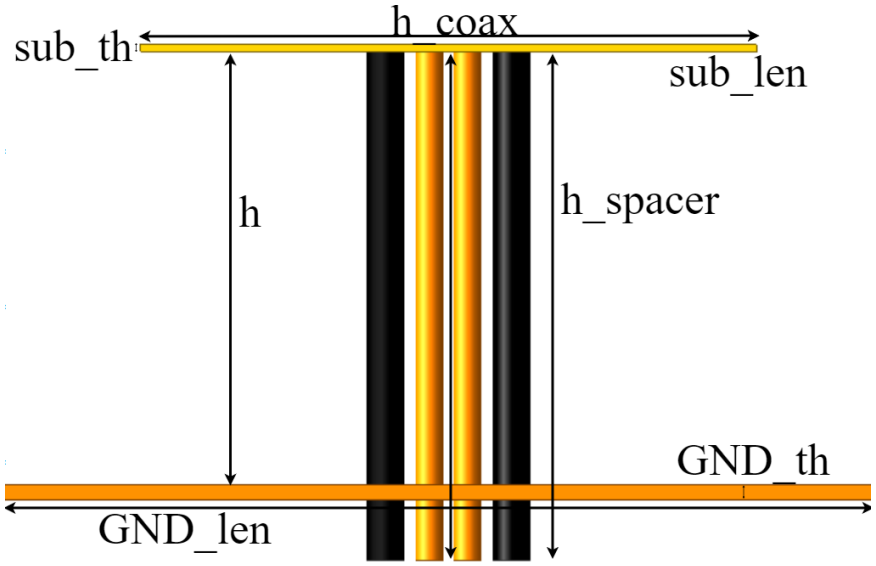

Figure 3.97: LB antenna parameters from side view

Table 3.4: LB Antenna Dimensions

LB Dimensions	Value (mm)	MB Dimensions	Value (mm)
sub_len	81.3	gap	1.3
YFAL	14.4	DAW	1
FLW	1.14	DAL	39.35
YFCL	1.5	sub_th	1
VR	1.2	s	11.68
YFAW	1.14	s2	16.51
YFTL-1	2.11	W1	3.54
YFTL-2	4.03	spa_dia	5
h	57	GND_len	250
h_spacer	67	h_coax	67
GND_th	2	t	0.043

3.5.3 Low Band Antenna Simulations

S-parameters of the simulated LB antenna are plotted in Figure 3.98. The bandwidth is 1-1.6 GHz, and isolation is better than 20 dB within this range. Furthermore, the radiation pattern simulation results are given in Figure 3.99 with frequencies of 1 GHz, 1.3 GHz, and 1.6 GHz. Single-port simulations are almost the same, and gain values are promising, as is the circular polarization case.

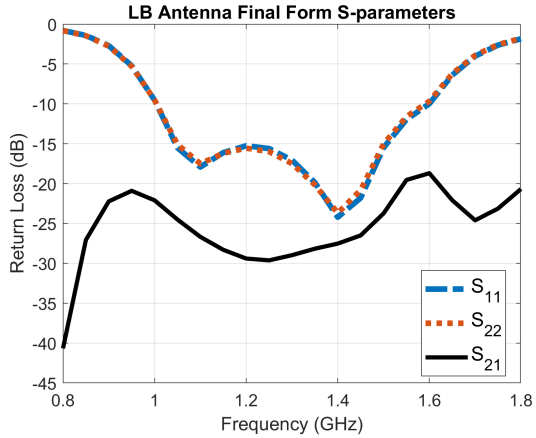

Figure 3.98: LB final form S-parameters

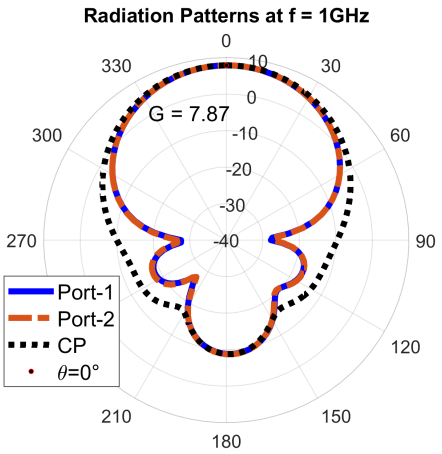

(a)

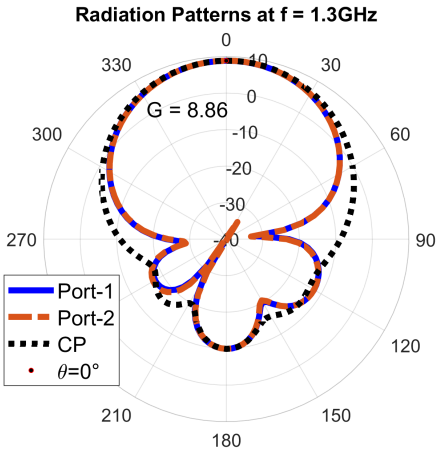

(b)

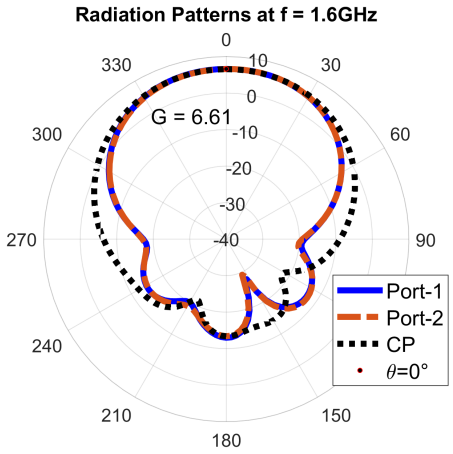

(c)

Figure 3.99: LB radiation patterns at specific frequencies of (a) f = 1 GHz, (b) f = 1.3 GHz, (c) f = 1.6 GHz

Similar to the MB antenna, the no-patch LB antenna is also tested in the simulation environment. Its shape is shown in Figure 3.100. The LB antenna S-parameters with patch and without patch are given in Figure 3.101. S-parameters are almost the same with minor differences. The dual polarization pattern comparison at 1.3 GHz is given in Figure 3.85. Patterns are almost identical, but the antenna with no patch has a higher gain compared to the antenna with the patch.

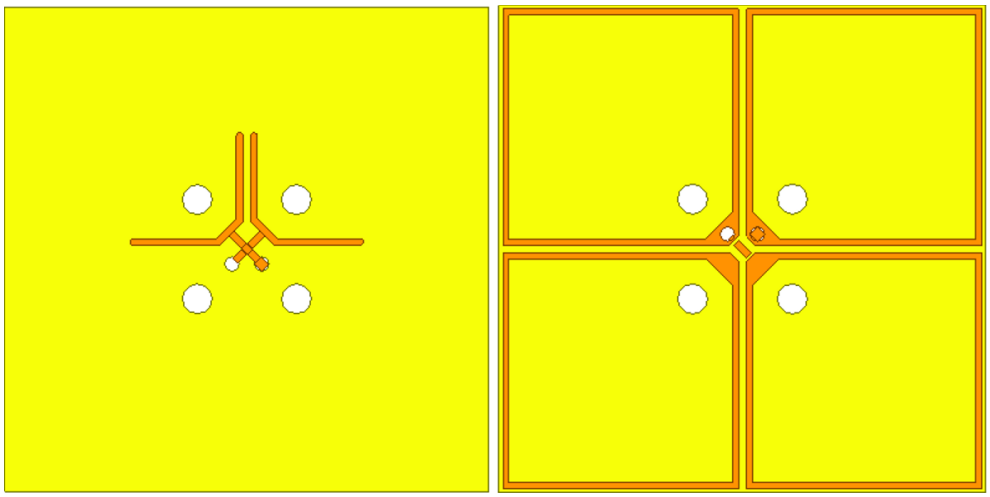

(a) (b)

Figure 3.100: LB antenna with no patch (a) top layer and (b) bottom layer

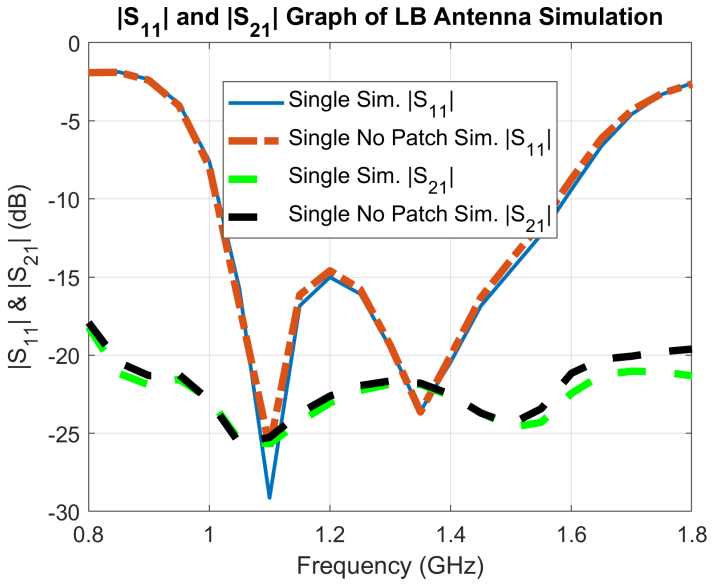

Figure 3.101: LB S-parameters with and without patch

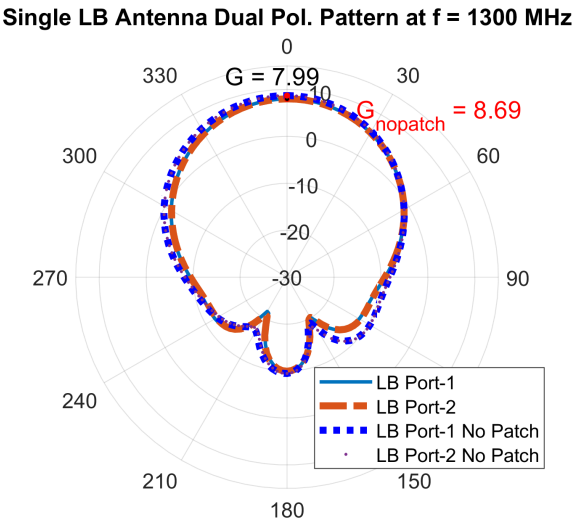

Figure 3.102: LB radiation pattern with and without patch

3.5.4 Low Band Antenna Measurements

LB antenna prototype is fabricated and can be seen in Figure 3.103 and 3.104. RF coax cable is "SUCOFORM-141" and has a length of 130 mm for the LB antenna since the LB antenna is planned to be placed on top of the MB and HB antennas. Similar to the MB antenna, spacers are close to the center to provide enough space for the other antennas.

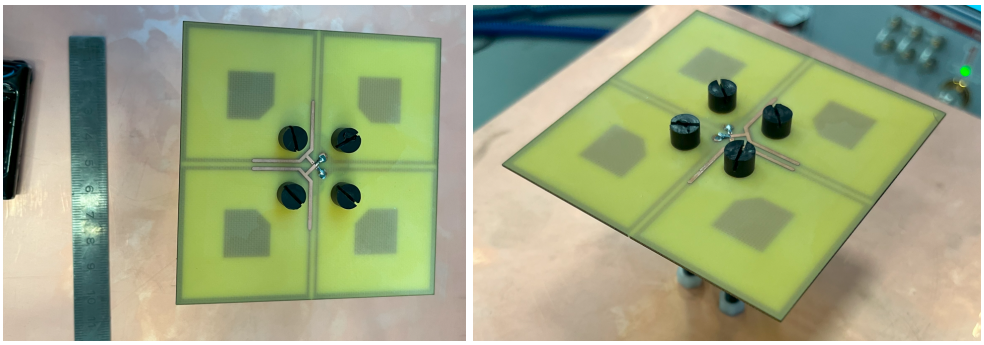

Figure 3.103: LB antenna prototype

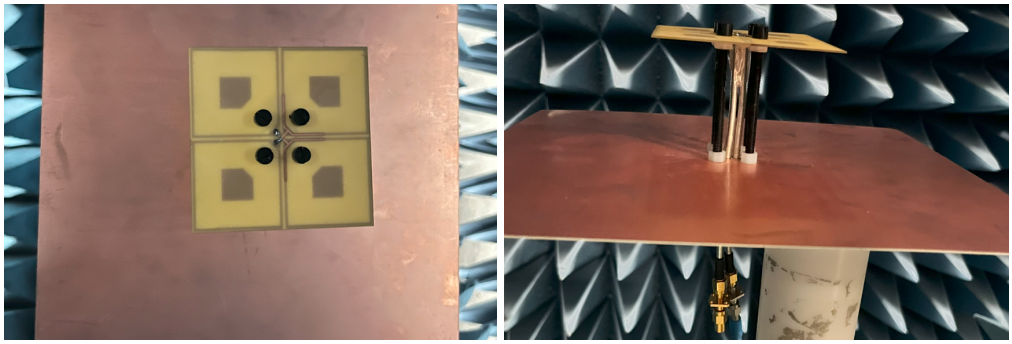

Figure 3.104: LB antenna inside of an anechoic chamber

S-parameters of both simulation and measurements are given in Figure 3.105. Low-frequency cutoffs of impedance bandwidth are the same, but measured high cutoffs are at larger frequencies; hence, measured results show that the antenna has a larger bandwidth than expected. Two resonance points can be seen for both results, but, isolation results are nonidentical. Measured results are much worse than the simulated results. The reason is that dipole arms are close to each other, so the Y-feedings are close; as a result, Y-feeding arms are close, and there would be a coupling between the two arms, which deteriorates the isolation. Increasing $YFTL - 1$ length and gap distance in Figure 3.96 would increase the isolation, but increasing them too much would affect the impedance match negatively. Also, these changes would affect the EM transparency of the LB antenna. Thus, a detailed optimization process of parameters is required.

Port-1 radiation pattern is given in Figure 3.106. Radiation pattern curves of measurements and simulations are aligned between $\theta = \pm 90^{\circ}$. Gain values are close for 1000 MHz and 1300 MHz, but the measured gain is higher for 1600 MHz within the bandwidth. Besides, both ports' radiation characteristics are almost identical for dual-polarized patterns shown in Figure 3.107. Similar to the port-1 results, CP results of measurements and simulations are mostly aligned in Figure 3.108. Cross-polarization is at least 12 dB lower than the co-polar radiation pattern in the broadside direction.

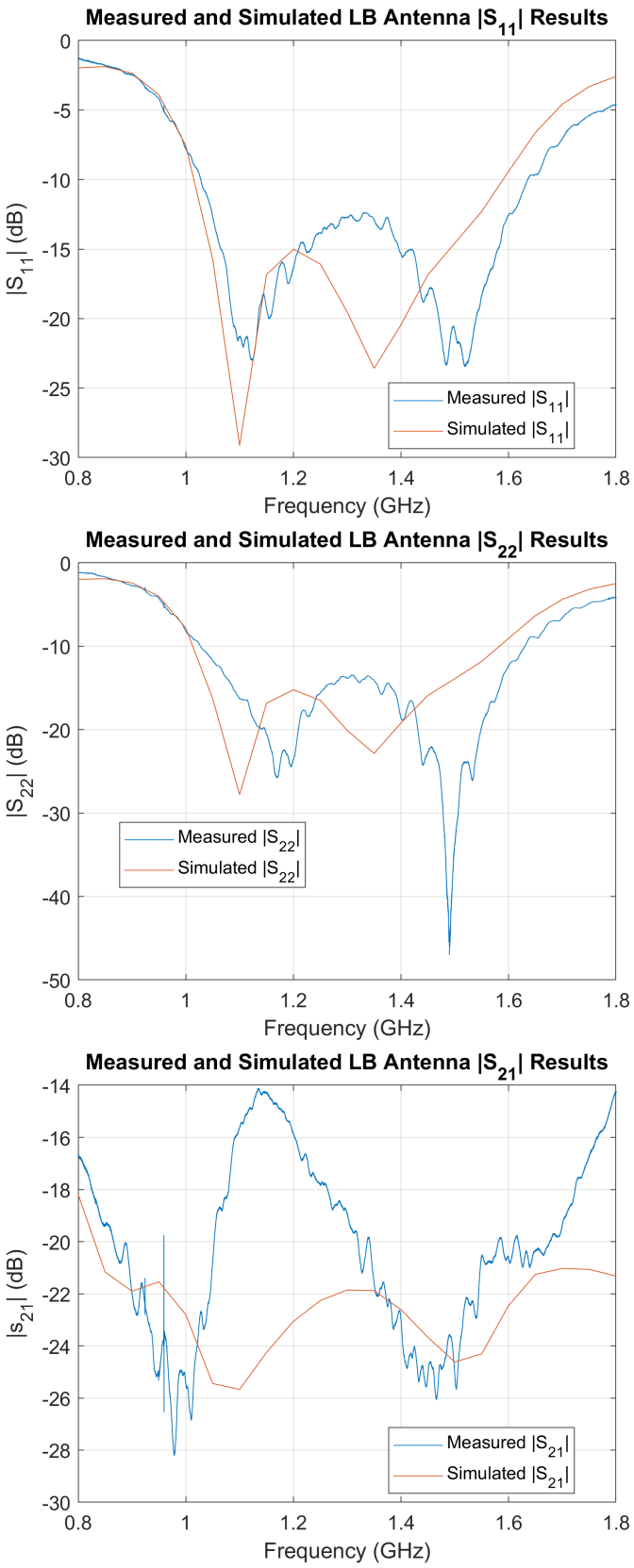

Figure 3.105: LB antenna prototype S-parameters vs. simulation

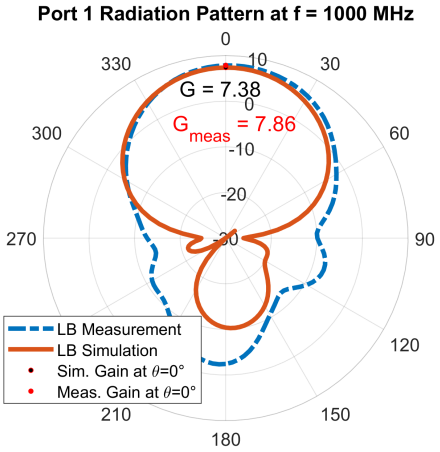

(a)

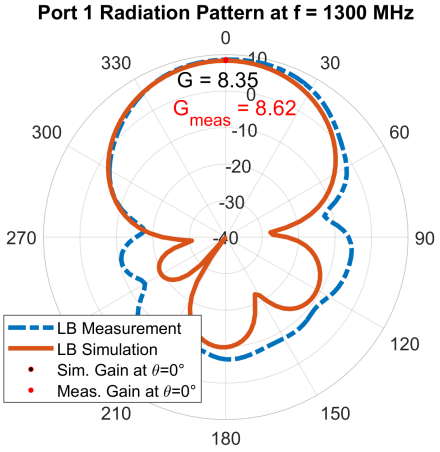

(b)

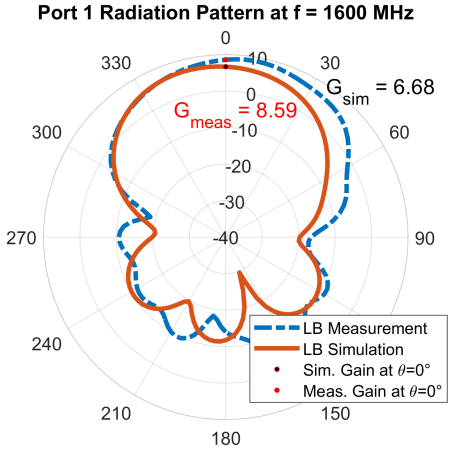

(c)

Figure 3.106: LB port 1 radiation patterns at specific frequencies of (a) f = 1 GHz, (b) f = 1.3 GHz, (c) f = 1.6 GHz

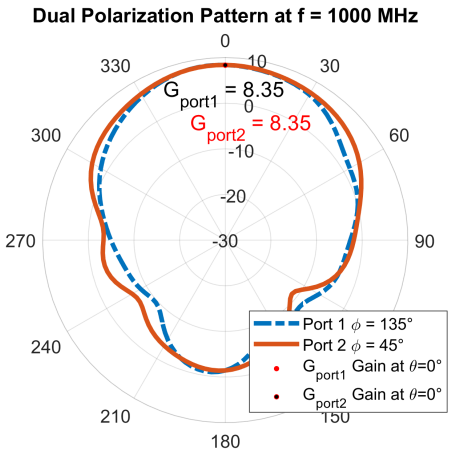

(a)

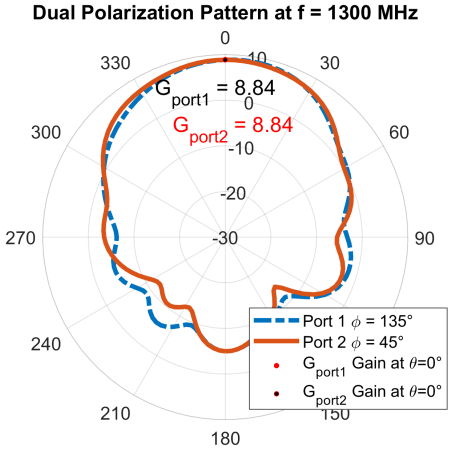

(b)

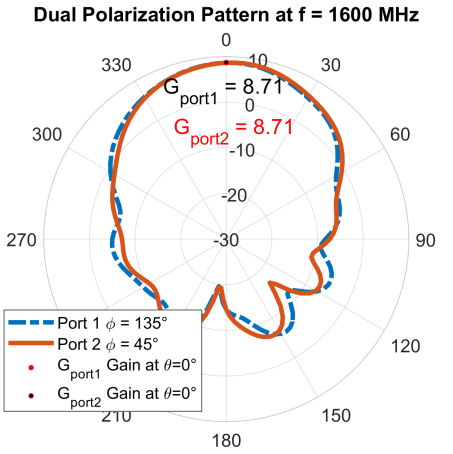

(c)

Figure 3.107: LB antenna dual polarization patterns at specific frequencies of (a) f = 1 GHz, (b) f = 1.3 GHz, (c) f = 1.6 GHz

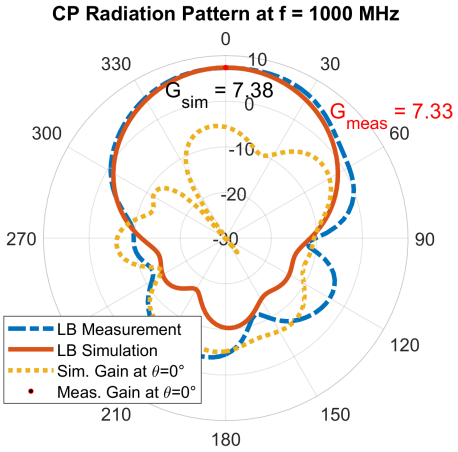

(a)

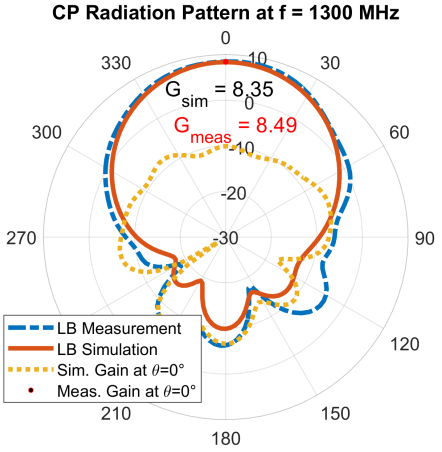

(b)

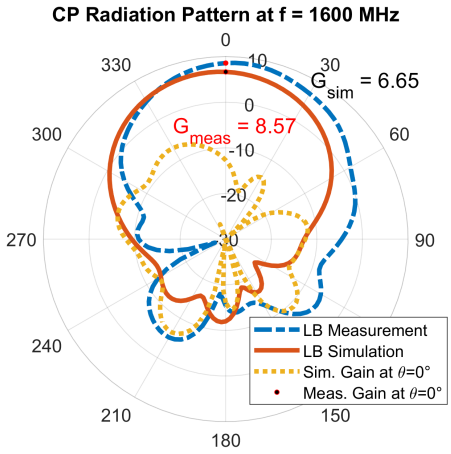

(c)

Figure 3.108: LB antenna RHCP patterns at specific frequencies of (a) f = 1 GHz, (b) f = 1.3 GHz, (c) f = 1.6 GHz

3.5.5 Chapter Conclusion

In this chapter, three different cross-dipole antennas for three different bands are designed. Antennas' different polarization capabilities are shown for different feeding cases. The reason behind the degradation is explained. Improvements in isolation and bandwidth are explained with design steps and design parameters. Radiation patterns for different polarizations are mentioned. Antenna designs with patch and without patch comparisons are made with the simulation environment results. Then, simulated antennas are fabricated and tested via a vector network analyzer and antenna measurement laboratory. Impedance bandwidths can be said to be similar with small differences, but isolations of HB and LB antennas are worse than expected. The reasons might be imperfect measurement and fabrication conditions; also, having closer feedings can cause coupling between two feedings. Simulated and measured radiation patterns are similar in general with the gain values. Dual-polarization and circular polarization results are promising for various applications.

CHAPTER 4

SHARED APERTURE TRIBAND ANTENNA DESIGN

4.1 Introduction

In the shared aperture design, different antennas share the same radiation area. These different antennas can be either single or can form an array. The main purpose is to have more antennas in a smaller area, which increases space reuse efficiency. Since antennas are placed much closer to each other, the crucial concern about shared aperture antennas is whether antennas can operate without distortion due to coupling or not. To ensure minimum coupling and distortion, induced currents on the antenna must be eliminated. As long as the couplings and deteriorations are prevented, dual-band, triband, or multiband antennas can be designed and used in shared aperture form. Some example designs and isolation methods will be explained in this section.

As mentioned, the main problem with the shared aperture systems is the interference between different bands, or namely cross-band coupling. Different solutions are found and applied to provide isolation, as aforementioned in Chapter 1. In [36], antennas that are operating in 0.82-0.96 GHz and 3.4-3.6 GHz form a dual-band shared-aperture antenna system. In order to provide isolation and eliminate induced high-band antenna current on the low-band antenna, inductances are defined on the low-band antenna. The designed antenna is shown in Figure 4.1. The blue antenna is the low-band antenna on the top, and the orange antenna is the high-band antenna at the bottom. The little red dots indicate the added inductances. The couple ring in the middle of the low band antenna is used to improve the impedance matching of the antenna.

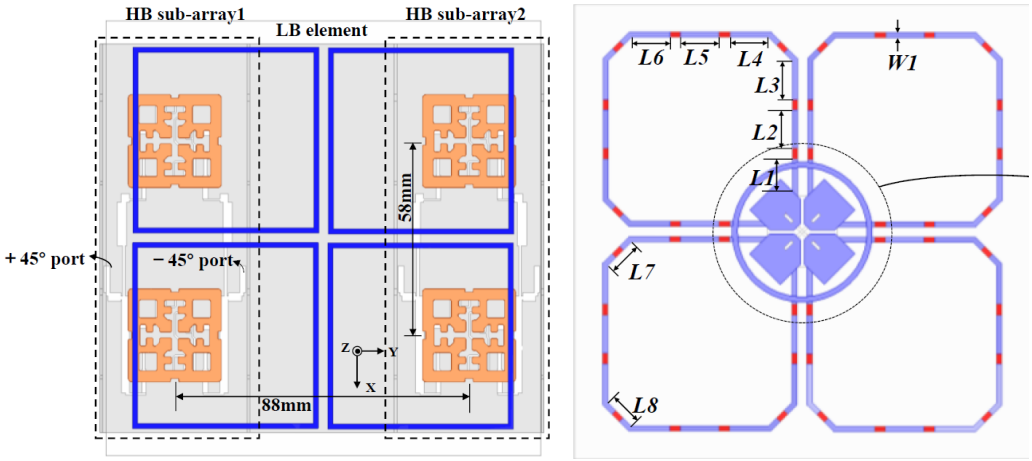

(a) (b)

Figure 4.1: (a) Designed shared aperture antenna system from top view and (b) top view low-band antenna

Another shared aperture antenna design is given in [34]. Low band antenna, shown in green color, has U-shaped and rectangular-shaped slots to redirect and eliminate the induced high-band antenna, shown in orange color, current on the low-band antenna in Figure 4.2. Antenna bandwidths are 1.71-2.69 GHz and 3.4-3.8 GHz.

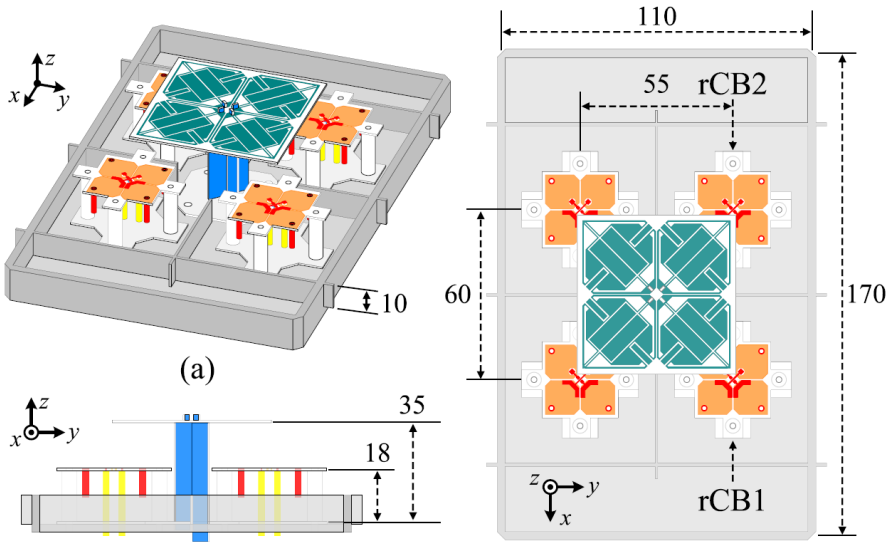

Figure 4.2: Designed multiband antenna system 2

In [11], a triple-band shared-aperture antenna system is designed. The low-band antenna is placed at the lowest point; then an FSS is placed. The high-band antenna

array comes next, and the middle-band antenna array is at the highest level. Shared aperture antennas and the design methodology is given in Figure 4.3. FSS acts as a passband filter for low-band antennas, while it acts as a stopband filter for both middle-band and high-band antennas. Middle-band antennas also have the EM transparent property for the high-band antenna array. Thus, all three different antenna types can radiate to broadside direction.

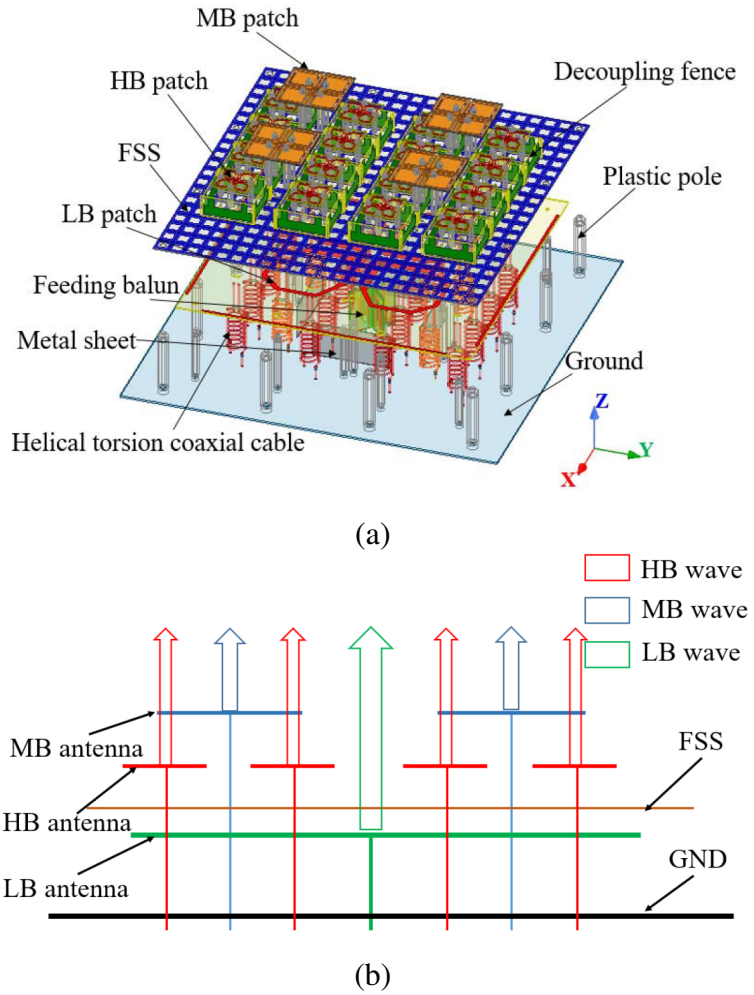

Figure 4.3: (a) Designed multiband antenna system 3 and (b) design methodology

It can be seen that shared aperture antennas can use different techniques to reduce cross-band coupling. In this chapter, a three-band shared aperture antenna system is designed, fabricated, and measured. This design is more similar to [11], but the difference is that the low-band antenna is on the top of the system with EM transparent property, so there is no FSS layer.

4.2 Triple Band Shared Aperture Antenna System Design

After the simulation and prototype measurements of the three different band antennas, a shared aperture antenna formation is set for these antennas in their vicinity. There is one LB antenna in the middle and at the highest level, and there are two MB antennas below the LB antenna with a distance of 76 mm between each other on the y-axis. Finally, there are four HB antennas on either side of the two MB antennas or the four corners of the LB antennas with a distance of 80 mm on the x-axis. All antennas are fixed to the 250 mm square GND plane with the same direction, shown in Figure 4.4. So, MB antennas form 2×1 array, and HB antennas form 2×2 array. The substrate with yellow color is the LB antenna, the gray colored substrate is the MB antenna, and the green colored substrate is the HB antenna. To reduce the overall size of the antenna, antenna spacers of the MB and LB antenna spacers are placed near the center, and this placement does not affect the radiation and EM transparency performance. Considering the substrates' transparency and antenna properties, the antenna system's basic block scheme is given in Figure 4.5. Even though the MB antenna does not have LB transparency, LB performance does not degrade significantly.

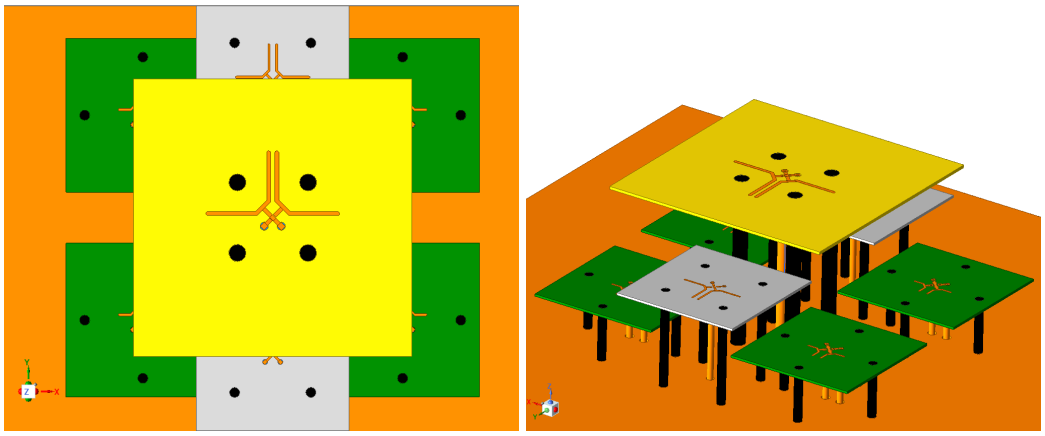

(a) (b)

Figure 4.4: (a) Designed multiband antenna system from top view and (b) isometric view

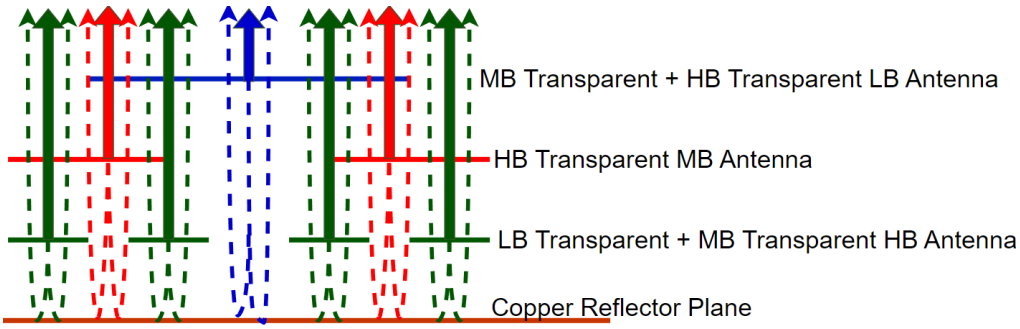

Figure 4.5: Block scheme of the multiband antenna radiation

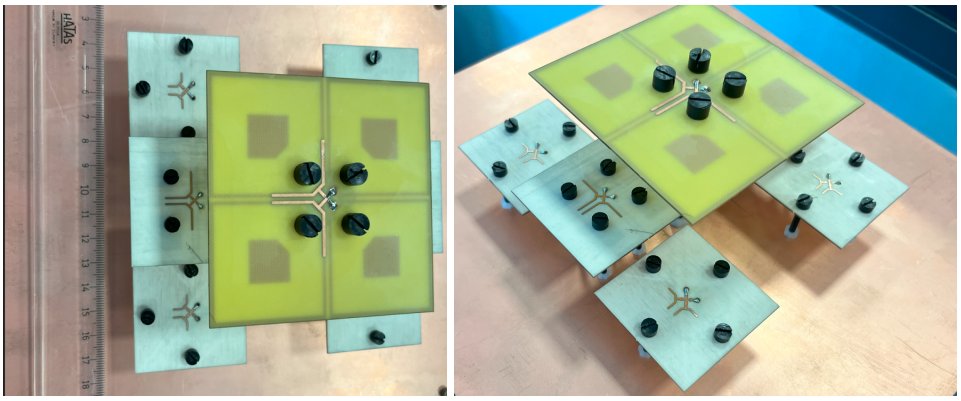

(a)

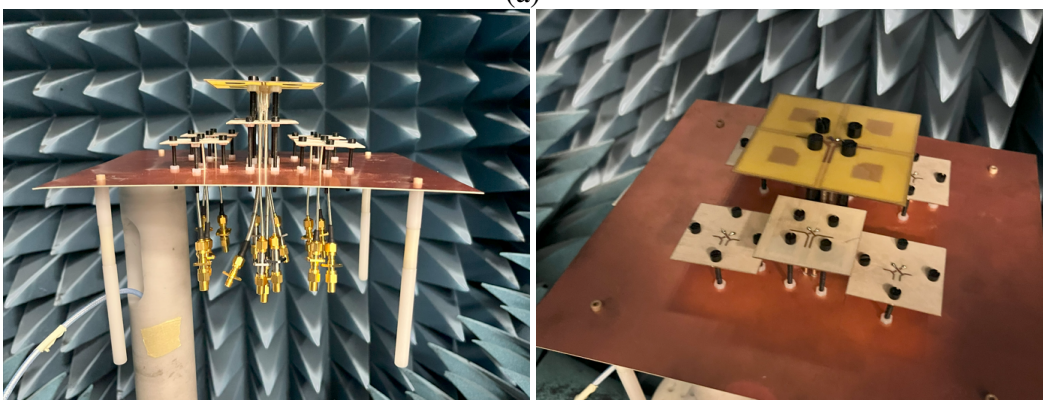

(b)

Figure 4.6: (a) Multiband antenna prototype and (b) multiband antenna inside of an anechoic chamber

Figure 4.6 displays the prototype integration of the shared aperture triband antenna system. While measuring the S-parameters and the radiation patterns, all the other ports are terminated with SMA 50Ω matched loads. Since the antenna pattern measurement system ™Satimo has only one input port, antenna measurements are post-processed to obtain MB & HB array antenna and LB antenna results. Antenna analysis is made separately for both simulation and prototype measurements. Then, the measurements are compared to each other to see the antenna performance and compatibility of both simulations and measurements.

4.3 Multiband Antenna S-Parameters

To see the difference between the results of antennas alone and in a multiband shared aperture form, firstly the S-parameters are compared. The LB antenna's S-parameter comparison for the cases of single antenna and multiband measurements with the simulated and measured results in Figure 4.7. In the figure 4.7 (a), simulations show that LB antenna bandwidth is lower in the multiband form. However, measurements show that multiband LB antenna bandwidth is a little larger than the single form. But it is harder to see the two resonances for the multiband case. Isolation simulation is better than 20 dB for the single antenna, but the measurement result is worse, as mentioned in Chapter 3.5.4. Isolation simulation in multiband form is expected better than 15 dB in the LB bandwidth, but the measurement result is similar to the single case result. There is also a peak point around 1.7 GHz. This frequency is very close to the end of the LB antenna bandwidth and the beginning of the MB antenna bandwidth, which can result in a coupling between LB and MB antenna ports, so isolation can be reduced between the same antenna ports.

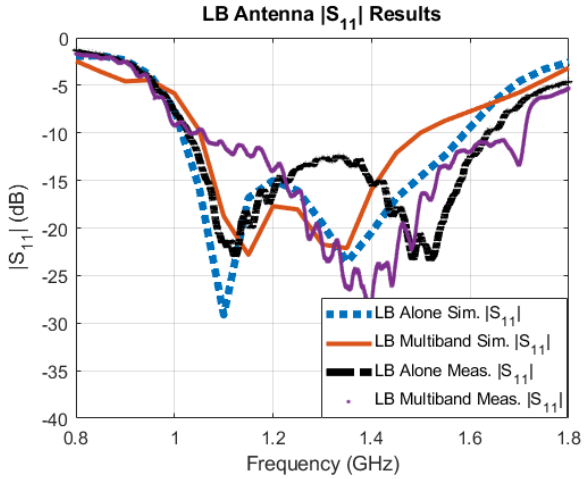

(a)

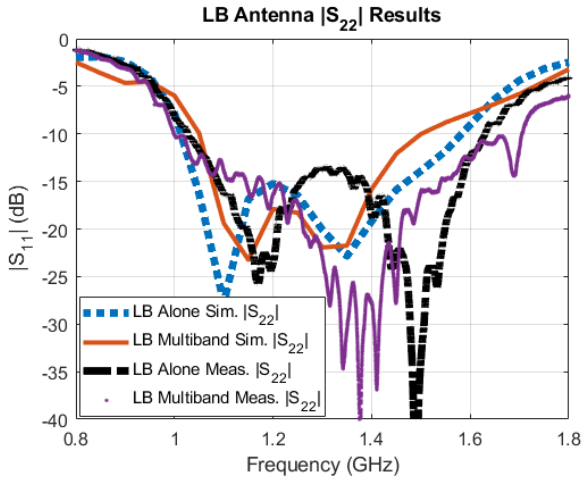

(b)

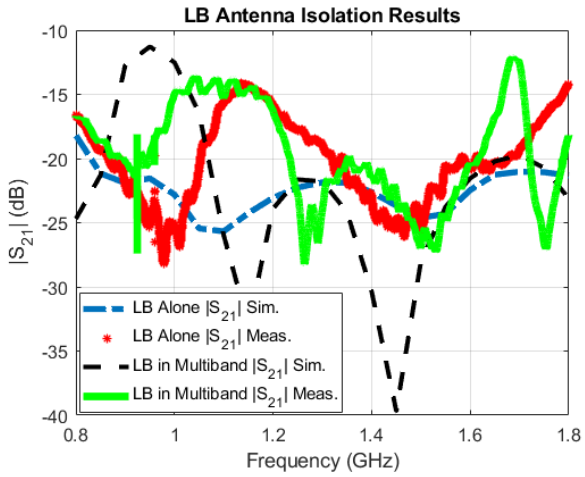

(c)

Figure 4.7: (a, b) LB antenna simulated and measured reflection losses and (c) isolation of ports

Figure 4.8 shows the MB antenna results. Multiband reflection loss simulation shows that both S_{11} and S_{22} become bigger than -10 dB around 2.25GHz, but they are on the border of -10 dB in the measurement results. Also, the isolation is around 10 dB around the same frequency, but measurement result shows that isolation is at least around 15 dB within the MB bandwidth. Similarly, Figure 4.9 shows the HB antenna results. Reflection losses are very similar for the single and multiband HB antenna. But reflection losses are different for the ports in the multiband measurements in terms of bandwidth and S-parameters. Isolation between the ports is better than 20 dB for the multiband isolation measurements.

Triband shared-aperture antenna simulations are also made with no-patch designs. The reflection loss simulation graph for the LB antenna is given in Figure 4.10. Multiband reflection losses are almost identical to each other and their bandwidth is narrower similar to the Figure 4.7 (a). Then the simulation plot for the MB antenna is displayed in Figure 4.11. Patch and without patch results are very close, with the error in 2.2 GHz like the Figure 4.8 (a). Finally, the simulation result for the HB antenna is shown in Figure 4.12. Discrepancies are higher for the HB antenna reflection losses but the results are similar.

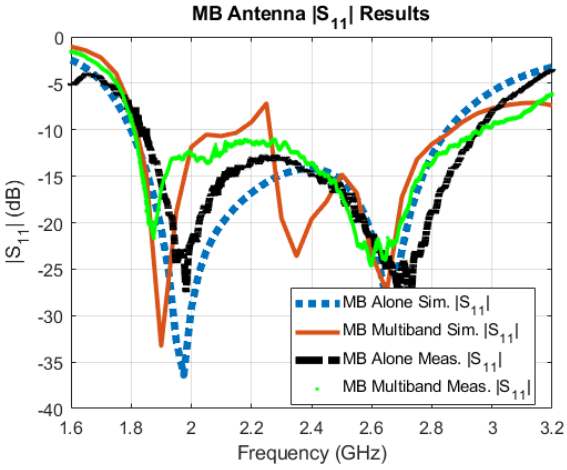

(a)

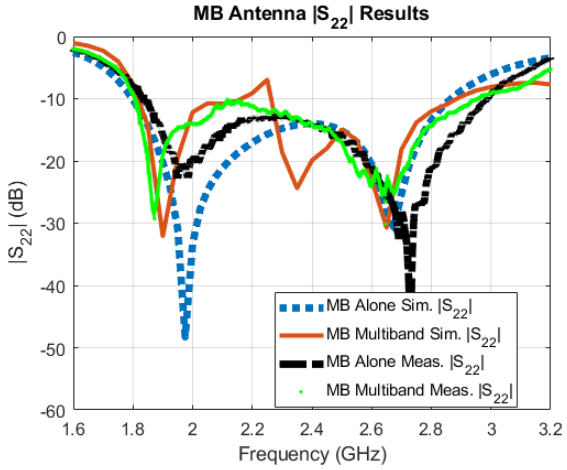

(b)

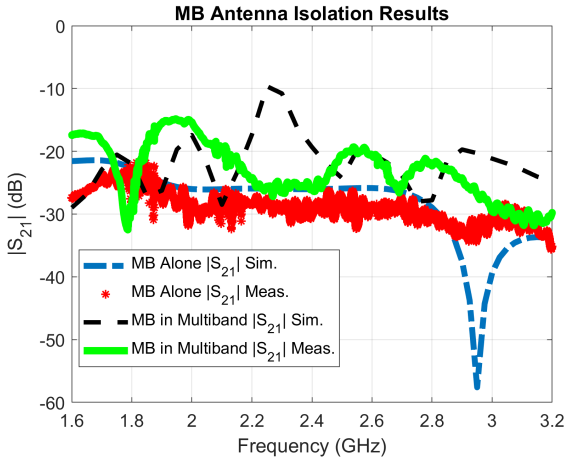

(c)

Figure 4.8: (a, b) MB antenna simulated and measured reflection losses and (c) isolation of ports

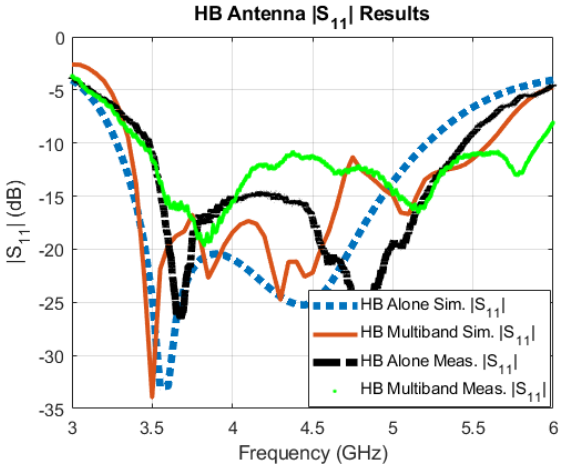

(a)

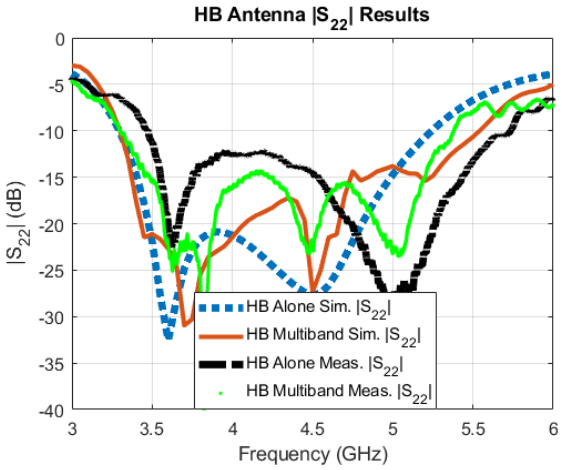

(b)

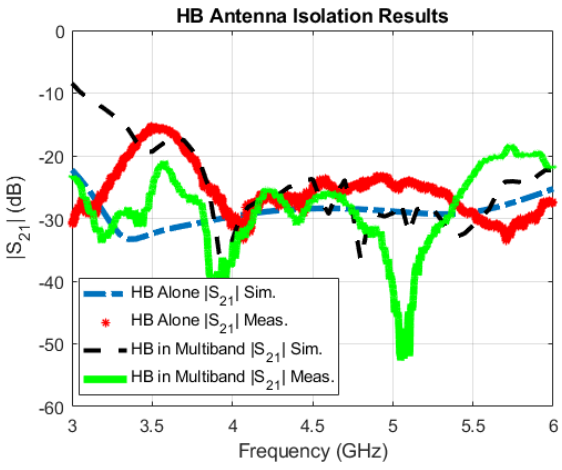

(c)

Figure 4.9: (a, b) HB antenna simulated and measured reflection losses and (c) isolation of ports

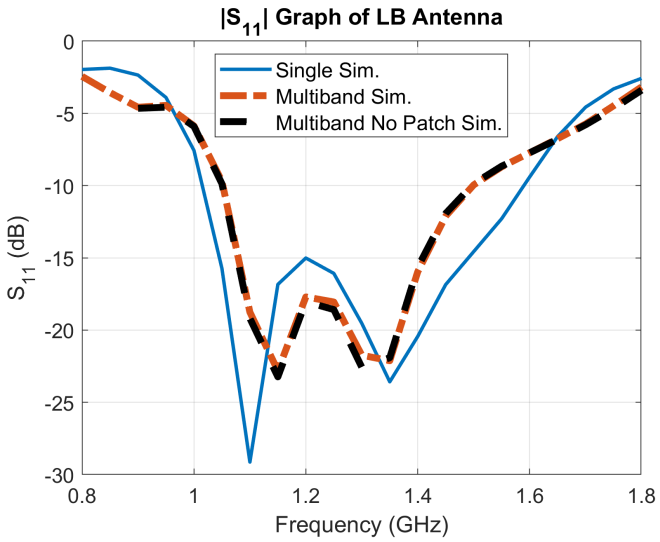

Figure 4.10: LB antenna reflection loss with and without a patch in the multiband

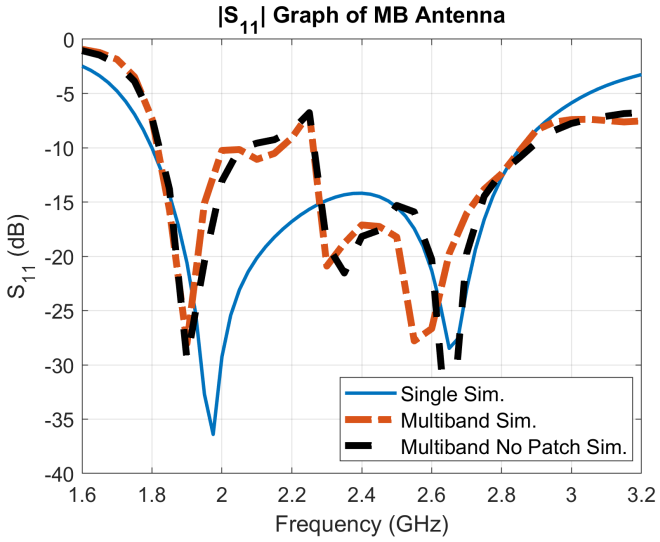

Figure 4.11: MB antenna reflection loss with and without a patch in the multiband

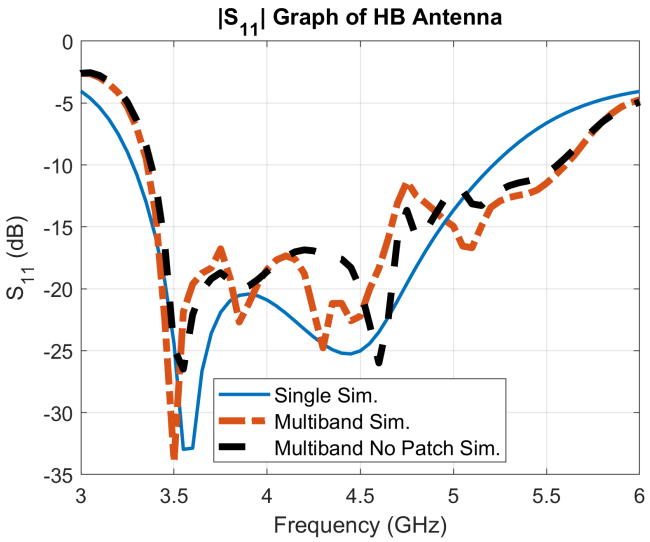

Figure 4.12: HB antenna reflection loss with and without a patch in the multiband

Cross-polarization is also important for the multiband antennas because they are very close in the shared aperture form, hence they can cause coupling easily. Figure 4.13 displays the worst-case isolation cases between the different band antennas. The top and middle plots are similar. The peak around 1.8 GHz is the cutoff frequency for both the LB and MB antenna. At that point, both antennas are close to impedance match and radiation, which can lead to coupling between each other, hence decreasing in isolation. Similar to the LB and MB case, the plot at the bottom isolation decreases around 3.1 GHz because this frequency is very close to the cutoffs of MB and HB antennas. The cross-polarization isolations except these plots have at least 16 dB of isolation between the antennas.

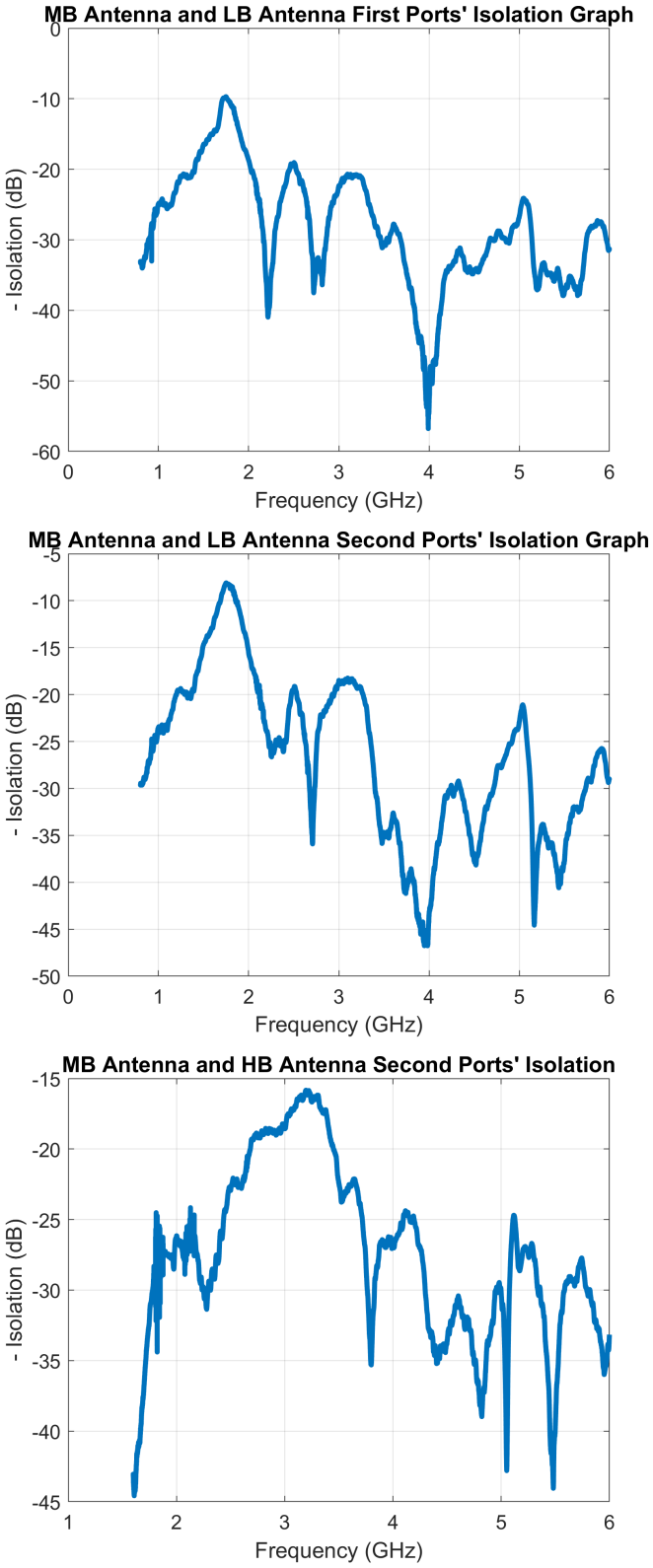

Figure 4.13: Worst case cross-polarization curves

4.4 Multiband Antenna Radiation Patterns

In the next step, the radiation patterns of the antennas for the single case and in a multiband form in the antennas' center frequencies. The radiation pattern comparison of the single antenna and multiband antenna of the LB antenna is given in Figure 4.14. Red dashed line curves show the multiband case simulations and measurements. First port simulations are similar for the broadside direction, and CP radiation characteristics are almost the same. MB antenna patterns are given in Figure 4.15. The peak gain of the MB antenna at port-1 is shifted towards around θ=-15° in spherical coordinates with respect to the z-axis in cartesian coordinates, due to its location shift. The gain difference is more obvious for the simulation case, and it is less obvious for the measured case. These angle shifts are also valid for CP, but these shifts are corrected with the array solution. HB antenna's patterns are displayed in Figure 4.16. From these measurements, it can be said that EM transparency surfaces affect the antenna performance minimally in the multiband form, with a loss between 1 and 2 dB at most for the broadside direction.

MB and HB antennas form an array structure in the multiband antenna system. Since the ™Satimo measurement setup has only one port measuring capability, the antenna array theory calculations are made to see the overall pattern characteristics of these antennas. From the measured electric fields and array pattern formula, antenna array characteristics can be extracted from single port measurements. Antenna array calculations are given in the Appendix D.

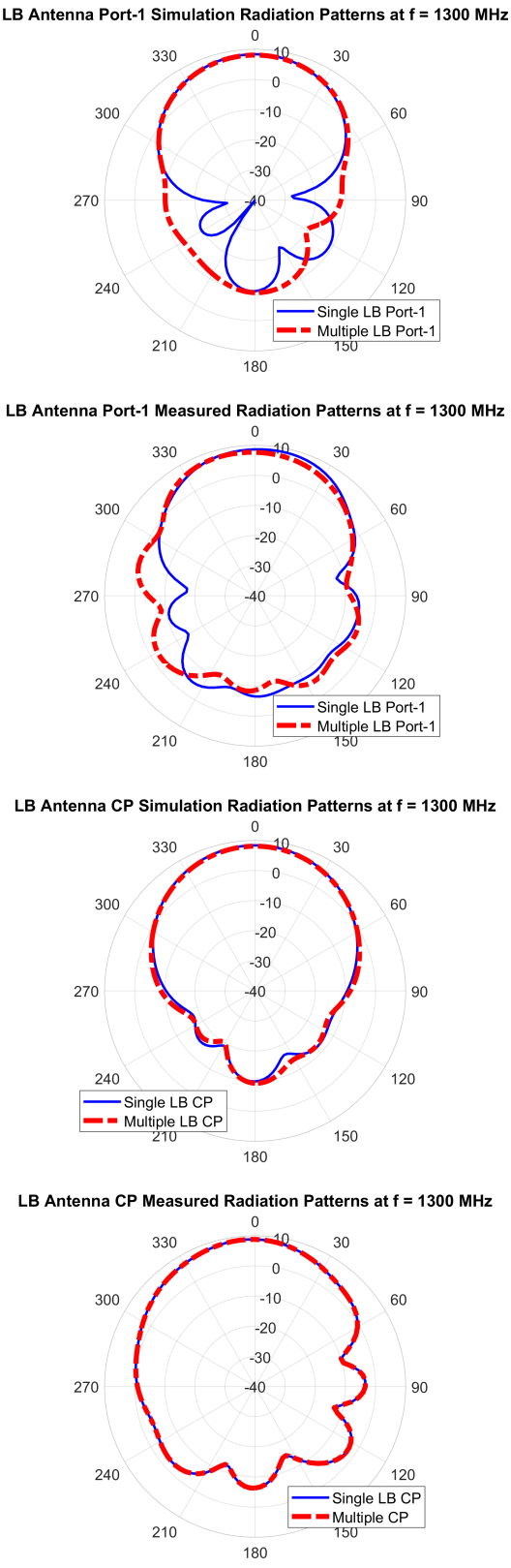

Figure 4.14: LB patterns for single and multiband simulations & measurements

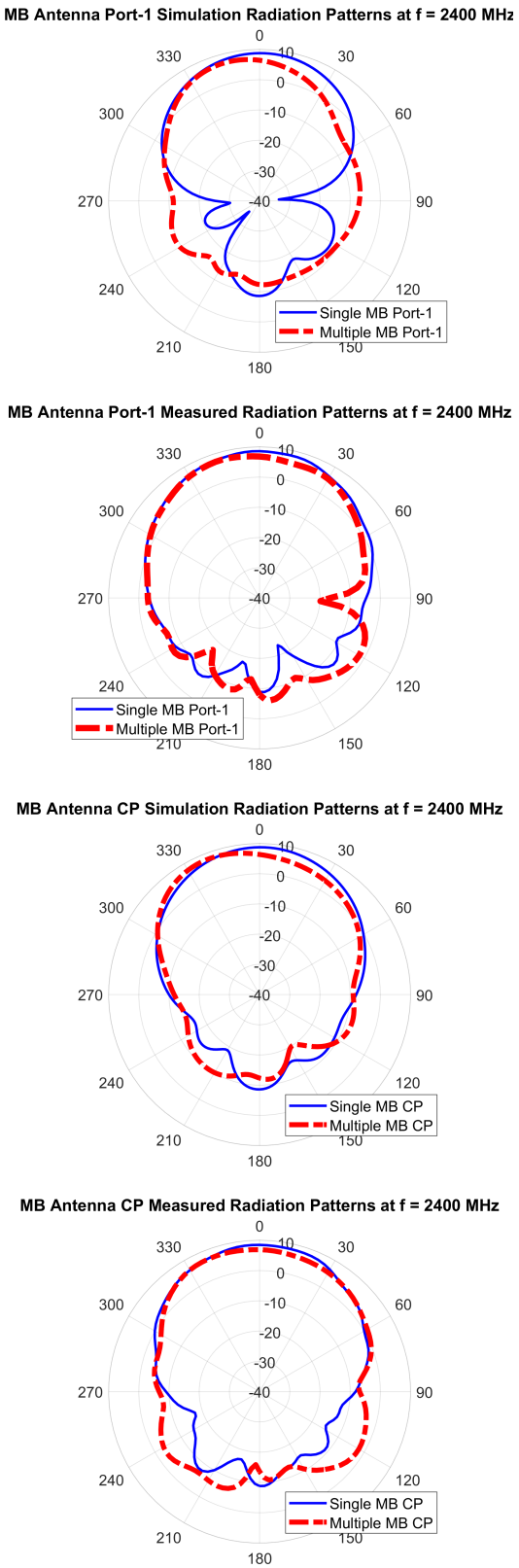

Figure 4.15: MB patterns for single and multiband simulations & measurements

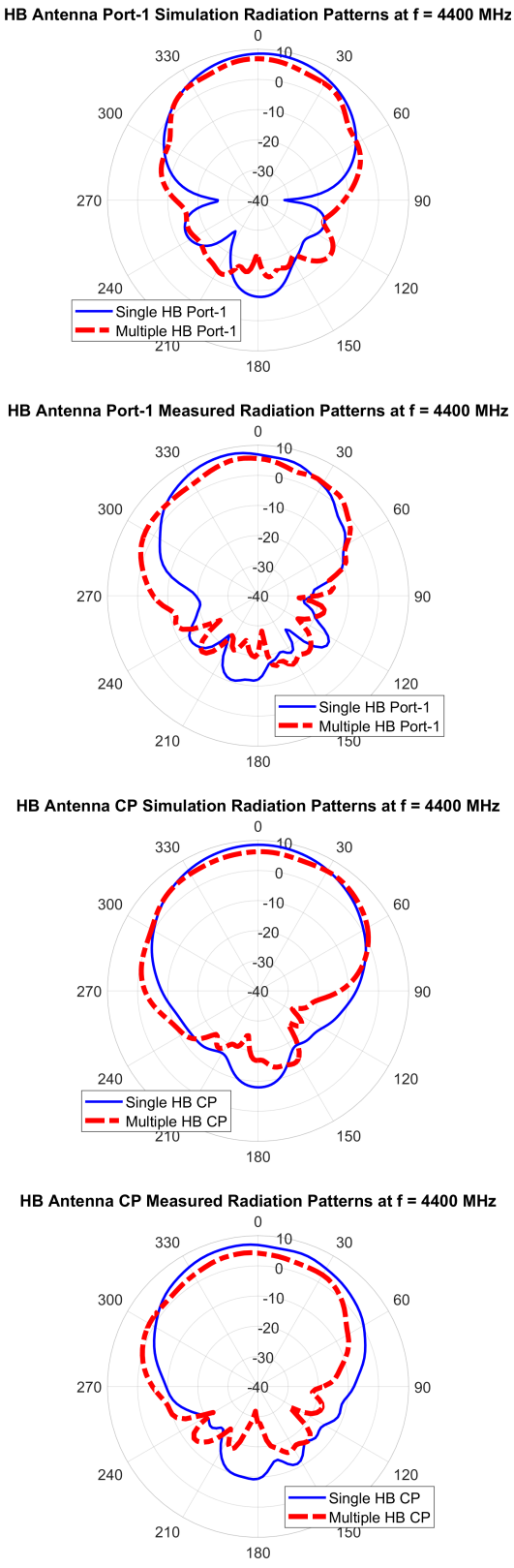

Figure 4.16: HB patterns for single and multiband simulations & measurements

Antenna radiation patterns in the multiband form are both simulated and measured. And their comparisons for specific frequencies are displayed. In Figure 4.17, the LB antenna's port-1 patterns are shown. Except f = 1 GHz, pattern characteristics are close to each other for both simulation and measurement. In the simulation case, the bandwidth is narrower than the measured bandwidth, and 1 GHz is close to the low cutoff frequency. The measurement result shows the expected antenna pattern with a desired gain value. This gain value difference can also be seen for the 1.6 GHz, which is the high cutoff frequency. Dual-polarization results are plotted in Figure 4.18. Both ports' patterns are very close to each other. Gains are improved with dual polarization, except for the 1.3 GHz. CP plots are given in Figure 4.19. CP simulation results are similar to the port-1 results for the simulation and measurement cases.

MB antenna array port-1 results are given in Figure 4.20. Due to the array of two elements, antenna gain is increased. Both simulation and measurement results are aligned with close gain values. Result alignments are also valid for the dual-polarized pattern in Figure 4.21, and the CP pattern in Figure 4.22. In all three figures, the gain value is lower for 2.9 GHz, which is the high cutoff frequency.

HB antenna array results are given in Figures 4.23, 4.24, 4.25, 4.26, 4.27, and 4.28. Gain values are higher than LB and MB antennas due to the four HB antenna elements. Simulation and measurement curves are similar in general. As frequency increases, side lobes become more visible with higher gains. This is expected since the ratio of antenna element distance to the kd/2 becomes higher with the frequency increase.

Apart from that, antennas with and without a patch case are compared in the triband shared-aperture form. All three antennas' results are given in Figure 4.29. LB antenna patterns can said to be identical with a minimal gain loss. MB antenna patterns are also very similar with a gain loss of 0.27 dBi. But the HB antenna pattern changes with the no patch cases of the LB and MB antennas. Gain decreases by 1.42 dBi and side lobes become stronger, especially at $\theta = \pm 60^{\circ}$. Thus, having a patch is more handy for the HB antenna array.

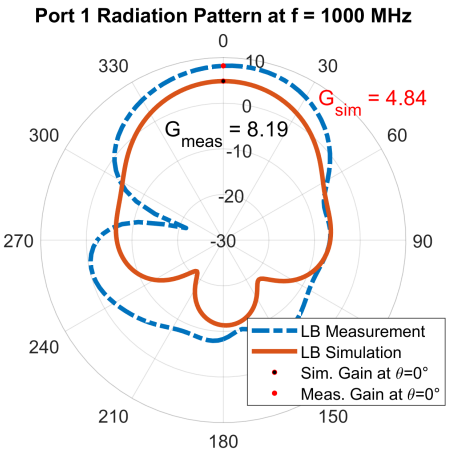

(a)

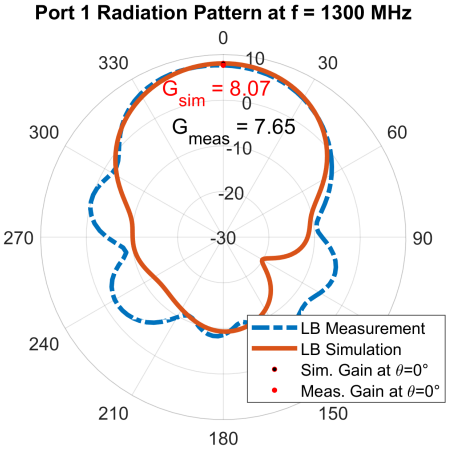

(b)

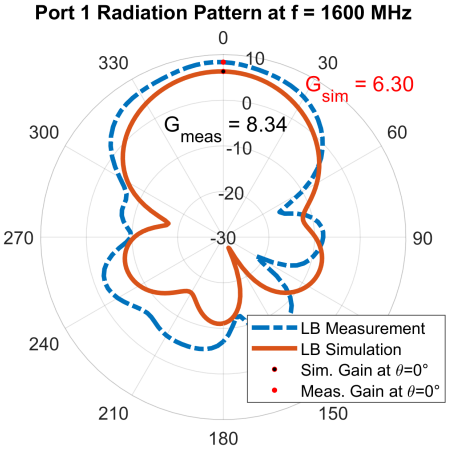

(c)

Figure 4.17: LB antenna port 1 radiation patterns at specific frequencies of (a) f = 1 GHz, (b) f = 1.3 GHz, (c) f = 1.6 GHz in multiband antenna

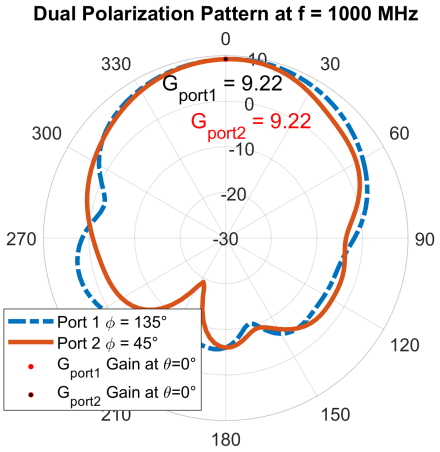

(a)

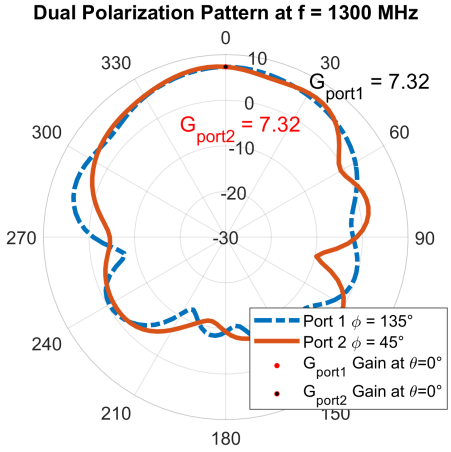

(b)

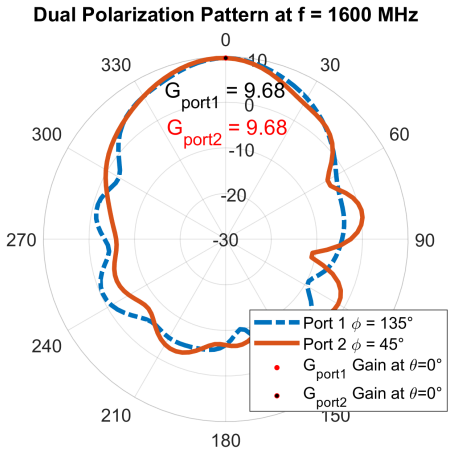

(c)

Figure 4.18: LB antenna dual polarized radiation patterns at specific frequencies of (a) f = 1 GHz, (b) f = 1.3 GHz, (c) f = 1.6 GHz in multiband antenna

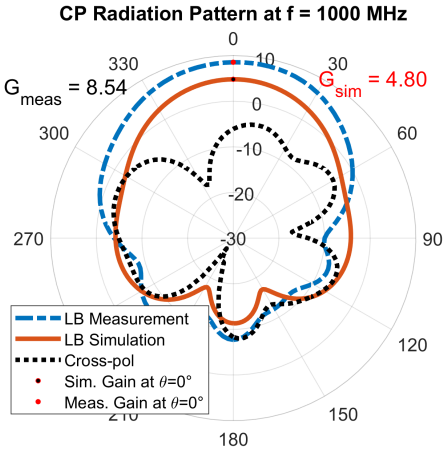

(a)

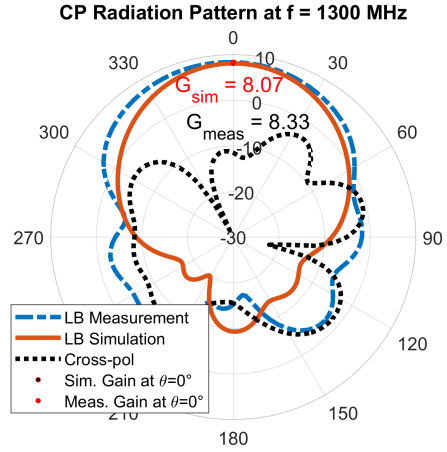

(b)

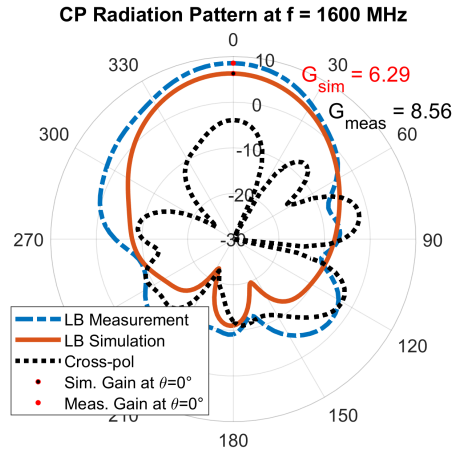

(c)

Figure 4.19: LB antenna RHCP patterns at specific frequencies of (a) f = 1 GHz, (b) f = 1.3 GHz, (c) f = 1.6 GHz in multiband antenna

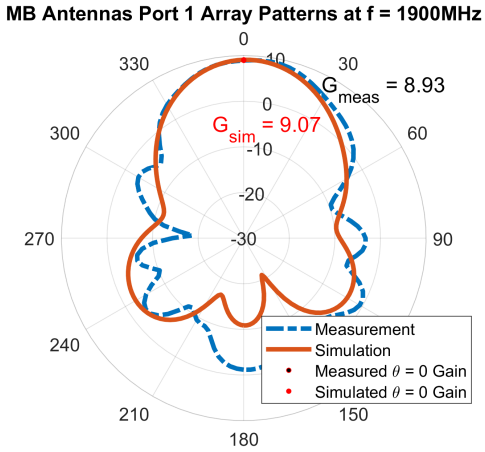

(a)

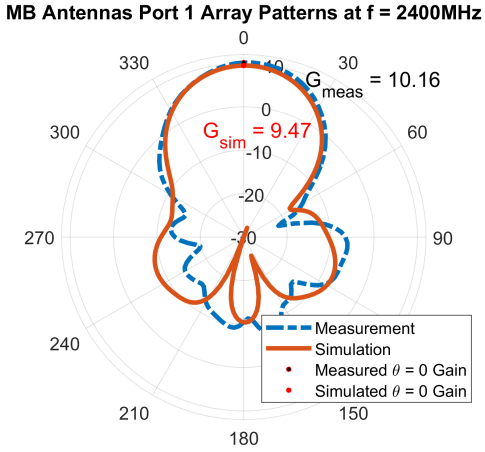

(b)

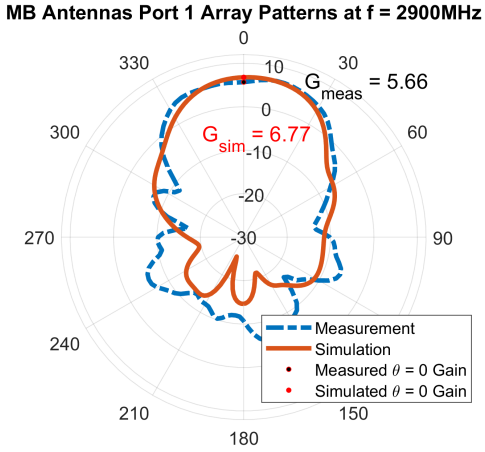

(c)

Figure 4.20: MB antenna port 1 radiation patterns at specific frequencies of (a) f = 1.9 GHz, (b) f = 2.4 GHz, (c) f = 2.9 GHz in multiband antenna

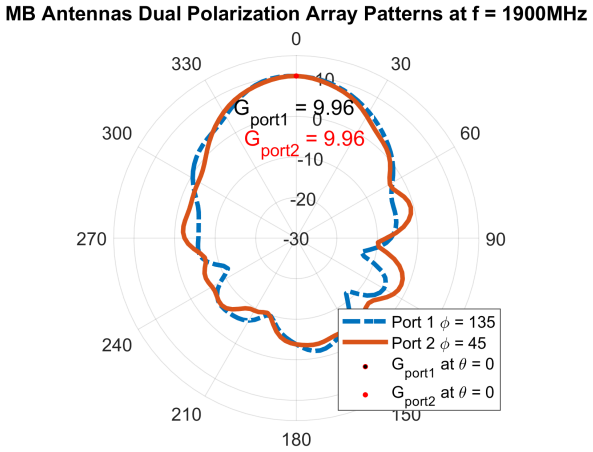

(a)

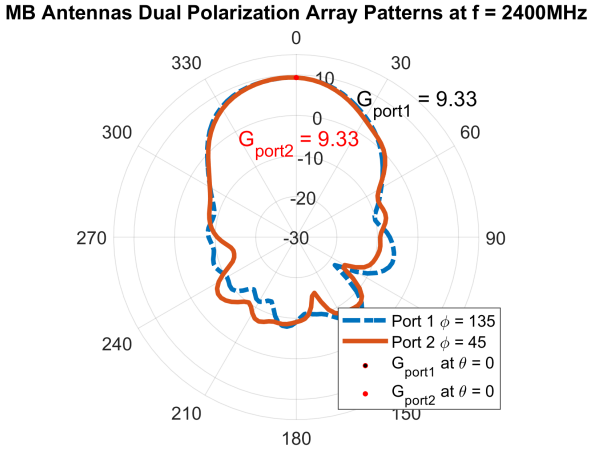

(b)

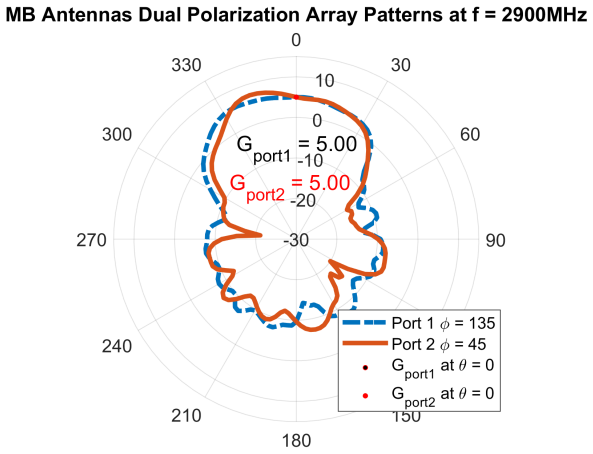

(c)

Figure 4.21: MB antenna dual polarized radiation patterns at specific frequencies of (a) f = 1.9 GHz, (b) f = 2.4 GHz, (c) f = 2.9 GHz in multiband antenna

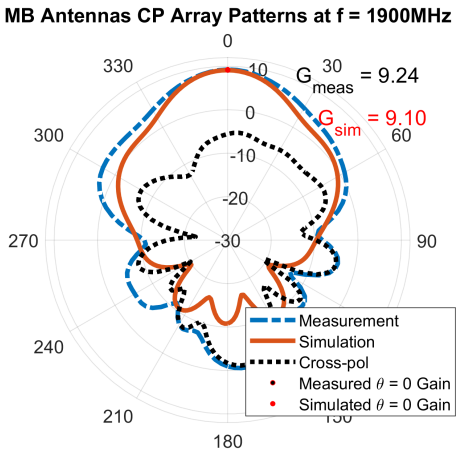

(a)

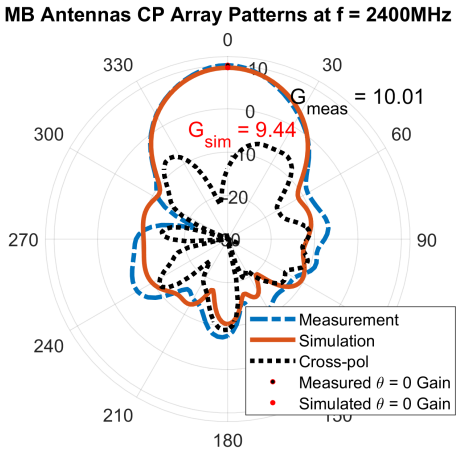

(b)

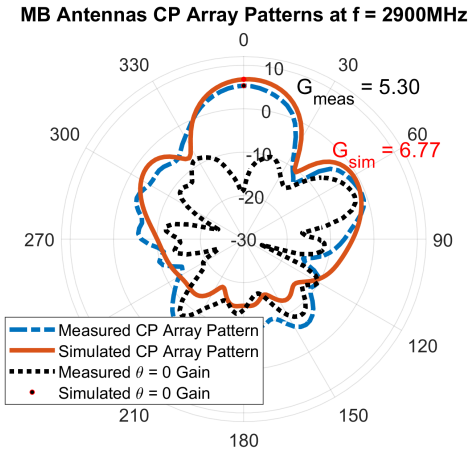

(c)

Figure 4.22: MB antenna RHCP patterns at specific frequencies of (a) f = 1.9 GHz, (b) f = 2.4 GHz, (c) f = 2.9 GHz in multiband antenna

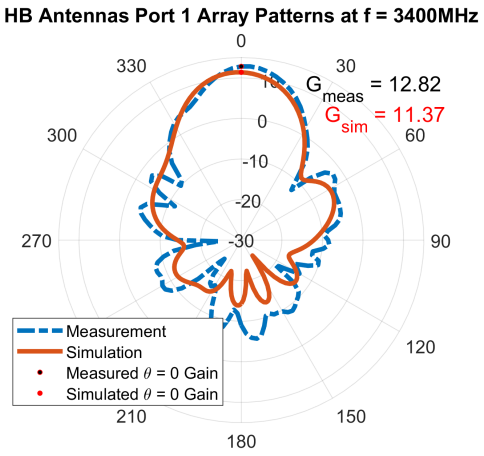

(a)

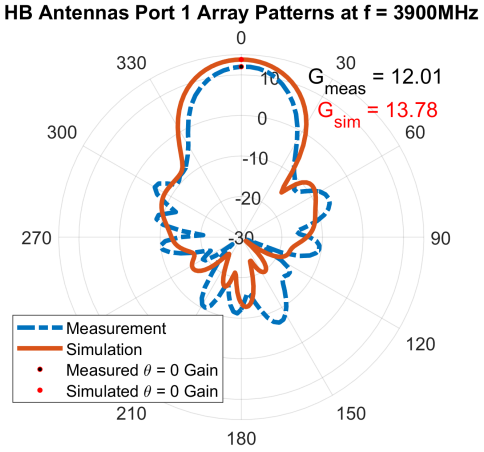

(b)

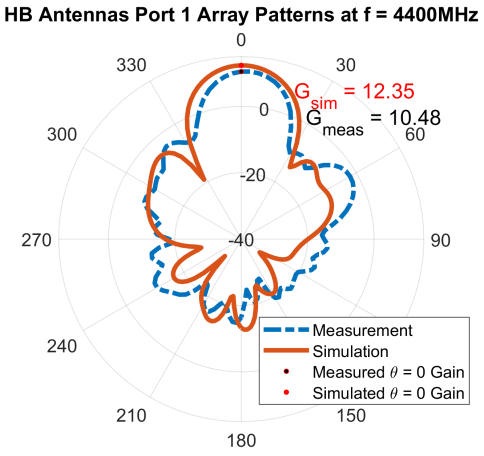

(c)

Figure 4.23: HB antenna port 1 radiation patterns at specific frequencies of (a) f = 3.4 GHz, (b) f = 3.9 GHz, (c) f = 4.4 GHz in multiband antenna

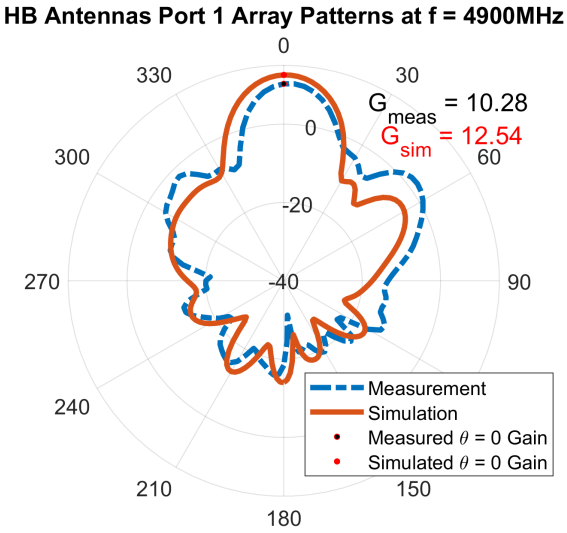

(a)

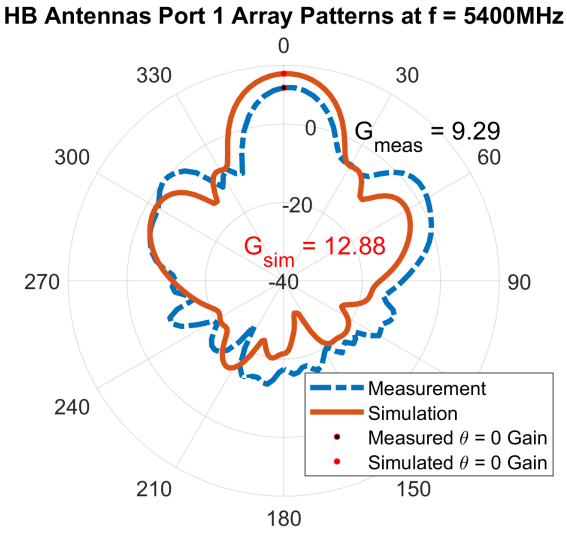

(b)

Figure 4.24: HB antenna port 1 radiation patterns at specific frequencies of (a) f = 4.9 GHz and (b) f = 5.4 GHz in multiband antenna

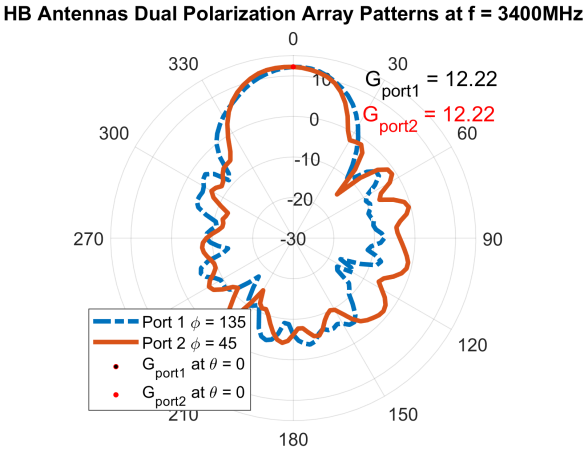

(a)

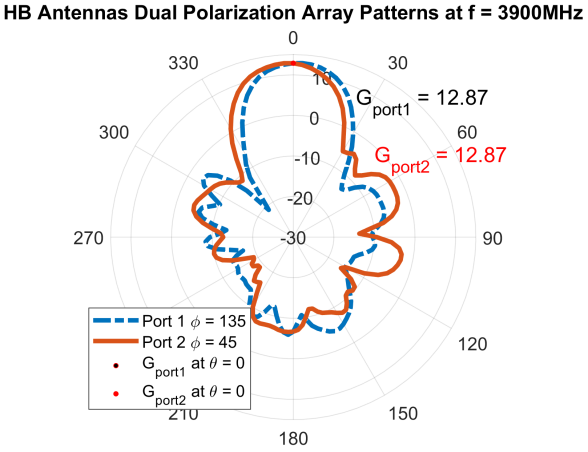

(b)

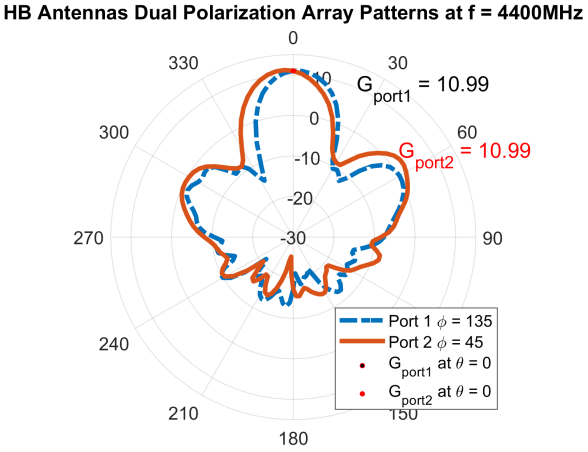

(c)

Figure 4.25: HB antenna dual-polarization array pattern at specific frequencies of (a) f = 3.4 GHz, (b) f = 3.9 GHz, and (c) f = 4.4 GHz in the multiband antenna

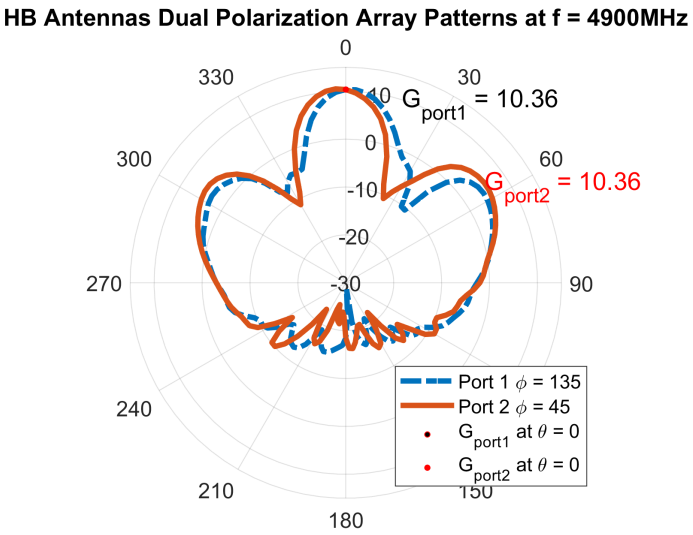

(a)

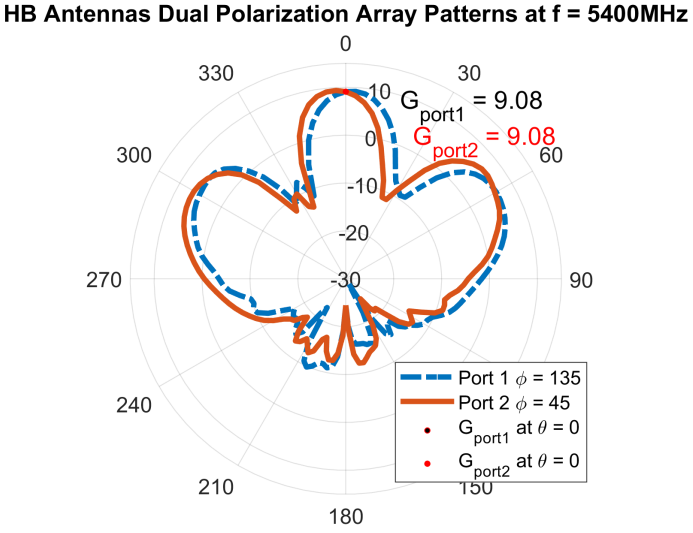

(b)

Figure 4.26: HB antenna dual-polarization array pattern at specific frequencies of (a) f = 4.9 GHz, and (b) f = 5.4 GHz in the multiband antenna

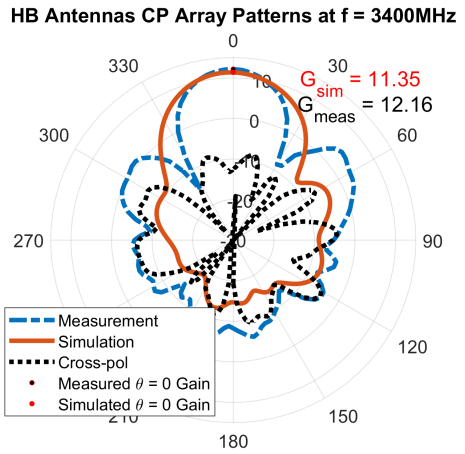

(a)

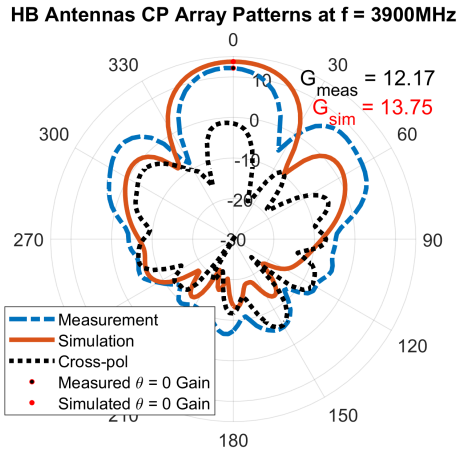

(b)

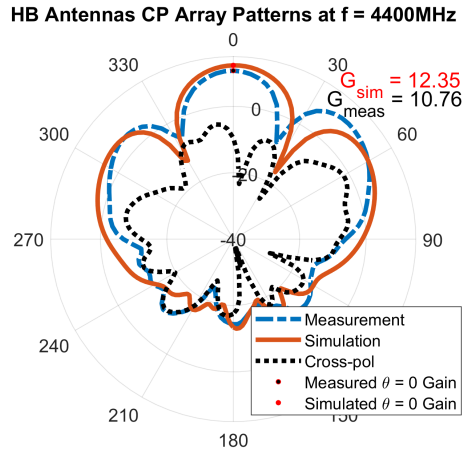

(c)

Figure 4.27: HB antenna CP array pattern at specific frequencies of (a) f = 3.4 GHz, (b) f = 3.9 GHz, and (c) f = 4.4 GHz in the multiband antenna

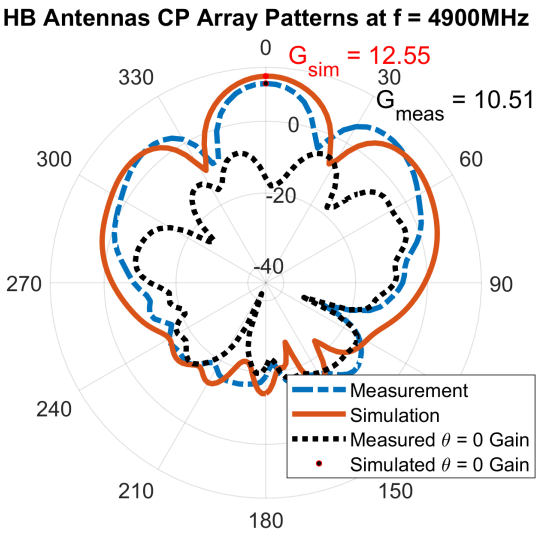

(a)

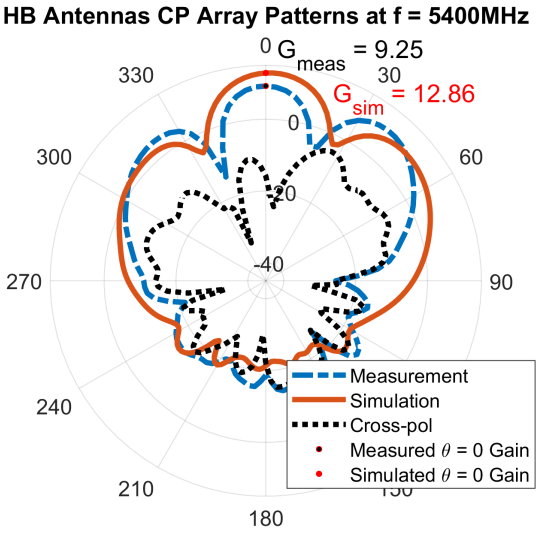

(b)

Figure 4.28: HB antenna CP array pattern at specific frequencies of (a) f = 4.9 GHz, and (b) f = 5.4 GHz

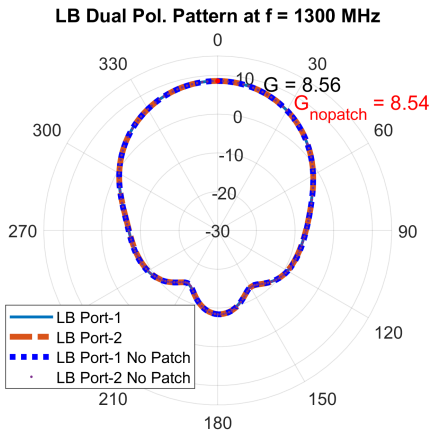

(a)

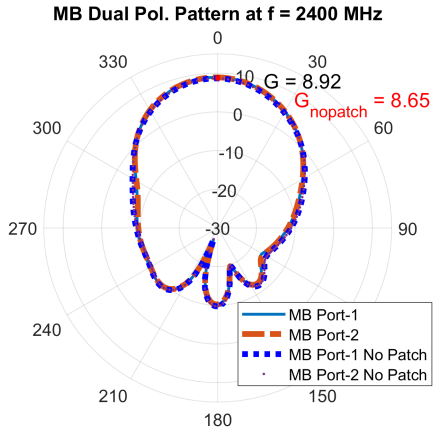

(b)

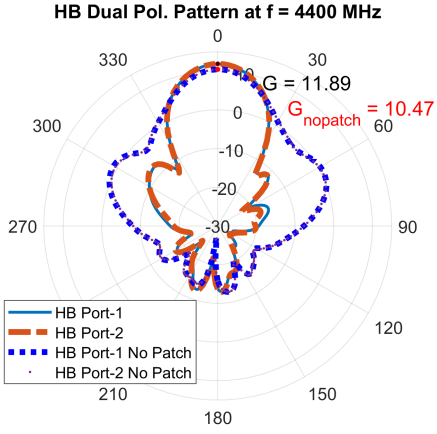

(c)

Figure 4.29: LB, MB, and HB antenna dual polarization pattern with a patch and without a patch at specific frequencies of (a) f = 1 GHz, (b) f = 2.4 GHz, and (c) f = 4.4 GHz in the multiband antenna

4.5 Chapter Conclusion

In this chapter, a multiband shared aperture antenna is formed with the designed antennas in Chapter 3. First, shared aperture simulations are made and it is seen that bandwidths and radiation patterns do not change significantly. Then fabricated prototype antennas are merged and their measurements are taken and compared with the simulation results. At some points, the results do not match exactly. The reasons may be measurement errors, simulation errors, fabrication errors, or mounting errors. But in general, the radiation pattern and S-parameters are close to each other, showing that the designed shared aperture antenna operates as desired. Radiation patterns with and without patch results are given. Having no patch increases the side lobe level of the HB antenna array, and does not affect the MB and LB antenna patterns significantly. Hence, having a patch is the better option for the HB array.

CHAPTER 5

CONCLUSION & FUTURE WORK

In this thesis, the shared aperture crossed-dipole antenna concept as one of the most intriguing antenna design methods recently used in many application fields is studied. Recent hot research concepts like FSS, shared-aperture antenna, crossed-dipole antenna with dual or circular polarization, and electromagnetic transparency are investigated and used throughout the design and prototype tests. Their structural and electromagnetic properties are analyzed in the simulation program as ™HFSS and their characteristics are extracted and calculated using MATLAB software. After the simulations are done, designed antennas are fabricated and tested via a ™Rohde-Schwarz ZVA 40 vector network analyzer and Satimo antenna measurement laboratory. Then these antennas are placed together to form a shared aperture antenna and analyzed again. The results are similar to the simulation results in general.

Throughout the designs, a low-frequency band (LB) antenna with a bandwidth of 1-1.6 GHz, a middle-frequency band (MB) antenna with 1.8-2.9 GHz, and a high-frequency band (HB) antenna with 3.3-5.5 GHz are designed. Besides, these antennas are electromagnetically transparent to each other, meaning that their radiation can pass through the antenna surface with minimal losses and radiation pattern distortion. Their transparency characteristic comes from the bandpass filter FSS unit cell design. While designing FSS unit cells, key parameters are the bandwidth, and filtering characteristics for higher incidence angles and having small size. For the MB antenna, key parameters are mostly satisfied; however, the LB antenna has problems with the parameters to obtain a wideband passband filter with the antenna design combined. Only four unit cells are used to obtain a cross-dipole antenna shape. So antennas have both transparent surface and antenna properties. Their design steps and im-

portant design parameters are explained. Different polarization capabilities are tested with different feeding phases to see the "quad-polarization" capability. Then antennas are used together in a shared aperture form. To improve the directivity, MB and HB antennas are designed as arrays, so their radiation performance is improved. Apart from that, EM transparent surface and cross-dipole antenna design methods used in this thesis can also be used for different frequencies. As a result, triband shared aperture antenna structure can be used in a variety of applications with three different frequencies with four different polarization options. Also, these antennas can be used alone or in a dual-band antenna form, their array can be designed and used. Thus, cross-dipole antennas and shared aperture antennas prove their promising aspects for today's and future design antenna designs.

In the design, some points need to be improved in future work. Firstly, isolation between the ports needs to be improved for the LB antenna. The design goal is to obtain at least 20 dB of isolation within the bandwidth. But LB antenna isolation decreases to 14 dB around 1.15 GHz in measurement. To improve the isolation, an optimized design can be made by changing the distances of dipole arms and extending Y-feeding tail lengths to have longer distances between Y-feeding arms. Also design changes such as chokes, slots, and vias can be added to improve isolation. The second problem is the isolation between different bandwidths. Since antenna bandwidths are close to each other, the isolation around frequencies between the cutoffs of antennas decreases significantly. Antenna bandwidths can be selected to be further from each other to improve cross-band isolation. Thirdly, the antenna height profile can be reduced by using structures like metamaterials, high impedance surfaces (HIS), artificial magnetic conductors (AMC), and FSSs. Hence the height distance between the reflective surface and the antenna does not have to be around $\lambda/4$, it can be reduced. Finally, the LB antenna's transparency characteristic is more lossy than the MB and HB surfaces. Designing the LB antenna with a different method or technique with a wide bandwidth of EM transparency would decrease the losses and improve the triband antenna performance.

REFERENCES

[1] B. A. Munk, *Frequency selective surfaces: theory and design*. John Wiley & Sons, 2000.

[2] Y. Pan, J. Dong, and M. Wang, "Equivalent circuit-assisted multi-objective particle swarm optimization for accelerated reverse design of multi-layer frequency selective surface," *Nanomaterials*, vol. 12, no. 21, p. 3846, 2022.

[3] M. Sun, S. Bie, L. Miao, Q. Chen, and J. Jiang, "An angular stabilized frequency selective surface by using capacitance layers structure," *Progress In Electromagnetics Research Letters*, vol. 87, pp. 97–103, 2019.

[4] B. S. da Silva, A. L. P. d. S. Campos, and A. G. Neto, "Equivalent circuit model for analysis of frequency selective surfaces with ring and double concentric ring apertures," *IET Microwaves, Antennas & Propagation*, vol. 14, no. 7, pp. 600–607, 2020.

[5] F. Huo, F. Liu, M. Zhu, and J. Bao, "Design of miniaturized and polarization-insensitive double-layer frequency selective surface based on meander lines," *International Journal of Antennas and Propagation*, vol. 2021, no. 1, p. 9576494, 2021.

[6] U. U. Hussine, *Circularly Polarized Antennas for GNSS Applications*. The University of Liverpool (United Kingdom), 2021.

[7] C. A. Balanis, *Advanced engineering electromagnetics*. John Wiley & Sons, 2012.

[8] V. Yadav, L. Kumar, and P. Kumar, "Evolution and development of wireless communication system," in *2019 International Conference on Computing, Power and Communication Technologies (GUCON)*, pp. 53–57, IEEE, 2019.

[9] Y. He, Z. Pan, X. Cheng, Y. He, J. Qiao, and M. M. Tentzeris, "A novel dual-band, dual-polarized, miniaturized and low-profile base station antenna," *IEEE*

Transactions on Antennas and Propagation, vol. 63, no. 12, pp. 5399–5408, 2015.

[10] G.-N. Zhou, B.-H. Sun, Q.-Y. Liang, S.-T. Wu, Y.-H. Yang, and Y.-M. Cai, "Triband dual-polarized shared-aperture antenna for 2g/3g/4g/5g base station applications," *IEEE Transactions on Antennas and Propagation*, vol. 69, no. 1, pp. 97–108, 2020.

[11] D. He, Y. Chen, and S. Yang, "A low-profile triple-band shared-aperture antenna array for 5g base station applications," *IEEE Transactions on Antennas and Propagation*, vol. 70, no. 4, pp. 2732–2739, 2021.

[12] Y. Chen and A. Raza, "A novel broadband$\pm$45° dual-polarized cross-dipole antenna with multimode resonance," *International Journal of RF and Microwave Computer-Aided Engineering*, vol. 2023, no. 1, p. 8847440, 2023.

[13] Y. Zhu, Y. Chen, and S. Yang, "Decoupling and low-profile design of dual-band dual-polarized base station antennas using frequency-selective surface," *IEEE Transactions on Antennas and Propagation*, vol. 67, no. 8, pp. 5272–5281, 2019.

[14] M. A. Honarvar, N. Hamidi, and B. S. Virdee, "Multiband antenna for portable device applications," *Microwave and Optical Technology Letters*, vol. 57, no. 4, pp. 956–959, 2015.

[15] C.-X. Mao, S. Gao, Y. Wang, and B. Sanz-Izquierdo, "A novel multiband directional antenna for wireless communications," *IEEE Antennas and Wireless Propagation Letters*, vol. 16, pp. 1217–1220, 2016.

[16] W.-J. Liao, S.-H. Chang, and L.-K. Li, "A compact planar multiband antenna for integrated mobile devices," *Progress In Electromagnetics Research*, vol. 109, pp. 1–16, 2010.

[17] P. Mei, X. Q. Lin, G. F. Pedersen, and S. Zhang, "Design of a triple-band shared-aperture antenna with high figures of merit," *IEEE Transactions on Antennas and Propagation*, vol. 69, no. 12, pp. 8884–8889, 2021.

[18] X. Yi, L. Zhou, S. Hao, and X. Chen, "Dual-band high-gain shared-aperture antenna integrating fabry-perot and reflectarray mechanisms," *Electronics*, vol. 11, no. 13, p. 2017, 2022.

[19] C. Chen, "A dual wideband compact shared-aperture microstrip patch/fabry–perot resonator cavity antenna," *IEEE Transactions on Antennas and Propagation*, vol. 70, no. 12, pp. 11526–11536, 2022.

[20] Y. Liu, H. Yi, F.-W. Wang, and S.-X. Gong, "A novel miniaturized broadband dual-polarized dipole antenna for base station," *IEEE Antennas and Wireless Propagation Letters*, vol. 12, pp. 1335–1338, 2013.

[21] C. Liao, B. Wang, C. Zhu, H. Hao, and B. Yin, "Broadband dual-polarized loop cross-dipole antenna for 5g base station applications," *Electronics*, vol. 9, no. 10, p. 1574, 2020.

[22] C.-X. Mao, S. Gao, Q. Luo, T. Rommel, and Q.-X. Chu, "Low-cost x/ku/ka-band dual-polarized array with shared aperture," *IEEE Transactions on Antennas and Propagation*, vol. 65, no. 7, pp. 3520–3527, 2017.

[23] X. Yang, L. Ge, J. Wang, *et al.*, "A differentially driven dual-polarized high-gain stacked patch antenna," *IEEE Antennas and Wireless Propagation Letters*, vol. 17, no. 7, pp. 1181–1185, 2018.

[24] H. H. Tran, I. Park, and T. K. Nguyen, "Circularly polarized bandwidth-enhanced crossed dipole antenna with a simple single parasitic element," *IEEE Antennas and Wireless Propagation Letters*, vol. 16, pp. 1776–1779, 2017.

[25] T. Li and Z. N. Chen, "Metasurface-based shared-aperture 5g S-/ K-band antenna using characteristic mode analysis," *IEEE Transactions on Antennas and Propagation*, vol. 66, no. 12, pp. 6742–6750, 2018.

[26] Y.-J. Liao, H.-L. Lin, *et al.*, "Polarization reconfigurable eccentric annular ring slot antenna design," *IEEE Transactions on Antennas and Propagation*, vol. 63, no. 9, pp. 4152–4155, 2015.

[27] Y. Cui, R. Li, and H. Fu, "A broadband dual-polarized planar antenna for 2g/3g/lte base stations," *IEEE transactions on antennas and propagation*, vol. 62, no. 9, pp. 4836–4840, 2014.

[28] S. X. Ta, I. Park, and R. W. Ziolkowski, "Crossed dipole antennas: A review," *IEEE Antennas and Propagation Magazine*, vol. 57, no. 5, pp. 107–122, 2015.

[29] R. Wu and Q.-X. Chu, "Multi-mode broadband antenna for 2g/3g/lte/5g wireless communication," *Electronics Letters*, vol. 54, no. 10, pp. 614–616, 2018.

[30] J. Wu, W. Yu, and J. Chen, "A broadband dual-polarized arm-overlapped dipole antenna for base station applications," *Progress In Electromagnetics Research C*, vol. 89, pp. 51–59, 2019.

[31] C. Zhao, X. Jin, and Q. Wei, "Wideband dual-polarized all-metal cross-dipole antenna with feeding column," *AEU-International Journal of Electronics and Communications*, vol. 153, p. 154246, 2022.

[32] F. Qin, S. S. Gao, Q. Luo, C.-X. Mao, C. Gu, G. Wei, J. Xu, J. Li, C. Wu, K. Zheng, *et al.*, "A simple low-cost shared-aperture dual-band dual-polarized high-gain antenna for synthetic aperture radars," *IEEE Transactions on Antennas and Propagation*, vol. 64, no. 7, pp. 2914–2922, 2016.

[33] V. K. Kothapudi and V. Kumar, "A single layer s/x-band series-fed shared aperture antenna for sar applications," *Progress In Electromagnetics Research C*, vol. 76, pp. 207–219, 2017.

[34] Q.-X. Chu, Y.-S. Wu, and Y.-L. Chang, "A novel electromagnetic transparent antenna in dual-band shared-aperture array," *IEEE Transactions on Antennas and Propagation*, vol. 70, no. 10, pp. 9894–9899, 2022.

[35] D. He, Q. Yu, Y. Chen, and S. Yang, "Dual-band shared-aperture base station antenna array with electromagnetic transparent antenna elements," *IEEE Transactions on Antennas and Propagation*, vol. 69, no. 9, pp. 5596–5606, 2021.

[36] C. Guo, G. Su, F. Xue, and B. Zhou, "A dual-polarized electromagnetic transparent antenna for dual-band antenna array," in *2022 IEEE MTT-S International Microwave Workshop Series on Advanced Materials and Processes for RF and THz Applications (IMWS-AMP)*, pp. 1–3, IEEE, 2022.

[37] J. Fan, J. Lin, J. Cai, and F. Qin, "Ultra-wideband circularly polarized cavity-backed crossed-dipole antenna," *Scientific Reports*, vol. 12, no. 1, p. 4569, 2022.

[38] S. X. Ta, H. Choo, I. Park, and R. W. Ziolkowski, "Multi-band, wide-beam, circularly polarized, crossed, asymmetrically barbed dipole antennas for gps applications," *IEEE Transactions on Antennas and Propagation*, vol. 61, no. 11, pp. 5771–5775, 2013.

[39] Y. Da, X. Chen, M. Li, Z. Zhang, A. A. Al-Hadi, A. Zhang, and A. A. Kishk, "Enhanced cross-polarization isolation of loop-dipole antenna array backed by dielectric cavities for 5g base stations," *Journal of Electromagnetic Waves and Applications*, vol. 35, no. 15, pp. 2034–2050, 2021.

[40] H.-H. Sun, H. Zhu, C. Ding, B. Jones, and Y. J. Guo, "Scattering suppression in a 4g and 5g base station antenna array using spiral chokes," *IEEE Antennas and Wireless Propagation Letters*, vol. 19, no. 10, pp. 1818–1822, 2020.

[41] H.-H. Sun, B. Jones, Y. J. Guo, and Y. H. Lee, "Suppression of cross-band scattering in interleaved dual-band cellular base-station antenna arrays," *IEEE Access*, vol. 8, pp. 222486–222495, 2020.

[42] R. C. Dai, H. Su, S. J. Yang, J.-H. Ou, and X. Y. Zhang, "Broadband electromagnetic-transparent antenna and its application to aperture-shared dual-band base station array," *IEEE Transactions on Antennas and Propagation*, vol. 71, no. 1, pp. 180–189, 2022.

[43] Y.-L. Chang and Q.-X. Chu, "Broadband dual-polarized electromagnetic transparent antenna for cross-band scattering suppression," *IEEE Antennas and Wireless Propagation Letters*, vol. 21, no. 7, pp. 1452–1456, 2022.

[44] C. F. Ding, X. Y. Zhang, Y. Zhang, Y. M. Pan, and Q. Xue, "Compact broadband dual-polarized filtering dipole antenna with high selectivity for base-station applications," *IEEE Transactions on Antennas and Propagation*, vol. 66, no. 11, pp. 5747–5756, 2018.

[45] J. Ren, Z. Wang, Y.-X. Sun, R. Huang, and Y. Yin, "Ku/ka-band dual-frequency shared-aperture antenna array with high isolation using frequency selective surface," *IEEE Antennas and Wireless Propagation Letters*, 2023.

[46] R. A. Pandhare, F. L. Lohar, C. Dhote, and Y. Solunke, "Design of fss based

radome wall for airborne radar application," *Journal of Microwaves, Optoelectronics and Electromagnetic Applications*, vol. 20, no. 4, pp. 855–869, 2021.

[47] M. M. Fakharian, P. Rezaei, and A. A. Orouji, "A reflectarray based on the folded sir patch-slot configuration backed on fss for low rcs," *Progress In Electromagnetics Research Letters*, vol. 47, pp. 119–124, 2014.

[48] G. H.-h. Sung, K. W. Sowerby, M. J. Neve, and A. G. Williamson, "A frequency-selective wall for interference reduction in wireless indoor environments," *IEEE Antennas and Propagation Magazine*, vol. 48, no. 5, pp. 29–37, 2006.

[49] R. S. Anwar, L. Mao, and H. Ning, "Frequency selective surfaces: A review," *Applied Sciences*, vol. 8, no. 9, p. 1689, 2018.

[50] A. Dalkılıç, "Analysis and design of conformal frequency selective surfaces," Master's thesis, Middle East Technical University, 2014.

[51] T. Hong, W. Xing, Q. Zhao, Y. Gu, and S. Gong, "Single-layer frequency selective surface with angular stability property," *IEEE Antennas and Wireless Propagation Letters*, vol. 17, no. 4, pp. 547–550, 2018.

[52] K. Sangeethalakshmi, S. R. Devi, N. Gangatharan, and P. Sivalakshmi, "Challenges & opportunities in frequency selective surfaces for emi shielding application: A theoretical survey," *Materials Today: Proceedings*, vol. 43, pp. 3947–3950, 2021.

[53] ANSYS Inc., *ANSYS HFSS, Release 2023R2*, 2023. `https://www.ansys.com/products/electronics/ansys-hfss`.

[54] D. S. Inc., *CST*, 2023. `https://www.3ds.com/products/simulia/cst-studio-suite`.

[55] F. Bayatpur, *Metamaterial-Inspired Frequency-Selective Surfaces.* PhD thesis, University of Michigan, 2009.

[56] N. Marcuvitz, *Waveguide handbook*. No. 21 in Radiation Laboratory Series, Iet, 1951.

[57] D. Ferreira, R. F. Caldeirinha, I. Cuinas, and T. R. Fernandes, "Square loop and slot frequency selective surfaces study for equivalent circuit model optimization," *IEEE Transactions on Antennas and Propagation*, vol. 63, no. 9, pp. 3947–3955, 2015.

[58] A. D. Inc., *LTSpice*, 2023. `https://www.analog.com/en/resources/design-tools-and-calculators/ltspice-simulator.html`.

[59] R. Yahya, A. Nakamura, and M. Itami, "Ultra-wideband fss-based antennas," in *UWB Technology and its Applications*, IntechOpen, 2018.

[60] M. Al-Joumayly and N. Behdad, "A new technique for design of low-profile, second-order, bandpass frequency selective surfaces," *IEEE transactions on antennas and propagation*, vol. 57, no. 2, pp. 452–459, 2009.

[61] K. Kaur and A. Kaur, "Polarization independent frequency selective surface for marine and air traffic radar applications," *Sādhanā*, vol. 47, no. 2, p. 81, 2022.

[62] S. Poddar, M. T. Hasan, and M. R. S. Rafi, "Computational approach of designing magnetfree nonreciprocal metamaterial," *arXiv preprint arXiv:2205.11038*, 2022.

[63] G. Feng, L. Chen, X. Xue, and X. Shi, "Broadband circularly polarized crossed-dipole antenna with a single asymmetrical cross-loop," *IEEE Antennas and Wireless Propagation Letters*, vol. 16, pp. 3184–3187, 2017.

[64] Q.-X. Chu, D.-L. Wen, and Y. Luo, "A broadband $\pm 45^{\circ}$ dual-polarized antenna with y-shaped feeding lines," *IEEE Transactions on Antennas and Propagation*, vol. 63, no. 2, pp. 483–490, 2015.

[65] R. Wu and Q.-X. Chu, "A broadband dual-polarized antenna with chamfers," *Microwave and Optical Technology Letters*, vol. 59, no. 3, pp. 631–635, 2017.

[66] Z. Bao, Z. Nie, and X. Zong, "A novel broadband dual-polarization antenna utilizing strong mutual coupling," *IEEE transactions on antennas and propagation*, vol. 62, no. 1, pp. 450–454, 2013.

[67] "Satimo." https://www.mvg-world.com/en/satimo-is-mvg. Accessed:August 2024.

[68] C. A. Balanis, *Antenna theory: analysis and design*. John wiley & sons, 2016.

Appendix A

DERIVATION OF PASSBAND FSS RESONANCE FREQUENCY

In this appendix, the LC resonator's passband resonance frequency expression will be derived.

The Equation 2.15 is the solution of the equivalent circuit given in Figure 2.18. It is well known that inductor reactance is $j\omega L$ and capacitance reactance is $1/j\omega C$. So Figure 2.18 can also be shown as Figure A.1. Capacitance is showed as X_C, and inductances are showed as X_{L1} and X_{L2}. X_{L2} and X_C are in series and they are parallel to X_{L1}. The equivalent reactance can be calculated as: [21]

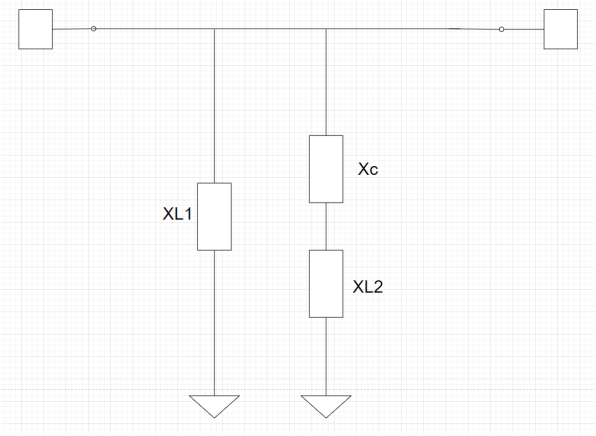

Figure A.1: EC model of FSS unit cell as reactances

$$X_{eq} = j\omega L_1 \,||\, \left(j\omega L_2 + \frac{1}{j\omega C} \right) \tag{A.1}$$

$$X_{eq} = j\omega L_1 \,||\, \left(\frac{1 - \omega^2 L_2 C}{j\omega C} \right) \tag{A.2}$$

$$X_{eq} = \frac{\left(\frac{1-\omega^2 L_2 C}{j\omega C}\right) * j\omega L_1}{\left(\frac{1-\omega^2 L_2 C}{j\omega C}\right) + j\omega L_1} \tag{A.3}$$

$$X_{eq} = \frac{j\omega L_1 - j\omega^3 L_1 L_2 C}{1-\omega^2 L_2 C - \omega^2 L_1 C} \tag{A.4}$$

$$X_{eq} = \frac{j\omega L_1 - j\omega^3 L_1 L_2 C}{1-\omega^2 \left(L_2 + L_1\right) C} \tag{A.5}$$

In Equation A.5, if nominator becomes zero, reactance becomes zero, meaning that the signal flows to ground and band stop filter characteristic is observed. If denominator becomes zero, reactance goes to infinity, so signal flows to other port, meaning that bandpass characteristic is observed. So,

$$1-\omega^2 \left(L_2 + L_1\right) C = 0 \tag{A.6}$$

$$\omega = 2\pi f_{res} = \frac{1}{\sqrt{\left(L_2 + L_1\right) C}} \tag{A.7}$$

$$f_{res} = \frac{1}{2\pi\sqrt{\left(L_2 + L_1\right) C}} \tag{A.8}$$

Appendix B

HORIZONTAL ELECTRIC DIPOLE ANTENNA ON A GROUND PLANE CHARACTERISTICS

In this appendix, the horizontal electric dipole antenna's main properties of the electric field, radiation intensity, gain, and radiation patterns will be explained.

Horizontal electric dipole on a ground plane can be examined for the antenna design [7]. Figure B.1 demonstrates the horizontal dipole antenna on a ground plane. The combined electric field expression of the antenna for far-field is given in Equation B.1, and the radiation intensity of the antenna is defined in Equation B.2 above the ground plane. Then, for the normalized gain pattern, the well-known antenna theory formulas can be applied. These formulas are given below in scalar form.

$$E(\theta,\phi) = \frac{j\eta k I_0 l e^{-jkr}}{4\pi r}\sqrt{1-sin^2(\phi)sin^2(\theta)}2jsin(khcos(\theta)) \tag{B.1}$$

$$U(\theta,\phi) \simeq r^2\frac{|E(\theta,\phi)|^2}{2\eta} = \frac{\eta}{2}\left|\frac{I_0 l}{\lambda}\right|^2\left(1-sin^2(\phi)sin^2(\theta)\right)sin^2(khcos(\theta)) \tag{B.2}$$

$$G(\theta,\phi) = \frac{4\pi U(\theta,\phi)}{P_{inc}} \tag{B.3}$$

$$G_{\text{norm}}(\theta,\phi) = \frac{G(\theta,\phi)}{max\left(G(\theta,\phi)\right)} \tag{B.4}$$

$$G_{dB}(\theta,\phi) = 10log(G_{\text{norm}}(\theta,\phi)) \tag{B.5}$$

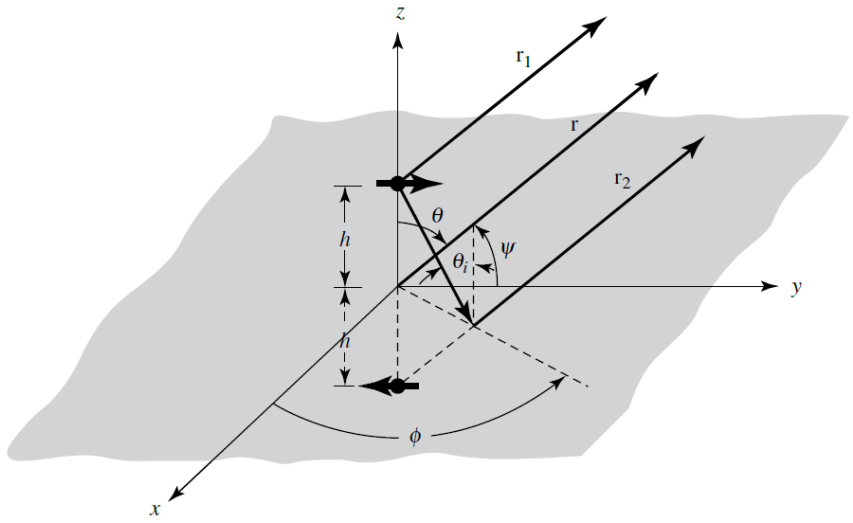

Figure B.1: Horizontal electric dipole antenna on a ground plane [7]

The normalized radiation pattern is plotted in Figure B.2. Plots are obtained for the distance of h = $\lambda/4$. For a given distance from the ground, the maximum radiation intensity is obtained at θ = 0° according to Equation B.2. Hence maximum gain and directivity values are obtained at θ = 0°, which can be calculated using Equation B.3 and Equation B.6, respectively. Directivity of the half-wave dipole antenna is calculated as $D_0 = 5.21$ or $D_0 = 7.17dB$. For both ϕ = 45° and ϕ = 135°, the radiation pattern is the same with half power beamwidth (HPBW) nearly equal to 100°. Designed crossed-dipole antennas are not exactly the same as the aforementioned dipole antenna since it is mounted on a PCB, and the dipole antenna shape is different. Their gain, directivity, HPBW, and orientation parameters differ from the theoretical calculations of the thin half-wavelength dipole antenna. However, theoretical calculations give intuition and an idea of the results of designed antennas.

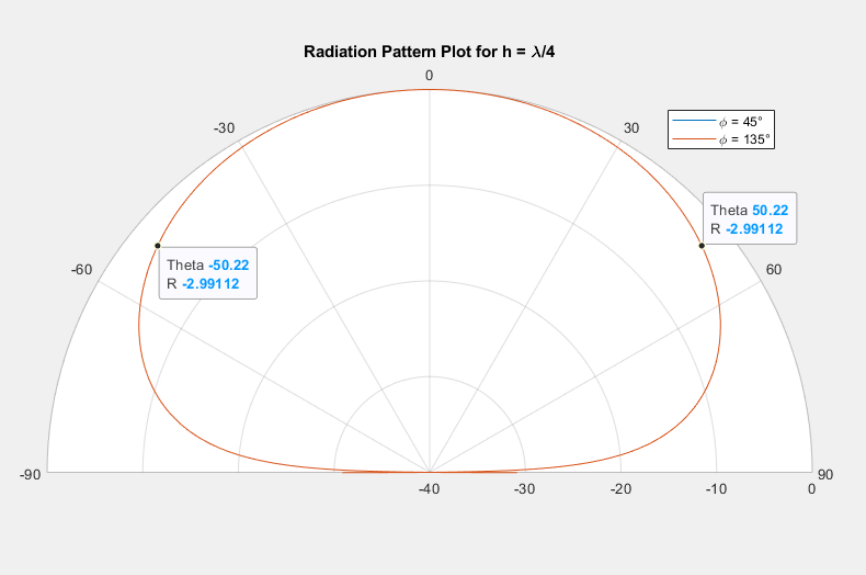

Figure B.2: Radiation pattern of the antenna at $\phi = 45°$ and $\phi = 90°$

$$D_0 = \frac{4\pi U_{\max}}{P_{\text{rad}}} = \begin{cases} \frac{4\sin^2(kh)}{R(kh)} & \text{if } (h \leq \lambda/4) \\ \\ \frac{4}{R(kh)} & \text{if } (h > \lambda/4) \end{cases} \tag{B.6}$$

$$R_{kh} = \frac{2}{3} - \frac{sin(2kh)}{2kh} - \frac{cos(2kh)}{(2kh)^2} + \frac{sin(2kh)}{(2kh)^3} \tag{B.7}$$

Appendix C

RADIATION PATTERN AND GAIN CALCULATION FOR THE DUAL AND CIRCULAR POLARIZATION

In this appendix, cross-dipole antenna pattern calculations for dual and circular polarization are explained.

One port feeding results can be superposed and two port patterns can be obtained. It is known that in the far field, the electric field is a function of θ and ϕ. As shown in Equation C.1, the electric field can be written as the sum of E_θ and E_ϕ. Since cross-dipole antenna has two ports, these fields are the superposition of the separate ports' fields, which is given in Equation C.2 and Equation C.3, where a_1 and a_2 are the port feeding coefficients. If one the coefficient is 0, then it corresponds to single-port feeding. Besides, a_1 and a_2 are complex, hence different phase and different magnitude feedings are possible. For dual polarization, a_1 = a_2; and for the circular polarization, $|a_1|$ = $|a_2|$ with 90° phase difference. The total electric field can be calculated with Equation C.4. In the next step, radiation intensity U can be calculated in Equation C.5, where η is the wave impedance in the free space equal to 120π. Then gain value G is obtained in Equation C.6 and finally gain is represented in logarithmic scale in Equation C.7 [68]. To see the cross-polarization for circular polarization, Equation C.8 or C.9 can be used whether the cross-polarization direction, where $\mathbf{E_R}$ is the right-handed electric field and E_L is the left-handed electric field obtained from E_θ and E_ϕ. In this thesis, only RHCP calculations are shown for simplicity, but LHCP results can also be calculated with these equations.

The relationship between radiated power P_{rad}, input power P_{in} and the efficiency e_{cd} is given in Equation C.10. The term $P_{in}^{'}$ in Equation C.6 is the input power of the antenna. Since the measured electric fields also include the antenna efficiency in

Satimo antenna measurement setup, the result in Equation C.11 is obtained. P_{rad} can be obtained in Equation C.12. In Satimo, measurements are made for the angles θ and ϕ with 3° steps. As a result, closed-form equation cannot e applied. Numerical expressions can be applied in MATLAB program to solve the $P_{in}^{'}$. Equation C.13 is the numerical expression to calculate the $P_{in}^{'}$ value [68].

$$\overline{E}(\theta,\phi) = \overline{E_\theta}(\theta,\phi)\hat{a_\theta} + \overline{E_\phi}(\theta,\phi)\hat{a_\phi} \tag{C.1}$$

$$\overline{E_\theta}(\theta,\phi) = a_1\overline{E_{1\theta}}(\theta,\phi)\hat{a_\theta} + a_2\overline{E_{2\theta}}(\theta,\phi)\hat{a_\theta} \tag{C.2}$$

$$\overline{E_\phi}(\theta,\phi) = a_1\overline{E_{1\phi}}(\theta,\phi)\hat{a_\phi} + a_2\overline{E_{2\phi}}(\theta,\phi)\hat{a_\phi} \tag{C.3}$$

$$E_{Total}(\theta,\phi) = \sqrt{|\overline{E_\theta}(\theta,\phi)|^2 + |\overline{E_\phi}(\theta,\phi)|^2} \tag{C.4}$$

$$U(\theta,\phi) = \frac{|E_{Total}(\theta,\phi)|^2}{2\eta} \tag{C.5}$$

$$G(\theta,\phi) = \frac{4\pi U(\theta,\phi)}{P_{in}^{'}} \tag{C.6}$$

$$G_{dB}(\theta,\phi) = 10log(|G(\theta,\phi)|) \tag{C.7}$$

$$E_R = \frac{E_\theta + E_\phi}{\sqrt{2}} \tag{C.8}$$

$$E_L = \frac{E_\theta - E_\phi}{\sqrt{2}} \tag{C.9}$$

$$P_{rad} = e_{cd}P_{in} \tag{C.10}$$

$$P_{in}^{'} = P_{rad} \tag{C.11}$$

$$P_{rad} = \int_0^{2\pi} \int_0^{\pi} U(\theta, \phi) sin(\theta)\, d\theta\, d\phi \tag{C.12}$$

$$P_{rad} = \left(\frac{\pi}{N}\right)\left(\frac{2\pi}{M}\right) \sum_{j=1}^{M} \sum_{i=1}^{N} U\left(\theta_i, \phi_j\right) sin\left(\theta_i\right) \tag{C.13}$$

Appendix D

ANTENNA ARRAY THEORY AND ITS APPLICATION

In this appendix, antenna arrays' pattern expressions will be extracted by using well-known array theory formulas.

Assuming that there are two horizontal infinitesimal dipoles placed along the z-axis, the far-field electric field expression of these dipoles is given in Equation D.1, with the far-field observations for the amplitude and phase variations [68]. The far-field observation is given in Figure D.1. Then the expression is rearranged to Equation D.2. In Equation D.2, field expression can be separated as the electric field of a single antenna on the reference point, or namely element factor, multiplied by the array factor term, which is shown in the Equation D.3. Hence, the two-element antenna array expression is given as Equation D.4.

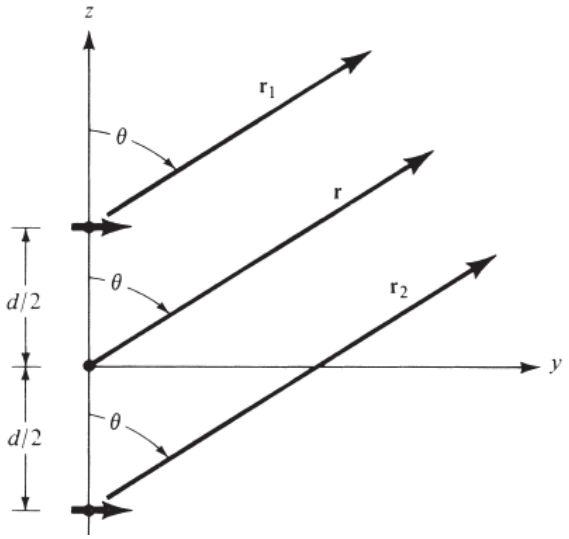

Figure D.1: Far-field observation for two-element antenna array

$$\overline{E} = \frac{j\eta k I_0 l e^{-jkr}}{4\pi r} cos(\theta)[e^{j(kdcos(\theta)+\beta)/2} + e^{-j(kdcos(\theta)+\beta)/2}]\hat{a_\theta} \tag{D.1}$$

$$\overline{E} = \frac{j\eta k I_0 l e^{-jkr}}{4\pi r} cos(\theta) 2cos\left[\frac{1}{2}kdcos(\theta)+\beta)\right]\hat{a_\theta} \tag{D.2}$$

$$\overline{E_{Array}} = \hat{a_\theta}\left(\overline{E}\, of\ single\ antenna\ element\ on\ reference\right) * Array Factor \tag{D.3}$$

$$AF = 2cos\left[\frac{1}{2}kdcos(\theta)+\beta)\right] \tag{D.4}$$

where k is the wave number, d is the distance between antenna elements, β is the phase. The array factor AF equation is given in Equations D.5 and D.6 for the N-element linear antenna array case.

$$AF = 1 + e^{j(kdcos(\theta)+\beta)} + e^{j2(kdcos(\theta)+\beta)} + ... + e^{j(N-1)(kdcos(\theta)+\beta)} \tag{D.5}$$

$$AF = \sum_{n=1}^{N} e^{j(n-1)(kdcos(\theta)+\beta)} \tag{D.6}$$

The array factor formula extends as Equation D.7 for the planar antenna array case with uniform excitation. Figure D.2 shows the planar array far-field observation.

$$AF = I_o \sum_{m=1}^{M} e^{j(m-1)(kd_x cos(\theta)+\beta_x)} \sum_{n=1}^{N} e^{j(n-1)(kd_y cos(\theta)+\beta_y)} \tag{D.7}$$

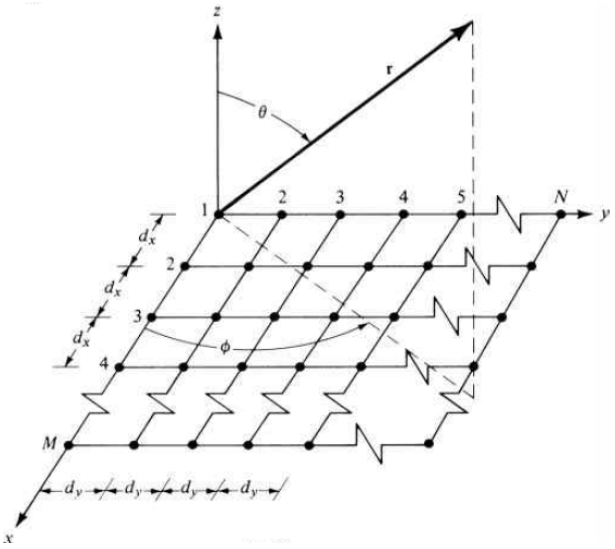

Figure D.2: Far-field observation for $M \times N$-element planar antenna array

In this thesis, there are two MB antennas and four HB antennas. So, the linear antenna array formula is applied for the MB antenna, and the planar array antenna is applied for the HB antenna due to the placements. The distance between MB antennas is 76mm. Four HB antennas are placed like rectangle corners with edge lengths of 76mm and 80mm.

Since measurements are taken port by port, all antenna ports' electric field components E_θ and E_ϕ values are extracted separately, then they are summed to obtain the total E_θ and E_ϕ of the array. Then the formulas explained in Appendix C are applied to attain the array pattern.